UNIVERSITÀ
DEGLI STUDI
DI TRIESTE

Dottorato di ricerca in Fisica

Ciclo XXXVII

Trapping, loading and imaging fermionic ytterbium atom arrays

Settore scientifico-disciplinare: Fis/03

Doctoral candidate:
Alessandro Thomas Muzi Falconi

Supervisor:
Prof. Francesco Scazza

Coordinator:
Prof. Francesco Longo

Academic year 2025-2026

Contents

Introduction

In the last decades, neutral-atom-based experiments have become one of the leading platforms for quantum science and technology. Atom cooling and trapping techniques have already brought outstanding scientific breakthroughs such as the first realization of a Bose-Einstein condensate [1, 2], the observation of a quantum phase transition from a superfluid to a Mott insulator [3] and the development of the most precise clocks in the world [4], to name just a few. However, recent technological advancements are driving the field towards fully programmable experiments, in which each atom can be manipulated and detected individually. In this context, a new generation of experimental platforms has emerged, aiming to harness single-atom control to achieve long-sought goals in quantum information processing, precision metrology, and quantum simulation [5, 6].

Optical tweezers–micrometer-sized traps capable of confining individual atoms–are one of the key ingredients enabling such level of control [7]. Neutral atoms trapped in tweezer arrays provide a means to realize programmable quantum systems in which each component can be individually manipulated and detected with high fidelity. This has extended the control available in quantum simulation experiments, allowing the investigation of defect-free, frustrated lattice models where each site can be individually positioned in the desired geometry [8, 9]. Moreover, tweezers can be combined with other optical traps to gain local control in extended systems [10–12] as well as to deterministically prepare mesoscopic ensembles of few fermionic atoms [13–16]. The capability to engineer many-body Hamiltonians and to realize low-entropy systems with a bottom-up approach may pave the way to the observation of phenomena that have so far eluded analog quantum simulators based on ultracold atoms [17–19].

Tweezer arrays are also the dominant platform for neutral-atom-based quantum information processing. In fact, each individually-trapped atom can serve as a physical qubit, by encoding information in one of the available two-level systems within its internal structure. Single qubits can be manipulated with controlled local operations and two-qubit entangling gates are typically performed via long-range Rydberg interactions [17, 20, 21]. The programmable nature of tweezer arrays is also crucial for realizing complex information processing architectures, with separated preparation, computation and readout zones which enable parallelized operations as well as to detect and correct errors [22–24]. Quantum error correction, a key requirement for fault-tolerant quantum processors, relies on entangling multiple physical qubits to form a single error-corrected logical qubit. This has further raised the bar for the number of atoms which need to be trapped, entangled and imaged with high fidelity for useful quantum computation. Furthermore, quantum error correction calls for the development of novel readout schemes capable of performing fast and minimally destructive mid-circuit detection, interleaved with other quantum operations.

Developing new tools and techniques to entangle and detect a large number of qubits also holds strong implications for quantum metrology. State-of-the-art optical lattice clocks have achieved unprecedented precision [25, 26] but are now approaching the so-called standard quantum limit, which poses a fundamental bound on the attainable uncertainty in uncorrelated systems. On the other hand, emerging tweezer-clock experiments [27–31] are exploring the possibility of harnessing single-atom control to prepare entangled states that could enhance the phase-estimation accuracy beyond this limit [32, 33]. Large and programmable arrays leveraging metrologically-useful entanglement and mid-circuit detection for continuous clock interrogation could eventually surpass the performances of optical-lattice clocks and allow to address open

questions in fundamental physics, including the possible variation of physical constants [34] and tests of general relativity [35–39].

The last years have already witnessed remarkable experimental achievements driven by novel tools in the manipulation and detection of individual neutral atoms, with scientific results ranging from investigations of the Fermi-Hubbard model in optical lattices [40–42] to the generation multi-particle entangled states [30, 31, 43]. In this context, lines between the different fields and applications appear somewhat blurred as each experiment contributes to the development of new tools that enhance our ability to manipulate and detect individual atoms.

Among the various atomic species that have been laser-cooled and trapped, alkaline-earth-like atoms (AEAs), such as ytterbium and strontium, have emerged as one of the most promising candidates for applications in quantum science and technology [4, 44–47]. This interest is motivated by their favorable atomic properties, which make them extremely versatile for many different applications. First, AEAs present a rich electronic structure, displaying multiple optical transitions with diverse features. The strong $^1\mathrm{S}_0 \rightarrow {}^1\mathrm{P}_1$ dipole-allowed transition provides a high photon-scattering rate, which can be employed for slowing an atomic beam before capture and for fast single-atom fluorescence imaging [48–51]. Conversely, the narrow-line $^1\mathrm{S}_0 \rightarrow {}^3\mathrm{P}_1$ intercombination transition is utilized for magneto-optical trapping as well as for single-atom imaging and coherent manipulation [52–54]. Finally, AEAs display an ultra-narrow $^1\mathrm{S}_0 \rightarrow {}^3\mathrm{P}_0$ clock transition which is the key frequency reference for state-of-the-art neutral-atom-based optical clocks [4]. The metastable clock state can also be exploited to implement a second ground state for qubit encoding and for simulation of multi-orbital models [45–47].

This rich level structure also manifests in a variety of available wavelengths for optical trapping of AEAs. These notably include magic wavelengths for different optical transitions, i.e. wavelengths providing the same confinement to the ground and excited state, a beneficial condition for cooling, imaging and manipulating trapped atoms [4, 52, 55]. Recent measurements [56, 57] have also identified wavelengths for which only one of involved states is confined while the other feels a vanishing potential. These so-called tune-out wavelengths can be exploited to engineer state-selective optical potentials, with strong implications for quantum simulation of localized impurity models [58], lattice gauge theories [59, 60] and quantum information processing [61] with AEAs.

Fermionic strontium and ytterbium isotopes, present a nuclear spin $I \neq 0$ which is decoupled from the electronic degrees of freedom for the ground and excited clock states. This results in a symmetry of interactions between all nuclear-spin states, which can be exploited to simulate SU(N)-symmetric models [47, 62–64] with $N \leq 6$ for fermionic ^{173}Yb ($I = 5/2$). Owing to their decoupling from external perturbations, nuclear-spin states of fermionic AEAs provide highly-coherent qubit encodings [53, 54]. In particular, the two nuclear-spin states of ^{171}Yb ($I = 1/2$) provide a textbook two-level system, which can be combined with the clock state to implement versatile qubit architectures [51, 65], making ^{171}Yb one of the prominent atomic species for quantum information processing.

Thesis overview

In this thesis, we report on the construction and first results of a new single-atom-resolved experimental apparatus for quantum science with ytterbium atoms. In particular, we aim to take advantage of optical tweezers and single-atom-detection schemes typical of quantum information protocols to investigate many-body physics with single atom resolution. We will report on the fundamental aspects of the experimental setup we have realized and on the tweezer-trapping and single-atom imaging of different ytterbium isotopes, focusing on fermionic species. In particular, we will discuss the first demonstration of trapping and detection of single ^{173}Yb atoms. We load our optical traps from a narrow-line magneto-optical trap in a five-beam geometry (5B MOT),

which had not been previously demonstrated for ytterbium. We will describe the properties of the 5B MOT and the experimental sequences we employ to load either an optical tweezer array or a larger optical dipole trap from the 5B MOT.

In the second part of this thesis we will focus on our results on fast, low-loss and number-resolved detection of ytterbium atoms. Taking advantage of the favorable properties of ytterbium, we demonstrate microsecond-scale single-atom imaging, achieving state-of-the-art detection fidelities with good survival probabilities. Our imaging scheme is also capable of number-resolved detection in multiply-filled traps, allowing us to count up to six atoms in a single tweezer. We exploit this capability to investigate the dynamics of light-assisted-collisions (LACs) employed to reach single-atom occupancy starting from multiply-filled traps, focusing on a regime that allows to reach almost deterministic tweezer filling [53, 66–68]. Moreover, our scheme also enables imaging of single-atoms in tightly-spaced arrays as well as in free flight after they are released from a trap. We will apply this versatile imaging technique to investigate many-body phenomena in mesoscopic fermionic systems, where few to few-tens of atoms are confined in a single trap.

The thesis is organized as follows:

- In Chapter 1 we review the atomic properties of ytterbium, describing the features of the most relevant optical transitions and the energy shifts induced by external magnetic fields. We then introduce the fundamental equations for describing atom-light interactions and present a detailed description of the procedure for computing the light shifts in multilevel systems starting from atomic transition data. We apply this polarizability model to the specific case of ytterbium and compare our theoretical predictions with known polarizabilities reported in the literature and spectroscopic measurements performed in the context of this work. We then briefly comment on the features of tweezer traps, focusing on heating mechanisms that limit the lifetime of trapped atoms and that lead to atom-loss during fluorescence imaging. To provide context to our work, we present a brief overview of recent advances in quantum information processing and metrology with alkaline-earth-like atoms, with special emphasis on applications that could benefit from a fast low-loss detection such as the one presented in this work. Finally, we focus on quantum simulation applications, describing the interaction properties of ytterbium and discussing possible investigations of two-orbital impurity models in our experimental setup.

- In Chapter 2 we describe the experimental apparatus we have built during the course of my PhD, discussing the features of our optical tweezer traps and presenting the first demonstration of tweezer-trapping and single-atom imaging of ^{173}Yb. We describe our ultra-high-vacuum system, our magnetic field coils and the properties of the different beams employed for slowing, cooling, trapping and imaging the atomic sample. We then present the laser-locking schemes used to stabilize the frequency of our laser sources, emphasizing how we can lock all our laser system to a single frequency reference, provided by a ultra-stable optical cavity, without the need of addressing an atomic transition. We then provide an overview of the properties of our one-dimensional optical tweezer array. We describe the setup for the generation of sub-micrometer traps, the scheme for determining the tweezers' waist and the homogenization procedures we employ to equalize the trapping conditions across the array. We then present our measurements of the differential light shifts for the $^1S_0 \rightarrow {}^3P_1$ and $^1S_0 \rightarrow {}^1P_1$ transitions in 532 nm traps for different ytterbium isotopes. We also discuss the lifetime of the trapped atoms and how we estimate the average temperature of individually-trapped atoms with the release and recapture technique. Finally, we present our single-atom fluorescence imaging setup. After describing the setup, we comment on the procedure we employ for measuring the fidelity and survival probability of the presented

single-atom detection schemes. We then report on a two-color imaging scheme through which we achieve single-atom imaging of ^{173}Yb.

- In Chapter 3 we discuss how we prepare a dense laser-cooled sample and how we load different optical traps. In particular, we present the first demonstration of a 5B MOT of ytterbium atoms. In the first part of the chapter we describe the working principle of the 5B MOT, recurring to Monte Carlo simulations of atomic trajectories to gain further insight into its functioning. We then present our experimental results, discussing the loading properties of the 5B MOT for all ytterbium isotopes and the intrinsic instability limiting the MOT lifetime. We also show how we compress the MOT to increase the phase-space density before loading atoms in optical traps. The final part of the chapter is devoted to the description of loading optical traps from the MOT. We first describe the procedure employed for loading a tweezer array and to achieve single-atom occupancy. Finally we report our recent results on loading a large optical dipole trap and on incoherent spin manipulation through optical pumping.

- In Chapter 4 we present our results on microsecond-scale low-loss single-atom imaging. We first discuss the advantages of our imaging scheme based on addressing a broad optical transition with alternated high-intensity pulses (*flash imaging*). We then describe how we implemented the flash imaging scheme, discussing the optical setup and RF circuits employed to realize the fast alternated pulses. After establishing the advantages of the flash imaging approach over continuous illumination, we present our results for fast low-loss detection of single ytterbium atoms. We discuss the imaging performances and the origin of the measured losses, identifying recoil-induced heating and off-resonant scattering as the two main sources of losses. As each detection injects motional excitations into the atoms, we implement a repeated-imaging scheme based on interleaved cooling and imaging pulses. We also show that our detection scheme can be applied for single-atom imaging in tightly-spaced arrays, akin to those employed in lattice experiments. Finally, we discuss how we employ flash imaging to detect single-atoms in free-flight upon being released from the trap and how we can use this to gain information on the thermodynamic properties of the trapped atoms.

- In Chapter 5 we focus on imaging and preparing multi-atom ensembles. First, we discuss how the fast timescale of our imaging protocol allows to detect multiple atoms confined in a single traps without inducing light-assisted collisions and how we can perform number-resolved imaging also in tightly spaced arrays. We then apply this atom-counting capability to investigate the dynamics leading to enhanced loading in optical tweezer arrays under the combined action of grey-molasses cooling and blue-detuned molecular potentials. In particular, we determine the rates of the relevant loss processes and identify the optimal regime for near-deterministic single-atom occupation. We also comment on prospects for repeated multi-atom detections. Finally, we describe our first steps towards the application of this imaging scheme to the investigation of many-body systems. We report on the capability of imaging multiple atoms expanding in free-space after being released from a single trap and discuss our current limitations in this regard. After that, we provide a brief outlook on the near future of our experiment. In particular, we show how we aim to extend to ytterbium the techniques for preparation of few-fermion systems developed for lithium atoms, taking advantage of our number-resolved detection.

Publications

The main results of this thesis are presented in the following publications:

- O. Abdel Karim, A. Muzi Falconi, R. Panza, W. Liu and F. Scazza, *Single-atom imaging of ^{173}Yb in optical tweezers loaded by a five-beam magneto-optical trap*, Quantum Science and Technology **10**, 045019 (2025)
- A. Muzi Falconi, R. Panza, S. Sbernardori, R. Forti, R. Klemt, O. Abdel Karim, M. Marinelli and F. Scazza, *Microsecond-scale high-survival and number-resolved detection of ytterbium atom arrays*, preprint: arXiv:2507.01011 (2025) (Accepted in Physical Review Letters, doi: https://doi.org/10.1103/n3bg-7yw7)

1

Quantum science with ytterbium atom arrays

Optically trapped alkaline-earth-like atoms (AEAs) are one of the leading platforms for quantum information processing, metrology and quantum simulation with neutral atoms. Their rich electronic structure enables a variety of laser-cooling schemes and allows optical trapping at visible and near-infrared wavelengths, including several magic and state-dependent wavelengths. Moreover, the nuclear spins of fermionic isotopes, which are decoupled from electronic degrees of freedom, and the metastable clock states provide robust and versatile qubit encodings [44, 45]. The ultranarrow clock transitions of AEAs also underpin state-of-the-art optical clocks [4]. These feature make array of individually trapped AEAs an unparalleled resource for quantum information processing and metrology, as well as for the simulation of novel quantum many-body systems [44, 45, 47, 62].

In this chapter we will describe the atomic properties of ytterbium and their relevance for applications in quantum science and technology. We will start with an overview of ytterbium's electronic structure, focusing on the optical transitions that are most relevant for cold-atoms experiments. We will then introduce the theoretical background necessary to compute the atomic polarizability in a multilevel system, and apply the presented model to the specific case of ytterbium. We will compare our predictions with experimentally determined polarizability values, identifying a variety of magic and tune-out wavelengths for the most relevant optical transitions. We will then describe the properties of tweezer traps allowing to confine and manipulate single atoms, focusing on the dominant heating mechanisms that limit the lifetime of trapped atoms and can lead to atom-loss during fluorescence imaging schemes. To provide context to our work, we will review some of the recent developments in the field of quantum science with AEAs arrays. In particular, we will discuss quantum information and metrology schemes that could benefit from fast mid-circuit readout, such as the one introduced in this work. Finally, we will comment on prospects of single-atom resolved quantum simulation of many-body systems with ytterbium atoms, focusing on quantum simulation of orbital impurities in mesoscopic systems.

1.1 Ytterbium properties

Ytterbium (Yb) is a rare-earth metal located in the lanthanide series with atomic number $Z = 70$. It is the last element of the f-block of the periodic table, meaning that the f-shell is complete and its full electronic configuration is [Xe] $4f^{14}$ $6s^2$. As electrons in the complete 4f shell are tightly bound to the nucleus, ytterbium's electronic structure is determined by the two outermost electrons in the 6s shell. Ytterbium's properties are therefore more similar to those of alkaline-earth atoms, such as strontium, than to other rare-earth elements like erbium and dysprosium. In the following we will describe the features of ytterbium which are most relevant for this work, while we point out a recent work Ref. [69] for an extensive discussion of ytterbium

Isotope	Relative abundance (%)	Nuclear spin	Statistics
^{168}Yb	0.13	0	bosonic
^{170}Yb	3.05	0	bosonic
^{171}Yb	14.3	1/2	fermionic
^{172}Yb	21.9	0	bosonic
^{173}Yb	16.12	5/2	fermionic
^{174}Yb	31.8	0	bosonic
^{176}Yb	12.7	0	bosonic

Table 1.1| Properties of stable ytterbium isotopes. Relative abundances data are taken from Ref. [70].

properties.

1.1.1 Physical properties

Owing to its complete shell, ytterbium is strongly diamagnetic. The temperatures required to produce an atomic flux for atomic physics experiments are around 400 °C, a value that does not pose particular experimental challenges. Due to its large atomic number, ytterbium has several stable isotopes and we report their most relevant properties in Table 1.1. Notably, the five isotopes with mass number $A > 170$ have significant natural abundances and can be employed for atomic physics experiments without the need of an enriched sample. These isotopes comprise both bosonic and fermionic species, enabling the exploration of systems with either quantum statistics, as well as Bose–Fermi, Bose–Bose, or Fermi–Fermi mixtures when multiple isotopes are used. As ytterbium has two valence electrons and an even atomic number ($Z = 70$), isotopes with even mass number are bosons with zero nuclear spin ($I = 0$). On the other hand isotopes with an odd number of neutrons, are fermionic and have a non-zero nuclear spin. Owing to their peculiar feaures, both fermionic isotopes ^{171}Yb ($I = 1/2$) and ^{173}Yb ($I = 5/2$) have attracted much attention for quantum simulation, information and precision metrology. As described in Sec. 1.5.1, different ytterbium isotopes also display different interaction properties, further broadening the spectrum of accessible physics in experiments based on this atomic species. In this work we will focus on the three isotopes which are mostly employed in cold-atom experiments: the bosonic ^{174}Yb and the two fermionic ^{171}Yb and ^{173}Yb.

1.1.2 Electronic structure

Owing to the complete 4f-shell and the two valence electrons, ytterbium and other AEAs, such as strontium, share an electronic structure similar to that of helium. This structure is well described by the LS-coupling (Russel-Saunder coupling), in which energy levels are simultaneous eigenstates of the total orbital angular momentum $\boldsymbol{L}$, the total electronic spin $\boldsymbol{S}$ and the total electronic angular momentum $\boldsymbol{J} = \boldsymbol{L} + \boldsymbol{S}$. Each electronic level is therefore labelled as: $^{2S+1}L_J$ [71]. While bosonic ytterbium isotopes have zero nuclear spin ($I = 0$), for fermionic isotopes ($I \neq 0$) we must consider the total angular momentum $\boldsymbol{F} = \boldsymbol{I} + \boldsymbol{J}$, which gives rise to an hyperfine structure for states with $J \neq 0$.

For two electrons, each with spin 1/2, the total spin can be either $S = 0$ or $S = 1$. Ytterbium's level structure is therefore characterized by two separate manifolds of singlet ($S = 0$) and triplet ($S = 1$) states which are connected only by narrow optical intercombination transitions. These transitions would be completely forbidden in the pure LS-coupling owing to the $\Delta S = 0$ dipole selection rule. However, the large mass of ytterbium results in a large spin-orbit interaction, which induces a significant mixing between the ^{1}P$_1$ and ^{3}P$_1$ states and allows

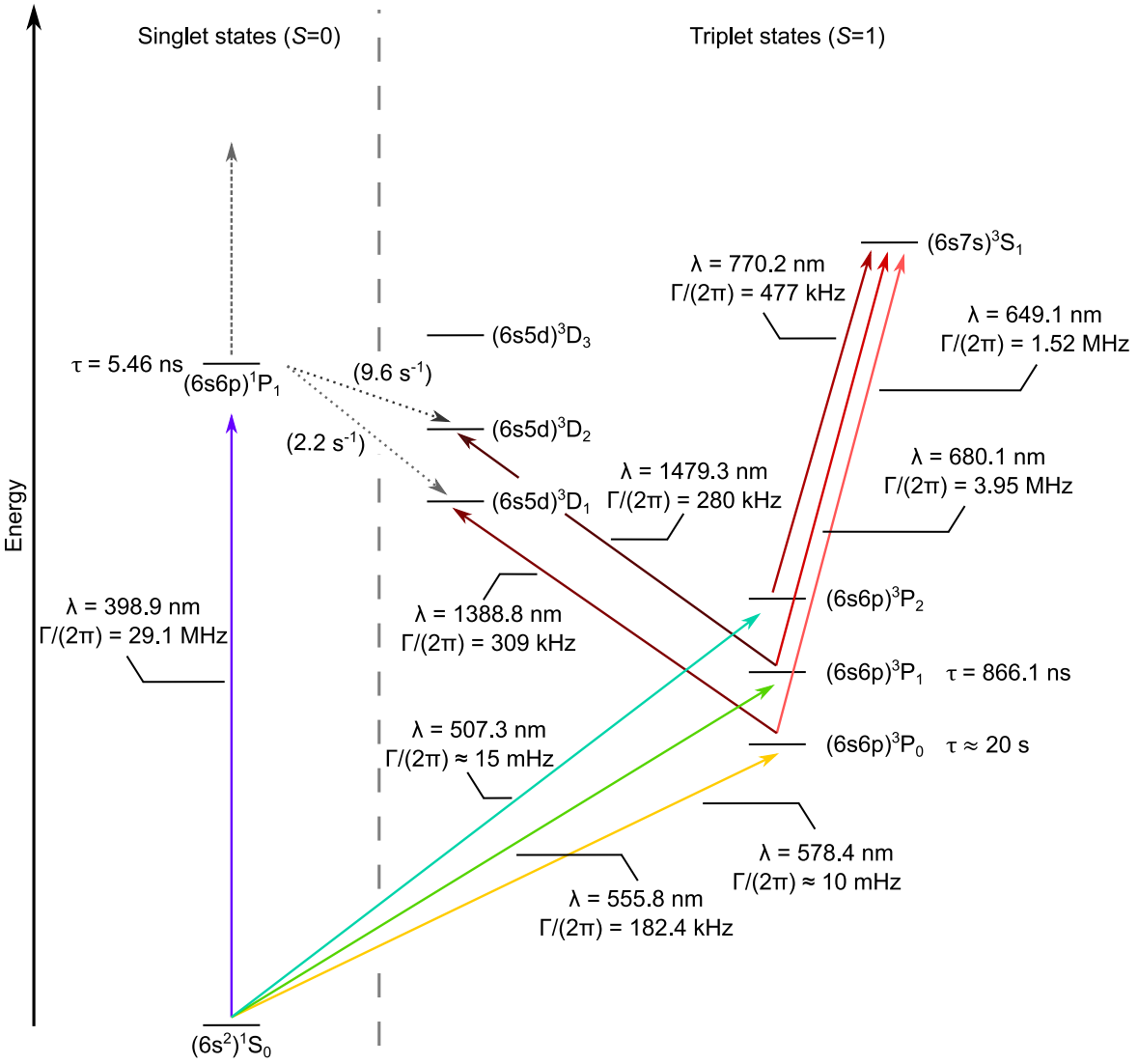

Figure 1.1| Ytterbium electronic levels and transitions. Solid arrows indicate relevant optical transitions, for which we report the wavelength and linewidth Γ. We also report the lifetime of the most relevant excited states. The dotted grey lines connecting the $^1\mathrm{P}_1$ to the $^3\mathrm{D}_{1,2}$ states indicate a decay channel with decay rates Γ indicated in parenthesis and taken from Ref. [72]. The dashed grey line pointing upwards from the $^1\mathrm{P}_1$ represents excitations to higher-lying singlet states. Transition data are taken from different references and we refer to Appendix B for further details on the transitions and on how to compute the linewidth Γ in presence of multiple decay channels. Energy levels are not to scale.

the intercombination transitions. Indeed, for lighter alkaline-earth atoms, such as strontium, the *LS*-coupling approximates better the electronic structure, and the intercombination transitions are less allowed, with a resulting narrower linewidth. Transitions between the $^1\mathrm{S}_0$ ground state and the $^3\mathrm{P}_0$ and $^3\mathrm{P}_2$ states are instead doubly forbidden by both the $\Delta S = 0$ and the $\Delta J = 0, \pm 1\,(J = 0 \not\to J' = 0)$ selection rules. For fermionic isotopes, the hyperfine interaction mixes the $^3\mathrm{P}_{0,2}$ states with the $^3\mathrm{P}_1$, enabling second-order ultranarrow transitions between the $^1\mathrm{S}_0$ and the $^3\mathrm{P}_0$ and $^3\mathrm{P}_2$ states. For the bosonic isotopes, a finite coupling between the $^3\mathrm{P}$ states can be created by applying a strong magnetic field, thus providing access to these transitions [73, 74].

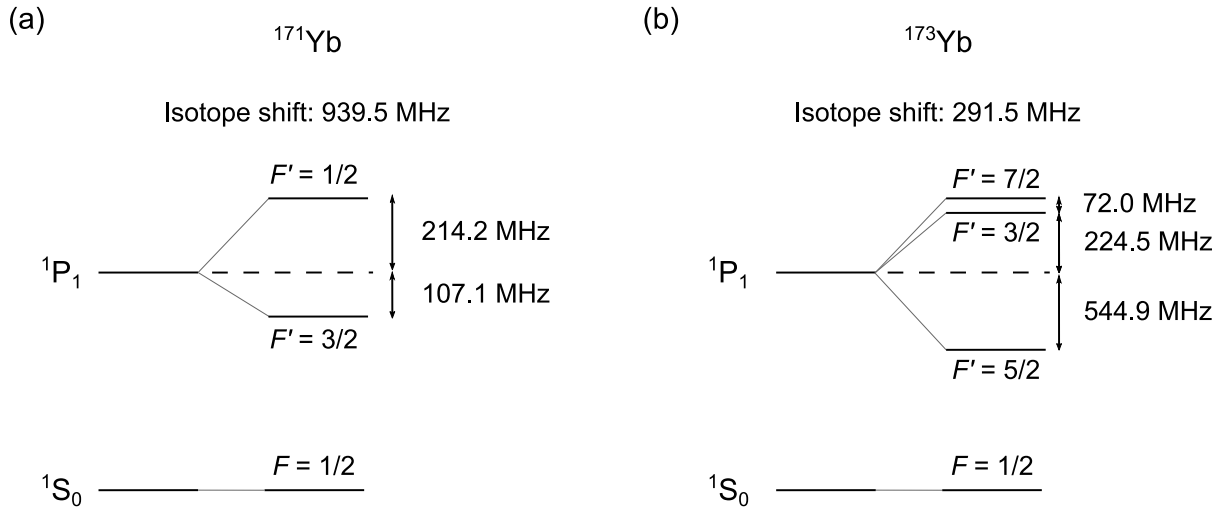

Figure 1.2| Isotope shift and hyperfine structure of the $^1S_0 \rightarrow {}^1P_1$ transition in fermionic isotopes (a) ^{171}Yb and (b) ^{173}Yb. The isotope shift refers to the centroid of the transition, indicated by the dashed lines.

We report a scheme of the most relevant ytterbium transitions in Fig. 1.1, including transitions between triplet excited states and other higher-lying electronic states. Notably, while intercombination transitions have a narrow or ultranarrow character, lines within the same singlet or triplet manifold are dipole-allowed and therefore display broader linewidths. We refer to Appendix B for a detailed table including more transitions and the references for all transition data.

The $^1S_0 \rightarrow {}^1P_1$ broad transition

The $^1S_0 \rightarrow {}^1P_1$ transition at 398.9 nm is a strong, dipole-allowed transition with a linewidth of $\gamma = \Gamma/(2\pi) = 29.13$ MHz and a saturation intensity $I_{\text{sat}} = 59.97\,\text{mW/cm}^2$. Owing to its broad character, this transition can provide a high photon-scattering rate and it is therefore well-suited for slowing an atomic beam as well as for producing 2D and 3D magneto-optical traps (MOTs) [72, 75]. Moreover, it is also the transition employed for absorption imaging and for fluorescence detection of single atoms, both in combination with cooling [52, 53, 55, 76, 77] and for fast imaging schemes [48–51, 78].

This transition is almost perfectly closed. In fact, atoms in $^1P_1$ have only a weak probability of decaying to the $(5d6s)^3D_{1,2}$ states, from which they can either decay to the $^3P_1$ state, and then back to the ground state after roughly $\tau_{^3P_1} = 866.1$ ns, or to one of the two metastable $^3P_{0,2}$ states and be effectively lost from the experimental sequence. The decay rates from $^1P_1$ to $(5d6s)^3D_1$ ($2.2\,\text{s}^{-1}$) and $(5d6s)^3D_2$ ($9.6\,\text{s}^{-1}$) have been calculated in Ref. [79]. The total decay rate from $^1P_1$ to the metastable states has been theoretically estimated as $6.6\,\text{s}^{-1}$ [79] and experimentally confirmed [72]. This has been particularly relevant in the first demonstrations of ytterbium MOTs as decays to the metastable states limit the number of captured atoms in 3D MOTs acting on the $^1S_0 \rightarrow {}^1P_1$transition. In this case repumpers from the $^3P_{0,2}$ to the $(6s7s)^3S_1$ state can be used to enhance the number of trapped atoms [72]. Moreover, decays to metastable states also lead to atom-loss when performing fluorescence imaging on the blue transition. While also in this case repumpers can mitigate this effect, the low decay rate makes these losses of the order of 0.001% and therefore not relevant for current detection schemes.

Owing to the lack of hyperfine structure, the $^1S_0 \rightarrow {}^1P_1$ transition is just a single line in ^{174}Yb. We instead report the isotope and hyperfine shifts of the $^1P_1$ state in the fermionic

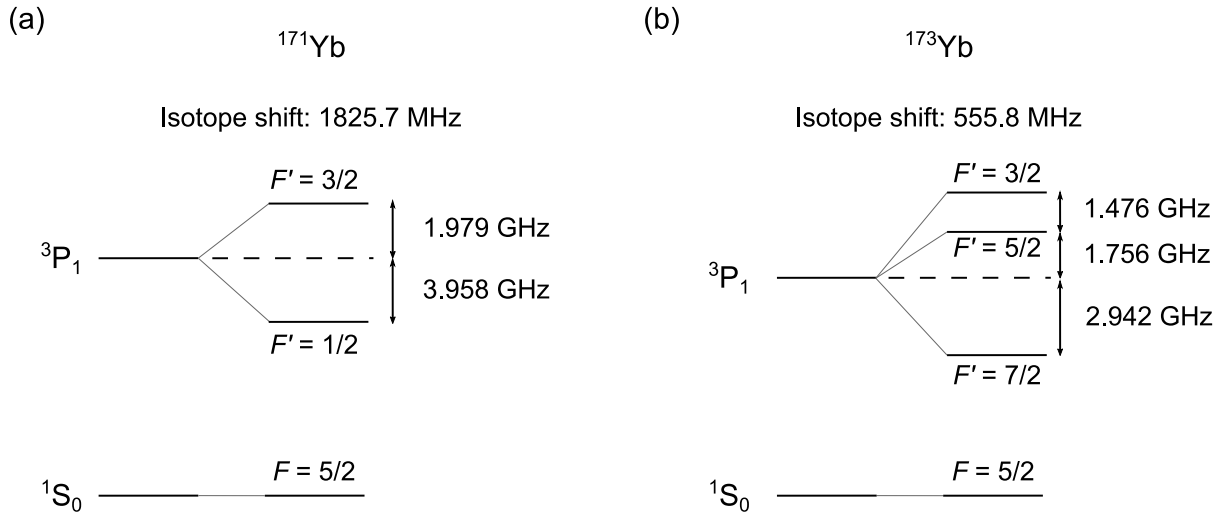

Figure 1.3| Isotope shift and hyperfine structure of the $^1\mathrm{S}_0 \rightarrow {}^3\mathrm{P}_1$ transition in fermionic isotopes (a) ^{171}Yb and (b) ^{173}Yb. The isotope shift refers to the centroid of the transition, indicated by the dashed lines.

isotopes in Fig. 1.2. Both shifts are much larger than the natural linewidth, allowing to address individual isotopes and hyperfine states. However, in the case of ^{173}Yb, the relatively small ($\simeq 70\,\mathrm{MHz}$) splitting between the $^1\mathrm{P}_1|F' = 7/2\rangle$ and $^1\mathrm{P}_1|F' = 3/2\rangle$ states results in typically reduced performance of slowing beams, which benefit from addressing the stretched $^1\mathrm{S}_0|F, m_F = \pm F\rangle \rightarrow {}^1\mathrm{P}_1|F' = F+1, m'_F = \pm F'\rangle$ transitions only.

The $^1\mathrm{S}_0 \rightarrow {}^3\mathrm{P}_1$ narrow transition

The $^1\mathrm{S}_0 \rightarrow {}^3\mathrm{P}_1$ transition at 555.8 nm is a narrow-line intercombination transition with a linewidth of $\gamma = \Gamma/(2\pi) = 182.4\,\mathrm{kHz}$ and a saturation intensity $I_{\mathrm{sat}} = 0.139\,\mathrm{mW/cm^2}$. This transition is forbidden in the LS-coupling scheme. However, due to the magnitude of the spin-orbit interaction in ytterbium[1], real electronic levels are not the unperturbed LS-coupling states, but rather linear combinations of them. The $^3\mathrm{P}_1$ state therefore contains a component of the unperturbed $^1\mathrm{P}_1^{(0)}$ state, which is coupled to the ground state by a strong dipole allowed transitions, and inherits part of this coupling [80].

The linewidth of the ytterbium $^1\mathrm{S}_0 \rightarrow {}^3\mathrm{P}_1$ transition is broad enough to yield a sufficient capture velocity to directly load a MOT on this intercombination transition, without the need of an intermediate broad-line MOT. The linewidth is, however, narrow enough to have a low Doppler temperature of $T_{\mathrm{D}} = \hbar\Gamma/(2/k_{\mathrm{B}}) \simeq 4.4\,\mu\mathrm{K}$. This transition is therefore well suited to cool atoms in a MOT as well as in optical traps, even though attractive and repulsive Sisyphus cooling in non-magic traps [12, 76, 81] and other techniques available for narrower lines are harder to achieve due to the relatively broad linewidth. It is instead possible to employ this transition to cool atoms to the motional ground state of tight optical traps through two-photon Raman sideband cooling [53]. The $^1\mathrm{S}_0 \rightarrow {}^3\mathrm{P}_1$ transition is also used to perform coherent and inchoerent manipulation of the nuclear-spin states of fermionic isotopes [53, 54, 65, 82, 83] and to perform single-atom fluorescence imaging [52, 54, 65, 82, 84]. Owing to the lack of hyperfine structure, this transition is a single line in ^{174}Yb, while it is split into hyperfine levels separated by few-GHz energy shifts for fermionic isotopes. We report the isotope and hyperfine shifts of the $^1\mathrm{S}_0 \rightarrow {}^3\mathrm{P}_1$ transition in fermionic isotopes in Fig. 1.3. Shifts are orders of magnitude

[1]The spin-orbit interaction strength is proportional to Z^4; $Z = 70$ for ytterbium.

larger than the natural linewidth and can be addressed without crosstalk. Moreover, the large hyperfine shifts can be exploited to address different F' states, which often require dedicated lasers, in different moments of the experimental sequence e.g. for optical pumping (OP) or optical Stern-Gerlach (OSG) detection of different nuclear-spin states [85, 86].

The $^1S_0 \rightarrow {}^3P_0$ clock transition

The $^1S_0 \rightarrow {}^3P_0$ transition at 578.4 nm is a doubly-forbidden transition with a natural linewidth $\gamma = \Gamma/(2\pi) \leq 10\,\mathrm{mHz}$ and a saturation intensity $I_{\mathrm{sat}} \leq 10\,\mathrm{pW/cm^2}$ [87]. This transition is allowed to second order in fermionic ytterbium due to the mixing of the unperturbed $^3P_0^{(0)}$ state with the $^3P_1$ state caused by the hyperfine interaction. The resulting second-order transition is extremely narrow and the lifetime of the excited state is of the order of 20 s [88], much longer than typical experimental dynamics.

Owing to its long lifetime, the metastable $^3P_0$ state (as well as the $^3P_2$ state, which shares similar properties) can be thought as a second ground state to perform quantum simulation of two-orbital or impurity models [47, 58, 89, 90]. Moreover, the stable ground and excited states provide an optical qubit that can be employed for qubit enncoding in quantum information schemes [44–46, 61]. In particular, the excited state is also be used to shelve nuclear-spin states in order to hide them from imaging or addressing light and achieve local and spin-selective manipulation or detection [65]. Finally, the extremely narrow linewidth of the $^1S_0 \rightarrow {}^3P_0$ transition results in a Q-factor above 10^{17}, making it a suitable frequency reference for the most stable and precise atomic clocks in the world [4, 36]. The $^1S_0 \rightarrow {}^3P_0$ transition is therefore appropriately denominated as clock transition.

Starting from the metastable state, dipole-allowed transitions to the $(6s5d)^3D_1$ and $(6s7s)^3S_1$ states can be excited. These can be used to quench $^3P_0 \rightarrow {}^1S_0$ decays, allowing to employ the clock transition as an extremely narrow-line cooling transition and perform subrecoil cooling as well as single-photon sideband-cooling also in shallow traps [91–93]. Moreover, the $^3P_0 \rightarrow (6s5d)^3D_1$ transition can be exploited for quantum communication and networks [94, 95], owing to its telecommunication-window wavelength of 1388.8 nm, where attenuation in optical fibers is minimal and fast and efficient photonic technologies are available. Finally, the long wavelength of transitions from the $^3P_0$ to higher-lying triplet states open the possibility of investigating collective light-atom effects in a sub-wavelength regime [96–99].

Due to the lack of hyperfine structure ($J' = 0$), the clock transition is a single line for all ytterbium isotopes.

Interaction with magnetic fields

Magnetic fields play a crucial role in most cold-atom experiments. The interaction between atomic magnetic moments and an external magnetic field can, for low enough fields, be treated as a perturbation to the hyperfine Hamiltonian. In the weak-field Zeeman regime, hyperfine sublevels are split by an energy shift

$$\Delta E_{\mathrm{Z}} = g_F\, \mu_{\mathrm{B}}\, m_F B \tag{1.1}$$

where $\mu_{\mathrm{B}} \simeq 1.3996\,\mathrm{MHz/G}$ is Bohr's magneton and m_F is the projection of the atomic angular momentum along the quantization axis, defined by the direction of the field B. The Landé g-factor g_F depends on the specific hyperfine state and is given by:

$$g_F = g_J \frac{F(F+1) + J(J+1) - I(I+1)}{2F(F+1)} + g_I \frac{F(F+1) + I(I+1) - J(J+1)}{2F(F+1)} \tag{1.2}$$

where g_J and g_I are the electronic and nuclear Landé factors respectively. For $J = 0$ and $F = I$, as in the case of the $^1S_0$ and $^3P_0$ states, the first term vanishes and the total g-factor is therefore:

$$g_F = g_I \frac{\mu_I}{\mu_B |I|} \tag{1.3}$$

where μ_I is the nuclear magnetic moment, which is approximately 2000 times smaller than μ_B, due to the ∼2000 times larger mass of protons compared to electrons. Therefore, the $^1S_0$ and $^3P_0$ states have an extremely weak dependence on magnetic fields, which makes them robust to environmental perturbations, a key feature for metrological applications [4, 80] and for quantum information processing, where nuclear-spin states of fermionic isotopes provide qubits with long coherence times [44, 45]. For all results presented in this work, we always neglect the Zeeman shift of the ground state and consider only the shift of the $^3P_1$ and $^1P_1$ excited states when computing transition energies in presence of external magnetic fields.

When the magnetic interaction energy is instead much larger than the hyperfine splitting, it cannot be treated as a perturbation to the hyperfine Hamiltonian and F is not a good quantum number anymore. In this high-field (Paschen-Back) regime, the eigenstates are product states $|J, m_J, I, m_I\rangle$ and the magnetic field shifts them according to the electronic and nuclear angular momenta projections:

$$\Delta E_{PB} = \mu_B \, g_J \, m_J \, B + \mu_N \, g_I \, m_I \, B \tag{1.4}$$

where μ_N is the nuclear magneton. In the intermediate regime, neither the $|F, m_F\rangle$ nor the $|J, m_J, I, m_I\rangle$ states are good approximations of the eigenstates and we need to numerically diagonalize the full interaction and hyperfine Hamiltonian to compute the energy shifts. However, when $I = 1/2$, as in the case of ^{171}Yb, we can analytically solve the energy spectrum and eigenstates using the Breit-Rabi formula [100–102]:

$$E_{J,m_J,I=1/2,m_I} = -\frac{E_{HF}}{2(2J+1)} + g_J \mu_B m_F B \pm \frac{E_{HF}}{2}\sqrt{1 - \frac{4m_F x}{2J+1} + x^2} \tag{1.5}$$

where $x = (g_J\mu_B + g_I\mu_N)B/E_{HF}$, $m_F = m_I + m_J$ and $E_{HF} = A(J + 1/2)$ with A being the hyperfine constant. We report in Fig. 1.4 the result of this calculation for the $^1P_1$ state in ^{171}Yb, for which $A = -216\,$MHz. At low fields, the hyperfine levels $F = 1/2$ and $F = 3/2$ are split, and different $|F, m_F\rangle$ states feel a linear energy shift with increasing field. At around 200 G, the states' energies cross and for larger fields the eigenstates are better approximated by $|m_J, m_I\rangle$. These states originate from the low-field hyperfine $|F, m_F\rangle$ levels, and, in general, are a linear combination of different $|m_J, m_I\rangle$ states giving the same $m_F = m_J + m_I$ value. It is only in the deep Paschen-Back regime that product states $|m_J, m_I\rangle$ are the real eigenstates of the Hamiltonian. Due to the large hyperfine splitting, in ytterbium the Paschen-Back regime is achieved for very high magnetic fields and the eigenstates remain superpositions of different $|m_J, m_I\rangle$ for up to ∼ 800 G. An exception to this are the $|m_J = 1, m_I = 1/2\rangle$ and the $|m_J = -1, m_I = -1/2\rangle$, which are pure eigenstates as they are derived from states with maximum $m_F = \pm 3/2$.

These states could be employed for spin-sensitive fast imaging schemes in ^{171}Yb by driving the $^1S_0 \rightarrow {}^1P_1$ transition between one of the two $^1S_0|m_F = \pm 1/2\rangle$ states and the corresponding $^1P_1|m'_J = \pm 1, m'_I = \pm 1/2\rangle$ state. Considering excitations to $^1P_1|m'_J = 1, m'_I = 1/2\rangle$, only ground-state atoms with $m_F = +1/2$ will be bright to the imaging light, as light cannot flip the nuclear spin. A possible complication arises as the broad line of the $^1S_0 \rightarrow {}^1P_1$ transition and the relatively small (∼ 250 MHz) shift between the $|m'_J = 1, m'_I = 1/2\rangle$ and the $|m'_J, = 1, m'_I = -1/2\rangle$ states might result in unwanted excitations of the dark spin state. While the amount of scattered photons by the dark state will be much smaller compared to the bright state, the admixture between $|m'_J, = 1, m'_I = -1/2\rangle$ and $|m'_J, = 0, m'_I = +1/2\rangle$ might result in spin flips,

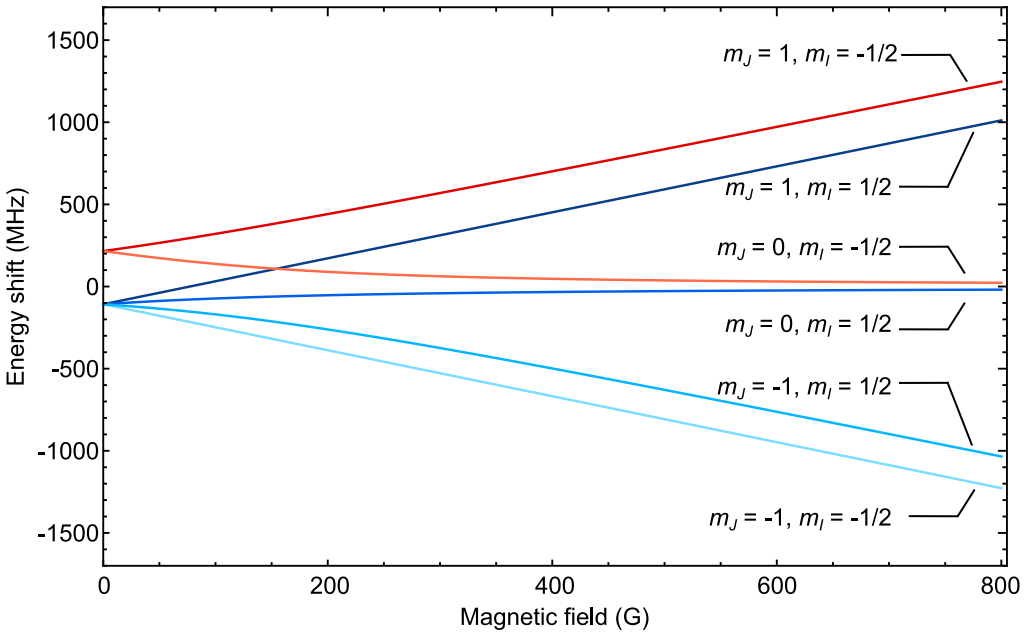

Figure 1.4| Energy shifts of the ^{171}Yb ^{1}P$_1$ state in external magnetic fields. We use the Breit-Rabi equation [Eq. (1.5)] to compute the energy shift in a broad range of magnetic fields. Red and blue lines indicate states originating from the $F = 1/2$ and $F = 3/2$ manifold respectively. m_J, m_I labels refer to the high-field Paschen-Back regime.

which could hinder high-fidelity spin-sensitive detection. For high enough fields ($B \sim 800\,\mathrm{G}$) the $|m'_J = 0, m'_I = +1/2\rangle$ component can be strongly suppressed to reduce the spin-flip probability. We therefore believe that employing high magnetic fields to reach the Paschen-Back regime could allow fast spin-sensitive detection.

1.2 Ytterbium coupling with light

All neutral-atom based experiments heavily rely on laser light to cool, trap and image the atoms [103]. In particular, the oscillating electric field generated by laser beams polarizes the atoms and the interaction between the field and the induced dipole lies at the heart of atom-light interactions. In a pictorial view, the light's electric field drives forced oscillations on the atomic dipole and the system's behavior depends on the difference between the laser frequency and the dipole's resonant oscillation frequency, as in the case of a driven mass on a spring. When the laser frequency is close to resonance, atoms have a significant probability of absorbing and re-emitting photons, which is the mechanism underlying atom slowing and cooling as well as fluorescence imaging. On the other hand, when the light is far detuned, the photon-scattering probability is extremely low and atoms feel a conservative force, whose sign depends on the sign of the detuning. This so-called optical dipole force can be employed to confine atoms in optical traps with the most different geometries.

To give a quantitative description of the atom-light interaction in the simple case of a two-level system, we will follow the approaches presented in Refs. [100, 103]. We start by writing the monochromatic electric field $\mathbf{E}$ and the induced dipole moment $\mathbf{d}$ as

$$\mathbf{E}(\mathbf{r}, t) = \frac{1}{2} E_0(\mathbf{r}) e^{-i\omega t}\, \hat{\epsilon} + c.c. \tag{1.6}$$

$$\mathbf{d}(\mathbf{r}, t) = d_0(\mathbf{r}) e^{-i\omega t} \hat{\epsilon} + c.c. \tag{1.7}$$

where E_0 and d_0 are the amplitudes of the electric field and of the induced dipole moment respectively, while $\hat{\epsilon}$ is the unit vector indicating the light's polarization direction. Note that both E_0 and d_0 are complex numbers and therefore include a phase, which in general is not the the same for these two quantities. We can define the polarizability $\alpha(\omega)$ to describe the relation between the external field and the induced dipole:

$$d_0(\mathbf{r}) = \alpha(\omega) E_0(\mathbf{r}) \tag{1.8}$$

This polarizability, often called dynamical due to its dependence on the laser light angular frequency ω, is a complex number, indicating that both amplitude and phase of the induced dipole depend on this quantity.

The potential energy of the induced dipole, can be written as:

$$V_{\mathrm{ac}}(\mathbf{r}) = -\frac{1}{2}\langle \mathbf{d}(\mathbf{r},t)\cdot\mathbf{E}(\mathbf{r},t)\rangle = -\frac{1}{2\epsilon_0 c}\mathrm{Re}(\alpha) I(\mathbf{r}) \tag{1.9}$$

where $I = \epsilon_0 c|E_0|^2/2$ is the light's intensity and the angle brackets indicate a time average over the fast oscillations of the field. V_{ac} is the optical potential induced by the light on the atoms and it is proportional to the real part of the atomic polarizability. This potential is often called ac-Stark shift or simply light shift as it effectively induces a shift fo the energy of an atomic state when it is immersed in an oscillating field. The force obtained by taking the derivative of this potential is the optical dipole force which is therefore proportional to the gradient of the light's intensity:

$$\mathbf{F}(\mathbf{r}) = -\nabla V_{\mathrm{ac}}(\mathbf{r}) = \frac{1}{2\epsilon_0 c}\mathrm{Re}(\alpha)\nabla I(\mathbf{r}) \tag{1.10}$$

Besides this conservative force, atoms also absorb power from the laser light, before re-emitting it in the form of spontaneous emission. The absorbed power due to photon scattering is

$$P_{\mathrm{sc}}(\mathbf{r}) = \langle \dot{\mathbf{d}}(\mathbf{r},t)\cdot\mathbf{E}(\mathbf{r},t)\rangle \tag{1.11}$$

with a corresponding scattering rate Γ_{sc} that is proportional to the imaginary part of the polarizability:

$$\Gamma_{\mathrm{sc}}(\mathbf{r}) = \frac{P_{\mathrm{sc}}}{\hbar\omega} = \frac{1}{\hbar\epsilon_0 c}\mathrm{Im}(\alpha) I(\mathbf{r}) \tag{1.12}$$

Polarizability of a two-level atom

To fully describe the atom-light interactions in the case of a single atom immersed in a laser field it is therefore necessary to know both the real and imaginary parts of the atomic polarizability $\alpha(\omega)$. Considering the simplified case of a two-level system, with ground state $|i\rangle$ and excited state $|f\rangle$, the real and imaginary parts of the polarizability can be written as:

$$\mathrm{Re}(\alpha) = \frac{2\, w_{if}}{\hbar\left(\omega_{if}^2 - \omega^2\right)}|\langle i|\hat{\epsilon}\cdot\mathbf{d}|f\rangle|^2 \tag{1.13}$$

$$\mathrm{Im}(\alpha) = \frac{2\,\omega_{if}^2\,\omega^3}{3\pi c^3\hbar^2\epsilon_0\left(\omega_{if}^2 - \omega^2\right)^2}|\langle i|\hat{\epsilon}\cdot\mathbf{d}|f\rangle|^4 \tag{1.14}$$

where $\hbar\omega_{if}$ is the energy of the $|i\rangle \to |f\rangle$ transition. The real part of the polarizability is positive for red-detuned light ($\omega < \omega_{if}$) and negative for blue-detuned light ($\omega > \omega_{if}$), resulting in attractive and repulsive optical potentials for red and blue detuning, respectively. Both components of the polarizability depend on the square matrix element $|\langle i|\hat{\epsilon}\cdot\mathbf{d}|f\rangle|^2$ which quantifies

the strength of the coupling between the ground and excited state. For a two-level system, the dipole matrix element can directly be computed from the linewidth Γ of the optical transition:

$$\Gamma = 1/\tau = \frac{\omega_{if}^3}{3\pi\epsilon_0\hbar c^3}|\langle i|\hat{\epsilon}\cdot\mathbf{d}|f\rangle|^2 \tag{1.15}$$

where τ is the excited state's lifetime. Large couplings between the ground and excited state result in broad transitions with short excited-state lifetimes. The dependence of the polarizability on the strength of the transition is crucial when extending this treatment beyond a simple two-level system, as multiple transitions give rise to competing light shifts. Finally, we stress that both Eq. (1.13) and Eq. (1.14) can be used to compute the polarizability of both the ground and the excited state by appropriately choosing the sign of the transition angular frequency ω_{if} (i.e. choosing a negative frequency for computing the polarizablity of the excited state).

An extremely useful quantity to describe the optical coupling between the ground and excited state, including the amplitude of the applied field, is the Rabi frequency Ω, defined as [71]:

$$|\Omega|^2(\mathbf{r}) = \frac{|E_0(\mathbf{r})|^2}{\hbar^2}|\langle i|\hat{\epsilon}\cdot\mathbf{d}|f\rangle|^2 \tag{1.16}$$

For an atomic transition we can also define the saturation intensity I_{sat} and the saturation parameter s:

$$I_{\text{sat}} = \frac{\pi}{3}\frac{hc}{\lambda^3\tau} \tag{1.17}$$

$$s = \frac{I}{I_{\text{sat}}} = 2\frac{|\Omega|^2}{\Gamma^2} \tag{1.18}$$

where λ is the wavelength of the considered transition. With these quantities we can write the following expression for the scattering rate:

$$\Gamma_{\text{sc}}(\mathbf{r}) = \frac{\Gamma}{2}\frac{s(\mathbf{r})}{1+s(\mathbf{r})+4\Delta^2/\Gamma^2} \tag{1.19}$$

where $\Delta = \omega - \omega_{if}$ is the detuning. This expression is extremely useful and it is often employed for computing the scattering rate when only one transition is relevant, as in the case of atoms in magneto optical traps or undergoing fluorescence imaging.

1.2.1 Light shifts in multi-level systems

The expressions above can be used when only one optical transition contributes significantly to the atomic polarizability, for example in the vicinity of a strong dipole-allowed resonance. On the other hand, for many situations we need to consider atoms as multi-level systems. Indeed, any electronic state displays multiple available excited states, and each transition contributes to the total polarizability. Computing the polarizability taking into account all electronic states is often complicated, but it is extremely important for atoms like ytterbium, where the contribution of different transitions gives rise to magic wavelengths, where two electronic states display the same polarizability, tune-out wavelengths, where the polarizability of one electronic state vanishes, and, in general, state-dependent optical potentials.

In the following, we will provide a detailed description of the procedure employed to compute the light shifts in multi-level atoms. We follow very closely the approaches presented in Refs. [104, 105], slightly modifying the notation and presentation in the hope of clarifying the often obscure and complicated procedure to compute multi-level light shifts.

Since we are interested in the real part of the polarizability, from now on we will drop the explicit reference to the real part and directly indicate $\alpha \equiv \text{Re}(\alpha)$. For a multi-level system, the

polarizability of an atom in a state $|i\rangle$ is given by the sum of the contributions of all electronic excited states $|f\rangle$:

$$\alpha(\omega) = \sum_f \alpha^{(f)}(\omega) = \sum_f \frac{2\, w_{if}}{\hbar(\omega_{if}^2 - \omega^2)} |\langle i|\hat{\epsilon}\cdot\mathbf{d}|f\rangle|^2 \tag{1.20}$$

where we call $\alpha^{(f)}(\omega)$ the contribution of a single $|i\rangle \to |f\rangle$ transition to the total polarizability. We keep the dependence on $|f\rangle$ explicitly indicated to specify when the polarizability is referred to a single $|i\rangle \to |f\rangle$ transition compared to the total polarizability of state $|i\rangle$.

Hyperfine structure

For fermionic isotopes of ytterbium we have to take into account the hyperfine structure and Zeeman sublevels. Therefore, the states that we have to consider are $|i\rangle = |L, S, J, F, m_F\rangle$ and $|f\rangle = |n', J', F', m'_F\rangle$. The sum over $|f\rangle$ is then a double sum over all possible fine-structure levels $|L', S', J'\rangle$ and, for each of these states, over all the hyperfine levels $|F', m'_F\rangle$, which we approximate to be degenerate for most of the cases[2]. For clarity's sake, we will describe the procedure for computing the multi-level light shift of hyperfine states considering a single fine-structure transition $|i\rangle \to |n', J'\rangle$. The total light shift is then trivially obtained by summing the contributions of all the fine-structure transitions.

To handle angular momentum degeneracy and hyperfine structure, the polarizability needs to be generalized to a tensor $\alpha_{\mu\nu}(\omega)$. This tensor can couple the field and atom in an anisotropic way and the induced dipole moment is:

$$d_\mu = \alpha_{\mu\nu}(\omega) E_\nu \tag{1.21}$$

The polarizability tensor can be explicitly written as [100]:

$$\alpha_{\mu\nu}(\omega) = \sum_{F', m'_F} \frac{2\, w_0}{\hbar(\omega_0^2 - \omega^2)} \langle i|d_\mu|F', m'_F\rangle\langle F', m'_F|d_\nu|i\rangle \tag{1.22}$$

where, again, we stress that the sum runs over all hyperfine levels of the considered fine-structure excited state and $\hbar\omega_0$ is the energy of the transition, which we approximate to be the same for all hyperfine states. The polarizability tensor can be split into its irreducible scalar (α_s), vector (α_v) and tensor (α_t) components to express the light shift as [100]:

$$\begin{aligned} V_\mathrm{ac}^{(n',J')}(F, m_F, \omega) = -\frac{I}{2\epsilon_0 c}\Bigg[& \alpha_\mathrm{s}(F,\omega) + \\ & + \alpha_\mathrm{v}(F,\omega)\, q\, (\hat{k}\cdot\hat{z})\frac{m_F}{F} + \\ & + \alpha_\mathrm{t}(F,\omega)\frac{3|\hat{\epsilon}_z|^2 - 1}{2}\frac{3m_F^2 - F(F+1)}{F(2F-1)}\Bigg] \end{aligned} \tag{1.23}$$

where q is the degree of circular polarization ($q = 0$ for linearly polarized light and $q = \pm 1$ for right and left circular polarization respectively[3]), $\hat{k}$ is the propagation direction of the light, $\hat{z}$ is the direction of the quantization axis and $\hat{\epsilon_z}$ is the projection along the quantization axis of the light polarization vector. We stress that this light shift is obtained considering a single $|i\rangle \to |n', J'\rangle$ fine-structure transition and it is not the total light shift in our multi-level calculation, as

[2]The only state for which we consider the hyperfine energy splitting is $^3\mathrm{P}_1$ due to its relevance for optical Stern-Gerlach detection schemes [85, 86].

[3]See Ref. [105] and references therein for elliptic polarization.

indicated by the superscript $^{(n',J')}$. Notably, the scalar component of the light shift only depends on the total angular momentum quantum number F, while the vector and tensor components also depend on the nuclear Zeeman state $|m_F\rangle$. Moreover, the vector light shift is non-vanishing only for light that is circularly polarized along the quantization axis (i.e. σ^+ or σ^--polarized) and it is proportional to m_F, creating an energy shift equivalent to a Zeeman shift and thus an effective magnetic field. On the other hand, the tensor light shift is symmetric for $|\pm m_F\rangle$ states as it depends only on the absolute value $|m_F|$ and it is maximal for light that is linearly polarized along the quantization axis (i.e. π-polarized).

The three components of the polarizability are explicitly written as [100]:

$$\begin{aligned}
\alpha_{\mathrm{s}}(F,\omega) &= \sum_{F'} \frac{2}{3}\frac{\omega_{if}}{\hbar(\omega_0^2-\omega^2)}|\langle F|\mathbf{d}|F'\rangle|^2 \\
\alpha_{\mathrm{v}}(F,\omega) &= \sum_{F'}(-1)^{F'+F+1}\sqrt{\frac{6F(2F+1)}{F+1}}\frac{\omega_f}{\hbar(\omega_0^2-\omega^2)}\begin{Bmatrix}1 & 1 & 1\\ F & F & F'\end{Bmatrix}|\langle F|\mathbf{d}|F'\rangle|^2 \\
\alpha_{\mathrm{t}}(F,\omega) &= \sum_{F'}(-1)^{F'+F}\sqrt{\frac{40F(2F+1)(2F-1)}{3(F+1)(2F+3)}}\frac{\omega_0}{\hbar(\omega_0^2-\omega^2)}\begin{Bmatrix}1 & 1 & 2\\ F & F & F'\end{Bmatrix}|\langle F|\mathbf{d}|F'\rangle|^2
\end{aligned} \tag{1.24}$$

where the terms in curly brackets are the Wigner 6-j symbols and $\langle F|\mathbf{d}|F'\rangle$ are the reduced dipole matrix elements. Importantly, the sum runs over all dipole-allowed transitions and we have to exclude from the sum those states that have $m'_F \neq m_F + q$. Inserting Eq. (1.24) in Eq. (1.23) we can compute the light shift associated to a single fine-structure transition. The total light shift of a state $|i\rangle$ is then given by the sum of the light shifts over all the fine-structure transitions:

$$V_{\mathrm{ac}}(F,m_F,\omega) = \sum_{n',J'} V_{\mathrm{ac}}^{(n',J')}(F,m_F,\omega) \tag{1.25}$$

Knowing the quantum numbers and transition energies of all the involved states, the only element that we are missing is an expression for the $\langle F|\mathbf{d}|F'\rangle$ terms.

Reduced dipole matrix element from excited states lifetimes

The squared reduced dipole matrix elements $|\langle F|\mathbf{d}|F'\rangle|^2$ quantify the strength of the coupling between two states and can be computed from the lifetime of the excited state in a similar fashion to what we did in the two-level case [see Eq. (1.15)]. First, we can relate the reduced matrix element of the hyperfine states to the one of the fine-structure levels, whose lifetimes are typically reported in literature [100]:

$$\langle F|\mathbf{d}|F'\rangle = \langle nJ|\mathbf{d}|n'J'\rangle(-1)^{F'+J+I+1}\sqrt{(2J+1)(2F'+1)}\begin{Bmatrix}J & J' & 1\\ F' & F & I\end{Bmatrix} \tag{1.26}$$

The reduced matrix element $\langle nJ|\mathbf{d}|n'J'\rangle$ quantifies the strength of the $|nJ\rangle \rightarrow |n'J'\rangle$ transition and it is therefore related to the transition linewidth:

$$\Gamma_{n'J'\rightarrow nJ} = \frac{\omega^3_{nJ\rightarrow n'J'}}{3\pi\epsilon_0\hbar c^3}\frac{2J+1}{2J'+1}|\langle nJ|\mathbf{d}|n'J'\rangle|^2 \tag{1.27}$$

where $\hbar\omega_{nJ\rightarrow n'J'}$ is the transition energy. However, this expression is not particularly useful as it relates the J reduced matrix element to the linewidth of a single fine-structure transition, and not to the lifetime of the excited state, which is the value reported in literature. In fact, the lifetime of the excited state $\tau(n'J')$ is the result of all possible decays to lower-lying energy

levels, and not only of $|n'J'\rangle \rightarrow |nJ\rangle$, which is the decay we are interested in. We therefore have to find a way to extract this value from the reported lifetime of the excited state. We can write the inverse lifetime (i.e. the Einstein A coefficient) as the sum of the linewidths over all fine-structure transitions:

$$\begin{aligned} 1/\tau(n', J') &= \sum_J \Gamma_{n'J' \rightarrow nJ} = \\ &= \frac{|\langle nL|\mathbf{d}|n'L'\rangle|^2}{3\pi\epsilon_0\hbar c^3} \frac{2L+1}{2L'+1} \sum_J \omega^3_{nJ\rightarrow n'J'} (2J+1)(2L'+1) \begin{Bmatrix} L & L' & 1 \\ J' & J & S \end{Bmatrix}^2 \end{aligned} \tag{1.28}$$

where the sum runs over all $|n, J\rangle$ states to which $|n', J'\rangle$ can decay. The inverse excited-state lifetime is proportional to a weighted sum of $\omega^3_{nJ\rightarrow n'J'}$, which we can re-define as:

$$\tilde{\omega}^3_{n'J'} \equiv \sum_J \omega^3_{nJ\rightarrow n'J'} (2J+1)(2L'+1) \begin{Bmatrix} L & L' & 1 \\ J' & J & S \end{Bmatrix}^2 \tag{1.29}$$

In this way we can extract the L reduced dipole matrix element:

$$|\langle nL|\mathbf{d}|n'L'\rangle|^2 = \frac{1}{\tau(n', J')} \frac{3\pi\epsilon_0\hbar c^3}{\tilde{\omega}^3_{n',J'}} \frac{2L'+1}{2L+1} \tag{1.30}$$

From the L reduced dipole matrix element we can extract the J reduced dipole element as:

$$\langle nJ|\mathbf{d}|n'J'\rangle = \langle nL|\mathbf{d}|n'L'\rangle (-1)^{J'+L+1+S} \sqrt{(2J'+1)(2L+1)} \begin{Bmatrix} L & L' & 1 \\ J' & J & S \end{Bmatrix} \tag{1.31}$$

Combining Eq. (1.30), Eq. (1.31) and Eq. (1.26) we have all the elements to compute the F reduced matrix element and the three polarizability components in Eq. (1.24).

To sum up, the procedure to compute the light shift of any state in a multi-level system is the following. For each transition connecting the state of interest to an excited state $|n', J'\rangle$, we find all possible decay channels $|n', J'\rangle \rightarrow |nJ\rangle$ and compute $\tilde{\omega}^3_{n'J'}$ with Eq. (1.29). Then, we extract the L reduced matrix element starting from the excited state lifetime and use Eq. (1.31) and Eq. (1.26) to obtain the F reduced matrix element. Once this is known, it is possible to compute the scalar, vector and tensor components of the polarizability [Eq. (1.24)] and the light shift [Eq. (1.23)] for the considered fine-structure transition. Repeating this procedure for fine-structure transition and summing over all contributions allows to compute the total light shift of the desired state.

Alternative approach to extract fermionic light shifts from bosonic results

The described approach allows to obtain the light shift of any state starting only from known transition data. Most of its intricacies are related to the hyperfine electronic states and the calculations simplify when the hyperfine structure is absent, as in the case of ^{174}Yb or for states with $J = 0$. Indeed, we find that the computed light shifts for the bosonic isotope and for states with $J = 0$ are slightly more accurate than the one obtained for states displaying an hyperfine structure. To take advantage of this, we can employ an alternative approach to compute the light shifts of the $^3\mathrm{P}_1$ and $^1\mathrm{P}_1$ states of the fermionic isotopes, starting from the values obtained for ^{174}Yb. In particular, we employ all the procedure described above to compute the light shifts of the $|m_J = 0\rangle$ and $|m_J = \pm 1\rangle$ states of ^{174}Yb and we extract the light shifts of the $|m_F\rangle$ states of fermionic isotopes expressing them as linear combinations of the light shifts of the ^{174}Yb $|m_J\rangle$ states.

This approach is justified by the fact that the $|F, m_F\rangle$ states can be written as superpositions of $|J, m_J; I; m_I\rangle$ states, whose amplitudes are the Clebsch-Gordan coefficients $\langle F, m_F|J, m_J; I, m_I\rangle$. We can the write the light shift of state $|F, m_F\rangle$ as:

$$V_{\mathrm{ac}}(F, m_F) = \sum_{m_J} |\langle F, m_F|J, m_J; I, m_I\rangle|^2 \, V_{\mathrm{ac}}(m_J) \tag{1.32}$$

with [106]:

$$\langle F, m_F|J, m_J; I, m_I\rangle = (-1)^{-J+I+m_I}\sqrt{(2F+1)} \begin{pmatrix} J & I & F \\ m_J & m_I & -m_F \end{pmatrix} \tag{1.33}$$

where the term in parentheses is the Wigner 3-j symbol. Writing the coefficients above explicitly we can express the light shifts of the $^3\mathrm{P}_1$ and $^1\mathrm{P}_1$ states of ^{171}Yb as:

$$\begin{aligned} V_{\mathrm{ac}}(F = 3/2, m_F = \pm 1/2) &= \frac{1}{3}V_{\mathrm{ac}}(m_J = \pm 1) + \frac{2}{3}V_{\mathrm{ac}}(m_J = 0) \\ V_{\mathrm{ac}}(F = 3/2, m_F = \pm 3/2) &= V_{\mathrm{ac}}(m_J = \pm 1) \end{aligned} \tag{1.34}$$

and those of ^{173}Yb as:

$$\begin{aligned} V_{\mathrm{ac}}(F = 7/2, m_F = \pm 1/2) &= \frac{3}{7}V_{\mathrm{ac}}(m_J = \pm 1) + \frac{4}{7}V_{\mathrm{ac}}(m_J = 0) \\ V_{\mathrm{ac}}(F = 7/2, m_F = \pm 3/2) &= \frac{11}{21}V_{\mathrm{ac}}(m_J = \pm 1) + \frac{10}{21}V_{\mathrm{ac}}(m_J = 0) \\ V_{\mathrm{ac}}(F = 7/2, m_F = \pm 5/2) &= \frac{5}{7}V_{\mathrm{ac}}(m_J = \pm 1) + \frac{2}{7}V_{\mathrm{ac}}(m_J = 0) \\ V_{\mathrm{ac}}(F = 7/2, m_F = \pm 7/2) &= V_{\mathrm{ac}}(m_J = \pm 1) \end{aligned} \tag{1.35}$$

Notably, the states with $m_F = \pm F$ display the same light shift for all isotopes as they have the same (maximal) Clebsch-Gordan coefficient.

1.2.2 State-dependent and magic trapping of ytterbium atoms

Owing to its rich electronic structure, the light shifts of different ytterbium states result from the contribution of many optical transitions, spanning a large range of wavelengths from the UV to the IR region. The resulting light shifts are therefore characterized by many resonances and crossings which are of great interest for the realization of state-dependent or magic trapping potentials.

For a given trapping wavelength, the light shift experienced by two electronic states is, in general, different. The first consequence of this is that, as each state is energy-shifted by a different amount, the energy of the optical transition is shifted by the difference between the ground and excited-state light shift, i.e. by the differential light shift. This can have detrimental effects when addressing the considered transition, particularly in the case of narrow and ultranarrow transitions. In particular, inhomogeneities across different traps, such as in optical tweezer arrays or optical lattices, lead to variations of the transition frequency across the system and to a diminished fidelity when addressing the transition globally. On the other hand, differential light shifts can provide a tool for local addressing in quantum simulation [10, 107] and quantum information schemes [61, 65, 82]. Moreover, atoms exploring different regions of the trapping potential due to e.g. having a lower or higher energy will also experience a differential light shift, making the resonant condition energy-dependent even for a single trap. While this is typically an unwanted effect, it is possible to take advantage of differential light shifts and narrow optical transitions to perform Sisyphus cooling in non-magic traps [12, 76, 81].

λ (nm)	Untrapped state	Trapped state potential (Hz W^{-1} cm^2)	Source
423	$^3P_0$	n.a.	[112, 113]
553.29	$^1S_0$	-3.8(1.3)	[56]
576.61	$^3P_0$	-15(3)	[57]

Table 1.2| Clock states tune-out wavelengths. Measured tune-out wavelengths for the $^1S_0 \rightarrow {}^3P_0$ transition. As both involved states have $J = 0$ and no hyperfine structure, the reported values are valid for all ytterbium isotopes. When available, we report also the value of the trapped-state potential with the associated error.

λ (nm)	Transition	Isotopes	Source
459.6	$^1S_0 \rightarrow {}^3P_0$	174, 171, 173	[56]
486.8	$^1S_0 \rightarrow {}^3P_1 \vert F' = 3/2, m'_F = \pm 1/2\rangle$	171	[54]
483	$^1S_0 \rightarrow {}^3P_1 \vert F' = 3/2, m'_F = \pm 3/2\rangle$ [1]	171	[82]
532	$^1S_0 \rightarrow {}^3P_1 \vert J' = 1, m'_J = 0\rangle$	174	[52, 114]
532	$^1S_0 \vert F\rangle \rightarrow {}^1P_1 \vert F' = F + 1, m'_F = F + 1\rangle$	174, 171, 173	This work, [78]
759.3	$^1S_0 \rightarrow {}^3P_0$	174, 171, 173	[4, 115]
759.3	$^1S_0 \rightarrow {}^3P_1 \vert J' = 1, m'_J = 0\rangle$ [2]	174	[57]
759.3	$^1S_0 \rightarrow {}^3P_1 \vert F' = 3/2, m'_F = \pm 1/2\rangle$ [3]	171	[54, 65]

[1] Achieved for magnetic field orthogonal to the trapping light polarization.
[2] Achieved via a $\sim 36^\circ$ angle of the magnetic field.
[3] This transition is almost magic at 759.3 nm and can be made so with small angle-tuning.

Table 1.3| Ytterbium magic wavelengths. Measured magic wavelengths for different ytterbium transitions. For transitions involving states with $J \neq 0$ (i.e. $^1P_1$ and $^3P_1$) magic conditions are typically obtained for π-polarized trapping light. We instead indicate when the magic-conditions is obtained via angle-tuning [55].

The second consequence of differential light shifts is related to the different confinement felt by atoms in the two states. It is in fact possible that a confining potential for the electronic ground state is much less confining, or even repulsive, for the excited state. This typically leads to large atoms loss or heating effects when driving the optical transition if the trap potential is not switched off [108]. On the other hand, the different confinement between two electronic states can be a powerful tool to implement different mobility bands or effective mass imbalance when the two electronic states are both long-lived, as in the case of the clock states of AEAs [109–111].

An extreme situation is that of a so-called tune-out wavelength, for which one electronic state is trapped while the other has a vanishing light shift. This case is particularly relevant to engineer state-selective optical potentials which confine only one electronic state, one of the requirements to perform quantum simulation of localized impurity models [58] or lattice gauge theories [59, 60] with ytterbium atoms. We report measured values of tune-out wavelengths for the $^1S_0$ and $^3P_0$ clock states of ytterbium in Table 1.2.

The opposite scenario happens for so-called magic wavelengths, corresponding to a crossing of the light shift of the two states. In this case, the trapping is the same for both electronic states, and the differential light shift is zero, a condition that is extremely beneficial for clock interrogation [4, 116–118] as well as for single-atom imaging schemes where heating due to fluorescence photons scattering needs to be compensated by efficient laser cooling [52, 54, 55, 65]. We report a list of measured magic wavelengths for the relevant optical transition in different ytterbium isotopes in Table 1.3. Notably, for transitions in which the excited state displays multiple $|m'_F\rangle$ (or $|m'_J\rangle$) Zeeman sublevels magic-trapping can be obtained for one of the states

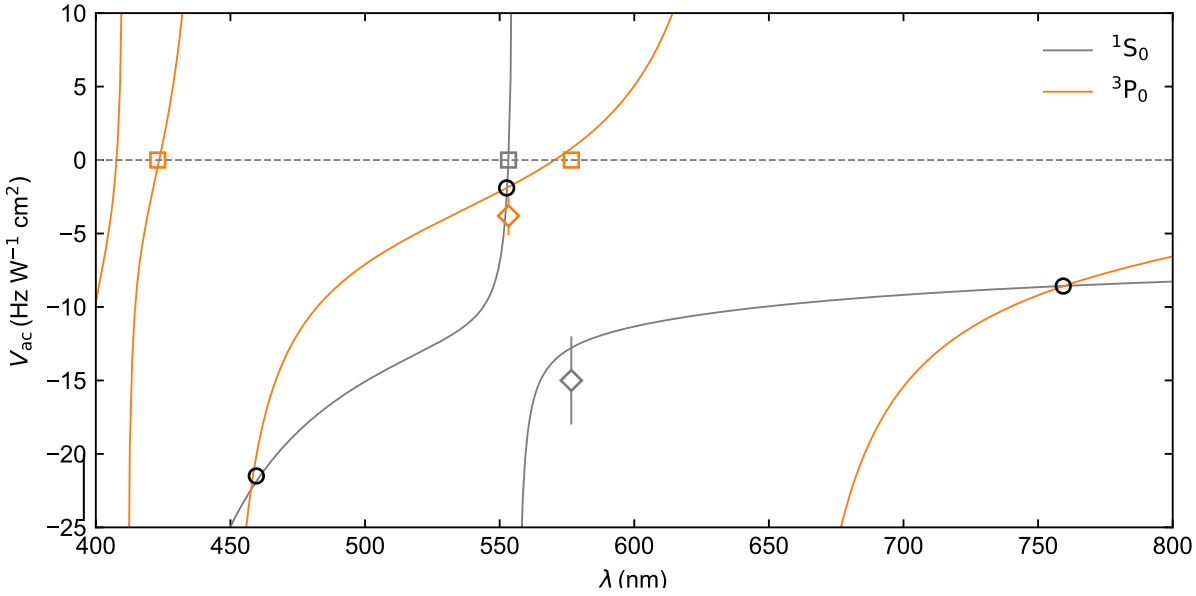

Figure 1.5| Ground and clock state light shifts. We plot the computed light shifts for the $^1P_1$ (grey line) and $^3P_0$ (orange line) states of ytterbium. We indicate tune-out wavelengths with squares and diamonds to represent the untrapped and trapped state's light shift respectively. Values and errorbars are obtained from Tables 1.2 and 1.3. We report measured magic wavelengths with black circles; note that the vertical position of these markers is only determined by the crossing of the polarizability curves. Owing to the lack of hyperfine structure ($J = 0$), the calculated light shifts are the same for all ytterbium isotopes. We apply a rigid shift of $-1.0\,\mathrm{Hz\,W^{-1}\,cm^2}$ to the $^3P_0$ light shift to match the well-established magic wavelength at 759.3 nm and the value of the static polarizability of the clock state [119].

by an appropriate tuning of the angle between the quantization axis (defined by a sufficiently strong magnetic field) and the linear polarization of the trapping light [55]. In particular, magic trapping via angle-tuning can be achieved when different $|m'_F\rangle$ states have differential light shifts with opposite sign, i.e. when some states have a smaller and some have a larger light shift than the ground state. In this case, an appropriate mixing of the states, obtained through the applied magnetic field, can result in a vanishing differential light shift for one of the states.

Calculation of ytterbium light shifts

Owing to the relevance of magic and state-dependent trapping for numerous scenarios, we employ the polarizability model described in the previous sections to compute the light shift of the most relevant electronic states for all ytterbium isotopes discussed in this work. The transition data employed for computing the light shifts and all the considered states are reported in Appendix B.

In Fig. 1.5 we show the computed light shifts for the $^1S_0$ ground and $^3P_0$ clock states. We find that the ground-state calculations correctly match the value of the static polarizability $\alpha_{^1S_0}(\omega = 0) = 141(6)$ a.u. [119], while we have to apply a rigid shift of $-1.0\,\mathrm{Hz\,W^{-1}\,cm^2}$ to the $^3P_0$ light shift to match the correct static polarizability $\alpha_{^3P_0}(\omega = 0) = 302(14)$ a.u. [119]. With this rigid shift, our results show good agreement with experimentally measured magic and tune-out wavelengths, indicated by different markers in the figure. In particular, our calculations reproduce the magic wavelength at 759.3 nm [4, 115] and we find a very small discrepancy for the one at $\simeq 460$ nm [56]. We also correctly predict the ground state tune-out wavelength at 553 nm [56] while we find a small discrepancy for the clock state tune-out at $\simeq 576$ nm [57].

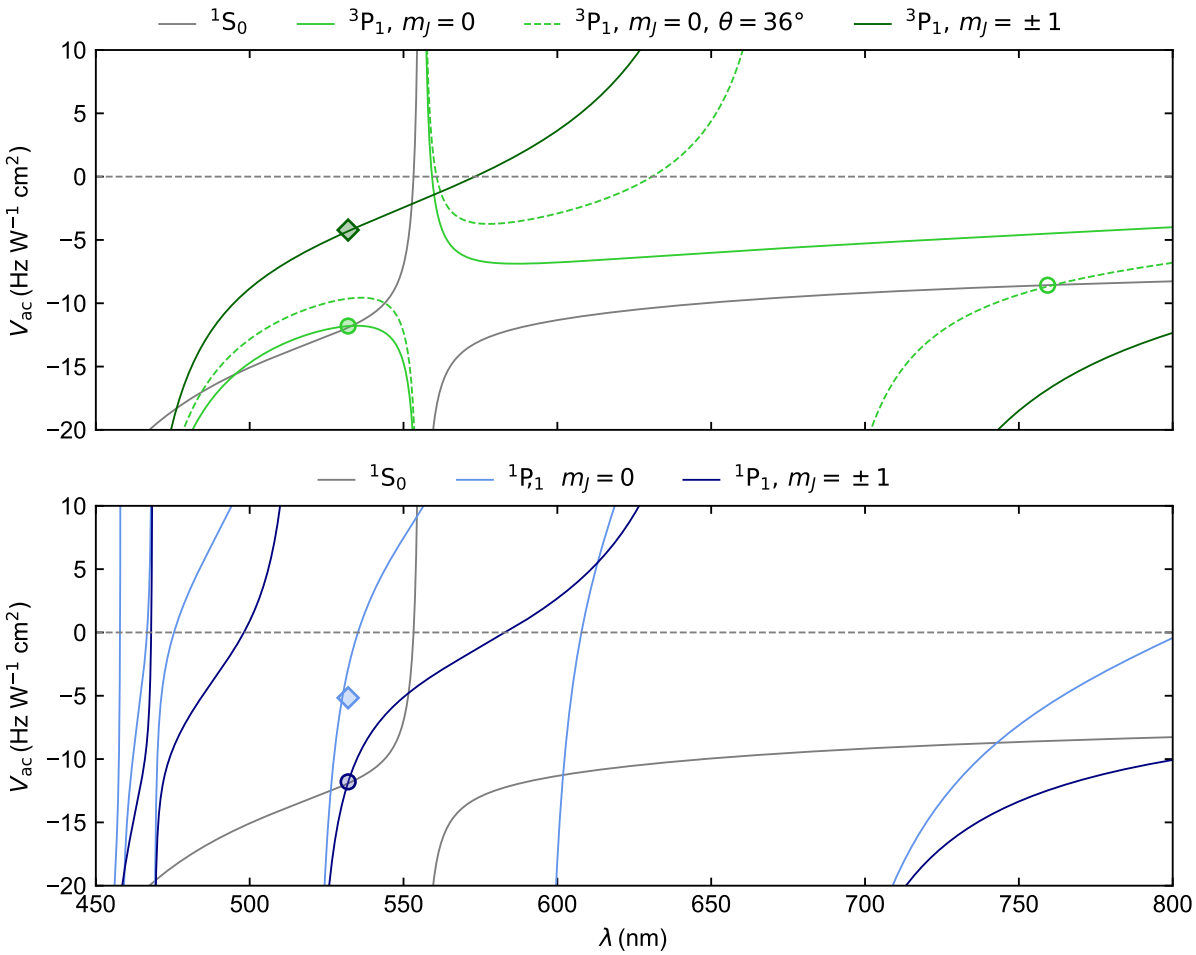

Figure 1.6| Light shifts of the $^1S_0$, $^1P_1$ and $^3P_1$ states in ^{174}Yb for linearly polarized trapping light. Top: computed light shifts for the $^1S_0$ (grey), and $^3P_1$ (green) states. Solid lines are obtained with π-polarized trapping light, while the dashed line indicates the results for a 36° angle between trap polarization and magnetic field, which guarantees magic trapping at $\simeq 759$ nm [57]. Bottom: computed light shifts for the $^1S_0$ (grey), and $^1P_1$ (blue) states. Different shades of green(blue) represent different $|m_J\rangle$ sublevels of the $^3P_1(^1P_1)$ state. Circles indicate measured magic wavelengths for the $^1S_0 \rightarrow {}^3P_1$ transition [see Table 1.3] and the 532 nm magic wavelength for the $^1S_0 \rightarrow {}^1P_1|J = 1, m'_J = \pm 1\rangle$ transition measured in this work; note that the vertical position of these markers is only determined by the crossing of the polarizability curves. Diamond markers indicate the light shift for the non-magic Zeeman sublevels at 532 nm, obtained from spectroscopic measurements [see Sec. 2.3.4]. We employ empty and filled markers for polarizablity values obtained from literature and from spectroscopic measurements presented in this work, respectively. A rigid shift of $-1.5\,\mathrm{Hz\,W^{-1}\,cm^2}$ is applied to the $^3P_1$ light shifts to match the well-established magic wavelength at 532 nm.

For both tune-out wavelengths we find good agreement also with the values reported for the trapped state. As the considered states have both $J = 0$ and therefore no hyperfine structure, these results are valid for all ytterbium isotopes.

We instead have to differentiate between hyosotpes for the $J = 1$ $^3P_1$ and $^1P_1$ states. We report the results for ^{174}Yb in Fig. 1.6. We consider π-polarized trapping light (i.e. with the polarization aligned with the quantization axis) and apply a rigid shift of $-1.5\,\mathrm{Hz\,W^{-1}\,cm^2}$ to

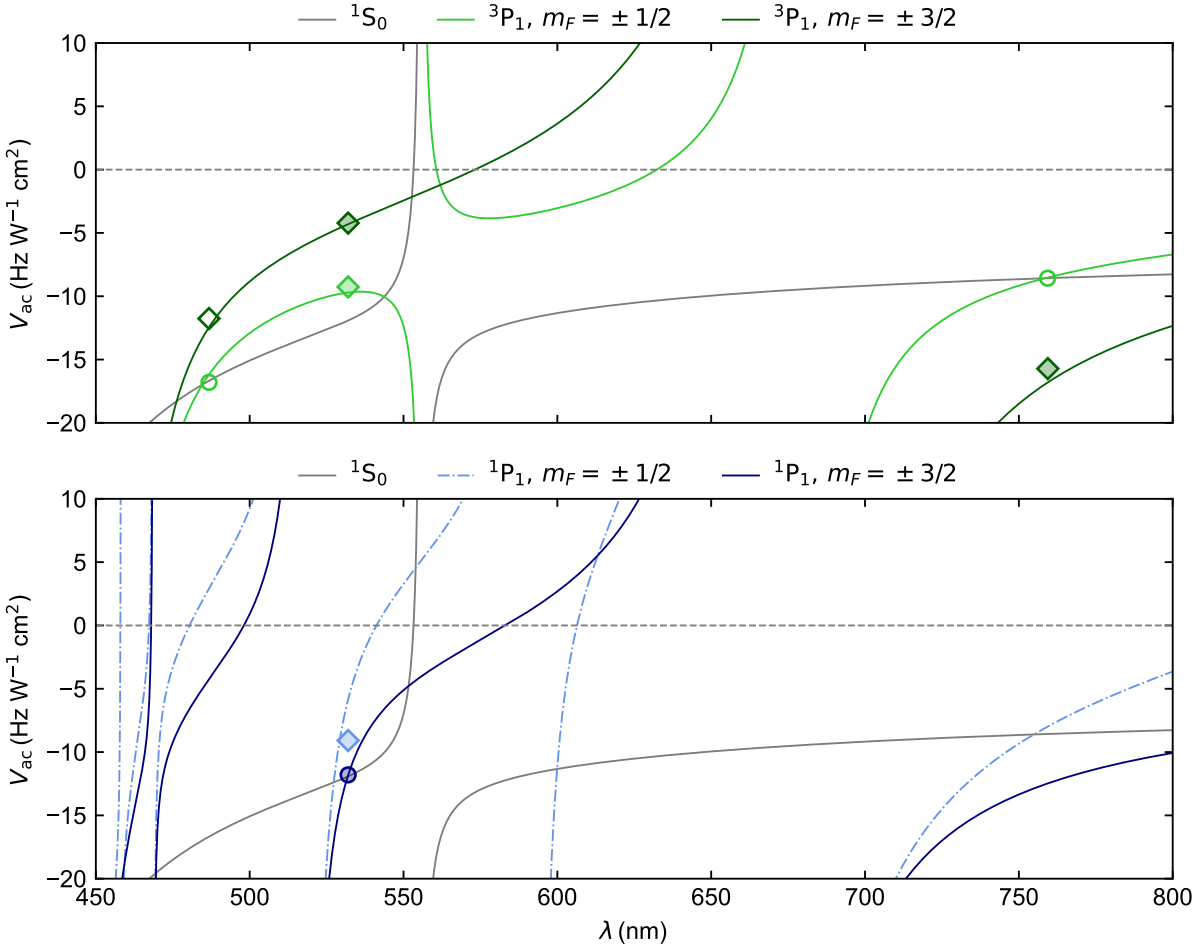

Figure 1.7| Light shifts of the $^1S_0$, $^1P_1$ and $^3P_1$ states in ^{171}Yb for π-polarized trapping light. Top: computed light shifts for the $^1S_0$ (grey), and $^3P_1$ (green) states. Bottom: computed light shifts for the $^1S_0$ (grey), and $^1P_1$ (blue) states. Different shades of green(blue) represent different $|m_F\rangle$ states of the $^3P_1(^1P_1$) manifold. The dashed-dotted line indicates that the light shift is computed with Eq. (1.34). Circles indicate measured magic wavelengths for the $^1S_0 \rightarrow {}^3P_1$ transition [see Table 1.3] and the 532 nm magic wavelength; note that the vertical position of these markers is only determined by the crossing of the polarizability curves. Diamond markers indicate the light shift of non-magic Zeeman sublevels at 532 nm, obtained from spectroscopic measurements [see Sec. 2.3.4]. We employ empty and filled markers for polarizablity values obtained from literature and from spectroscopic measurements presented in this work, respectively. We apply the same $-1.5\,\mathrm{Hz\,W^{-1}\,cm^2}$ rigid shift to the $^3P_1$ light shifts as for ^{174}Yb.

the $^3P_1$ light shift to match the 532 nm magic wavelength for the $^1S_0 \rightarrow {}^3P_1|J' = 1, m'_J = 0\rangle$ transition. With this shift we are able to reproduce the light shifts of the $^3P_1|J' = 1, m'_J = \pm 1\rangle$ states measured in this work and in Refs. [52, 77]. We also correctly find that $\simeq 759$ nm can be rendered magic for the $^1S_0 \rightarrow {}^3P_1|J' = 1, m'_J = 0\rangle$ transition by angle tuning the magnetic field with $\theta = 36°$, as reported in Ref. [57]. For the $^1P_1$ state, we find that we correctly reproduce the 532 nm magic wavelength for the $^1S_0 \rightarrow {}^1P_1|J' = 1, m'_J = \pm 1\rangle$ transition measured in this work and in the associated Ref. [78] without any rigid shift. We also find good agreement with the measured $^1P_1|J' = 1, m'_J = 0\rangle$ light shift.

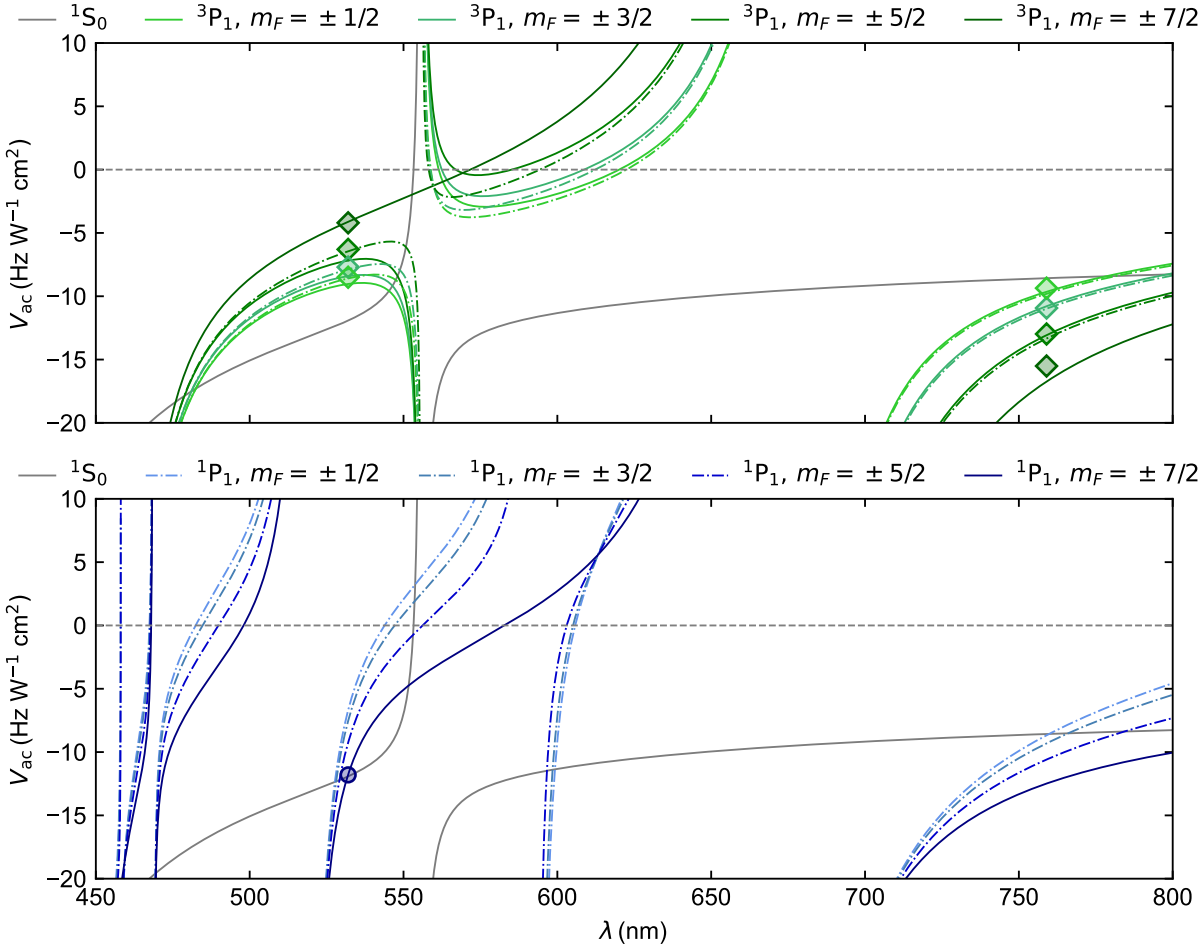

Figure 1.8| Light shifts of the $^1S_0$, $^1P_1$ and $^3P_1$ states in ^{173}Yb for π-polarized trapping light.. Top: computed light shifts for the $^1S_0$ (grey), and the $^3P_1$ (green) states. Bottom: computed light shifts for the $^1S_0$ (grey), and the $^1P_1$ (blue) states. Different shades of green(blue) represent different $|m_F\rangle$ states of the $^3P_1(^1P_1$) manifold. Solid and dashed-dotted lines represent results obtained directly for the fermionic isotope (solid lines) or extracted with Eq. (1.35), respectively. The blue circle indicates the 532 nm magic wavelength while green diamonds indicate the light shift for non-magic Zeeman sublevels at 532 nm, obtained from spectroscopic measurements [see Sec. 2.3.4]. We employ empty and filled markers for polarizablity values obtained from literature and from spectroscopic measurements presented in this work, respectively. We apply the same $-1.5\,\mathrm{Hz\,W^{-1}\,cm^2}$ rigid shift to the $^3P_1$ light shifts as for all other isotopes.

We present our results for the fermionic ^{171}Yb in Fig. 1.7. We apply the same shift as for ^{174}Yb and we reproduce the magic wavelengths for the $^1S_0 \rightarrow {}^3P_1|F' = 3/2, m'_F = \pm 1/2\rangle$ transitions at $\simeq$ 759 nm and $\simeq$ 487 nm [54]. We also match the measured light shifts for the $^3P_1|F' = 3/2, m'_F = \pm 3/2\rangle$ states, which are the same as the ones of the $^3P_1|J' = 1, m'_J = \pm 1\rangle$ for ^{174}Yb as they are all connected to the ground state by stretched transitions. For the $^1P_1$ state, we confirm the magic trapping of the stretched transition (same as ^{174}Yb) and we find relatively good agreement between our calculations and the measured light shift of the $^1P_1|F' = 3/2, m'_F = \pm 1/2\rangle$ states, which we compute with Eq. (1.34) as we find that it provides a more reliable estimate.

Finally, we report the results for ^{173}Yb in Fig. 1.8. We shift the $^3\mathrm{P}_1$ light shift by the same amount as the other isotopes and we find good agreement with the measured light shifts of all $^3\mathrm{P}_1|F' = 7/2, m'_F\rangle$ Zeeman sublevels at 532 nm [77]. We note that the agreement is slighlty better when we extract the light shifts from the ones of ^{174}Yb (dashed-dotted lines) compared to the full a-priori calculation (solid lines). As expected, we find that the stretched $^1\mathrm{S}_0 \rightarrow {}^1\mathrm{P}_1$ transition is also magically-trapped at 532 nm.

1.3 Optical tweezers

More than 20 years after the first observation of a single atom confined in a focused optical trap [120], optical tweezers have become one of the leading platforms for quantum science with ultracold neutral atoms and molecules [7]. This large interest is motivated by the fact that optical tweezers provide the experimental tool to trap, manipulate and detect individual neutral particles, taking advantage of the large light shift produced by tightly focused laser light.

Possibly the most crucial parameter of an optical tweezer trap is its waist, which, for a given power, determines the strength of the trapping potential. In a first approximation, this can be determined by the size of the Airy disk produced by the circular aperture of the focusing lens:

$$R_{\mathrm{Airy}} = 0.61\frac{\lambda}{\mathrm{NA}} \tag{1.36}$$

where λ is the wavelength of the trapping light and NA is the numerical aperture of the lens or objective employed for producing the tweezer's focus. The expression above is however only a crude approximation. In fact, it originates from Fraunhofer diffraction theory and it is strictly valid only for a plane wave diffracted by the objective aperture. Real Gaussian beams, however, are not plane waves and Eq. (1.36) remains a good approximation only if the incident beam waist is much larger than the aperture radius. If this is not the case, computing the waist and the geometric properties of a tweezer trap requires to solve the Fresnel diffraction equations for the propagation of the field through the objective lens. We refer to Refs. [121, 122] for further details on how to compute the shape of the trapping potential for different sizes of the tweezers beam with respect to the objective aperture.

For our experimental setup, the tweezers beam waist before the objective is roughly half of the aperture and our traps have a mostly Gaussian shape. The three dimensional confinement is therefore determined by the shape of a Gaussian beam:

$$U(r,z) = -U_0\left(\frac{\omega_0}{\omega(z)}\right)^2 e^{-2r^2/\omega(z)^2} \tag{1.37}$$

where ω_0 is the beam waist at its smallest (which we just refer to as waist) and $\omega(z)$ is the beam waist at position z, as defined by Gaussian optics. Neglecting optical aberrations, the trap is cylindrically symmetric along the propagation direction $\hat{z}$. Performing an expansion in r and z we can get the harmonic approximation of the Gaussian potential:

$$U(r,z) \simeq -U_0 + \frac{2U_0}{\omega_0^2}r^2 + \frac{U_0}{z_R^2}z^2 \tag{1.38}$$

where $z_R = \pi\omega_0^2/\lambda$ is the Rayleigh range. From this expression we obtain the radial and axial trap frequencies, which provide the relevant time and energy scales for atomic motion within the trap, as well as the separation between the quantum harmonic oscillator levels:

$$\omega_r = \sqrt{\frac{4U_0}{mw_0^2}} \qquad \omega_z = \sqrt{\frac{2U_0}{mz_R^2}} \tag{1.39}$$

While it is possible to cool the atoms down to the harmonic oscillator ground state [53, 93, 123], in general they will occupy oscillator levels $|n > 0\rangle$. When atoms lose energy, e.g. through sideband cooling [53, 93, 123–125], they decrease their average $\langle n \rangle$, while they increase it if they acquire energy, a process that we typically think of as heating. When the atomic energy is such that it overcomes the depth of the potential and reaches an unbound state, the atom is lost. This is one of the main processes limiting the lifetime of tweezer-trapped atoms and the survival probability in single-atom fluorescence imaging scheme.

When no light other than trapping is directed on the atoms, the so-called dark lifetime is limited by a number of mechanisms, from residual-gas background collisions to three-body losses in the case of interacting gases. Considering individually-trapped atoms and for sufficiently good vacuum conditions, the dark lifetime is often limited by trap-induced heating. This can be both of fundamental or technical origin.

Heating from technical noise

Technical noise induces heating through fluctuations of the trapping potential. In a simple 1D case, the Hamiltonian of an atom trapped in a harmonic potential with a fluctuating trap frequency can be written as [126, 127]:

$$H = \frac{p^2}{2m} + \frac{1}{2} m \, \omega_{\text{trap}}^2 \left[1 + \epsilon(t)\right] x^2 \tag{1.40}$$

where ω_{trap} is the trap frequency and $\epsilon(t) = \left(I(t) - I_0\right)/I_0$ is the fractional fluctuation of the trap intensity. The induced heating rate can be determined using first-order time-dependent perturbation theory to compute the transition rates between harmonic oscillator states $|n\rangle \to |m > n\rangle$. The perturbation of interest is the one caused by the trap intensity fluctuations:

$$H' = \frac{1}{2} \epsilon(t) \, m \, \omega_{\text{trap}}^2 x^2 \tag{1.41}$$

The quadratic dependence on position results in a $|\langle m|x^2|n\rangle|^2$ term in the $R_{n\to m}$ transition rate, which, for symmetry reasons, is non-zero only if $m = n + 2$ [126, 127]. Therefore, intensity fluctuations inject excitations between states that are separated in energy by $2\hbar\omega_{\text{trap}}$. This result in an exponential increase of the average energy

$$\langle \dot{E} \rangle = \Gamma \langle E \, \rangle \tag{1.42}$$

with rate

$$\Gamma = \pi^2 \nu_{\text{trap}}^2 S_\epsilon(2\nu_{\text{trap}}) \tag{1.43}$$

where $\nu_{\text{trap}} = \omega_{\text{trap}}/2\pi$ is the trap frequency and $S_\epsilon(\nu)$ is the one-sided power spectral density of the laser intensity noise [126, 127].

Trap-intensity noise at twice the radial or axial trapping frequency results in a strong so-called parametric heating and consequently leads to a reduction of the atomic lifetime. This effect can be exploited to measure the trapping frequency by purposefully modulating the trap [see Sec. 2.3.2]. However, this is in general a highly detrimental effect that needs to be mitigated by stabilizing the intensity of the trapping light in the appropriate frequency range, which for most tweezers experiments lies within 10 and 500 kHz, but can be reach even higher values for lattice experiments [128]. In the latter case, parametric heating can excite atoms out of the ground-state lattice band or create unwanted defects in the lattice, limiting access to the low-temperature regimes of the investigated models and making intensity stabilization even more crucial.

For an atom array, parametric heating can also originate from cross-talk between different traps causing relative fluctuations of the trap intensities even when the total trapping power is constant. This effect is particularly detrimental in AOD-generated tweezer arrays, where nonlinear effects lead to intermodulation between different RF tones driving the AOD crystal [129]. In particular, the nonlinear response of the AOD crystal and RF amplifier leads to the development of new RF tones at sums and differences of the initial ones. These new tones can mix again with the original ones resulting in interference effects and intensity noise. Moreover, complicated dynamics of intensity fluctuations between RF tones have also been observed [130]. Intermodulation noise can be mitigated by appropriately choosing the phase of the various RF tones driving the AOD [131] and the spacing between the tweezer traps [132].

Atoms can also increase their energy due to pointing noise of the trapping potential. In this case, we can follow the same perturbative approach employed for intensity fluctuations to find the resulting heating rate [126, 127]. For pointing noise, the perturbation term is linear (and not quadratic) in position and the relevant excitations are thus between states $|n\rangle$ and $|m = n + 1\rangle$. The resulting energy increase is:

$$\langle \dot{E} \rangle = 4\pi^4 m \, \nu_{\mathrm{trap}}^4 S_x(\nu_{\mathrm{trap}}) \tag{1.44}$$

and depends on the power spectrum of the position fluctuations $S_x(\nu)$ evaluated at the trapping frequency. In general, accessing $S_x(\nu)$ is more challenging than measuring the power spectrum of intensity fluctuations, and heating induced by pointing fluctuations is typically minimized by holding the optical components of the trapping potentials on stable mounts placed on stable optical breadboards.

Heating rate from photon recoils

Besides technical noise, atoms confined in optical traps can increase their energy through off-resonant scattering of trap photons. We can define the energy gained by the emission or absorption of one photon as the recoil energy $E_{\mathrm{rec}} = \frac{\hbar^2 k^2}{2m}$. When photon scattering occurs, an atom absorbs a photon from a directional beam, increasing its energy by one full recoil along that direction, and emits another photon in a random direction. Approximating the spontaneous emission as isotropic, on average the energy increases by $E_{\mathrm{rec}} + E_{\mathrm{rec}}/3$ along the beam's direction and by $E_{\mathrm{rec}}/3$ along the other two directions. The total energy increase is therefore $2E_{\mathrm{rec}}$ per scattering event, not surprisingly as two photons are involved in each event. Considering the photon scattering rate Γ_{sc}, the total thermal energy increases with a rate $\dot{E} = 2E_{\mathrm{rec}}\Gamma_{\mathrm{sc}}$.

At thermal equilibrium in a three-dimensional trap, the relation between mean kinetic energy and temperature is $E_{\mathrm{kin}} = 3/2 k_{\mathrm{B}} T$. In the specific case of harmonic confinement, the equipartition theorem ensures that energy is equally divided between kinetic and potential, such that the total energy is $E = 2E_{\mathrm{kin}} = 3k_{\mathrm{B}}T$. Differentiating both sides of this equation we get the relation between the heating rate and the photon scattering rate in a harmonic trap [103]:

$$k_{\mathrm{B}}\dot{T} = \frac{2}{3} E_{\mathrm{rec}} \Gamma_{\mathrm{sc}} \tag{1.45}$$

where Γ_{sc} is the photon scattering rate, typically computed with Eq. (1.19). This expression, albeit often considered in the case of off-resonant scattering in far-detuned optical traps, can also be employed to compute the heating rate associated to resonant driving of an atomic transition when performing e.g. fluorescence imaging.

Loss model of single trapped atoms

Regardless of the source, atoms can be lost from the trap upon excessive heating. In particular, an atom is always lost whenever its energy is larger than the trap depth U_0. To determine the

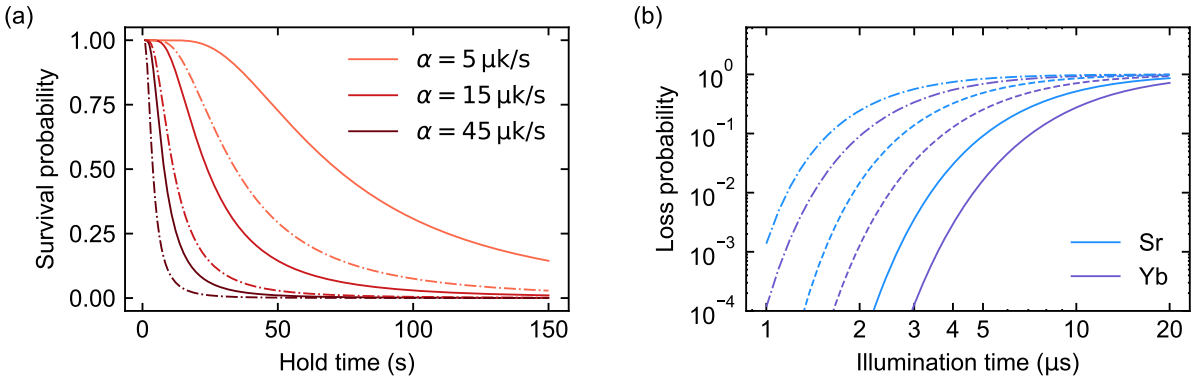

Figure 1.9| Simulation of heating-induced losses. (a) Survival probability as a function of holding time for atoms trapped with $U_0 = 1\,\mathrm{mK}$ (solid lines) and $U_0 = 0.5\,\mathrm{mK}$ (dashed-dotted lines). Darker shades of red represent different heating rates α. (b) Loss probability during fast imaging as a function of illumination time for trap depths $U_0 = 2\,\mathrm{mK}$ (solid lines), $U_0 = 1\,\mathrm{mK}$ (dashed lines), $U_0 = 0.5\,\mathrm{mK}$ (dashed-dotted lines). Different colors indicate simulations considering the atomic properties of strontium and ytterbium. The difference between the two atomic species lies in their heating rates: $\alpha \simeq 31\,\mu\mathrm{K/\mu s}$ (Sr) and $\alpha \simeq 21\,\mu\mathrm{K/\mu s}$ (Yb). For both panels we neglect losses induced by vacuum-background collisions.

loss probability we therefore need to consider the energy distribution of single atoms in optical tweezers, which we do following the approach presented in Ref. [133].

We consider a Boltzmann distribution for atoms inside the trap, emphasizing that, since we are working with single atoms, the probability distribution refers to different realizations of the same experiment rather than to an atomic ensemble. The normalized energy distribution reads:

$$f_{\mathrm{th}}(E) = \frac{1}{2(k_B T)^3} E^2 e^{-E/k_B T} \tag{1.46}$$

This is a thermal distribution, where the temperature is defined from the average atomic energy over many realizations. For a given temperature, the probability than an atom remains confined in the trap is given by the probability that the atom has an energy lower than the trap depth:

$$P_{\mathrm{surv}}(U_0) = \int_0^{U_0} f_{\mathrm{th}}(E) dE = 1 - \left[1 + \eta + \frac{1}{2}\eta^2\right] e^{-\eta} \tag{1.47}$$

where $\eta = U_0/k_B T$. This implies that atoms within a trap follow a truncated Boltzmann distribution, with an upper threshold set by the drap depth. Heating results in an increase of temperature over time, with a corresponding shift of the distribution center towards higher energies. This leads to a larger probability of atoms having an energy $> U_0$ and a reduction of survival probability.

We compute the loss probability caused by heating mechanisms and vacuum background collisions as:

$$P_{\mathrm{h,v}}(U_0, T, t) = 1 - \left[1 - \left(1 + \eta + \frac{1}{2}\eta^2\right) e^{-\eta}\right] e^{-t/\tau_{\mathrm{v}}} \tag{1.48}$$

where τ_{v} is the vacuum-limited lifetime measured from e.g the MOT lifetime. For a constant heating rate α, we can write $T = T_0 + \alpha t$, where T_0 is the initial temperature. In this case, the survival probability remains high as long as the thermal atomic distribution is centered on values much smaller than the trap depth, while it drops quickly for longer times, when the statistically-average energy is sufficiently high to result in a considerable probability of

overcoming the trap depth. We show the simulated survival probability as a function of the holding time for different trap depths and heating rates in Fig. 1.9(a), neglecting losses induced by collisions with background residual gas.

As discussed in detail in Chapter 4, this model can also be applied to heating-induced losses during fluorescence imaging. In fact, scattering of fluorescence photons leads to a temperature increase described by Eq. (1.45), with a much higher heating rate compared to off-resonant scattering from the trap. However, if the acquired energy during imaging remains small, the atoms have a high probability of surviving the imaging process. We show the simulated loss probability for fast imaging on the $^1S_0 \rightarrow {}^1P_1$ transition with the atomic properties of strontium and ytterbium atoms in Fig. 1.9(b) indicating that, for sufficiently short illumination times, high-survival probabilities remain possible even without active cooling.

1.4 Quantum science with single alkaline-earth-like atom arrays

The first pioneering works demonstrating optical trapping of individual atoms have been focused on alkalis [120, 134], as the single valence electron allows for simple and robust laser cooling schemes. However, after the successful laser cooling and trapping of other atomic species, much effort is being directed towards tweezer-trapping of alkaline-earth-like atoms and lanthanides [52–55, 135, 136]. This interest is motivated by the additional degrees of freedom offered by these atomic species compared to alkalis, which might expand the scope of scientific applications [44]. In particular, the rich electronic structure of AEAs and lanthanides allows for efficient single-atom imaging and cooling schemes as well as for coherent manipulation of the internal degrees of freedom. In the following we will provide a brief overview of some of the recent developments in quantum science and technology with arrays of individually-trapped AEAs.

1.4.1 Quantum information schemes

Neutral-atom arrays are one of the proposed platforms for the development of a universal quantum processor [21–24, 43, 137]. Such systems satisfy several key requirements for quantum information processing, including long coherence times and good scalability of the number of qubits, a crucial feature for fault-tolerant quantum computing.

In this context, one of the central challenges is posed by the sensitivity to errors intrinsic in quantum states, which prevents reliable computation. Quantum error correction (QEC) theory provides a conceptual solution to this problem by delocalizing logical information on multiple physical qubits. This requires to entangle many redundant physical qubits, such that, if any physical qubit fails, the logical information remains protected in the other ones. This redundancy comes at a significant hardware cost, as hundreds or even thousands of physical qubits may be required for each logical qubit [23, 137]. Neutral-atom arrays, in which each individually-trapped atom implements a physical qubit, offer excellent scalability properties. In particular, there have been recent demonstrations of single-particle trapping and detection for up to thousands of atomic qubits, where optical tweezers are employed to rearrange and shuttle atoms between different locations [12, 138–142]. While much effort is directed towards the realization of such large-scale arrays, a complementary approach is to delocalize quantum information processing on multiple smaller-scale processing units, connected by optical fibers [94, 95, 143].

One of the key advantages of AEAs compared to alkalis lies in the long coherence times of their internal states, which offer robust qubit econdings. In strontium and ytterbium, digital quantum computing typically relies on the optical clock qubit [31, 50] and, in the specific case of ^{171}Yb, on the two nuclear-spin states [53, 54]. Focusing on ytterbium, both qubit encodings display long coherence times, owing to their decoupling from external perturbations. In

particular, the absence of coupling between nuclear and electronic degrees of freedom results in coherence times of many seconds for the nuclear-spin qubit states [48, 53, 54, 65]. For these states single-qubit gates can be performed through two-photon [53] and RF [54] transitions, achieving fidelities $> 99.9\%$. Similar fidelities are also achieved for the optical qubit [48, 65]. Notably, in ^{171}Yb the presence of the nuclear-spin qubit in both the ground and metastable states of the clock transition realizes so-called optical-metastable-ground-state (omg) architecture. The recent demonstration of high-fidelity manipulation of all three qubit encodings [51, 65] paves the way to mid-circuit measurement and operations where data qubits are shelved in the clock state and measurements are performed on ground-state atoms.

The optical qubit features other appealing properties for quantum information schemes. First, its differential trapping compared to ground-state atoms allows to employ light shifts produced by tightly-focused laser beams to achieve local control on qubit rotations, enabling separation of data and ancilla qubits without the need of extended systems and atom shuttling [65]. On the other hand, it is possible to leverage selective trapping of either of the optical qubit states to implement selective movements aimed at realizing collisional two-qubit gates through spin-exchange interactions [61]. The metastable qubit encoding also provides a simple way to detect errors resulting from atoms decaying to the ground state and exiting the computational subspace, which can be independently detected and, possibly, corrected [48–51, 144, 145].

In AEAs, the $^3P_0$ clock state is also employed for Rydberg excitation, which is typically required to implement high-fidelity two-qubit gates. In fact, the inter-particle distance of atoms in optical tweezer arrays is too large for any significant tunneling to take place, with the notable exception of very light lithium atoms [146]. Owing to to the speed and robustness of two-qubit gates based on Rydberg excitation, entanglement between physical qubits is typically achieved via long-range dipole-dipole interactions through the Rydberg blockade mechanism [17]. Compared to alkalis, where Rydberg excitations are performed via two-photon transitions, the metastable states of AEAs provide useful intermediate states from which Rydberg excitation can be performed with a single UV photon. A central challenge to experiments with Rydberg atoms is that they are typically repelled by traps that are confining for atoms in the ground state and therefore require to extinguish the trapping during Rydberg excitation, limiting interaction times to few-microseconds and reducing two-qubit gate fidelities. In this context, AEAs offer several advantages compared to alkalis. In fact, when one of the two valence electrons is excited to the Rydberg state, the atom retains a structure similar to a singly-charged ion and displays a significant polarizability, which allows trapping of the Rydberg state, enhancing the fidelity of two-qubit gates [147].

While in this brief review we have focused on the fundamental features of AEAs for digital quantum computing, such properties are also appealing for quantum simulation of many-body Hamiltonians [47]. Owing to their versatility and the recent advancements in their cooling, imaging and manipulation, AEAs are nowadays one of the most appealing choices for quantum information and simulation schemes, as evident from the rapidly growing number of experimental platforms based on trapped strontium and ytterbium atoms [12, 27, 52, 53, 55, 56, 82, 84, 148].

1.4.2 Mid-circuit measurements

Following the successful demonstration of the fundamental building blocks of a neutral-atom-based quantum processor, in the last few years much effort has been directed towards the implementation of quantum error correction protocols. This requires to encode quantum information in logical qubits and to perform operations in a fault-tolerant way. Error correction protocols allow to suppress errors on logical gates as long as the error probability during each operation remains below a threshold, which depends on the nature of the noise in the physical qubits [144].

A particularly favorable type of noise consists in qubits leaking out of the computational subspace. These so-called erasure conversions, or detectable leakages, can be detected and corrected with relative ease and lead to a high error-probability threshold for accessible fault-tolerant quantum computation. In AEAs erasure conversion errors occur naturally when encoding qubits in the metastable states [48–51, 144, 145]. For ^{171}Yb, the qubit is typically encoded in the spin-1/2 levels of the $^3P_0$ state, while for bosonic strontium ($I = 0$) there have been demonstrations of erasure detections for a $^3P_0$-Rydberg state qubit and for a $^3P_0$-$^3P_2$ qubit [49, 50]. In all cases, computation is performed by exciting atoms from the long-lived triplet states to a Rydberg level to implement two-qubit gates between neighboring atoms. Any atom in the $^1S_0$ ground state is therefore out of the computational qubit space. Atoms can be found in $^1S_0$ due to imperfect excitation to the clock state or due to spontaneous decays from the qubit subspace, which can be both considered computational errors. Owing to atoms in the metastable states being dark to imaging light addressing the $^1S_0 \rightarrow {}^1P_1$ transition, it is possible to image atoms in the ground state without perturbing those in the qubit states so that errors can be detected and, possibly, corrected.

From a practical point of view, error correction with detectable leakages consists in interleaving quantum operations with mid-circuit detections, to verify if, and where, an error has occurred. When a leakage error is detected, the faulty qubit can be re-initialized before proceeding with successive operations. As the whole detection and re-initialization sequence needs to be repeated every N operations (possibly $N = 1$) its overall speed is one of the key limitations to the number of repeated operations that can be performed, given the coherence and lifetime of the physical qubits. Therefore, this scheme greatly benefits from fast atom readout. This has been demonstrated for both ytterbium and strontium by taking advantage of the broad $^1S_0 \rightarrow {}^1P_1$ transition, which allows to achieve microsecond-scale single-atom detection [48–51, 145]. However, implementations have so far been destructive for the detected atoms, meaning that error correction can only consist in post-selection or in replacing the physical qubit through re-loading from an atomic reservoir. While this should not pose an unbearable overhead in hardware resources, as shown by recent demonstrations of continuous array reloading [138, 142, 149], a non-destructive fast imaging scheme would allow to detect and correct errors without the need of atom replacement.

Besides erasure conversions, applications of non-destructive mid-circuit measurements notably include detection of phase errors [150], measurement-based quantum computation [151] and metrology [31, 152]. Mid-circuit measurements are particularly powerful when they are applied to only selected ancilla qubits, without affecting the coherence of unperturbed data qubits. Such capability has been demonstrated by taking advantage of cavity-assisted readout [153], through spatial separation of data and ancilla qubits [23], or by shelving data qubits in a dark hyperfine substate [154]. Finally, an even more radical approach is to employ a second "spectator" atomic species which acts as a sensor that can be measured without affecting the data qubits encoded in the other species of a biatomic mixture [150]. AEAs allow to reproduce this condition by shelving data qubits in the metastable state, which can indeed be thought of as a second atomic species in quantum simulation experiments [111]. In particular, through local light shifts it is possible to selectively shelve atoms in the $^3P_0$ clock state and perform high-fidelity non-destructive imaging on the remaining atoms, preserving the coherence of shelved data qubits [65]. By selectively exciting only one nuclear-spin state, clock shelving also enables readout of the nuclear-spin qubit state. Similar results can also be obtained by leveraging the narrow $^1S_0 \rightarrow {}^3P_1$ transition in ytterbium atoms and employing hiding beams to induce large local light shifts to protect data qubits and large magnetic fields to perform spin-sensitive detection [82, 84].

To the best of our knowledge, the fastest high-fidelity non-destructive mid-circuit detection,

without invoking e.g. cavity assisted readout, is the one presented in Ref. [65] with an imaging timescale of 3.5 ms. While this is impressive and much faster than the first demonstrations of single-atom detection with fluorescence imaging, it still remains a relatively time-consuming operation which could limit the circuit depth in case of multiple interleaved detections. The non-destructive fast imaging scheme presented in Chapter 4 could offer a valuable alternative for mid-circuit measurements in many different experiments, provided that recooling after detection can be performed in sufficiently short times or parallelized with the advancement of the quantum circuit.

1.4.3 Optical clocks

The ultranarrow clock transitions in AEAs provide very precise frequency references, with Q-factors above 10^{17}. Constraining a local oscillator to tick at the same frequency, i.e. locking a laser, results in an extremely precise and stable clock [4]. In the last decades, atomic clocks based on optical transitions of AEAs have indeed become the leading candidates for next-generation time frequency standards [155] and might open new prospects for the investigation of fundamental physics, from tests of variations in physical constants [34] to detection of gravitational waves and dark matter [35–39]. Despite recent impressive progresses [25, 26, 118, 156], considerable effort is still being directed towards the reduction of uncertainty and optimization of resources in optical clocks.

Leading clock platforms based on atom arrays can be thought of as an ensemble of uncorrelated clocks ticking in parallel, where the high number of particles reduces the uncertainty in the phase (or frequency) estimation. For a system with N particles, the uncertainty is limited by the so-called standard-quantum-limit $\Delta\theta_{\mathrm{SQL}} = 1/\sqrt{N}$ [32, 33]. On the other hand, for a correlated quantum system the uncertainty can be reduced to the Heisenberg limit $\Delta\theta_{\mathrm{HL}} = 1/N$ [32, 33]. This can be achieved through spin-squeezed atomic states, which reduce the projection noise associated to quantum measurements, or through maximally entangled GHZ states [4, 33]. In this context, research aimed at expanding the degree of control on quantum systems and the development of entangling gates for quantum information processing with neutral atoms extremely benefit quantum metrology. This has motivated the development of a novel class of atomic clocks based on AEAs in tweezer arrays [27–29]. Leveraging Rydberg interactions, recent experiments have demonstrated the realization of spin squeezing [157] and entangled states [30, 31, 158] for metrological gain.

Entanglement introduces quantum correlations between probes, resulting in enhanced sensitivity but also enhanced vulnerability to errors. Therefore, complementary approaches to reduce uncertainty in optical clocks are also under investigation. These notably include the successive interrogation of multiple clock ensembles, which enhances the dynamic range and the stability of the measured phase. Harnessing the local control provided by programmable tweezer arrays is one way of realizing such multi-ensemble clocks [159]. Fast, repeated clock interrogation is also crucial for mitigating the Dick effect, causing uncertainty in the phase estimation due to aliasing of laser noise in the dead-time between interrogations. The dead-time can be reduced by interleaved interrogation of multiple lattice clocks [26], which, while impressive, requires a significant hardware overhead. On the other hand, optical tweezer clocks allow to mitigate the Dick effect owing to the reduced state preparation time, which is minimized for continuous operation [138, 142, 149], and to their programmable nature which allows to separate interrogation and preparation zones. Finally, entanglement between a clock and an ancilla atom has allowed to perform fast, repeated interrogations of the clock transition through mid-circuit readout of the ancilla [31]. In this case, fast detection and reset will allow to further reduce the dead-time and mitigate the instability caused by the Dick-effect.

1.5 Engineered many-body systems

The same properties that render AEAs attractive for quantum information processing and metrology also lend themselves to quantum simulation of many-body systems. In optical tweezer arrays, quantum simulation is commonly performed by exploiting long-range Rydberg interactions [8, 9, 160]. Although AEAs can provide several advantages over alkali atoms in this context, their most distinctive capabilities as quantum simulators arise from short-range contact interactions. In particular, the clock state of AEAs can be employed as a second ground state to implement two-orbital models [47, 109, 161, 162], which have strong implications for quantum simulation of impurity models [58, 89, 111] and lattice gauge theories [59, 64]. Owing to the decoupling between nuclear and electronic degrees of freedom, fermionic AEAs also lend themselves to the investigation of models displaying an enlarged SU(N) symmetry of interactions [47, 62, 63, 161, 163–166]. Leveraging the programmability afforded by optical tweezers will be possible to engineer and investigate such many-body systems with single atom resolution and to explore effects which are still lacking a cold-atoms implementation.

1.5.1 Ytterbium interactions

Contact inter-atomic interactions are key to most ultracold atom experiments and have been already thoroughly discussed in numerous works, such as Ref. [167]. For the specific case of ytterbium we point to Refs. [87, 105, 168], from which we extracted most of the information presented in this section. Here we will provide a short overview of the interaction properties that are most relevant for this and future works within our research group; we direct the reader to the references above for further details and derivations of the results presented here.

We limit our discussion to low-temperature, spherically symmetric (s-wave) interactions considering only binary elastic collisions. In this regime, the collision process is completely described by the s-wave scattering length a, which quantifies the effective range, and thus the strength, of the interactions. Notably, s-wave interactions can be modeled with a simple contact pseudo-potential $V(r) \propto a\delta(r)$, indicating that positive(negative) scattering lengths correspond to repulsive(attractive) interactions.

When considering mixtures with more than two components, such as a mixture of fermions with spin $> 1/2$, multiple scattering channels arise and, in general, each is described by a different scattering length. Moreover, the spin states of individual atoms are not eigenstates of the interaction Hamiltonian which mixes the spin states so that, after the collision, atoms are found in different spin states compared to the initial ones. In the case of ytterbium, however, the nuclear-spin states are decoupled from the electronic degrees of freedom governing inter-atomic interactions, which therefore do not depend on the spin state. This results in symmetric collisions between all $(2F + 1)$ spin projections for atoms in the $^1\mathrm{S}_0$ and $^3\mathrm{P}_0$ states. Therefore, interactions between two ground-state or two clock-state atoms are described by single scattering lengths a_{gg} and a_{ee}, leading to the emergence of SU($N = 2F+1$)-symmetric interactions. As the Hamiltonian is symmetric for different projections of the nuclear spin, m_F is a good quantum number and it is thus conserved during a collision. SU(N) symmetry therefore manifests itself in an absence of spin-changing collisions.

SU(N) symmetry holds for all states with $J = 0$, that is for $|gg\rangle$, $|ee\rangle$ and $|ge\rangle$ interactions, where $|g\rangle(|e\rangle)$ represents atoms in the ground(clock) state. We note that while $|gg\rangle$ and $|ge\rangle$ collisions are essentially elastic, $|ee\rangle$ interactions between two clock-state atoms lead to considerable inelastic losses which need to be take into account when dealing with multiple interacting atoms in the clock state [161].

Inter-orbital interactions

When interactions happen between atoms in different orbitals, a single scattering length is not sufficient to describe all possible interaction channels. In particular, we need to consider both the symmetric and antisymmetric orbital channels.

As a consequence of Pauli exclusion principle, fermionic wavefunctions need to be antisymmetric under particle exchange. For two atoms in the same electronic state, the total wavefunction is given by the product state of a symmetric orbital component and an antisymmetric spin:

$$\begin{aligned} |gg\rangle &\equiv |gg\rangle \otimes |s\rangle \\ |ee\rangle &\equiv |ee\rangle \otimes |s\rangle \end{aligned} \tag{1.49}$$

where $|s\rangle = (|\uparrow\downarrow\rangle - |\downarrow\uparrow\rangle)/\sqrt{2}$ is the spin-singlet state. For simplicity we can think of $|\uparrow\rangle$ and $|\downarrow\rangle$ as the $|m_F = +1/2\rangle$ and $|m_F = -1/2\rangle$ states of ^{171}Yb but this reasoning remains valid for all couples of nuclear-spin states also in ^{173}Yb. For inter-orbital interactions, the wavefunction can be antisymmetric in either the spin or the orbital degree of freedom. We therefore have two interaction channels, corresponding to wavefunctions that have a symmetric orbital component and antisymmetric spin component ($|eg^+\rangle$) and to wavefunctions that have an antisymmetric orbital component and a symmetric spin component ($|eg^-\rangle$):

$$\begin{aligned} |eg^+\rangle &= \frac{1}{\sqrt{2}}(|eg\rangle + |ge\rangle) \otimes |s\rangle \\ |eg^-\rangle &= \frac{1}{\sqrt{2}}(|eg\rangle - |ge\rangle) \otimes |t\rangle \end{aligned} \tag{1.50}$$

where $|t\rangle$ denotes the symmetric spin-triplet state. These two channels have different scattering lengths a_{eg^+} and a_{eg^-} as well as different energies U_{eg}^+ and U_{eg}^-.

Starting from a pseudo-potential accounting for the two interaction channels, it is possible to write the interaction term of the two-orbital Hamiltonian as a sum of a direct (V_d) and exchange (V_ex) terms, defined as:

$$\begin{aligned} V_\mathrm{d} &= \frac{1}{2}(U_{eg}^+ + U_{eg}^-) \\ V_\mathrm{ex} &= \frac{1}{2}(U_{eg}^+ - U_{eg}^-) \end{aligned} \tag{1.51}$$

The exchange term lifts the degeneracy between singlet and triplet spin states and leads to the development of the observed spin-exchange dynamics between atoms in the ground and in the clock state [87, 161, 162, 169]. Notably, the two states in Eq. (1.50) are eigenstates of the interaction Hamiltonian and the spin-exchange dynamics develops only between superpositions of these states. In particular, spin-exchange drives coherent oscillations between:

$$\begin{aligned} &|eg\uparrow\downarrow\rangle = \frac{1}{\sqrt{2}}(|eg^-\rangle + |eg^+\rangle) = \frac{1}{\sqrt{2}}(|e\uparrow\rangle|g\downarrow\rangle - |g\downarrow\rangle|e\uparrow\rangle) \\ &\text{and} \\ &|eg\downarrow\uparrow\rangle = \frac{1}{\sqrt{2}}(|eg^-\rangle - |eg^+\rangle) = \frac{1}{\sqrt{2}}(|e\downarrow\rangle|g\uparrow\rangle - |g\uparrow\rangle|e\downarrow\rangle) \end{aligned} \tag{1.52}$$

at a frequency $\omega_\mathrm{ex} = |V_\mathrm{ex}|/h$. Such spin-exchange interactions are the central mechanism enabling quantum simulation of orbital magnetism with AEAs [47]. Notably, for $V_\mathrm{ex} > 0$ the orbital-singlet and spin-triplet state has the lowest energy, indicating a ferromagnetic interaction, whereas for $V_\mathrm{ex} < 0$ the orbital-triplet and spin-singlet state has the lowest energy,

	^{174}**Yb**	^{173}**Yb**	^{171}**Yb**
$a_{gg}(a_0)$	104.9(1.5)[a]	199.4(2.1)[a]	-2.8(3.6)[a]
$a_{eg^+}(a_0)$	94.7(1.6)[b]	1878(37)[c]	240(4)[d]
$a_{eg^-}(a_0)$	n/a	219.7(2.2)[c]	389(4)[d]
$a_{ee}(a_0)$	126.7(2.3)[e]	306(10)[e]	104(7)[d]

Table 1.4| Ytterbium scattering lengths. s-wave scattering lengths of intra- and inter-orbital interaction channels for different ytterbium isotopes, measured in units Bohr radius a_0. The table is adapted from Ref. [170] and values are taken from [a] [171], [b] [172], [c] [173], [d] [174], [e] [161]. Similar values for the inter-orbital interactions in ^{171}Yb have also been measured in Ref. [169].

indicating an antiferromagnetic interaction. We report in Table 1.4 an overview of the measured scattering lengths for the isotopes discussed in this work. Almost all scattering lengths are positive and sizeable, with the notable exception of the ground-state scattering length in ^{171}Yb, which has an almost vanishing negative value. Concerning inter-orbital interactions, we note that $a_{eg^+} > a_{eg^-}$ in ^{173}Yb resulting in $V_{ex} > 0$ and a ferromagnetic behavior in the spin degree of freedom. Conversely, in ^{171}Yb $a_{eg^+} < a_{eg^-}$ and the interactions are antiferromagnetic.

At zero magnetic field all spin states are degenerate and both states in Eq. (1.50) are eigenstates of the interaction Hamiltonian, albeit with different eigenenergies. At finite magnetic fields, however, the differential Zeeman shift arising due to the different Landé g-factor for atoms in $|g\rangle$ and $|e\rangle$, induces a mixing between $|eg^+\rangle$ and $|eg^-\rangle$ states. This leads to the appearance of off diagonal terms in the interaction Hamiltonian and to a modification of the eigenstates and eigenvalues. In particular, the new eigenvalues are:

$$E_{\pm}(B) = V \pm V_{\mathrm{ex}}\sqrt{1 + \left(\frac{\delta(B)}{V_{\mathrm{ex}}}\right)^2} \tag{1.53}$$

where $\delta(B)$ is the differential Zeeman shift between atoms in ^{1}S$_0$ and ^{3}P$_0$. Notably, for large magnetic fields, where $\delta(B) \gg V_{\mathrm{ex}}$, the eigenstates become $|eg\uparrow\downarrow\rangle$ and $|eg\downarrow\uparrow\rangle$ and spin-exchange is suppressed. These two states are the eigenstates of the interaction Hamiltonian also for smaller fields and larger inter-atomic separation, for which atoms are almost non-interacting and $U_{eg}^{\pm} \to 0$. As these states have a different magnetic moment, their relative energy can be tuned with an external magnetic field, providing access to a so-called orbital Feshbach resonance [173, 174].

Feshbach resonances can occur when particles have two possible collision channels: an available open channel and a higher-energy closed channel featuring a bound state for relatively small inter-particle separation. When the closed-channel bound state is brought to resonance, typically through an external magnetic field, with the energy of the incoming atoms in the open channel a Feshbach resonance emerges and the s-wave scattering length can be tuned with the applied field [167]. In alkalis, the open and closed channel correspond to ground-state spin-triplet and singlet states and magnetic Feshbach resonances allow to tune the scattering length between ground-state atoms in different spin states. For AEAs, the decoupling between nuclear and electronic degrees of freedom prevents the appearance of intra-orbital Feshbach resonances in the ^{1}S$_0$ and ^{3}P$_0$ states. However, the different magnetic moment of $|eg\uparrow\downarrow\rangle$ and $|eg\downarrow\uparrow\rangle$ allows to exploit a magnetic inter-orbital Feshbach resonance to tune the magnitude of inter-orbital interactions [173, 174].

1.5.2 Few-fermion impurity systems

The interaction properties of AEAs allow to investigate models beyond SU(2)-symmetric single-band Hamiltonians. In recent years, novel experimental platforms aiming to employ ytterbium and strontium atoms in optical lattices for quantum simulation of such models with single-atom resolution have started to appear [56, 148]. Programmable tweezer arrays offer a complementary approach to quantum simulation and provide a high-degree of control that enable the realization of low-entropy defect-free arrays. This could help to overcome the experimental challenges in observing low energy-scale phenomena emerging in these models. However, AEAs atoms, especially ytterbium, have a high atomic mass and therefore low tunneling rates, making the realization of tunnel-coupled arrays highly challenging. Optical tweezers could therefore be combined with extended traps to gain local control on e.g. single lattice sites to engineer low-entropy arrays with a bottom-up approach [10, 11, 107].

An alternative approach is instead to employ optical tweezers to prepare small-scale atomic ensembles, where interactions happen within each multiply-filled trap. In this context, pioneering works in the group of Selim Jochim (Heidelberg University) have introduced techniques for the preparation, manipulation and detection of a mesoscopic system with single particle resolution, where the system consists of few fermions confined in a single tweezer trap [13, 14, 175, 176]. This allows to retain the bottom-up approach typical of tweezer platforms while allowing to investigate models governed by short-range contact interactions, also for atomic species displaying low tunneling rates. While these techniques have been developed for lithium atoms, adapting them to other atomic species, such as AEAs, could allow to extend the investigation of multi-orbital SU(N) models to mesoscopic ensembles [19].

Few-particle systems are prepared by initially loading multiple atoms into a single trap and performing a fast evaporation to reach the degenerate regime. In this case the high density resulting from tight confinement is favorable to both enhance the evaporation rate and increase the Fermi temperature, allowing to reach very low T/T_F values. This results in low-entropy configurations where atoms fill all the available harmonic oscillator states up to the Fermi energy with very low defect probability. From this state it is possible to apply a controlled tilt to the confining potential to remove atoms above an energy threshold and achieve deterministic preparation of few-fermion systems [13]. This has allowed to investigate the crossover from a few-particle to a many-body state, exploring the role of particle number and interaction strength in the development of hydrodynamic behavior [16] as well as the emergence of a Fermi sea and Cooper pairing in mesoscopic systems [15, 177]. We will comment on how we plan to extend such techniques to ytterbium atoms at the end of Chapter 5.

Realizing deeply degenerate ensembles of few AEAs will allow to investigate the emergence of many-body effects in systems displaying SU(N)-symmetric interactions. In particular, it could be possible to explore the thermodynamic properties of SU(N) Fermi gases [178], leveraging single-atom resolution both in the preparation stage to tune the particle number and in the detection stage to perform number-fluctuation thermometry [179]. Moreover, by engineering orbital impurities through the clock state it will be possible to extend the investigation of polaronic impurities [180–182] to mesoscopic systems. Single-atom atom resolution will allow to address questions such as how many particles are required for correlations to develop and to measure observables beyond average values to take advantage of the theoretical framework of full counting statistics.

A particularly interesting scenario is that of a localized magnetic impurity in an itinerant Fermi bath. In this case, strong coupling between the bath and the impurity leads to the emergence of the celebrated Kondo effect [183]. The effect was originally discovered from the surprising observation of a low-temperature increase of the resistivity in metals with a small concentration of magnetic impurities. After extensive theoretical work, the effect was under-

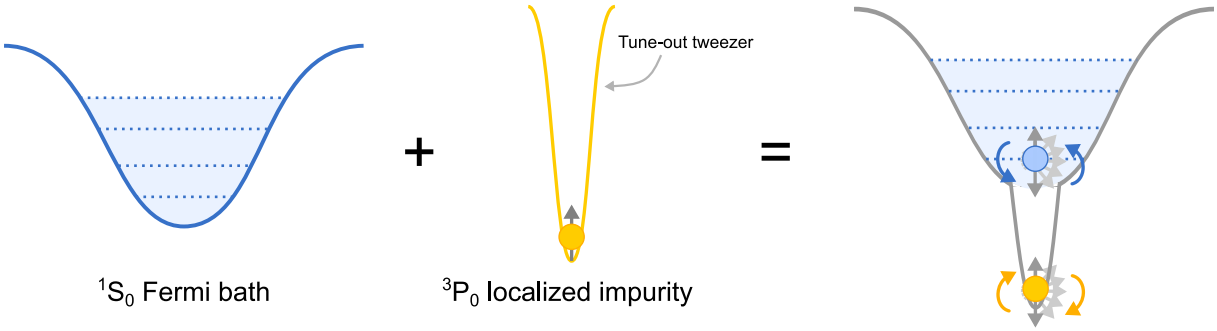

Figure 1.10| Quantum simulation of the Kondo effect in a mesoscopic system. A tightly-focused tweezer trapping a single clock-state atom at the $^1S_0$ tune-out wavelength is overlapped to a larger tweezer providing a deeply degenerate bath of few ground-state atoms. After a magnetic field quench, the spin-exchange coupling between the localized impurity and the bath is triggered.

stood as the result of spin-exchange dynamics leading to the formation of a spin-singlet state between the impurity and the conduction electrons [184]. This phenomenon is ubiquitous in electron systems with localized spins, from quantum dots [185, 186] to heavy-fermion materials, where a periodic lattice of localized spins gives rives to a large effective mass of the conduction electrons [184, 187, 188].

AEAs in state-dependent traps are a promising choice for the implementation of the Kondo problem on cold-atom-based platforms [47, 58, 89, 189–191], with ^{171}Yb being the best candidate to investigate the antiferromagnetic (AFM) Kondo model due to the negative sign of its inter-orbital coupling [169] and the negligible scattering length between ground-state atoms. However, experimental observation of the Kondo effect in cold-atom systems are still lacking. Leveraging the techniques for the preparation of deeply degenerate few-fermion systems and the local control provided by optical tweezers and tune-out wavelengths [56, 57] could allow to observe signatures of the Kondo effect in mesoscopic samples. In Fig. 1.10 we sketch a possible scheme for the quantum simulation of the Kondo impurity problem in a few-fermion system. A degenerate ensemble of few ytterbium atoms in the $^1S_0$ state is trapped in an optical tweezer with a relatively large waist, providing a Fermi sea that acts as a bath for the impurity problem. By preparing a single clock-state atom in a separate tweezer at the ground-state tune-out wavelength [56] and overlapping the two traps we can introduce a localized orbital impurity. Importantly, during the initialization we need to employ a magnetic field to suppress the spin-exchange interactions. By quickly switching off the field it will be possible to quench the spin-exchange dynamics and induce impurity-bath correlations, which could be measured by monitoring the magnetization of the impurity. Through spin-resolved multi-atom detection, e.g. after expansion in an harmonic potential [175, 192], it will be also possible to detect the magnetization of atoms in the bath. We also note that a similar scheme can be employed to study polaronic impurities, taking advantage of the orbital Feshbach resonance to quench strong inter-orbital interactions. In this case, localization of the impurity leads to the so-called Anderson orthogonality catastrophe which has been proposed to be observed with ultracold atoms in state-dependent potentials [193]. For both scenarios of polaronic and magnetic impurities, performing experiments in tweezer traps will allow to access the 1D regime of the investigated phenomena and to address open questions regarding the out-of-equilibrium dynamics of impurity models [193], the formation of the Kondo singlet [194] and the development of correlations in mesoscopic systems.

2

An ytterbium tweezers experiment

A functioning ultracold-atom experimental platform requires numerous components, each of which must be carefully designed and constructed to meet the specifications necessary to access the desired physical regimes. These notably include the vacuum system to isolate atoms from external perturbations and the magnetic field coils to produce gradients and uniform fields. As laser light is the fundamental tool to cool and manipulate atoms, the optical setups and laser-frequency stabilization system is a crucial part of every atomic physics experiment. Achieving single-atom resolution requires specific care in the design and construction of the high-resolution optical setups employed for trapping and imaging individual atoms. In tweezer-based experiments, it is necessary to produce a homogeneous array of micrometer-sized traps through a high numerical aperture (NA) objective and characterizing the properties of such traps is fundamental to proceed with more complicated experiments. Single-atom imaging is performed by collecting atomic fluorescence with a high-NA objective, possibly the same employed for tweezer projection, and focusing the single-atom signal on a scientific camera. By simultaneous cooling and imaging the atoms, it is possible to mitigate atomic losses and single-atom imaging with high detection fidelity and high survival probability can be achieved.

In this chapter we will present the ytterbium experiment we have set up during the course of my PhD as well as some characterization measurements of our tweezer-trapped ytterbium atom arrays. We refer the reader to Ref. [122] for further details on the experimental setup design. Moreover, we will report on the first demonstration of single-atom trapping and imaging of ^{173}Yb atoms. We will first provide an overview of our experimental apparatus, discussing the different sections of the vacuum system and the magnetic field coils. We will also present the full optical setups for slowing, cooling, trapping and imaging atoms in our science cell. Then, we will describe our laser-locking scheme which allows us to frequency-stabilize all our lasers without the need of an atomic reference by means of a scanning transfer cavity. Next, we will focus on the high-resolution setup required to reach single atom resolution. We will describe our optical tweezers setup and how we have measured the waist of our optical traps as well as the spectroscopic technique we employ to homogenize our tweezers. We will then provide measurements of the differential light shifts of the cooling and imaging $^1\mathrm{S}_0 \rightarrow {}^3\mathrm{P}_1$ and $^1\mathrm{S}_0 \rightarrow {}^1\mathrm{P}_1$ transitions in our 532 nm traps for all ytterbium isotopes studied in this work. After that, we will conclude the characterization of the tweezer array by discussing the lifetime and heating mechanisms. Focusing on single-atom detection, we will describe the fluorescence imaging setup and the model-free approach we adopt to measure the performances of our imaging schemes. Finally, we will discuss the the two-color imaging scheme we have implemented to demonstrate high-fidelity single-atom detection of tweezer-trapped ^{173}Yb atoms, also achieving good atom-survival probability.

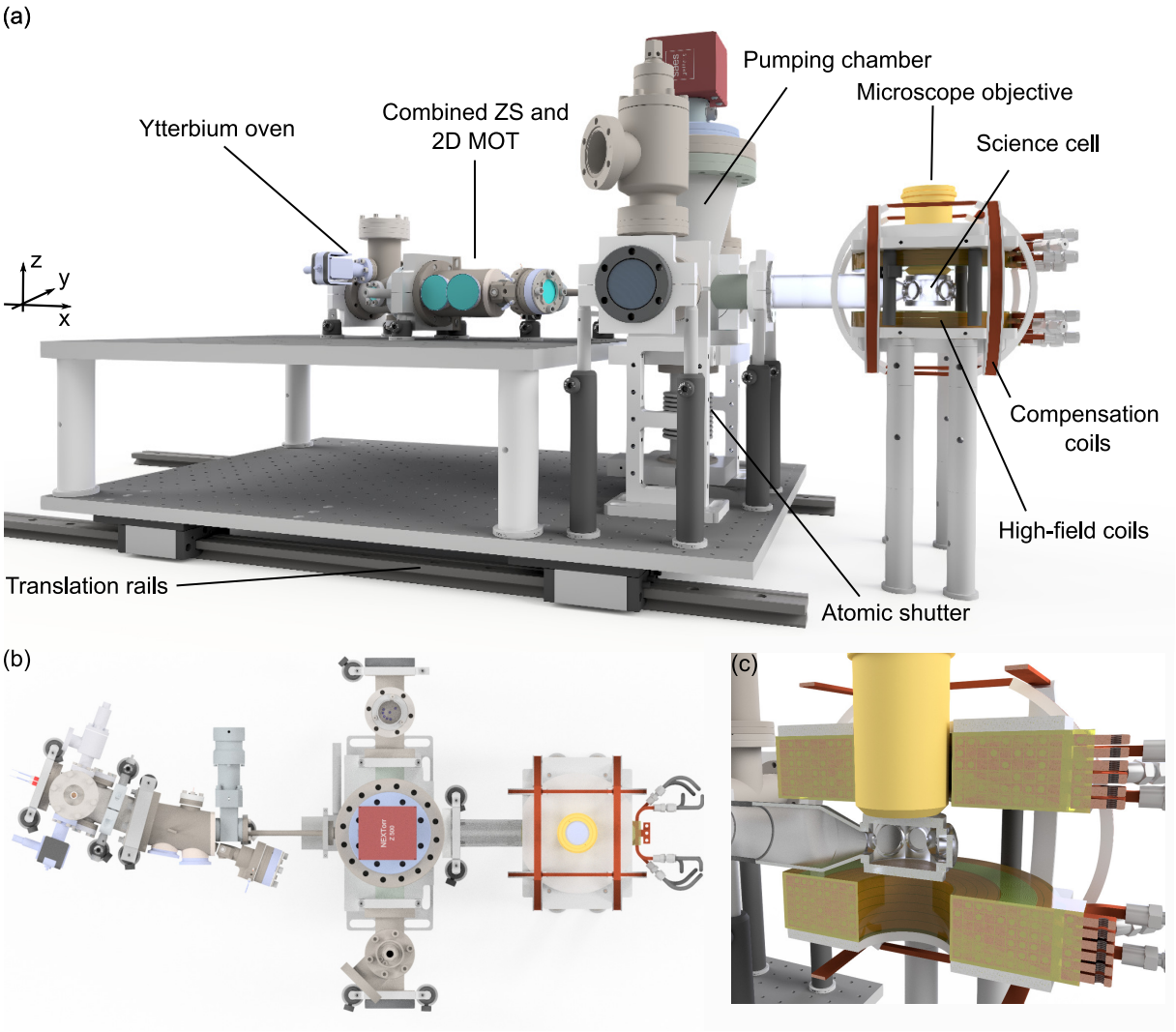

Figure 2.1| Experimental setup overview. (a) 3D CAD rendering of the main components of the experimental setup. (b) Top view of the experimental setup. (c) Zoom on the glass cell, microscope objective and magnetic field coils.

2.1 Experimental apparatus

In atomic physics experiment it is crucial to isolate the atoms from the external environment. This is done by performing experiments under ultra-high-vacuum (UHV) conditions, which helps in reducing collisions with the background gas, which lead to atom loss and reduced sample lifetime. We show a complete overview of the vacuum system in Fig. 2.1. Ytterbium atoms are heated in an atomic oven and a cold beam is produced by our atomic source. This is obtained by combining a permanent-magnet Zeeman slower (ZS) and a 2D MOT to decelerate and deflect the atomic beam towards the science chamber. The longitudinal velocity of the atomic beam ($\sim 40\,\mathrm{m/s}$) is sufficiently high to allow the beam to reach the glass cell without excessive transversal spread or parabolic fall caused by gravity, while being slow enough to directly load a narrow-line MOT after crossed-beams slowing [195, 196]. The middle part of the vacuum system consists of a pumping chamber where a single hybrid non-evaporable getter (NEG)/sputter ion pump (SIP) maintains the required vacuum. This chamber also houses a mechanical shutter designed to block any residual atomic flux from the source to the cell. The

pumping chamber is connected through a glass tube to the glass science cell, where atoms are trapped and all experiments are performed. The glass cell is surrounded by both high-field and bias magnetic field coils. Our high-numerical aperture (NA) microscope objective is located above the glass cell. The whole vacuum system has been designed to be compact, with a total length of approximately 70 cm from the atomic oven to the center of the science cell.

A key feature of our setup is the ability to translate the whole vacuum system by sliding it on a set of rails[1] and carriages[2]. This allows to extract the glass cell from its location and place it back into position with satisfactory reproducibility. This capability is particularly useful to diagnose beam profiles at the atoms' location and it reduces the risks and difficulties of working close to the delicate glass cell.

An important element of every experimental apparatus is the control system employed for managing the experimental sequence. In our lab, we use a control system based on a programmable FPGA with a firmware developed by A. Trenkwalder [197]. Through a buffer board, the FPGA sends instructions to a bus that is connected to both digital and analog output modules in a modular structure which can be easily expanded if more modules or more FPGAs are needed. We use the FPGA with a 1 MHz sampling rate, allowing us to have a time resolution of 1 µs, but sampling rates up to 40 MHz are achievable [197]. We employ independent RF sources to drive optical modulators, typically using the analog and digital outputs of the control system to apply amplitude and frequency modulations as well as to switch them on or off. We also make large use of other FPGA modules (Red Pitaya STEMlab 124-14) to perform specific tasks such as laser locking or to generate the alternated flash imaging pulses. The hardware system is controlled through the labscript suite software [198], which provides a flexible framework for the operation of a cold-atom experiment. In particular, labscript is a python-based environment, allowing easy coding of both the experimental sequence and of real time analysis scripts. Moreover, new devices, such as cameras or waveform generators, can be programmed and inserted in labscript to be controlled both in an offline manual mode and within the experimental sequence.

2.1.1 Atomic beam source

For our Yb beam source, we use a commercial atomic beam system by AOSense[3]. The beam source consists of an ytterbium oven with an integrated permanent-magnet Zeeman slower and a 2D MOT stage to generate a slow and collimated atomic beam. The source is kept under UHV conditions by a combination of getter and ion pumps and it is largely decoupled from the main vacuum chamber by a differential pumping tube. During daily operation we operate the oven between 360 and 380° C. This results in a vacuum pressure of 5×10^{-10} mbar inside the oven, measured by the source ion pump controller, and a very moderate increase of $\sim 1 \times 10^{-12}$ mbar in the pressure of the main chamber. The oven is heated using an in-vacuum thermal resistive heater and the supplied current is typically regulated by stabilizing the oven's temperature with a PID loop. We encountered a few problems with this oven design. After around one year of daily operation, the thermocouple measuring the oven temperature started to read unphysically low values, resulting in the controller supplying a huge current while trying to stabilize the temperature. Fortunately, this current burst lasted for only a few minutes before we noticed it and manually interrupted the current supply. We suspect that this accident was caused by an ytterbium filament that formed somewhere around the pins of heater which also affected the voltage read by the thermocouple. Following a few open-loop heating and cooling cycles the thermocouple returned to a reliable reading condition, possibly thanks to the ytterbium filament being destroyed upon repeated heating. To avoid similar events, we now work in an open loop

[1] Igus drylin TS-01
[2] Igus drylin TW-01
[3] AOSense Beam-RevC-Yb

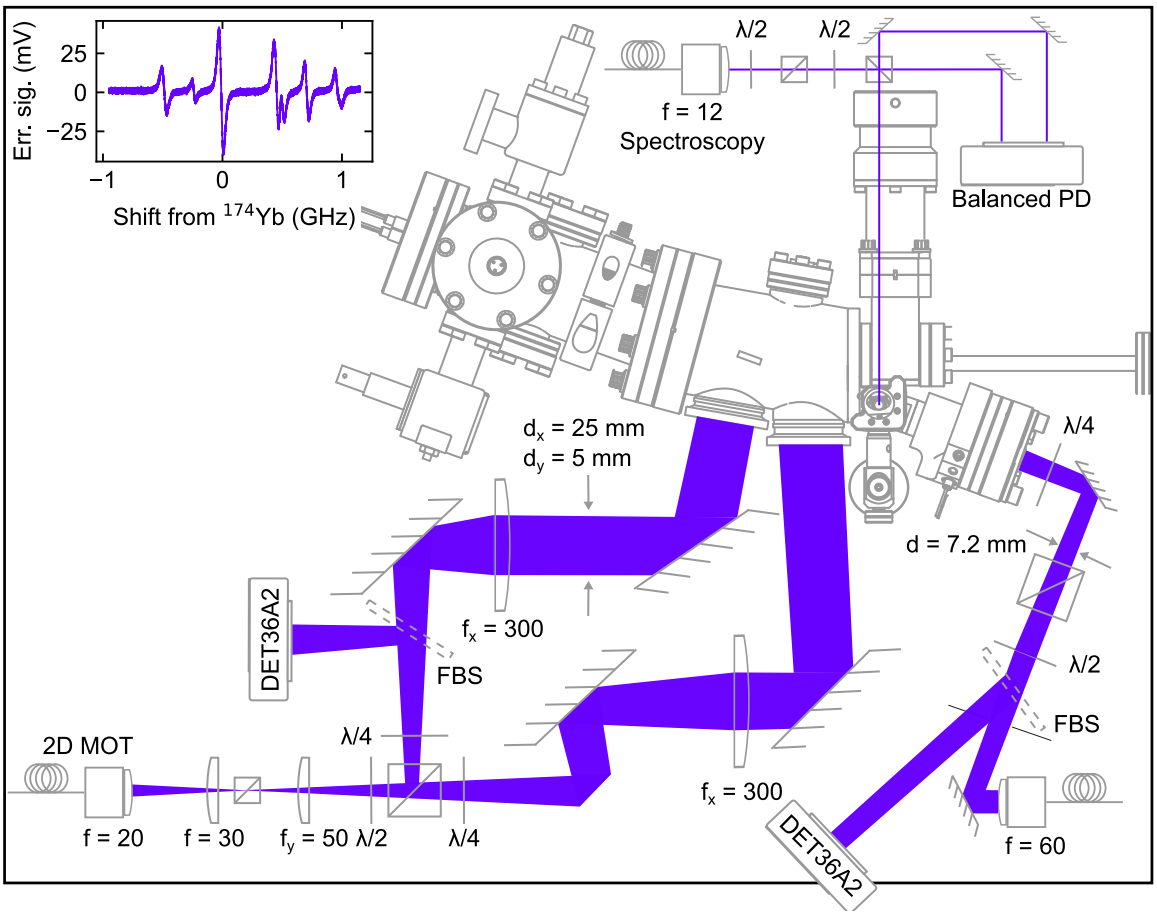

Figure 2.2| Layout of the atomic source optical setup. The sketch represents the 2D MOT (bottom left) and ZS (bottom right) setups, indicating also the beam $1/e^2$ diameters in mm. The dashed components indicated as FBS are flipping beamsamplers for power monitoring and fiber alignment. We also show the spectroscopy path initially employed to lock the 399 nm master laser. The spectroscopy light is directed towards the atomic beam vertically and it is then retro-reflected and directed towards the second input of the balanced photodiode. The vertical components of the spectroscopy setup are not visible in this top-view. Inset: error signal of the FM absorption spectroscopy signal showing a series of dispersive features corresponding to different isotopes.

configuration and we set the desired current to the oven heater looking at the pressure increase to know that we are at the correct working temperature (360-380 °C).

The ZS viewport is conveniently oriented at 20° relative to the beam output tube to avoid crossing the glass cell with the ZS beam and decouple the cold atomic beam from the not-slowed atoms. This geometry allows to keep the ZS beam on during the whole experimental cycle without noticeable detrimental effects on the MOT and tweezers lifetime as well as without directing stray light on the camera employed for single-atom detection. The ZS beam has a waist diameter of 7.2 mm and is typically operated at a detuning of $\simeq -570$ MHz (with $\simeq \pm 10$ MHz variation across different isotopes) and ≃100 mW power. The 2D MOT stage provides cooling in the transverse direction and allows to deflect the atomic beam by the 20° angle required to direct the atoms in the differential pumping tube and towards the glass cell. For the 2D MOT, we employ $\simeq 25$ mW of power, which is split in the two branches with a roughly 2:1 ratio and work with a $\simeq -23$ MHz detuning. Each beam is shaped to be elliptical such that the final beam

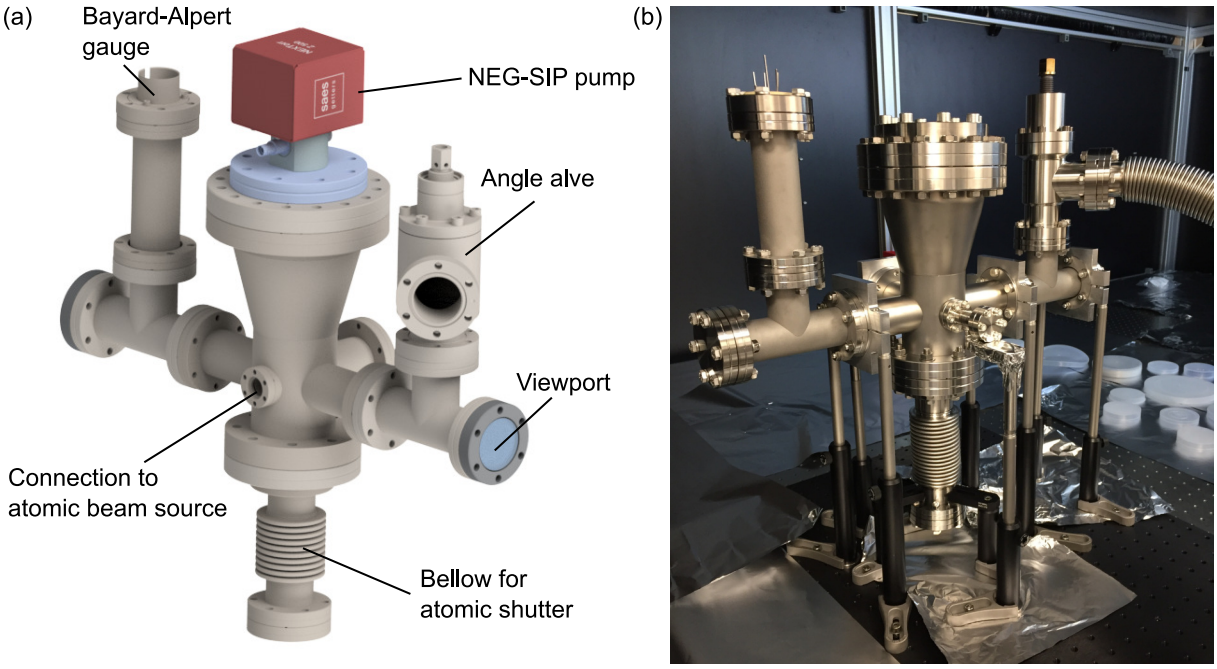

Figure 2.3| Pumping chamber. (a) 3D model of the pumping chamber highlighting its main components. (b) Picture of the assembled pumping chamber before the first bakeout. The NEG pump was attached after the first, high-temperature, bakeout.

waist diameters are 25 mm and 5 mm along the horizontal and vertical directions respectively, as instructed by the atomic beam source manufacturers. The source provides a cold atomic flux of $\sim 10^{11}$ atoms/s with an axial velocity of ~ 40 m/s and transverse temperature $T_\perp < 3$ mK[4].

Our atomic source also provides viewports to perform FM absorption spectroscopy via transverse interrogation of the atomic beam. The spectroscopy light is divided into two paths, one is directed towards the atomic beam and the other to one of the inputs of a balanced photodiode. The light that interacts with the atomic beam is then retro-reflected and directed towards the other input of the photodiode. This setup allows us to lock our 399 nm master laser to the $^1S_0 \rightarrow {}^1P_1$ line of different isotopes via FM spectroscopy. While we initially locked our laser in this way, we observed a degrading amplitude of the error signal after roughly 1.5 years of operation. We suspect that this is caused by coating of the viewports, as more and more power was required to obtain a satisfactory signal. We therefore upgraded our experimental setup to be able to lock our 399 nm master laser without any atomic reference, by transferring the stability of our 556 nm laser through a home-built scanning transfer cavity [see Sec. 2.2.2].

2.1.2 Pumping chamber

The pumping chamber[5] is entirely made of AISI 316L. It consists of a cross with a cone on top, which hosts the main pump of our vacuum system [Fig. 2.3]. Two arms of the cross are used to connect to the atomic beam source and to the glass cell, while on the other two we installed a couple of Tees with viewports which have been of some use for obtaining a first diagnosis

[4]These are the nominal values indicated in the atomic beam source datasheet and we did not perform any measurement to verify their accuracy. As the optimized crossed beams parameters are not very different from those expected from simulations based on these values, we expect the properties of our atomic beam to roughly match the ones indicated.

[5]Mori Meccanica SRL

on the presence of an atomic flux towards the cell. On the other arms of the two Tees we installed a Bayard-Alpert gauge to read the vacuum pressure and an angle valve which can be opened for connecting a turbo molecular pump (TMP) to the system e.g. during bakeout. The bottom flange of the chamber is connected to a flexible bellow containing a flat rod. In case of need, during the experimental sequence the bellow can be tilted with a motorized control so that the rod blocks the line of sight between the atomic source and the cell. This allows to block any residual unwanted atomic flux from the beam source to the glass cell. For our current experiments, we do not employed this atomic shutter

The cone on top of the science chamber has been designed to host our hybrid pump[6], combining a Non-Evaporable Getter (NEG) pump and a sputter ion pump (SIP). This pump configuration provides a NEG pumping speed fo 580 l/s for H_2 and a SIP pumping speed of 5 l/s. The pressure in the main chamber is 2×10^{-11} mbar measured with the Bayard-Alpert gauge. To reach the UHV regime, we have first cleaned the (appropriate) vacuum components and then performed a bakeout procedure consisting of several stages. A detailed description of our bakeout process and the problems we encountered is reported in Ref. [122]. Here we just comment that the main troubles we had have been related to the NEG pump activation, after which we could not reach the target $\sim 10^{-11}$ mbar pressure. After the high-temperature activation recommended by the manufacturer (572 °C, 60 min), the chamber pressure did not fall below 10^{-10} mbar. Inspired by discussions with Leticia Tarruel's group (ICFO), we verified with a residual gas analyzer (RGA) connected to the pumping chamber that the contaminant causing this high pressure was methane produced during the NEG activation and not efficiently pumped out. We solved this problem by performing bake-out cycles on the NEG cartridge alone employing its own heater to keep it at 120 °C while pumping with the TMP and checking with the RGA the amount of methane left. After most of the methane had been pumped out, we successfully reached our final vacuum pressure of few 10^{-11} mbar.

2.1.3 Science cell

The science cell is the core of an experimental apparatus, where atoms are trapped, cooled and all experiments are performed. This requires to have large optical access on as many directions as possible and to enclose the cell in magnetic field coils. Combining all these requirements in experimental setup employing high-NA optical components is often rather complicated and some experiments opt to prepare the MOT in a separate chamber and then transport the atoms to the science cell [199]. In our experiment, we load the MOT and perform all the experiments in a single glass cell. Indeed, glass cells are particularly advantageous for single-atom resolved experiment as they provide larger optical access due to the lack of metallic parts compared to their steel counterpart. This, combined with our in a five-beam (5B) MOT geometry [see Chapter 3] allows us to perform essentially all stages of the experimental sequence within the same cell.

Our custom-made[7] fused silica glass cell has an octagonal geometry. This geometry, compared to e.g. a rectangular one, has been chosen to maximize the number of available directions in which we can shine laser beams at almost perpendicular angles with respect to the windows surfaces. The eight windows are optically contacted to the core structure and have different diameters, as reported in Fig. 2.4(a). The side windows have a thickness of 3.4(2) mm and alternate between larger and smaller diameters to shrink the cell dimensions as much as possible while providing high numerical aperture on half of the windows. The top and bottom window have a larger thickness of 5.00(3) mm and provide a NA of 0.82, larger than the one of our micro-

[6] SAES NEXTorr Z 500
[7] Manufactured by PGB of Colorado, USA

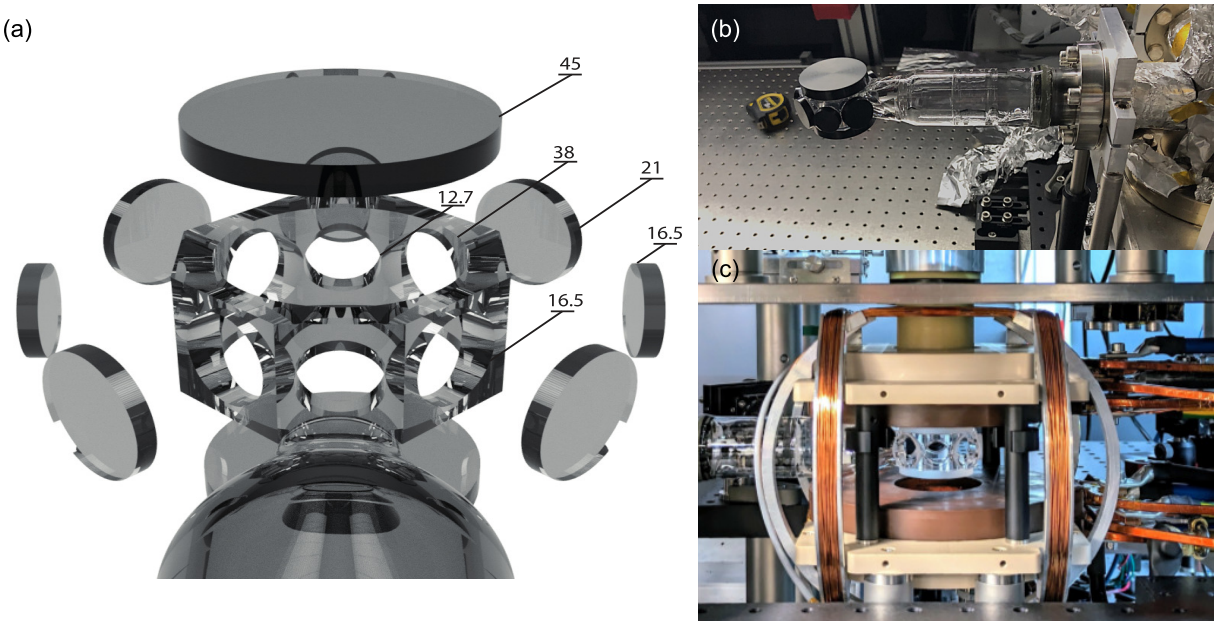

Figure 2.4| Glass cell. (a) 3D CAD rendering of the glass cell in exploded view. All dimensions refer to diameters in mm. (b) Glass cell immediately after connection to the pumping chamber. Windows are covered with black caps to avoid damage to the nanostructured coating. The rotatable flange employed to align the cell is also visible on the right. (c) Picture of the final experimental configuration with the glass cell, microscope objective and magnetic field coils.

scope objective. Since these are the viewports employed for single-atom imaging and addressing, they have stringent requirements on flatness (peak-to-valley $< \lambda/10$) and parallelism between the two window surfaces. The latter is guaranteed within a tolerance of 10 arcsec, which has been verified by checking the parallelism of retro-reflections from the first and second surface.

To minimize reflections, a Random Anti-Reflection Microstructures (RAR-M) coating[8] is applied to both the internal and external side of all windows. This consists in a random distribution of sub-wavelength microstructures whose effect is to minimize reflections without affecting the properties of the substrate.[9] Our coating ensures a reflectivity below 0.1% in the relevant range of $400 - 870$ nm for perpendicular incidence. Precise alignment of the glass cell parallel to the optical table has been achieved by rotating the cell with the rotatable flange visible in Fig. 2.4(b) and aligning the retro-reflection of a vertical reference beam.

2.1.4 Magnetic field coils

In ultracold atoms experiments, magnetic field coils are required to generate the magnetic gradient during the MOT stage and to produce uniform fields in other experimental stages. The employed coils need to guarantee both precise control on the fields and large operation range. Magneto-optical trapping requires anti-Helmholtz coils with typical gradients of few Gauss per centimeter, which are then ramped up to few tens to increase the MOT density in the compression stage. Already when loading the MOT, it is important to also have three pairs of Helmholtz coils which are used to compensate stray fields (including Earth's magnetic field) and to shift the center of the quadrupole gradient to finely tune the MOT position. Moreover, these coils, called

[8] TelAztec RAR Nano-Texture

[9] These coatings are often called Motheye as they are inspired from the eyes of nocturnal moths that have evolved an AR microstructure to avoid detection by their main predator, the owl.

compensation or bias coils, are useful to define and rotate the quantization axis of the system as well as to split the states of hyperfine manifolds. In some experiments, it is also necessary to work at high fields to take advantage of Feshbach resonances or to approach the Paschen-Bach regime when splitting Zeeman sublevels. This requires large coils capable of reaching fields much higher than those typically attainable by bias coils only.

The design of our magnetic field coils is the result of all the considerations above. We show a 3D CAD render of our coils system in Fig. 2.5(a). The main coils[10] are aligned with the vertical axis ($\hat{z}$) and are enclosed in an epoxy block for insulation. The coils are glued to a Polyether Ether Ketone (PEEK) plastic support with an epoxy resin. These coils have two main roles: they produce the magnetic field gradient for the MOT and they can generate high, uniform magnetic fields to massively split Zeeman sublevels and to exploit the orbital Feshbach resonances of fermionic ytterbium isotopes [173, 200]. To this end, fields as high as $\sim 1300\,\mathrm{G}$ in the case of ^{171}Yb [174] need to be reached, which require large currents flowing in the coils. The coils wires are therefore hollow-cored to allow water flow inside them, which provides cooling and prevents overheating when they are operated at high current.

Owing to their dual role of generating both high fields and field gradients, we decided to divide the coils into two separate sections which can be controlled independently. In particular, we divide the coils in an internal section, comprised of 2 layers, and an external one, comprised of 4 layers; each layer in both section is formed by 9 windings. The first two internal layers are in the Helmholtz configuration and are powered by a 50 A power supply[11]. They are connected to a fast switch composed of an insulated gate bipolar transistor (IGBT) and a flyback diode which allows to switch them off as fast as $\sim 5\,\mu\mathrm{s}$. This feature is particularly useful when the field needs to be quickly switched off (or reduced if other layers are also employed) as in the case of rapid quenching of inter-orbital interactions or to change the splitting between spin states in spin-sensitive imaging schemes. The four external layers are instead connected to an H-bridge circuit to allow switching between anti-Helmholtz and Helmholtz configurations. These coils are powered by a 220 A power supply[12] and are employed to generate the MOT quadrupole field and for reaching the highest fields.

The quadrupole field generated by the external coils has been calibrated by measuring the MOT displacement for a known applied bias field, finding $(\partial B/\partial x,\, \partial B/\partial z) \simeq (0.7,\, 1.4)$ G/(cm A). To calibrate the coils in the Helmholtz configuration we have instead performed blow-out spectroscopy [see Section 2.3.3] of the $^1\mathrm{S}_0 \to {}^3\mathrm{P}_1$ transition on single atoms in optical tweezers. We show an exemplary spectra in the inset of Fig. 2.5(c), where we display a spectroscopy of the $^1\mathrm{S}_0|F = 1/2, m_F = -1/2\rangle \to {}^3\mathrm{P}_1|F' = 3/2, m'_F = +1/2\rangle$ transition in ^{171}Yb for different values of the current flowing in the external coils. By fitting the data with Lorentzian peaks we can extract the frequency shift in MHz/A [see Fig. 2.5(c)]. The corresponding Gauss to Ampere conversion is obtained from the Zeeman shift of the excited state, as the ground state is effectively insensitive to magnetic fields [see Eq. (1.1)]. With this procedure we obtain a conversion factor of 2.77 G/A and 3.22 G/A for the internal and external layers respectively. The calibration coefficients between the two coils are similar because the internal coils, despite having less layers than the external ones, are closer to the atoms and therefore provide a larger field. Nonetheless, to reach fields greater than $\sim 950\,\mathrm{G}$ we would need to connect also the inner layers to the 220 A power supply, as 50 A would not be sufficient. The X and Y bias coils are held around the PEEK mount by four aluminum holders while the Z bias coils are encapsulated within the same epoxy block of the main coils. The holders of the X and Y bias coils are designed to have an almost circular shape without conflicting with the steel table holding the objective

[10] Manufactured by Krämer Energietechnik GmbH
[11] Delta Elktronika SM18-50
[12] Delta Elktronika SM18-220

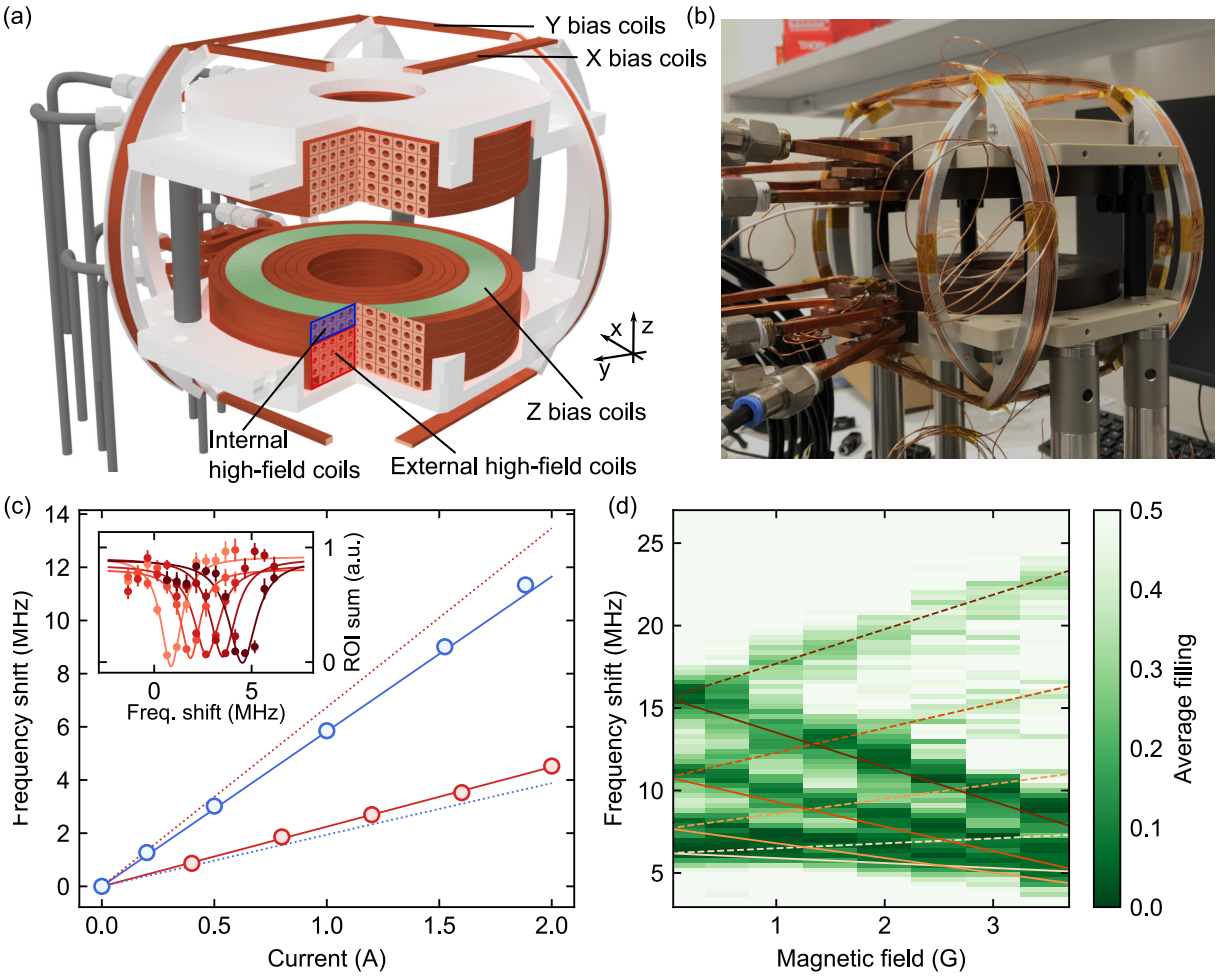

Figure 2.5| Magnetic field coils. (a) 3D model of the coils assembly. The high-field coils are glued to two PEEK supports and are separated in two groups, internal (2X9) and external (4x9), that can be controlled independently. The copper wire of these coils are hollow-cored to allow water cooling when operated at high current. Four collars provide safety support for the top main coils, preventing accidental detachment due to gravity. (b) Picture of the assembled coils before installation in the experimental apparatus. (c) Calibration of the high-field coils. Inset: blow-out spectroscopy of the $^1\mathrm{S}_0|F=1/2, m_F=-1/2\rangle \rightarrow {}^3\mathrm{P}_1|F'=3/2, m'_F=+1/2\rangle$ transition of single ^{171}Yb atoms in tweezers. Solid lines are Lorentzian fits to the data and darker shades of red indicate larger currents flowing in the external coils. Main plot: frequency shift as a function of current flowing in the internal (blue) and external (red) coils. Solid lines are linear fit to the data, providing the MHz/A calibration. To better distinguish the curves, we report data obtained addressing the $^1\mathrm{S}_0|F=1/2, m_F=-1/2\rangle \rightarrow {}^3\mathrm{P}_1|F'=3/2, m'_F=1/2\rangle$ and the $^1\mathrm{S}_0|F=1/2, m_F=+1/2\rangle \rightarrow {}^3\mathrm{P}_1|F'=3/2, m'_F=3/2\rangle$ transitions for the external and internal coils respectively. The dotted lines indicates fitted frequency shift for the other $m_F\rangle$ state. (d) Blow-out spectroscopy of the ^{173}Yb $^1\mathrm{S}_0 \rightarrow {}^3\mathrm{P}_1|F'=7/2\rangle$ transition. Orange lines correspond to the expected Zeeman shift for the eight different $|m'_F\rangle$ states with darker shades indicating larger $|m'_F|$ values. Solid and dashed lines indicate negative and positive m'_F values, respectively. The zero-field splitting is caused by the different tensor light shifts at our trap depth of around 1.1 mK. The magnetic field is generated by the Y bias coils after calibration.

above the glass cell. The X, Y and Z bias coils have 35, 33 and 25 windings respectively and can generate fields of 2.6 G/A, 2.7 G/A and 4.4 G/A. These values have been first calibrated by performing fluorescence spectroscopy on the beam generated by our atomic beam source [see Ref. [122] for details] and this calibration has been refined by more precise blow-out spectroscopy measurements of single atoms in tweezers [Fig. 2.5(d)]. The bias coils are composed by relatively thin wires (0.71 mm) and are not water cooled, therefore they can be employed to produce only small fields up to 10-15 G.

2.1.5 Slowing and cooling beams

We report a top-view of the layout of the optical setup of the main experimental breadboard in Fig. 2.6. The atomic beam exiting our combined ZS and 2D MOT setup has an average longitudinal velocity of around 40 m/s. This is too fast to be directly captured by a narrow-line MOT acting on the $^1S_0 \rightarrow {}^3P_1$ transition, which has a capture velocity of around 10 m/s. To slow the incoming atoms we adopt a crossed beams (CB) scheme, already demonstrated for ytterbium [170, 196] and dysprosium atoms [195]. To realize this slowing stage, we employ two beams acting on the $^1S_0 \rightarrow {}^1P_1$ transition and crossing approximately 22 mm upstream from the MOT center. These beams are angled by 21° relative to the atomic beam direction and have a diameter of 10 mm, providing a region of slowing right before the MOT but without interfering with it. Prior to their implementation, we chose the optimal geometrical properties of the crossed beams by performing Monte Carlo simulations of atomic trajectories [see Sec. 3.1.2] and maximizing the number of atoms captured in the MOT as a function of the CB parameters. We refer to Ref. [122] for details on the optimization of the other CB parameters and report only the final values. The final detuning is ~ -80 MHz from the $^1S_0|F\rangle \rightarrow {}^1P_1|F' = F+1\rangle$ transition, with ± 5 MHz variations across different isotopes isotopes. We employ the CB with around 4.5 mW per beam, corresponding to a saturation parameter $s \simeq 0.2$. The beams are circularly polarized and we find that independent control on their polarization is beneficial to increase the number of captured atoms in the MOT. We therefore install a dedicated $\lambda/4$ waveplate for each beam. We also use a flipping beamsampler which we insert in the beam path when we want to measure the power in the CB and align the optical fibers.

Once the atoms have been slowed by the crossed beams, we capture them in our 3D MOT acting on the $^1S_0 \rightarrow {}^3P_1$ transition. For our horizontal MOT beams we employ a pair of orthogonal retro-reflected beams with a diameter of 16.5 mm. The beams are circularly polarized, with opposite polarization between the forward and retro-reflected beam. To continuously monitor the MOT beams power we decided to avoid beamsamplers, which would cut and deflect the beams as mentioned above. Instead, we align battery photodiodes[13] on the reflections of the polarization cleaning PBSs. This requires to sacrifice a little amount of power in order to avoid large changes in the photodiodes signal due to relative fluctuations in the power of the PBSs loss. While we rarely employ the full available power, the maximum saturation intensity we can achieve with the MOT beams is around $270\, I_{\mathrm{sat}}$, where I_{sat} is the saturation intensity of the $^1S_0 \rightarrow {}^3P_1$ transition. As described in the next chapter, our 3D MOT is in a five-beam (5B) configuration, where we omit the top vertical beam as its role is provided by gravity alone. We therefore use a single vertical MOT beam directed upwards from the optical table and not depicted in Fig. 2.6. This beam has a diameter of 10 mm, smaller compared to that of the horizontal beams as we do not require a large diameter to increase the capture velocity along the vertical direction. While we can reach intensities corresponding to many saturations also with the vertical beam, its purpose is mainly to compensate gravity, for which we typically operate it a few I_{sat}. The beam is circularly polarized with σ^- polarization, chosen to match the

[13] DET36A2

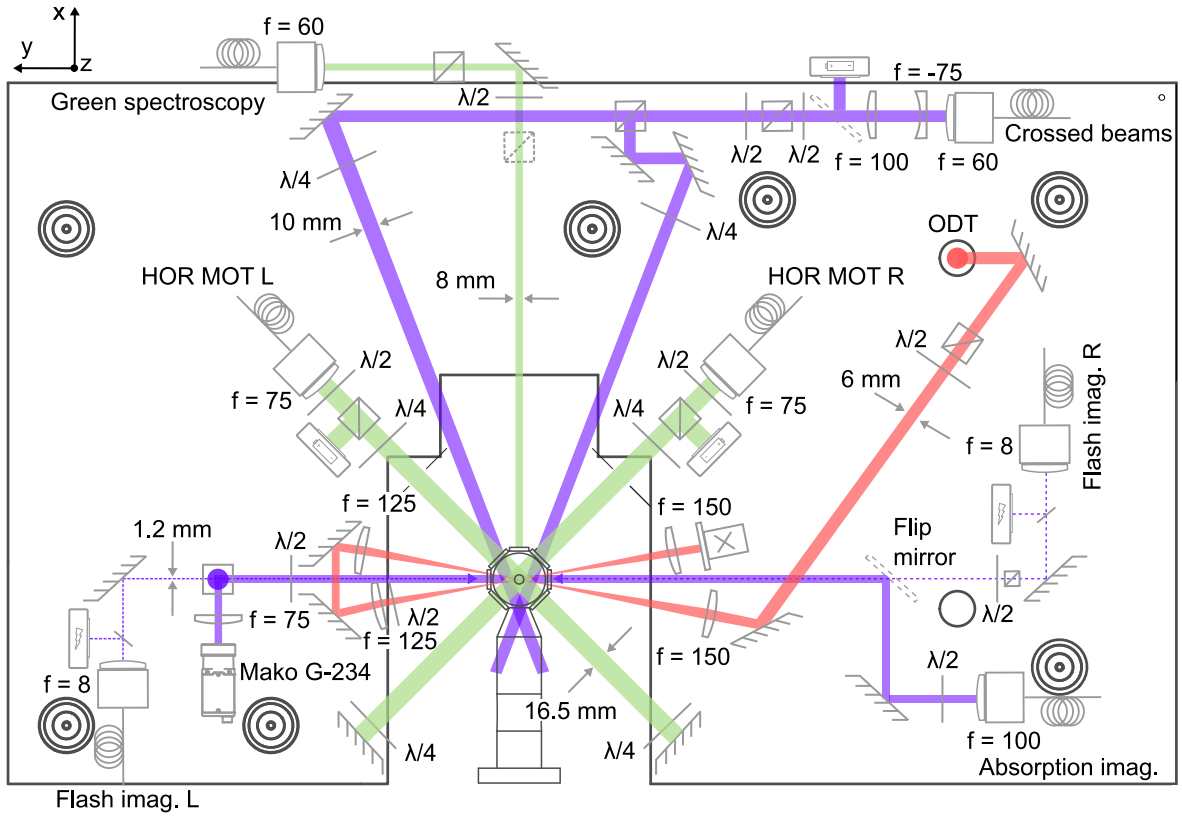

Figure 2.6| Main optical setup. Top view of the main breadboard optical setup. The flash imaging beams are represented as a dashed line. All focal lengths units are in mm and the size of the beams indicates their diameter. This is obtained through appropriately tuned apertures for the CB, MOT and absorption imaging beams while we refer to the Gaussian $1/e^2$ waist diameter for the other beams. The single vertical MOT beam and the tweezers setup are not depicted in the figure. The purple and red circles in the ODT and absorption imaging path indicate that the beam is being directed upwards. Purple, green and red beams indicate light at 399, 556 and 759 nm respectively. Battery and lighting symbols on photodiodes represent battery (DET36A2) and amplified (PDA36A2) photodetectors.

orientation of the quadrupole vertical magnetic field. We note that our vertical bias coils and main coils, when switched in the Helmholtz configuration, provide a field for which the bottom beam is still σ^--polarized, allowing us to use it to perform blow-out spectroscopy and optical pumping with a well-defined and clean polarization.

Alternatively, we can use another horizontal beam to perform both spectroscopy and optical pumping on the $^1S_0 \rightarrow {}^3P_1$ transition. For this we use a diameter of 8 mm at low intensity. The linear polarization of this beam is cleaned by a PBS and can be tuned to any angle in the $y-z$ plane. This is the beam we typically use for the blow-out spectroscopies presented later this thesis.

We use a flip mirror in the imaging path to switch between absorption imaging and fluorescence imaging. The single-atom imaging beams have a 1.2 mm $1/e^2$ Gaussian waist diameter, while the absorption imaging beam has a 10 mm diameter, obtained by cutting a larger beam with an aperture. After passing through the glass cell, the absorption beam is decoupled from the left flash imaging beam by a PBS transmitting the second and reflecting the first upwards to optimize space on the breadboard. After the absorption beam is deflected, we focus it with a

a single $f = 75\,\text{mm}$ lens on a CMOS camera[14]. The imaging system is not in a 4f configuration and the distances between atomic sample, lens and camera sensor yield a total magnification of $\times 0.3$, i.e. a demagnification by roughly a factor 3, which we calibrate from the free-fall trajectory of the MOT.

We use two $\sim 1\,\text{mm}$ diameter beams addressing the ${}^1S_0 \rightarrow {}^1P_1$ transition as blast beams directed on the compressed MOT to provide a horizontal and vertical reference when aligning new beams. In particular, the vertical beam has been fundamental for aligning the microscope objective and the horizontal one for aligning the optical dipole trap. As we often move and re-align these beams when we need to add a new beam to the setup, we have omitted them from Fig. 2.6

We note that the diameters of the CB, MOT and absorption imaging beams indicated in the Figure and in the text are obtained by cutting the beam with irises at the indicated aperture and therefore correspond to sharp edges of the beam rather than typical $1/e^2$ values. For the other beams we indicate their Gaussian waist diameters.

2.1.6 Optical dipole trap

We recently introduced an optical dipole trap (ODT) in our setup, in order to increase the number of atoms loaded in an optical tweezer compared to the typical loading from the MOT. We report a scheme of the ODT optical setup in Fig. 2.7. In our setup, the ODT breadboard depicted on the left is placed directly below the right side of the main optical setup shown in Fig. 2.6.

The ODT beam is obtained from a Ti:Sapph laser source[15] yielding an output power of around 8 W at a tunable wavelength. We operate the laser at 759.3 nm wavelength, but Ti:Sapph can indeed the be tuned to operate in a broad range of wavelengths (around 700-900 nm). This wavelength has been chosen to guarantee magic trapping conditions for the clock transition, which will also enable future implementations of clock-cooling schemes [91, 93]. To mitigate fast fluctuations of the ODT power we use an AOM[16] in a noise-eater configuration. This consists in directing the zero order of the AOM towards the atoms and modulate the power in the diffracted order to compensate fast fluctuations in the zero order. This scheme allows to reduce intensity noise on the atoms without sacrificing power, even though it does not allow to compensate long term drifts or modulate the ODT power. We couple the zero order of our AOM in a photonic crystal fiber and monitor the output power with a photodiode[17] to have an error signal for our stabilization loop, obtained through a digital PID module within an FPGA development board[18]. After the fiber, the light is coupled into another AOM[19] which we employ to implement intensity ramps in open loop.

After this AOM, the ODT beam diameter is increased to around 6 mm by a 75/400 mm telescope and the beam is directed upward towards the main optical breadboards with a periscope. The ODT is then focused at the center of the glass cell with an achromatic $f = 150\,\text{mm}$ lens. Owing to its large collimated diameter, the ODT has a small $1/e^2$ waist radius $\omega_0 \simeq 14\,\mu\text{m}$ on the atomic plane, which has been measured on a test setup and roughly verified by in-situ fluorescence images of atoms trapped in the ODT. The choice of such small waist is motivated by the need to achieve sufficient trap depths to directly load atoms from the MOT as well as to provide tight vertical trapping to confine atoms in the objective focal plane. In particular, for

[14] Mako G-234
[15] Sirah Matisse C
[16] G&H 3110-120
[17] DET36A2
[18] Red Pitaya STEMlab 124-14
[19] G&H 3200-1214

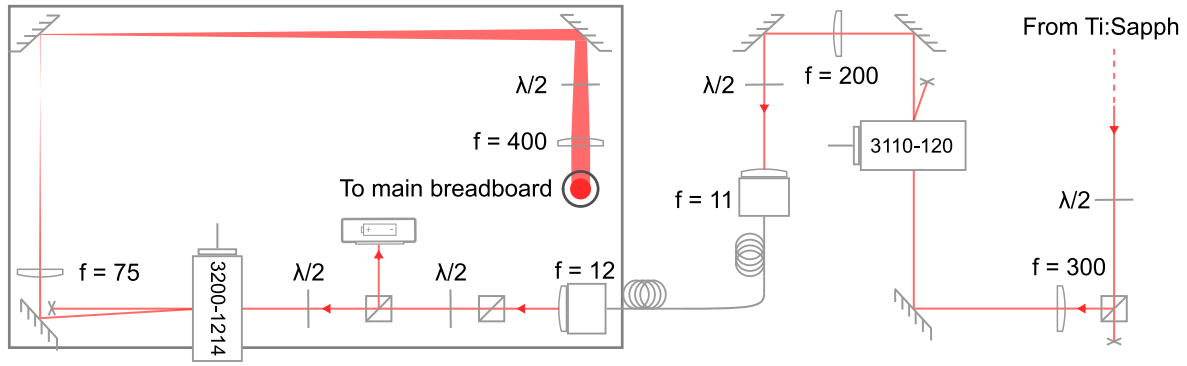

Figure 2.7| Optical dipole trap setup. The ODT beam is produced by a Ti:Sapph laser source and stabilized against power fluctuations by a noise-eater AOM. The light is directed on a dedicated breadboard located below the main experimental setup through a photonic crystal fiber. The power is monitored by a DET36A2 photodetector which is used intensity stabilization. We employ an AOM in open loop to both ramp the power of the ODT and for beam painting in order to increase its effective waist along the horizontal direction. The ODT beam size is then enlarged by a telescope before directing the beam upwards towards the main breadboard with a periscope.

the maximum $\simeq 2\,\mathrm{W}$ power that we can shine on the atoms avoiding Brillouin scattering in the fiber[20], we expect a trap depth of $\sim 300\,\mu\mathrm{K}$ and we measured a $2.8\,\mathrm{kHz}$ trap frequency for the tightly-confined direction.

In order to increase the capture volume of the ODT, we sweep the frequency of the RF driving the last AOM around its central frequency with a rate much higher than the relevant trap frequencies. This results in a fast sweep of the diffracted AOM angle, reflected in a displacement of the trap center on the atomic plane. This so-called painting of the trap, produces a time-averaged harmonic potential displaying a strong anisotropy between the painted and unpainted direction and allows to effectively increase the size of the trap along the painted direction. We sweep the AOM frequency at a $\simeq 20\,\mathrm{kHz}$ rate in a $\pm 15\,\mathrm{MHz}$ range with an arccosine shape, which produces a time-averaged potential with a shape close to that of an unmodulated Gaussian beam [201]. This results in an effective harmonic trap with a waist of $\simeq 14\,\mu\mathrm{m}$ along the vertical direction and a tunable waist between $\simeq 14\,\mu\mathrm{m}$ and $\simeq 75\,\mu\mathrm{m}$ in the horizontal direction.

The ODT is directed towards the glass cell at a $\simeq 7\,^\circ$ angle with respect to the flash imaging beams (aligned along the $\hat{y}$ axis ouf our setup). After the cell, the beam is recollimated, directed again towards the cell and focused to obtain a crossed-ODT (cODT). This allows to recycle the ODT power and increase the effective trap depth to enhance the capture from the MOT. To avoid interference between the first and second beam, the polarization of the latter is rotated by $90\,^\circ$. Even thought we have installed all the optics and aligned the cODT, we are currently not using the recycled beam path as yet. While the recycled beam may be beneficial to enhance the density in the ODT and favor evaporative cooling, it might also lead to complications due to its orthogonal polarization with respect to the first beam. In fact, as discussed in Sec. 3.3.2, the differential light shifts induced by $759\,\mathrm{nm}$ light on the ${}^1\mathrm{S}_0 \rightarrow {}^3\mathrm{P}_1$ transition depend on the trap-light polarization and might play an important role in the loading of the ODT from the MOT.

Aligning the beam and achieving a first signal of trapped atoms in the ODT has required considerable effort. To load atoms, the ODT needs to be roughly aligned and focused on the cMOT postion but to see any sign of loading with fluorescence imaging, it also has to be in the

[20] S&K photonic crystal fiber

$\simeq 2\,\mu m$ focal plane of the objective. We employed a beam at 399 nm blasting the cMOT as a guide over which to superimpose the ODT. This beam was counter-propagating with respect to the ODT and roughly focused in the center of the glass cell, thus providing a geometric reference for position but not for the ODT focussing. We therefore placed the ODT focusing lens to its theoretical optimal position and carefully aligned the ODT on the blast beam. Despite this reference, we still had to make a few movements along the vertical direction before getting any fluorescence signal of atoms in the ODT. After getting a signal, we further optimized the alignment and focused the ODT by moving the its lens with a translator. This procedure has required a few iterations of focusing and alignment. We note that the atoms trapped in the ODT could be observed through absorption imaging, possibly facilitating the search of the initial signal.

2.2 Laser locking without an atomic reference

To reliably address an atomic transition, any laser need to satisfy two fundamental conditions. First the laser frequency needs to be kept at a fixed detuning from the atomic resonance, avoiding any long-term drifts. Second, the laser linewidth must be much narrower than the one of the transition itself. In general, the distinction between slow drifts and fast fluctuations leading to line broadening is not so clear as they are both caused by noise sources at different frequencies. From a practical point of view, we can consider as drifts changes in laser frequency happening on timescales that are longer compared to the typical interaction times with the atoms, i.e. fluctuations that happen between successive pulses within an experimental sequence or between successive sequences. Even without any stabilization, the free-running linewidths of lasers typically employed for cooling beams remain well below 1 MHz for integration times as long as hundreds of milliseconds, and addressing a MHz-broad line, such as the $^1S_0 \rightarrow {}^1P_1$ transition in ytterbium, requires only to compensate for the slow drifts. On the other hand, to address a narrow line it is typically necessary to also reduce the laser linewidth and more care needs to be dedicated to the locking scheme. To this end, optical cavities provide a better frequency reference compared to atomic lines, as the their spectral feature can be designed at will through the reflectivity of the cavity mirrors. In particular, highly reflective mirrors lead to cavities with higher finesse and narrow linewidths, which, in turn, result in steeper slopes of the error signal, allowing to narrow the laser linewidth through fast feedback.

In this section we provide an overview of the laser-locking schemes we employ in our experiment. We also describe the main optical components in the beam paths employed for laser locking, without discussing the paths of cooling beams as they have been already described in Ref. [122]. We frequency lock all the lasers addressing an atomic transition, namely the 399 nm and 556 nm lasers for addressing the $^1S_0 \rightarrow {}^1P_1$ and $^1S_0 \rightarrow {}^3P_1$ cooling transitions and the 578 nm laser for addressing the $^1S_0 \rightarrow {}^3P_0$ clock transition. The 556 nm and 578 nm lasers are locked to a single ultra-low-expansion (ULE) glass cavity[21] via the Pound-Drever-Hall (PDH) technique [202]. Notably, for our 556 nm laser we employ a two-stage lock based on a pre-stabilization cavity to narrow the laser linewidth before locking it to the ULE to achieve long term stability. We have also implemented a scheme which allows us to essentially transfer the long term stability of the ULE to our 399 nm master laser. In this way we lock all our laser system without the need of an atomic reference. While it is rather common to avoid direct spectroscopy on an atomic line for lasers addressing narrow transitions, lasers addressing the broad $^1S_0 \rightarrow {}^1P_1$ transition are typically locked via FM spectroscopy on an atomic beam or vapor cell. We instead avoid this and employ a scanning Fabry-Perot cavity to transfer the long-term stability of the ULE-locked 556 nm laser to our 399 nm source.

[21] Menlo Systems

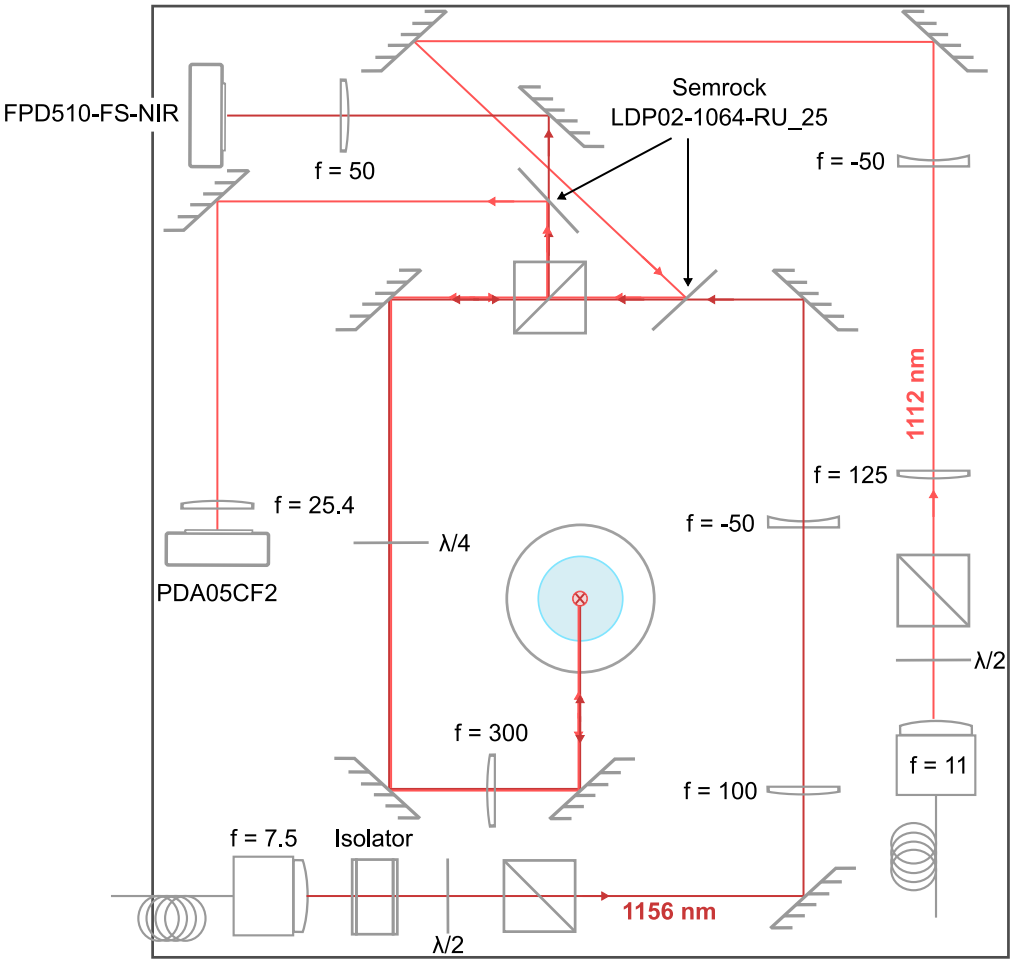

Figure 2.8| Layout of the otpical paths on the ULE breadboard. We couple both the 1112 nm (light red) and the 1156 nm (dark red) lights in the same ULE cavity. Both beams are appropriately beam-shaped to match the required waist inside the cavity. The beams are overlapped with a long-pass dichroic mirror and are coupled into the cavity. The cavity reflections are then decoupled with another dichroic mirror and focused into fast photodiodes for PDH locking.

2.2.1 ULE lock

In our setup, we lock both the 556 nm laser addressing the $^1S_0 \rightarrow {}^3P_1$ transition and the 578 nm laser addressing the $^1S_0 \rightarrow {}^3P_0$ transition to the same ULE cavity. Our 556 nm green laser is a VECSEL[22] featuring intra-cavity second-harmonic-generation to duplicate the frequency of the main 1112 nm source. Our clock light is instead generate by a 1156 nm amplified laser source[23], which we then frequency double in a waveguide with a periodically poled lithium niobate crystal[24] [203]. For both lasers, we employ the infrared light before SHG for locking. This is motivated by the larger frequency difference between the green and clock lasers in the IR compared to after SHG. Such large difference allows to employ the same coating for the ULE mirrors to achieve large different reflectivity, and thus different finesse, for the two wavelengths. Our ULE cavity is designed to have a high $\sim 50 \times 10^3$ finesse at 1112 nm and an even higher

[22] Vexlum VALO SHG
[23] Toptica TApro
[24] Moglabs Waveguide doubler

value $\sim 500 \times 10^3$ at 1156 nm, allowing to reach the desired laser linewidths for addressing the green and clock transitions of ytterbium. The ULE is kept under low vacuum at approximately 3×10^{-9} mbar and it is temperature stabilized to 25.77°, corresponding to the zero-crossing of the ULE glass thermal expansion coefficient. In these conditions, we observe a drift of the cavity resonant frequency of around 8(2) kHz/day, which we monitor through spectroscopy on the $^1S_0 \rightarrow {}^3P_1$ transition. We enclose the ULE in a box whose walls are covered in foam to provide isolation against acoustic noise. The ULE is 12.1 cm long with a plano-concave 1-meter radius incoupling mirror and a plano-planar output mirror. The corresponding free spectral range is $\mathrm{FSR} = c/2L = 1.24$ GHz.

We show the layout of the optical components on the ULE breadboard in Fig. 2.8, indicating the paths for both the 1112 nm and 1156 nm lights. Both beams are shaped to mode-match the cavity and achieve a desired waist of $\simeq 350$ µm on the plano-planar mirror. For the clock light we also employ an optical isolator[25] at the output of the fiber to avoid backreflections which could create unwanted interference effects in the fiber and the fiber-EOM crystal. The two wavelengths are combined with a razor-edge dichroic mirror[26] which is operated at an angle in order to reflect 1112 nm while transmitting 1156 nm light. The two overlapped beams are then coupled into the cavity and their retro-reflections are split with another dichroic mirror. Each reflection is then focused into a fast photodiode[27] for PDH locking. The phase-modulation of the PDH is obtained for both lasers by fiber coupled EOMs[28] which we drive with two tones to also the large sidebands for offsetting the laser frequency compared to the ULE resonance. For both the green and clock laser we also use a double-pass infrared AOM in the cat-eye configuration [204] before the fiber to vary the detuning of the whole laser during our experiments, as the low-noise, high-frequency RF sources we employ to drive the EOMs have a small frequency modulation bandwith.

Unfortunately, the frequency noise of our VECSEL laser prevents us from directly locking it to the high-finesse ULE cavity. In fact, the free-running linewidth of the laser exceeds the 24 kHz cavity linewidth and the available piezo actuators on the VECSEL cavity do not allow for a sufficient low-frequency gain to compensate frequency fluctuation and keep the laser in lock. Therefore, before locking to the ULE we need to reduce the laser linewidth with the pre-stabilization Fabry-Perot cavity lock described below.

On the other hand, we can directly lock our clock laser to the ULE. We refer the reader to the master thesis Ref. [203] for a detailed characterization of the clock laser stabilization and SHG. Here, we just report the measured ULE finesse $F = 521626(31)$ at 1156 nm and the achieved 1 ms laser linewidth of $\simeq 1$ Hz. We are therefore in the position to direct our clock-laser light on the atoms and interrogate the clock transition.

Pre-stabilization to a Fabry-Perot cavity

As mentioned above, we cannot directly lock our green laser to the ULE. We therefore implement a pre-stabilization lock to a visible Fabry-Perot (FP) cavity[29] which allows us to narrow the laser linewidth enough to lock it to the ULE. The Fabry-Perot has a 3 GHz FSR, and a FWHM linewidth $\delta\nu = 1.6(1)$ MHz, with a corresponding finesse of $F = \mathrm{FSR}/\delta\nu = 1900(100)$. The broad linewidth of the FP cavity allows us to directly lock our 556 nm laser to it, employing the PDH scheme to narrow its line compared to the free-running value.

We do not discuss the PDH technique as many references already describe its functioning in depth (see e.g. Ref. [202]). Here we will just briefly comment on its working principle when

[25] Thorlabs IO-4-1150-VLP
[26] Semrock LPD02-1064RU-25
[27] Thorlabs PDA05CF2 for 1112 nm and Menlo Systems FPD510-FS-NIR for 1156 nm
[28] iXblue NIR-MPX-LN-02 for 1112 nm and NIR-MPX-LN-0.1 for 1156 nm
[29] Thorlabs SA30-47-VH

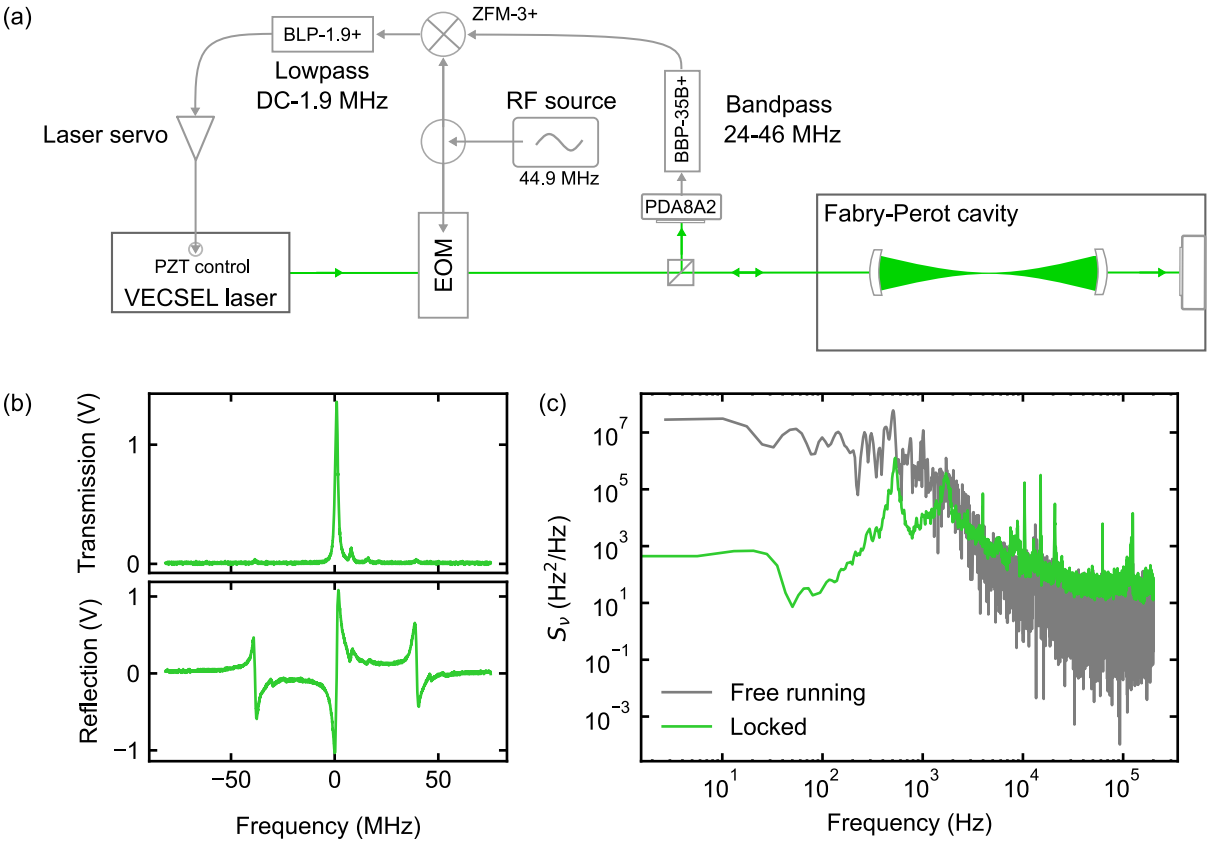

Figure 2.9| Fabry-Perot PDH lock. (a) Sketch of the scheme of the PDH lock to the FP cavity. A beam obtained from the output of our VECSEL laser at 556 nm is phase-modulated at 44.9 MHz by a free-space EOM. We use a fast photodiode (PD) to monitor the intensity reflected by the cavity. The PD outuput is mixed with the RF driving the EOM and low-passed to obtain the error signal which is fed to a laser servo PID acting on the piezo control of the laser cavity to lock its frequency. (b) Transmission (top) and error signal (bottom) of the Fabry-Perot cavity. (c) Measured power spectral density of the 556 nm laser when free running (grey) and when locked to the FP cavity (green).

describing the PDH scheme for the FP lock presented in Fig. 2.9(a). We couple part of the visible output of our laser source into an optical fiber and direct it to a dedicated lock breadboard (not depicted in the figure). We then employ a home-built free-space EOM to modulate its phase and add a pair of sidebands at 44.9 MHz to its frequency spectrum, making sure that the modulation frequency is large enough to have the sidebands well outside of the cavity peak. We tune the modulation depth in order to achieve a 0.42 power ratio between the carrier and the sidebands in order to maximize the error signal slope and hence the lock speed [202]. We then couple the light in the cavity and monitor the reflection of the first mirror with a fast photodiode[30]. We use a 24-46 MHz bandpass filter[31] to remove the noise at frequencies different than our modulation frequency and use a mixer[32] to demodulate the PD output and get the error signal. We remove high-frequency components from the error signal with a lowpass filter [33] and feed it to a laser

[30]PDA8A2
[31]MiniCircuits BBP-35B+
[32]MiniCircuits ZFM-3+
[33]MiniCircuits: BLP-1.9+

servo PID[34]. The laser servo provides both a slow and fast output which actuate on the two piezos of the VECSEL laser cavity. The fast output is amplified by a voltage amplifier[35] while the slow is directly fed to the piezo control. We show the transmission of the FP cavity and the obtained error signal in Fig. 2.9(b).

The reflection off the FP is the coherent sum of the beam that is immediately reflected by the first mirror and does not enter the cavity and the leakage of the cavity [202]. Whenever there is phase mismatch between these beams, we get a non-zero error signal. The PDH scheme therefore allows to immediately detect deviations between the istantaneous laser frequency and the "previous" laser frequency stored in the optical cavity. This enables very fast feedback on the laser frequency and effective narrowing of its linewidth. In Fig. 2.9(c) we compare the measured power spectral density (PSD) of the frequency fluctuations of the 556 nm laser in the free-running and locked cases. We compute the PSD from the measured noise spectrum as follows. We first acquire a frequency noise spectrum of the error signal with a spectrum analyzer[36], moving the laser on the cavity line for the free-running case. The obtained power spectrum in dBm is then converted to voltage and successively to frequency knowing the calibration between the voltage of the error signal and the corresponding changes in laser frequency. With the obtained frequency-noise spectrum $f(\nu)$ we compute the PSD (in $\mathrm{Hz}^2/\mathrm{Hz}$) as $S_\nu(\nu) = |f(\nu)|^2/\mathrm{RBW}$, where RBW is the resolution bandwidth of the acquired spectrum.

The PSD of the frequency fluctuations yields information on the laser linewidth. In particular, we can estimate the RMS linewidth at a certain timescale by integrating the PSD for frequencies larger than the considered time [205]:

$$\delta\nu_{\mathrm{RMS}} = \sqrt{\int_{\nu_{\min}}^{\nu_{\max}} S_\nu(\nu) d\nu} \tag{2.1}$$

where $\nu_{\min}$ is the inverse of the considered timescale and $\nu_{\max}$ is the maximum Fourier frequency of the collected data. This procedure estimates the laser linewidth at a certain timescale by integrating all frequency fluctuations that are happening faster than the considered timescale and thus contribute to the linewidth, while treating lower frequency fluctuations as drifts. We measure a 100 ms RMS linewidth of 77.8 kHz and 13.7 kHz for the free-running and locked case, respectively. By reducing the integration window and considering a 1 ms timescale we get a narrower line of 23.9 kHz and 11.4 kHz for the two discussed scenarios. An alternative approach to the estimation of the laser linewidth is the so-called β-line method [206]. In this case, the laser linewidth is estimated as the integral of the PSD for values that lie above the β-line $\beta(\nu) = 8\ln(2)\nu/\pi^2$:

$$\delta\nu_\beta = \int_{\nu_0}^{\nu_{\max}} S_\nu(\nu)\, \theta(S_\nu(\nu) - \beta(\nu)) d\nu \tag{2.2}$$

where ν_0 is the minimum measured frequency and θ is the Heaviside step function. With this approach we obtain linewidths of 186.3 kHz and 30.0 kHz for the free-running and locked cases. Regardless of the estimation procedure, our Fabry-Perot lock significantly reduces the measured laser linewidth, allowing us to lock the pre-stabilized laser to the ULE.

Combined ULE and Fabry-Perot lock

While we can successfully lock our laser to the Fabry-Perot cavity and narrow its linewidth, the Fabry-Perot is not a stable frequency reference. In fact, due to thermal effects and changes of air pressure in the lab we observe drifts of few-MHz/minute of the FP resonant frequency. As

[34] Vescent D2-125
[35] Veschent Slice DHV
[36] Signal Hound

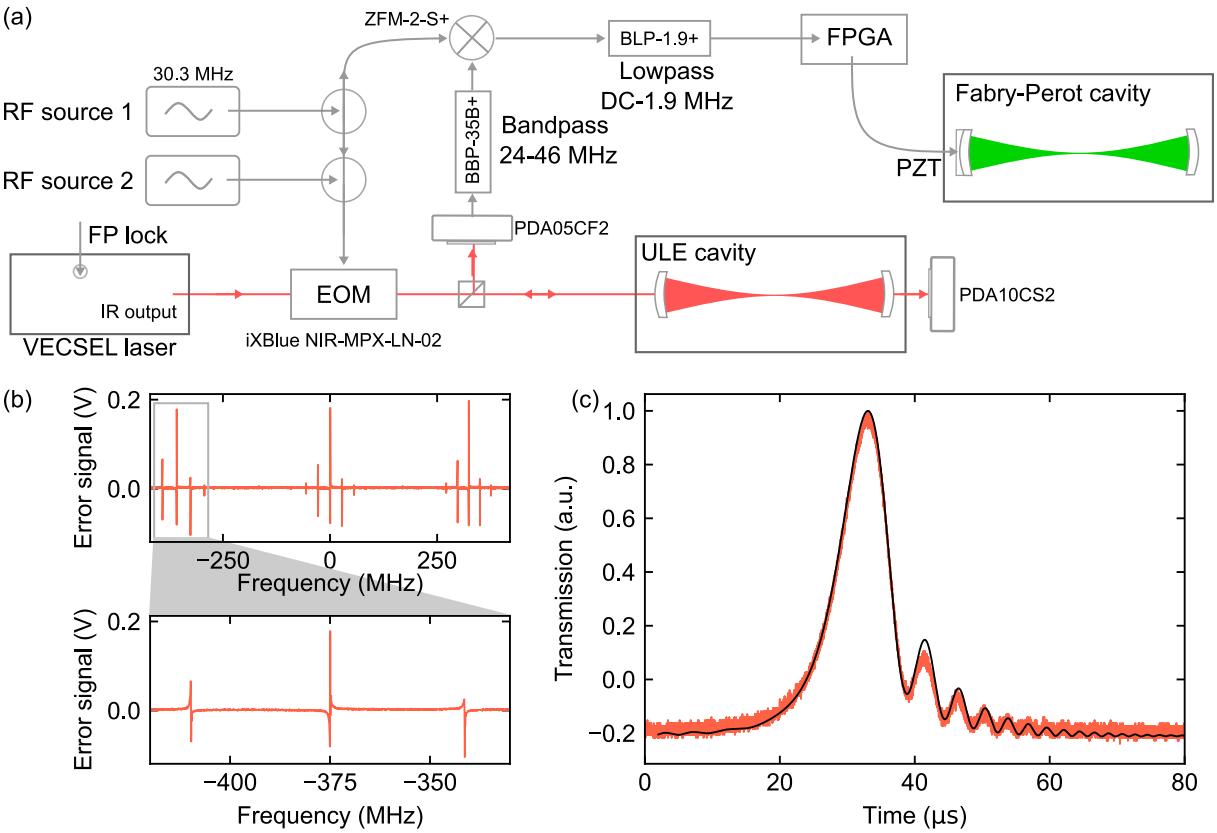

Figure 2.10| ULE PDH lock. (a) Sketch of the scheme for the ULE PDH lock. The IR output of our VECSEL laser is phase-modulated by an EOM driven with two RF tones. One of the tones is employed to generate the 30.3 MHz sidebands of the PDH scheme while the other provides a tunable frequency offset between the laser and the ULE resonance. The light reflected by the ULE is monitored by a fast photodiode, mixed with the first RF tone to demodulate it, and filtered to produce a DC error signal. We use a digital PID module of an FPGA to feedback on the piezo of the Fabry-Perot cavity in order to keep the laser locked to it resonant with the ULE. (b) Top: frequency spectrum of the modulated IR light showing the small ($\simeq 30$ MHz) sidebands for the PDH lock and the large sidebands ($\simeq 375$ MHz) for frequency offset. Bottom: zoom on the error signal of the left sideband, which is the one we typically use for locking. (c) Transmission curve of the ULE when a 2 kHz frequency sweep is applied to the laser. The black line is a fit to the data from which we determine the ULE finesse at 1112 nm $F = 51.5 \times 10^3$.

our 556 nm laser is locked to the FP, its frequency follows the same drifts. We fix this issue by locking the FP to the ULE.

To produce an error signal on the ULE, we implement the PDH scheme sketched in Fig. 2.10(a). We modulate the phase of the IR output of our VECSEL laser with a commercial fiber EOM[37] which we drive with two RF tones. The first one is at a frequency of 30.3 MHz and it is used to generate the sidebands for the PDH scheme, while the second is generated by a separate RF source to produce larger-frequency sidebands with variable frequency Ω'. We show the resulting spectrum, measured from the reflection of the ULE, in Fig. 2.10(b). The large frequency sidebands produce copies of the PDH signal at $\pm\Omega'$. By locking on either the left of right sideband, rather than on the central carrier, we can introduce a tunable frequency offset Ω' between the laser frequency and the ULE resonance. This is of course crucial for any locking scheme based

[37] iXBlue NIT-MPX-LN-02

on a ULE reference as it is highly unlikely that the atomic resonance will exactly match the one of the ULE. Similarly to the FP case, we monitor the light reflected off the ULE, filtering it to remove any frequency component that is far from the PDH sideband frequency and mix the obtained signal with the first RF tone to demodulate it. We filter the demodulated signal to obtain a DC error signal that we feed to the digital PID module of a FPGA board[38]. The board's output is amplified by the second channel of our voltage amplifier[39] and then connected to the piezo control of the Fabry-Perot cavity.

By locking the laser to the FP cavity we make sure that its line is narrow enough to remain within the ULE peak, as long as the FP is stable. If the FP starts to drift, the laser will follow it and the ULE lock will produce a non-zero error signal which is used to feedback on the FP piezo to bring it back on resonance with the ULE. With this cascade lock we are able to transfer the long term stability of the ULE to the Fabry-Perot cavity. A downside of this scheme is that the FP-to-ULE lock has a rather small bandwidth as it is optimized to compensate drifts and not to fight fast fluctuations, thus limiting the speed of the frequency ramps that we can perform in our experiments without losing the ULE lock.

The small width of the ULE peaks, in combination with the large frequency noise of the VECSEL laser, has caused major complications in our locking scheme, as it has been the motivation for the implementation of the pre-stabilization cavity. We therefore report in Fig. 2.10(c) an exemplary curve for measurement of the cavity linewidth and finesse. In general, the finesse and linewidth of an optical cavity can be estimated from the time required by light to exit the cavity in a ring-down measurement. However, this requires to have a laser locked to the cavity in the first place. An alternative approach, which does not require to lock the laser, consists in sweeping the laser frequency across the resonance and measuring the transmitted or reflected light [104]. The measured lineshape shows an interference pattern between the light stored in the cavity and the light that was not coupled to the cavity. The measured intensity can be quantitatively expressed as:

$$|E(t)|^2 = |E_i|^2 \sqrt{\frac{\pi}{2}} \left| e^{-\frac{t-t_0}{2\tau} + \frac{i}{2}\left(\dot{\omega}(t-t_0)^2 - \frac{1}{\dot{\omega}4\tau^2}\right)} + i\sqrt{2}D\left(\frac{i + \dot{\omega}2\tau(t-t_0)}{\sqrt{2i\dot{\omega}4\tau^2}}\right)\right|^2 \tag{2.3}$$

where $\dot{\omega}$ is the laser angular frequency sweep rate, τ is the intensity decay time and $D(x) = e^{-x^2}\int_0^x e^{t^2}dt$ is the Dawson integral. By fitting our measured transmission curve with this expression we obtain a decay time $\tau = 6.6\,\mu s$ and a corresponding cavity linewidth $\delta\nu = 1/(2\pi\tau) = 24\,kHz$. Considering the known 1.24 GHz FSR, this corresponds to a finesse $F = 51547$.

2.2.2 Transfer cavity lock

To address the broad $^1S_0 \rightarrow {}^1P_1$ transition we do not need to reduce the linewidth of our 399 nm laser source, which we only have to stabilize against slow drifts. We do this by implementing a home-built scanning cavity coupled to both the 556 nm and the 399 nm light which transfers the stability of the locked 556 nm laser to the 399 nm one [207]. Before discussing in detail the transfer cavity lock we will briefly describe the lock path of our 399 nm laser, which is sketched in Fig. 2.11.

Our laser source consists of a master ECDL[40] providing $\sim 70\,mW$ output power. This laser acts as a seed for two injection-locked amplifiers (ILAs). Even though these are multimode diodes, by properly injecting them with a single-mode seed it is possible to concentrate all the optical gain in a single mode, matching the one of the seed. In our setup we employ a commercial

[38] Red Pitaya STEMlab 124-14
[39] Vescent Slice DHV
[40] Moglabs ILA seed

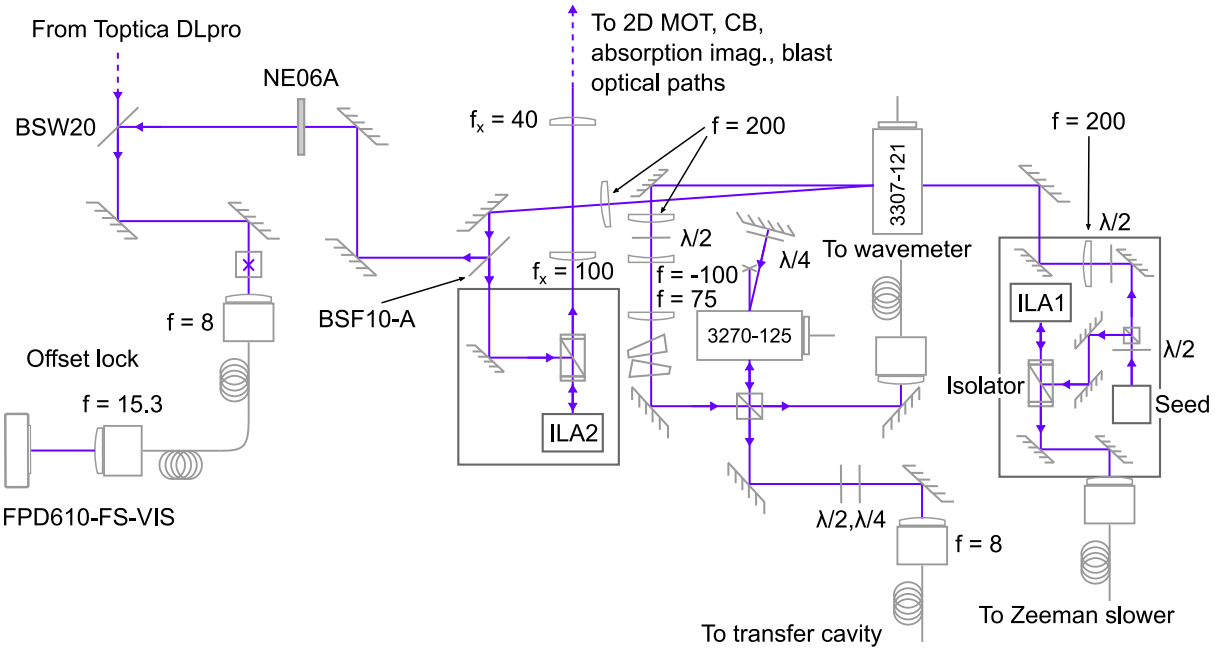

Figure 2.11| Layout of the frequency-lock paths of the 399 nm setup. Our master seed laser injects two ILAs. ILA1 is the source of the ZS light; it is directly injected and thus has the same frequency of the seed laser. ILA2 is injected after a $\sim +300$ MHz shift and thus has a smaller red detuning. We pick off part of the light injecting ILA2 with a beamsampler and combine it with light from the Toptica DLpro used for fast single-atom imaging to realize the offset lock for the fast imaging laser. The zero order of the AOM employed to shift the light injecting ILA2 is recycled for frequency locking the master laser through the transfer cavity setup. The two trapezoidal shapes in the beam path indicate a pair of anamorphic prisms employed to render the beam profile circular, while the square with a cross before the offset lock fiber represents a vertically-oriented PBS for cleaning the polarization.

seed-ILA system within a single chassis (ILA1) and a second, custom-made, external injection-locked amplifier (ILA2). Each ILA was supposed to provide ~ 250 mW of output power for ~ 15 mW of injection, offering a good alternative to SHG for the short 399 nm wavelength. Unfortunately, the ILA2 diode proved to be very problematic, being short-lived and requiring many replacements, each followed by downtoned specifications. To prolong the diodes lifetime we are therefore employing lower driving currents, resulting in around 150 mW output power for each ILA.

Despite the limited power, one advantage of this modular setup with multiple amplifiers is that it allows to frequency-offset them by hundreds of MHz without compromising on optical power, as the frequency shift is applied to the seed light. This is particularly valuable at 399 nm, where AOM diffraction efficiencies and fiber couplings are typically lower than for other wavelengths and each optical component induces significant power loss. In our setup, we use a quartz AOM[41] between the seed laser and ILA2 to shift the frequency of the latter by around +300 MHz from that of the master laser and ILA1. As we keep our seed laser and ILA1 at a $\simeq -570$ MHz detuning, corresponding to the ZS frequency, the ~ 300 MHz frequency shift allows to partially compensate the large red-detuning of the seed laser, bringing ILA2 closer to resonance. This is particularly helpful as we derive other slowing beams, which need to operate at smaller detuning, from the ILA2 output. Before injecting ILA2, we also pick-off a

[41] G&H 3307-121

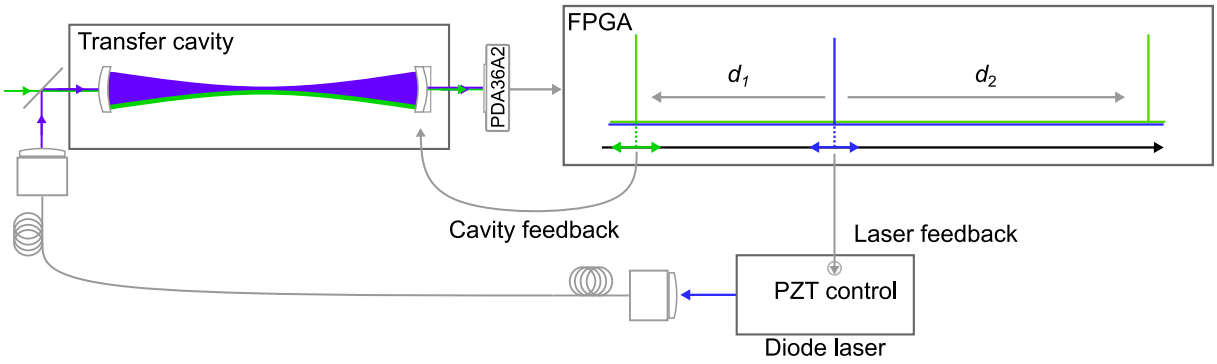

Figure 2.12| Conceptual scheme of the transfer cavity lock. Light from two independent sources is coupled into a single scanning cavity. One source (green) is already frequency stabilized and acts as reference while the second (blue) corresponds to the target source that needs to be stabilized. The cavity transmission is fed to an FPGA which recognizes the peaks corresponding to the reference and the target laser. One of the FPGA outputs feedbacks on the piezo of the scanning cavity in order to maintain the same position of the reference peaks within the scan. The second FPGA output feedbacks on the target laser, in order to maintain the same relative distance between one of its peaks and two of the reference peaks. This allows to stabilize the frequency difference between the reference and the target laser.

small portion of the master laser to produce the beat note for the offset lock of the laser source dedicated to fast single-atom imaging [see the next section and Sec. 4.2.1]. The zero-order of the AOM is instead directed towards the transfer cavity for frequency locking of the master laser. Originally, we employed this beam to lock our laser via FM spectroscopy on the atomic beam produced by our atom-beam source. The double pass AOM reported in the figure was therefore needed to produce the shift between the atomic line and the ZS frequency for the ytterbium isotopes discussed in this work. With our updated transfer cavity lock this AOM is now not necessary as the transfer cavity lock set point can be chosen digitally.

We sketch the conceptual scheme of the scanning transfer cavity lock in Fig. 2.12. Two, or more, laser lights are coupled within the same optical cavity, whose piezo is scanned at a certain frequency f_s. Importantly, one of the coupled lights needs to be already frequency-stabilized and acts as a reference, to which all the other lasers are locked. The transmission of the cavity is monitored by a photodiode and the resulting signal, consisting of many peaks, is fed to a FPGA. The FPGA is tasked to find the peaks in the measured signal and assign them to the different sources. The first step is to stabilize the center of the cavity scan on the reference laser. This is done by identifying the position of one reference peak within the scan and feedbacking on the offset of the piezo ramp to keep this position stable. After the length of the scanning cavity has been stabilized, we identify the peaks corresponding to the other lights and feedback on their laser sources to maintain their relative distance between two copies of the same reference peak. While a feedback signal can also be obtained by fixing the position of the target peak within the scan, employing multiple reference peaks belonging to different FSRs improves the lock stability. In fact, if the piezo response to an applied voltage changes due to e.g. thermal effects, the frequency distance between two points of the scan changes as well. Therefore, locking the target laser to a fixed position within the scan results in frequency drifts over long timescales. On the other hand, the frequency distance between two copies of the same reference peak is fixed by the cavity FSR and stabilizing the relative position of the target peak between them ensures better long-term stability.

This scheme allows to transfer the stability of the reference laser to another source and it

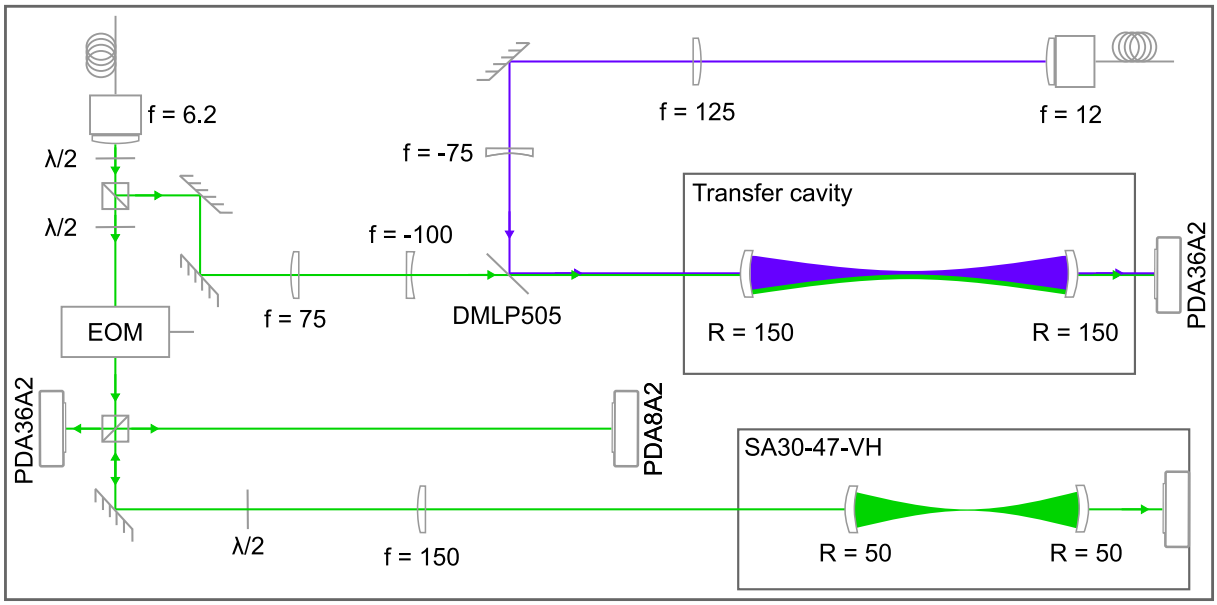

Figure 2.13| Optical layout of the pre-stabilization and transfer cavity breadboard. The 556 nm pre-stabilization Fabry-Perot and the transfer cavity are placed on the same breadboard. We separate the 556 nm light into a path dedicated to the PDH scheme for the pre-stabilization cavity lock and a path dedicated to the transfer-cavity lock. For the latter, we combine the green light with a 399 nm beam from our master laser and we couple both the lights in the transfer cavity. We monitor the transmission of the transfer cavity with an amplified photodiode.

can be easily scaled to lock multiple sources. As the feedback signal is generated once for every transfer cavity scan, the rate at which we act on the laser is limited to f_s, which is typically smaller than 1 kHz. Moreover, the precision of the lock is also limited by the precision at which the center of the peaks can be detected by the FPGA. Therefore, this kind of lock is well-suited to stabilize lasers addressing a broad atomic line and it is not thought to be employed for narrow-line lasers.

In our setup, we employ the ULE-locked 556 nm light as a reference and lock the 399 nm master laser to it. We show a sketch of the optical setup of both the transfer cavity and the pre-stabilization cavity of the 556 nm lock in Fig. 2.13. Both Fabry-Perot cavities are located on the same breadboard which is enclosed in a wooden box whose internal walls are covered in foam to damp acoustic vibrations. We divide the 556 nm into two paths, one employed for the PDH lock to the pre-stabilization cavity and one for the transfer-cavity lock. The blue and green light are combined with a dichroic mirror[42] and coupled to the scanning transfer cavity.

The cavity is formed by two 150 mm-radius mirrors at a 81.5 mm distance in a near-confocal configuration, resulting in a 1.84 GHz FSR. One of the two mirrors is glued on the piezo-electric transducer employed to tune and scan its length. The cavity is fabricated in Invar metal, an alloy of nickel and iron displaying a very low thermal expansion coefficient. Moreover, the cavity sits on four rubber balls in order to isolate it from mechanical vibrations and it is enclosed in the sealed aluminum housing displayed in Fig. 2.14(a). We have not evacuated the cavity housing, even though this might be beneficial to further reduce sensibility to external perturbations. However, we temperature-stabilize it with a Peltier cell to mitigate the effect of thermal drifts.

[42] Thorlabs DMLP505

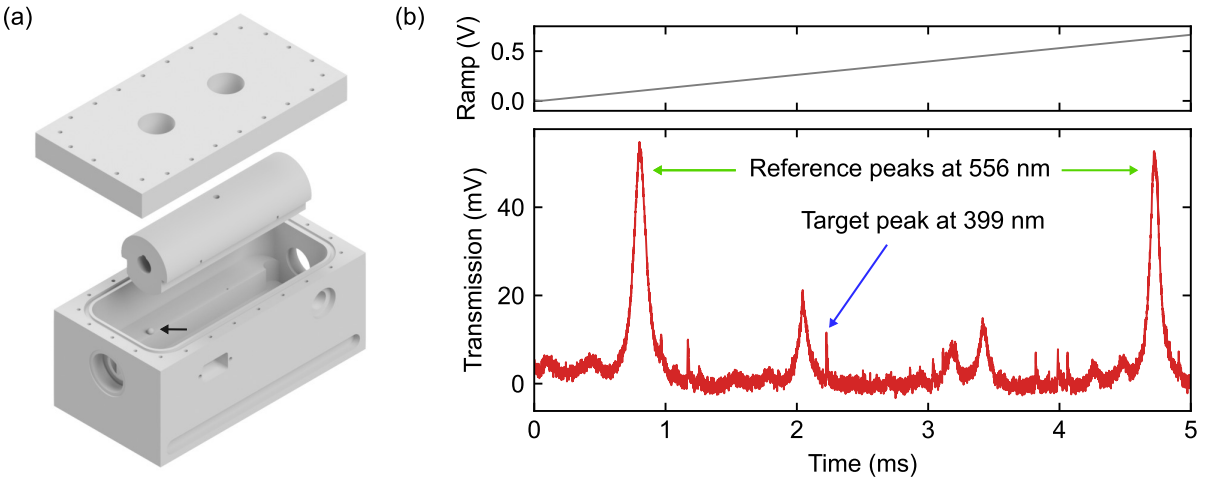

Figure 2.14| Transfer cavity. (a) Render of the transfer cavity Invar cylinder and its aluminum housing. The cavity sits on four rubber balls as the one indicated in the render. The cavity housing is sealed with a rectangular O-ring and includes aperture for wedged viewports to incouple the light as well as holes for the cables for piezo control and temperature stabilization. (b) Top: slope of the triangular ramp employed to scan the cavity piezo. Bottom: transmission signal of the scanning cavity when both 556 nm and 399 nm light is coupled to the cavity. The piezo span covers more than one FSR, allowing to employ two copies of the main 556 nm peak as reference.

The housing includes two apertures with wedged viewports[43] for injecting the beams and two side holes for the temperature stabilization and piezo control cables.

We report an example of the piezo ramp and the cavity transmission signal in Fig. 2.14(b). We typically employ 100 Hz symmetric triangular ramps in order to avoid stressing the piezo with voltage jumps at the end of saw-tooth ramps. We generate the ramps with the FPGA we use for locking the scanning cavity peaks[44], whose output is amplified by a piezo driver[45]. We feed the cavity transmission signal to the FPGA and we identify the peaks and generate the feedback error signal with a custom firmware. As displayed in Fig. 2.14(b), the reference peaks at 556 nm are much broader than the target peaks at 399 nm due to the lower reflectivity of the mirrors at that wavelength. We measure a finesse of 41 and 4026 at 556 nm and 399 nm, resulting in a FWHM peak width of 44.6 MHz and 457 kHz respectively. In a future iteration of the cavity, we plan to replace these mirrors with new ones displaying a finesse of 600 for both wavelengths, which should improve the lock stability. We also note that the cavity does not need to be extremely well aligned for the transfer lock scheme, as we can limit our peak-search to selected times within the scan, thus excluding undesired peaks.

With our scanning transfer cavity lock we can successfully lock our 399 nm master seed laser and perform all our experiments. This scheme does not rely on an atomic line and, as long as the laser piezo has enough range, the lock cannot fall. In fact, this effectively is not a lock to a frequency reference but rather a periodic compensation of frequency drifts. We note that we still observe few-MHz drifts of the laser after many hours of continuous operation but the broad character of the $^1S_0 \rightarrow {}^1P_1$ transition ensures that these drifts do not affect our experiments significantly. We have not fully identified the cause of such drifts and we do not exclude that they could originate from the ECDL electronics rather than from the cavity lock, as we saw a

[43] Thorlabs WWW22050-A
[44] Red Pitaya STEMlab 124-14
[45] PiezoDrive PDu150

similar effect also when locking to the atomic line via FM spectroscopy. As mentioned, a possible improvement on our configuration could be replacing the current mirrors with mirrors displaying a higher reflectivity at 556 nm, which could help to increase the fidelity of the identification of the reference peaks by reducing their width. We also note that, as the blue laser is frequency-locked to the green, changes in the green frequency during the experimental sequence are reflected in changes of the 399 nm laser frequency. This is typically not a problem as the changes in detuning on the $^1S_0 \rightarrow {}^3P_1$ transition are small compared to the $^1S_0 \rightarrow {}^1P_1$ transition linewidth. Replacing the 556 nm reference light with a beam derived from the clock laser will help in further reducing the absolute frequency changes during the sequence. Nonetheless, this is not really necessary as we employ the blue slowing beams only during the MOT loading stage, when the frequency of the green laser is fixed, and we use a separate source, which is offset-locked with a tunable frequency to the master laser, to perform fast single-atom imaging. In general, the setpoint of the transfer cavity lock can be set digitally and could be moved during the sequence to change the relative distance between the green and blue laser in order to maintain or change the detuning from the $^1S_0 \rightarrow {}^1P_1$ transition at different stages. We have already assembled and tested a similar transfer cavity with IR-coated mirrors to lock the infrared repumpers to address the $^3P_0 \rightarrow {}^3D_1$ transition at 1389 nm.

2.2.3 Fast imaging offset lock

We employ a distinct source of 399 nm light to perform fast single-atom imaging. This ECDL laser[46] is offset-locked to our master laser in order to tune its frequency in a wide range and perform fast jumps of the imaging frequency. As sketched in the left side of Fig. 2.11, we produce a beat note signal combining light from the Toptica laser with part of the light seeding ILA2, reducing the power of the latter with a neutral density filter to enhance the contrast of the beat note. We focus the combined light on a fast photodiode[47], enabling us to detect beat notes up to ~ 610 MHz. As sketched in Fig. 2.15, we couple a small fraction of the signal to a spectrum analyzer and direct the main signal to an evaluation board[48]. The board compares the phase of the beat note with that of an external RF source and generates a sharp error signal through a phase-locked loop (PLL). This signal is then fed to a lock module[49] which actuates on the laser current directly from the laser head (after a 6 dB attenuation) and on the laser piezo through the diode laser control system.

We typically tune the offset lock frequency to keep the fast imaging beams resonant with the $^1S_0 \rightarrow {}^1P_1$ transition but we can also use it perform blow-out spectroscopy, such as when measuring the differential light shifts of the $^1S_0 \rightarrow {}^1P_1$ transition or to perform Zeeman spectroscopy at high magnetic fields. In this case, the large tuning range of the offset lock is extremely beneficial, as it allows to span frequency ranges of hundreds of MHz. We also explored the possibility of performing fast jumps of the offset lock frequency. We find that we can perform frequency jumps as large as ~ 400 MHz in ~ 100 µs, which could be sufficient to perform spin-sensitive imaging in high magnetic fields. In particular, through a large (600-800 G) magnetic field we could split different spin states of ^{171}Yb by hundreds of MHz. By jumping with the imaging frequency we could perform successive images of the different spin states or even a first spin-sensitive image at high field and a second spin insensitive image at low field. The speed of the offset lock jumps allows us to do so also for atoms propagating in a weak harmonic confinement [175]. Questions remain on whether this scheme can be actually employed for high-fidelity spin-sensitive imaging as the presence of spin-flips would be extremely detrimental to the detection fidelity.

[46] Toptica DLpro
[47] MenloSystems FPD610-FS-VIS
[48] AD9615-0
[49] Toptica FALCpro

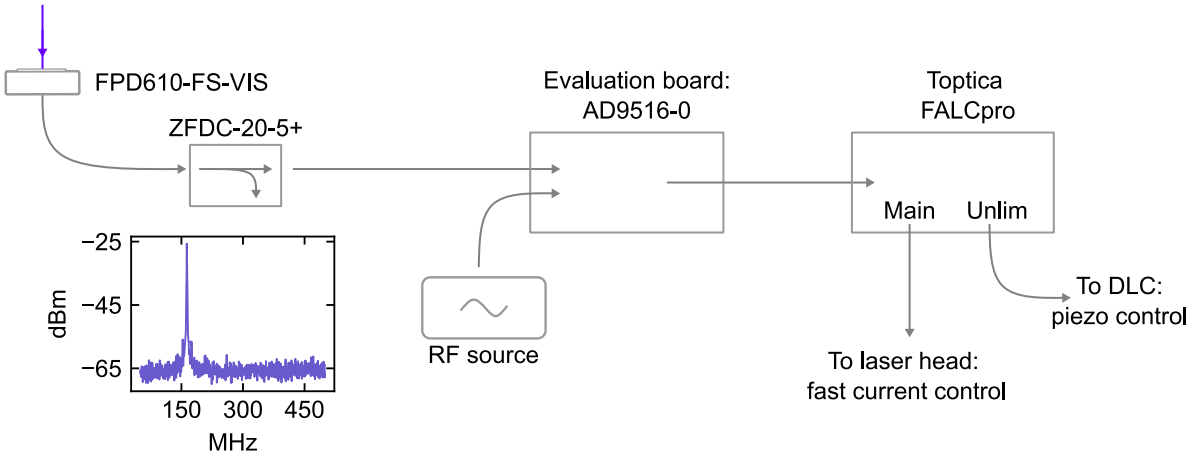

Figure 2.15| Scheme of the fast imaging offset lock. The beat note signal measured from a fast photodiode is directed into an evaluation board which acts as a PLL. The PLL output is fed to a PID module which actuates on the laser current and frequency to keep it phase-locked to an external RF source. The inset shows the measured beat note signal when the laser is locked.

These could be suppressed by reaching the deep Paschen-Back regime and performing a first image on a stretched transition, featuring the lowest spin-flip probability, and then a second spin-insensitive image at zero field.

2.3 Trapping individual ytterbium atoms

In our experiments, we trap single ytterbium atoms in a one-dimensional (1D) tweezer array at a trapping wavelength of 532 nm. This choice of wavelength is motivated by the magic condition for the $^1S_0 \rightarrow {}^3P_1|J' = 1, m'_J = 0\rangle$ cooling transition in ^{174}Yb, which is particularly beneficial for both single-atom imaging and cooling [52, 114], and by the successful demonstration of trapping and imaging individual ^{171}Yb atoms in 532 nm traps [53]. Moreover, plenty of commercial solutions based on SHG of 1064 nm light are available as laser sources.

In this section we present the properties of our optical tweezer traps at 532 nm. We start by describing the optical setup we use for generating and projecting a 1D array of tightly focused traps. We then discuss how we measure and minimize the tweezers' waist on the atomic plane through parametric heating and how we can take advantage of non-magic trapping conditions to enhance trap-depth homogeneity across our tweezer array. As differential light shifts play a crucial role in cooling and imaging single atoms, we present a characterization of the differential light shifts at 532 nm of both the $^1S_0 \rightarrow {}^3P_1$ and $^1S_0 \rightarrow {}^1P_1$ transitions for all isotopes discussed in this work. Finally, we report the lifetime of tweezer-trapped atoms, describing how we can measure the atomic temperature and gain insight on the phenomena affecting the lifetime of single trapped atoms.

2.3.1 Tweezers projection setup

Our trapping light at 532 nm is derived from a frequency-doubled single-mode fiber laser[50] at 1064 nm. This source outputs ~ 10 W at 532 nm, providing ample power for our tweezer traps. Moreover, the laser displays an additional output of ~ 28 W at 1064 nm, which we can use

[50] AzurLight Systems

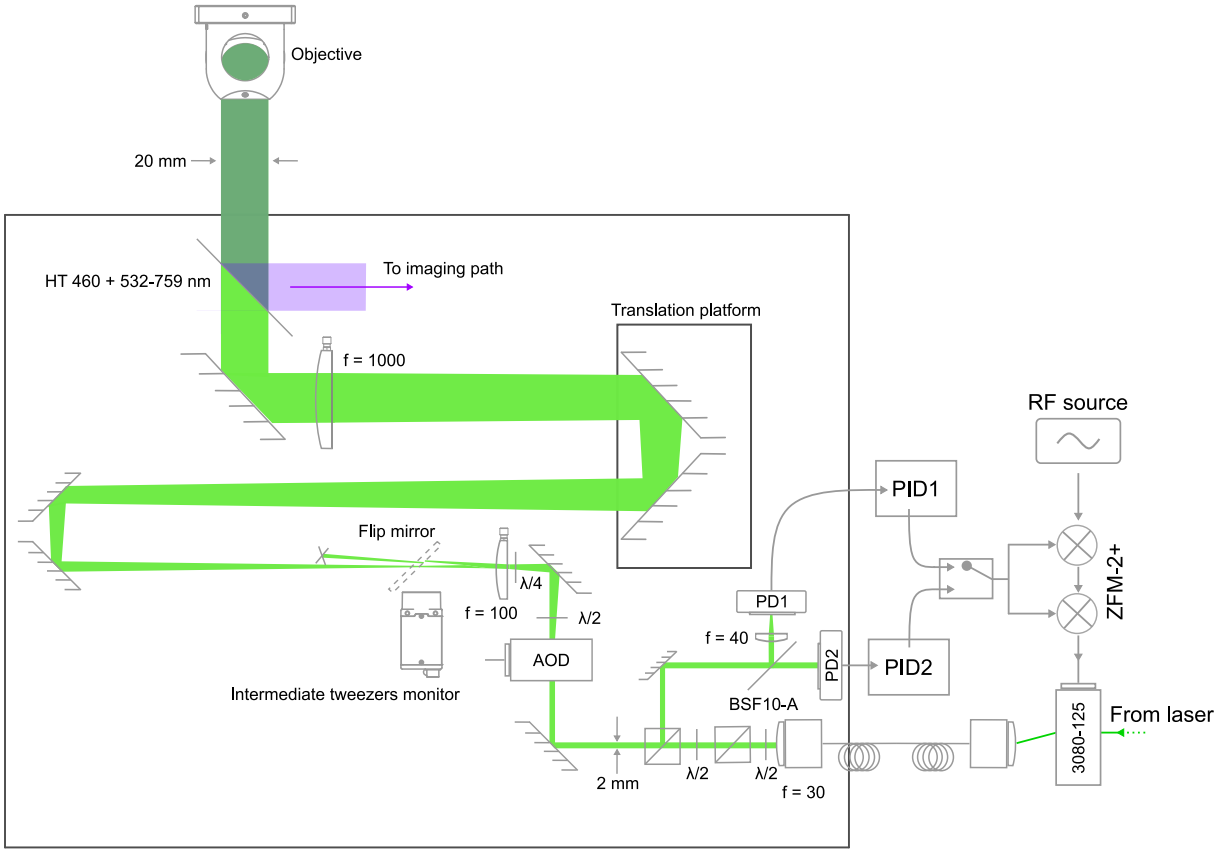

Figure 2.16| Layout of the tweezers optical setup. The 1D array is generated by an AOD and focused by the $f = 100\,\text{mm}$ scan lens to produce the so-called intermediate tweezers, which can be monitored with a flipping mirror and a camera. The intermediate tweezers are projected on the atomic plane by a telescope formed by the $f = 1000\,\text{mm}$ tube lens and the objective. The distance between the scan lens and the tube lens can be finely tuned by moving two mirrors on a translation platform. A dichroic mirror splits the tweezers' light from the atomic fluorescence. The tweezers' beam power is stabilized by two battery photodiodes (PD1 and PD2) with different transimpedance gain. Each photodiode's output is directed to a PID module which modulates the output of two mixers in series to tune the RF power in an AOM. We switch between the two PIDs when we switch from normal operation (PID1) to very low tweezer power (PID2).

for future implementations of other optical traps. The 532 nm beam is deflected by an AOM[51], providing intensity control and stabilization, and it is coupled to a photonic crystal fiber directed to the tweezers' projection breadboard. A scheme of this laser setup can be found in Ref. [122].

We sketch the layout of the tweezers' projection setup in Fig. 2.16. The setup is realized on a stable honeycomb breadboard[52] to enhance stability. This breadboard is located above the main experiment setup and the objective is aligned to the top viewport of the glass cell. Upon exiting the fiber, the tweezers beam is polarization cleaned by a PBS and part of its power is directed towards a couple of photodiodes[53] for intensity monitoring and stabilization. The monitor beam is split with a beam sampler[54] and the small reflected fraction is directed towards

[51] G&H 3080-125
[52] Standa 1HB045-06-04-NM
[53] DET36A2
[54] BSF10-A

the first photodiode (PD1), with a transimpedance gain of 2.7 kΩ. This is the photodiode used for monitoring and stabilizing the tweezer light in most of the applications presented in this thesis. Recently, we have introduced a second photodiode (PD2) with a larger 100 kΩ transimpedance gain. This photodiode is employed when the tweezer power is strongly reduced during evaporation [see Sec. 5.3.2]. The larger fraction of the monitor beam directed towards PD2 and the large transimpedance gain ensure a good signal-to-noise ratio even for very low tweezer power. The output of the two photodiodes is directed towards two independent analog PID controllers[55] which actuate on two mixers in series[56] to control and stabilize the tweezers power through the amplitude of the RF in the AOM on the laser setup. We use an electronic switch[57] to switch from the high (PID1) to the low (PID2) power stabilization.

The stabilized beam is directed into an AOD[58] which creates the 1D array. We drive the AOD with multiple RF tones generated by an arbitrary waveform generator[59]. In particular, the driving signal can be written as:

$$f(t) = \sum_{i=1}^{N} A_i \cos(2\pi f_i t + \phi_i) \tag{2.4}$$

where A_i, f_i and ϕ_i are the amplitude, frequency and phase of the i-th tone. When driving the crystal with multiple frequencies we have to deal with non-linear effects in the AOD, as well as in the RF amplifier[60]. These result in the generation of new tones at frequencies that are sums and differences of the input tones, leading to the so-called intermodulation noise, and in the presence of interference effects which limit the diffraction efficiency. To mitigate these effects, the phase of each tone is adjusted according to the Kitayoshi's algorithm [122, 131].

The AOD is placed in the conjugate focal plane of the scan lens so that the rays deflected at an angle by the AOD are converted into parallel beams in the focal plane of the scan lens, producing the so-called intermediate tweezers. These tweezers have a waist radius of $\simeq 34\,\mu m$ and a distance $d = f\tan(\lambda\delta f/v_s)$, where $\lambda = 532\,nm$ is the light' wavelength, $f = 100\,mm$ is the scan lens focal length, $v_s = 650\,m/s$ is the speed of sound in the TeO2 crystal of the AOD and δf is the spacing between AOD tones in rad/s. For small deflections we can approximate $d \propto \delta f$ and tune the difference between RF tones to tune the spacing of our tweezer array. In this work we mainly operate with $\delta f = 4\,MHz$ when we want to generate a 10-site array with a 8.6 µm spacing or $\delta f = 1.5\,MHz$ when we want to generate a 30-site array with a 3 µm spacing. We use a flipping mirror and a CMOS camera to monitor the properties of the intermediate tweezers and homogenize their amplitudes.

The intermediate tweezers are mapped on the atomic plane by the telescope formed by the tube lens ($f = 1000\,mm$) and the microscope objective (EFL $\simeq 26.5\,mm$ at 532 nm), resulting in a $\times 1/38$ demagnification. The tube lens also forms a telescope with the scan lens, producing a collimated beam with a waist diameter of $\sim 20\,mm$, smaller than the objective aperture $\sim 32\,mm$. The ratio between the tweezers beam diameter and the objective aperture plays a crucial role in determining the properties of the traps, as a larger diameter results in geometrically smaller traps, but the loss in power caused by the objective cutting the beam reduces the trap depth [122]. In out setup we operate in an intermediate regime, with a ratio of ~ 0.63 between the beam waist diameter and the objective aperture.

[55] Stanford SIM960
[56] MiniCircuits ZFM-2+
[57] MiniCircuits ZYSWA-2-50DR+
[58] A&A DTSX-400-532.556
[59] Spectrum Card M4i.6621-x8
[60] MiniCircuits ZHL-1-2W-S+

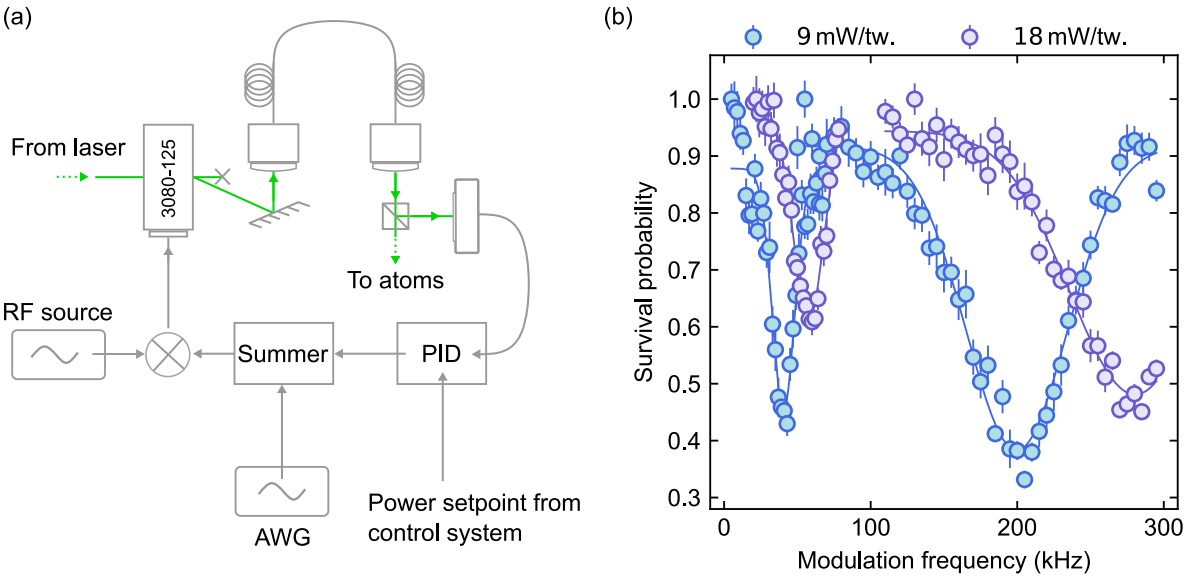

Figure 2.17| Trap frequency measurements via parametric heating. (a) Scheme for parametric modulation of the trap depth. The output of the PID is combined with the signal generated by an AWG through an active summer circuit to introduce a sinusoidal modulation of the tweezers power. (b) Spectrum obtained from the atomic survival probability after 100 ms parametric modulation in a 10-tweezer array with two different powers per tweezer. Solid lines are Gaussian fits employed to extract the axial and radial trap frequencies.

As we employ a single microscope objective for both projecting the tweezer array and collecting atomic fluorescence, we use a dichroich mirror[61] at 45° to decouple the imaging from the tweezers light. This mirror has a high transmittivity for all wavelengths in the 532-759 nm range. This allows us to use it to project other light through the objective, such as tightly focused light at 556 nm to perform optical Stern-Gerlach for single-atom spin-sensitive detection [85] or state-selective optical traps [56].

2.3.2 Trap frequency measurements

The trap frequency of an optical trap is a crucial parameter that describes the strength of the optical confinement. While for large traps the trap frequencies can be measured by observing the movement of atoms within the trap e.g. after a sudden displacement, this scheme is hardly applicable to individually-trapped atoms. A common experimental technique to directly measure the trap frequencies of optical tweezers is parametric heating. This scheme consists in injecting noise at a specific frequency by periodically modulating the intensity of the traps. Such intensity fluctuations can lead to motional excitation of the trapped atoms, resulting in atom-loss upon excessive heating. In particular, the injected energy is maximized when the modulation frequency equals twice of one of the trap frequencies [see Sec. 1.3]. By observing peaks in the atom-loss probability spectrum under parametric modulation it is therefore possible to directly extract both the axial and radial trapping frequencies.

We show a sketch of the circuit employed for this kind of measurement in Fig. 2.17(a). We apply the parametric modulation to the output of the PID control actuating on the AOM which controls the tweezers intensity. The periodic signal is produced by an FPGA[62] used as an

[61] Optoman HRu 399 nm, HTp 460 + 532-759 nm
[62] Red Pitaya STEMlab 124-14

arbitrary waveform generator to generate sinusoidal functions with frequencies from few to few-hundred kHz. This signal is combined with the PID output by an active home-built summer circuit, and the total signal is used to modulate the RF power driving the AOM through a mixer[63]. For these measurements we employ high-power tweezers and the electronic components represented refer to the high-power stabilization path.

In Fig. 2.17(b) we show the measured loss-spectrum after 100 ms of parametric modulation for two different trap intensities in a 10-tweezer array of single ytterbium atoms. The per-trap power reported in the figure is estimated by measuring the total tweezers beam power close to the focus of the scan lens, dividing by the number of traps and taking into account losses induced by transmission through the dichroic mirror and the microscope objective as well as cuts of the beam tails (total losses $\sim 23\%$). For both spectra we observe a low-frequency peak, corresponding to twice the axial trap frequency, and a high-frequency peak, corresponding to twice the radial trap frequency. The presence of a single radial resonance indicates the absence of astigmatism in the optical tweezer traps. By fitting both the peaks we extract the trap frequencies and find $\omega_z/(2\pi) = 28.9(4)\,\mathrm{kHz}$ and $\omega_r/(2\pi) = 140(2)\,\mathrm{kHz}$ for a single-trap power of $\simeq 18\,\mathrm{mW}$.

From the measured trap frequencies, we indirectly determine the tweezer waist by expressing it in terms of the ratio of the radial to axial trap frequencies [see Eq. (1.39)]. This approach removes dependence on the trap depth, allowing the tweezer waist to be written as:

$$\omega_0 = \frac{\lambda}{\pi\sqrt{2}} \frac{\omega_r}{\omega_z} \tag{2.5}$$

Using this relation we extract our tweezer waist $\omega_0 = 578(4)\,\mathrm{nm}$. We note that this value is obtained after optimizing the objective tilt [122]. In particular, misalignments between the objective lens and the top glass cell viewport introduce aberrations and lead to a reduction in both trap depth and trap frequencies. To remove aberrations, we have tuned the tilt of the objective mount, maximizing the measured axial trap frequency in successive iterations before performing the final trap frequencies measurement and estimating the tweezers waist. Knowing the waist, we can then convert the tweezers power in mW into a trap depth, given prior knowledge on the atomic polarizability. We note that throughout this work we employ a polarizability value $\alpha = -11\,\mathrm{Hz/W\,cm^2}$ extracted from our polarizability model, which agrees with the value reported in Ref. [56], while being $\sim$30% larger than what reported in Ref. [114].

2.3.3 Homogenization in non-magic traps

In optical tweezer arrays, each atom is confined in an independent trap. While this enables local addressing and rearrangement, it also implies that atom confinement is, in general, different from trap to trap. Such inhomogeneities are particularly detrimental when working with non-magic wavelengths and narrow optical lines. In this case, the different potential experienced by atoms in the ground and excited state of an atomic transition, i.e. the differential light shift, induces a frequency shift of the considered resonance. As the differential light shift is proportional to the intensity of the trapping light, inhomogeneities between different traps result in a varying resonance across the array, hindering the efficiency of global operations.

Our 532 nm traps are non-magic for the $^1\mathrm{S}_0 \rightarrow {}^3\mathrm{P}_1$ transition of fermionic ytterbium isotopes, with the $^3\mathrm{P}_1$ excited state being less confined than the $^1\mathrm{P}_1$ state. To efficiently address the $^1\mathrm{S}_0 \rightarrow {}^3\mathrm{P}_1$ transition in our tweezer array we therefore perform a two-stage homogenization of our tweezer traps, greatly inspired by the technique presented in Ref. [53]. Notably, in the second stage of our homogenization protocol we take advantage of the non-magic nature of our

[63] MiniCircuits ZFM-2+

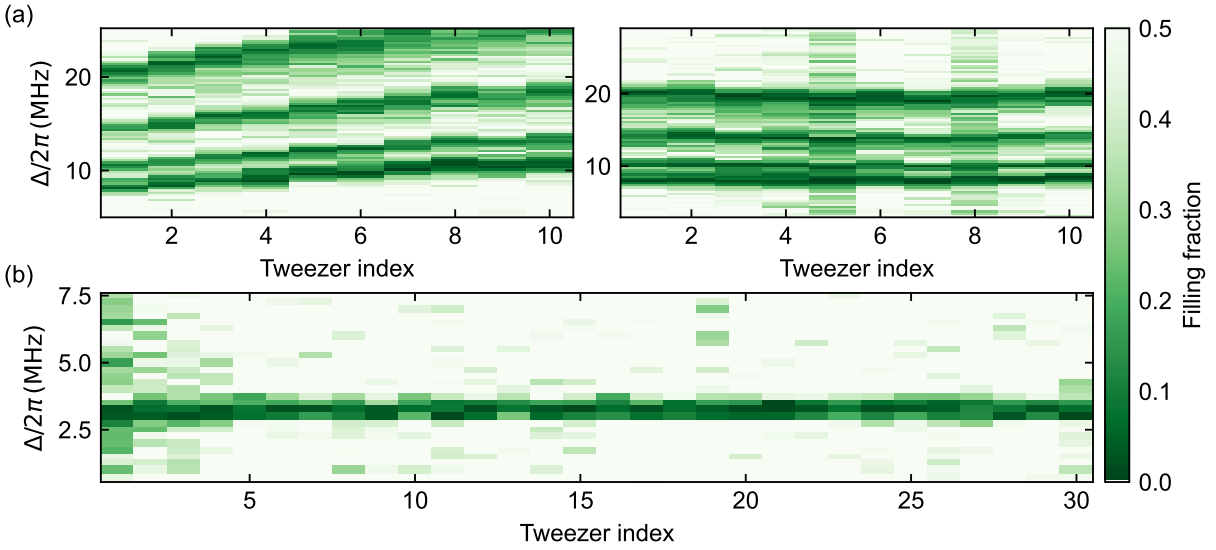

Figure 2.18| Tweezers intensity homogenization in non-magic traps. (a) Site-resolved blow-out spectroscopy of the $^1S_0 \rightarrow {}^3P_1$ transition for a 10-tweezer array of ^{173}Yb atoms before (left) and after (right) the light shifts homogenization. We measure the filling fraction of the array as a function of tweezer trap and detuning $\Delta/2\pi$ from the free-space resonance. The four spectroscopic lines correspond to the four $^1S_0 \rightarrow {}^3P_1|F' = 7/2, m'_F = \pm 7/2, \pm 5/2, \pm 3/2, \pm 1/2\rangle$ transitions and we employ a blow-out beam with tilted linear polarization in order to address all possible transitions. (b) Site-resolved blow-out spectroscopy of the $^1S_0 \rightarrow {}^3P_1|F' = 3/2, m'_F = \pm 1/2\rangle$ transition in a 30-site array of ^{171}Yb atoms after homogenization. The employed trap depths are $U_0 \simeq 1.7\,\mathrm{mK}$ $U_0 \simeq 0.7\,\mathrm{mK}$ in (a) and (b), respectively. Each point is obtained from averaging ~ 30 independent measurements.

traps to obtain information on the array inhomogeneity through the measured differential light shifts.

In the first stage, we homogenize the amplitude of the intermediate tweezers produced by the scan lens after the AOD by imaging them on an auxiliary CMOS camera. We fit the image of the array with a sum of Gaussian peaks and determine the amplitude I_i of each spot, defining an error E_i as:

$$E_i = \frac{I_i - \langle I \rangle}{\langle I \rangle} \tag{2.6}$$

where $\langle I \rangle$ is the average of the I_i values. We then update the amplitudes A_i of the RF tones driving the AOD with a correction factor proportional to E_i: $A_i^{\mathrm{new}} = A_i^{\mathrm{old}} - p\,E_i$. We iterate this feedback loop until the amplitude homogeneity reaches a stationary value. This protocol allows us to compensate for inhomogeneities arising from nonlinearities in the AOD crystal and RF amplifier. However, homogenizing trap amplitudes after the scan lens does not guarantee homogeneous trapping on the atomic plane as it does not account for aberrations introduced by downstream optics which may lead to e.g. variations in the tweezers waist across the array. For this reason we apply a second homogenization step, employing a spectroscopic signal as a probe for tweezer homogeneity.

For this second homogenization stage, we prepare a tweezer array of single atoms and perform blow-out spectroscopy on the $^1S_0 \rightarrow {}^3P_1$ transition. Spectroscopy is performed by illuminating the trapped atoms with near-resonant light in order to heat the atoms and induce losses via

photon recoils. For appropriate choices of blow-out intensity and duration, atoms are expelled by the trap only for resonant light and we can resolve spectroscopic features as small as the natural linewidth of the addressed transition. We note that single-atom occupancy is crucial for performing such spectroscopy on tight traps, as the presence of multiple atoms leads to the observation of light-assisted collisions features rather than measurement of the atomic resonance.

Through blow-out spectroscopy, we measure $^1S_0 \rightarrow {}^3P_1$ resonance for each trap, and determine its deviation from the median value [Fig. 2.18(a)]. This light shift allows us to employ Eq. (2.6) again and further feedback on the amplitudes of the RF tones driving the AOD. We note that for this step we define $I_i = \frac{\delta\nu_i}{M(\delta\nu_i)}$, where $\delta\nu_i$ is the measured deviation of the $^1S_0 \rightarrow {}^3P_1$ transition from the free-space resonance, i.e. the differential light shift, and $M(\delta\nu_i)$ is the median across the array [53]. Compared to the amplitude homogenization of the intermediate tweezers, at this stage I_i contains also information on the shape of the i-th trap, as it is directly proportional to the intensity of the considered trap.

After a few (typically 3 or 4) iterations of this feedback protocol, we can reduce the relative RMS variation of the differential light shifts from around 7%, which is the value we obtain with the intermediate homogenization only, to around 1.5% for arrays of up to 30 independent traps [Fig. 2.18(b)]. While this is a satisfactory value for us, the performances of the homogenization could be further improved by appropriate tuning of the proportional gain of the feedback loop, which we reduce to 50 and 25% of the initial value for the last two homogenization rounds. As the fundamental requirement of this technique is a non-magic condition for a cooling transition, this scheme can be applied to any atomic species. In our experiments we implement the homogenization by performing blow-out spectroscopy on the non-magic $^1S_0 \rightarrow {}^3P_1$ transition of fermionic isotopes but also on the non-magic $^1S_0 \rightarrow {}^3P_1|J' = 1, m'_J = \pm 1\rangle$ transitions for ^{174}Yb.

2.3.4 Differential polarizability measurements

Information on the differential trapping between a ground and excited atomic state is crucial for a wide range of experiments. Differential light shifts measurements allow to identify magic wavelengths, which are very beneficial for cooling and imaging single atoms [52, 54, 55, 114] as well as for clock interrogation [4, 65, 115]. For non-magic traps, knowledge on the differential polarizability allows to enhance operation fidelity and can also be exploited to introduce local light shifts for quantum information processing [65, 82] or quantum simulation [58, 109, 111] schemes. In the following, we describe spectroscopic measurements we have performed to measure the differential light shifts of the $^1S_0 \rightarrow {}^3P_1$ and $^1S_0 \rightarrow {}^1P_1$ transitions at 532 nm for different ytterbium isotopes. To extract the differential light shifts, we perform blow-out spectroscopy on the considered transition at different trap depths. For linearly polarized tweezer light, the tensor light shift splits the degenerate $|m'_F\rangle$ excited states according to $|m'_F|$ and isolating the different $|m_F\rangle \rightarrow |m'_F\rangle$transitions allows to measure the differential polarizability for each $|m'_F\rangle$ sublevel. Assuming knowledge on the ground state polarizability, we also extract the polarizability of the $|m'_F\rangle$ excited states. We find good agreement between the measured data and our theoretical model described in Sec. 1.2.1.

Green transition

We show the results of the differential light shifts measurement of the $^1S_0 \rightarrow {}^3P_1$ transition in Fig. 2.19. In the case of ^{173}Yb, for linearly polarized tweezer light and very weak 0.2 G magnetic field aligned along the tweezers polarization (π-polarized tweezers), we clearly observe four peaks, corresponding to transitions from $^1S_0$ to $^3P_1|F' = 7/2, m'_F = \pm 1/2\rangle$, $^3P_1|F' = 7/2, m'_F = \pm 3/2\rangle$, $^3P_1|F' = 7/2, m'_F = \pm 5/2\rangle$ and $^3P_1|F' = 7/2, m'_F = \pm 7/2\rangle$ in this energy order [Fig. 2.19(a)]. We observe that all of the transitions are blue-shifted compared to the free-space resonance,

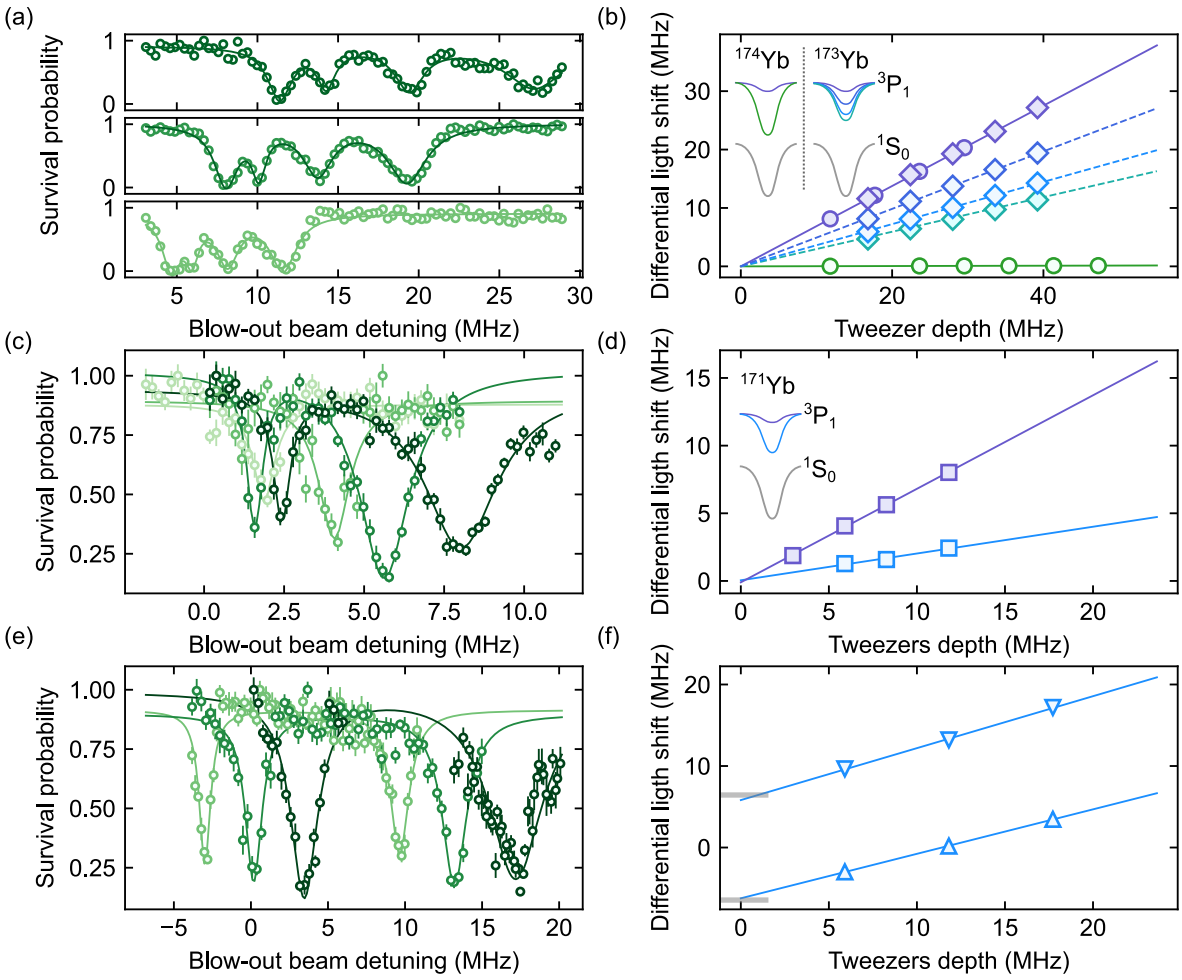

Figure 2.19| Differential light shifts of the $^1S_0 \rightarrow {}^3P_1$ transition at 532 nm. (a) Blow-out spectroscopy curves of the $^1S_0|F = 5/2\rangle \rightarrow {}^3P_1|F' = 7/2\rangle$ transition in ^{173}Yb. We plot the normalized atom number as a function of the blow-out beam detuning from the free space resonance for varying tweezer depths: $U_0 \simeq 0.8, 1.3, 1.8$ mK from bottom to top. (b) Differential light shifts for ^{174}Yb (circles) and ^{173}Yb (diamonds). Different $|m'_F\rangle$ states are indicated with different colors. For ^{174}Yb we show $|m'_F = 0\rangle$ (green) and $|m'_F = \pm 1\rangle$ (purple), for ^{173}Yb we employ a gradual transition from green ($|m'_F = \pm 1/2\rangle$) to purple ($|m'_F = \pm 7/2\rangle$) for the 4 excited states. Solid lines are fit to the data and dashed lines are the predictions of our polarizability model based on the Clebsch-Gordan approach [see Sec. 1.2.1]. The inset displays a conceptual scheme of the relative trap depths for the involved states. (c) Blow-out spectroscopy curves of the $^1S_0|F = 1/2\rangle \rightarrow {}^3P_1|F' = 3/2\rangle$ transition in ^{171}Yb for π-polarized tweezers. (d) Differential light shifts of the $^3P_1|F' = 3/2, m'_F = \pm 3/2\rangle$ (purple) and $^3P_1|F' = 3/2, m'_F = \pm 1/2\rangle$ (blue) states in ^{171}Yb for π-polarized tweezer light. (e) Blow-out spectroscopy curves of the $^1S_0|F = 1/2\rangle \rightarrow {}^3P_1|F' = 3/2\rangle$ transition in ^{171}Yb for σ-polarized tweezers. (f) Differential light shifts of the $^3P_1|F' = 3/2, m'_F = +1/2\rangle$ (downwards facing triangles) and $^3P_1|F' = 3/2, m'_F = -1/2\rangle$ (upwards facing triangles) states in ^{171}Yb for σ-polarized tweezer light. The grey bars indicate the Zeeman splitting between the two states at the employed 9.25 G field. For all the spectroscopy curves, darker shades of green represent deeper traps and solid lines are the Lorentzian fits employed to extract resonance centers. For the differential light shifts solid lines are linear fit to the data.

indicating lower confinement of the excited state. This is further confirmed by the increasing blue-shift of the $^1S_0 \rightarrow {}^3P_1$ transition for increasing tweezer intensity.

We summarize our results for ^{174}Yb and ^{173}Yb in Fig. 2.19(b). First, we verify that the $^1S_0 \rightarrow {}^3P_1|F' = 1, m'_F = 0\rangle$ transition is magic for π-polarized trapping light at 532 nm. We define the differential polarizability as the ratio between the measured differential light shift and the ground state trap depth: $\Delta\alpha = \frac{U_0 - U_1}{U_0}$, where U_0 and U_1 are the ground and excited state trap depths. We find a differential polarizability of 0.28(2)% for the $^1S_0 \rightarrow {}^3P_1|F' = 1, m'_F = 0\rangle$ transition, slightly smaller than the value reported in Ref. [52]. Conversely, the $^1S_0 \rightarrow {}^3P_1|F' = 1, m'_F = \pm 1\rangle$ transition is strongly light shifted, and we find $\Delta\alpha = 68.7(1)\%$, in good agreement with Ref. [52]. Similarly, we observe an increasingly large differential light shifts for increasing $|m'_F|$ in ^{173}Yb. We measure $\Delta\alpha = 29.7(2)\%$, 36.9(3)%, 49.8(6)%, 68(1)% for $|m'_F = \pm 1/2\rangle$, $|m'_F = \pm 3/2\rangle$, $|m'_F = \pm 5/2\rangle$ and $|m'_F = \pm 7/2\rangle$ respectively. As expected, the stretched transitions display the same differential polarizability across different isotopes. We find excellent agreement between our measurements and the polarizability model presented in Sec. 1.2.1.

We now focus on ^{171}Yb, showing an exemplary spectroscopy curve in Fig. 2.19(c). In this case, we observe two peaks, corresponding to excitations to the $^3P_1|F' = 3/2, m'_F = \pm 1/2\rangle$ and $^3P_1|F' = 3/2, m'_F = \pm 3/2\rangle$ states. We find $\Delta\alpha = 23(3)\%$, 67.2(3)% for $|m'_F = \pm 1/2\rangle$ and $|m'_F = \pm 3/2\rangle$ respectively [Fig. 2.19(d)]. Again, we observe that the stretched transitions display the same polarizability across different isotopes and we find good agreement with our theoretical predictions.

So far, we have only considered π-polarized trapping light, for which the polarization is aligned with the quantization axis. We make sure to respect this condition by employing a small 0.2 G magnetic field aligned with the tweezers polarization, which is small enough to produce negligible Zeeman splitting. This field is actually so small, that the quantization axis is defined by the tweezers polarization rather than by the field. In fact, we observe that we require a much larger magnetic field to overcome the tweezers polarization and define a new quantization axis. In this case, the angle between the quantization axis and the trapping light polarization allows to tune the differential light shifts to reach e.g. magic conditions [55, 57]. We have not investigated in detail the transition from a quantization axis defined by the trapping light polarization and one defined by the magnetic field direction but we expect that this will happen when the magnetic shift is larger than the maximal light shift [121]. For a sufficiently large magnetic field orthogonal to the tweezers light polarization, we observe a striking change in the differential polarizability. We use 9.25 G to split the $|m'_F = \pm 1/2\rangle$ states of ^{171}Yb by 12.9 MHz and we observe two peaks which shift in parallel for increasing trap depth [Fig. 2.19(e)]. We find a $\Delta\alpha = 54.3(5)\%$, 63(2)% for $|m'_F = -1/2\rangle$ and $|m'_F = +1/2\rangle$ respectively [Fig. 2.19(f)]. From our theoretical calculations we would expect a differential polarizability of $\simeq 59\%$ for both of the states for linearly polarized light orthogonal to the quantization axis. We ascribe the measured discrepancy between the two states to uncertainties in the peak fitting or in the linear fit for the differential polarizability extraction.

Blue transition

Differential trapping of the ground and excited states plays a crucial role also for fast detection schemes. In fact, for highly-saturated imaging light, the atoms spend roughly half of the time in the excited state of the imaging transition and a reduced confinement of such state results in higher atom-loss probability. Moreover, differential light shifts may also result in enhanced heating due to dipole force fluctuations [108]. Due to the relevance of fast, non-destructive detection for numerous quantum information processing [48–51] and metrology [31] schemes, we investigate the differential light shifts of the $^1S_0 \rightarrow {}^1P_1$ transition for π-polarized 532 nm

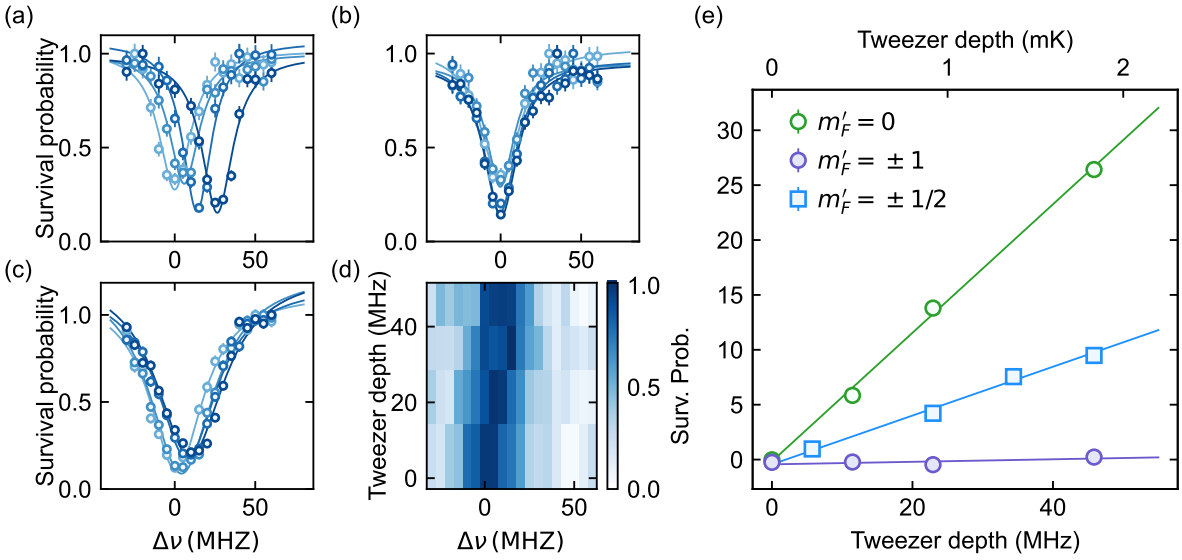

Figure 2.20| Differential light shifts of the $^1S_0 \rightarrow {}^1P_1$ transition at 532 nm. (a) Blow-out spectroscopy curves of the $^1S_0|F = 0, m_F = 0\rangle \rightarrow {}^1P_1|F' = 1, m'_F = 0\rangle$ transition in ^{174}Yb. (b) Blow-out spectroscopy curves of the $^1S_0|F = 0, m_F = 0\rangle \rightarrow {}^1P_1|F' = 1, m'_F = \pm 1\rangle$ transitions in ^{174}Yb. (c) Blow-out spectroscopy curves of the $^1S_0|F = 1/2, m_F = \pm 1/2\rangle \rightarrow {}^1P_1|F' = 3/2, m'_F = \pm 1/2\rangle$ transitions in ^{171}Yb. For all curves, we plot the normalized atom number as a function of the blow-out beam detuning $\Delta\nu$ from the free-space resonance for different tweezer depths, indicated by darker shades of blue. Solid lines are Lorentzian fits to the data. Spectroscopy light is π-polarized (a, c) or σ-polarized (b) to ensure that only the desired transitions are addressed. (d) Blow-out spectroscopy of ^{171}Yb for σ-polarized probe beam, exciting all allowed transitions. (e) Differential light shifts for ^{174}Yb (circles) and ^{171}Yb (squares) $|m'_F\rangle$ sublevels. Solid lines are linear fits to the data.

trapping wavelength.

In this case, resolving peaks corresponding to transitions to different $^1P_1|F' = F + 1, m'_F\rangle$ states is complicated by the broad line of the addressed transitions. We therefore differentiate between $|m'_F\rangle$ states by tuning the polarization of the probing beam and selectively exciting only the transitions of interest. For ^{174}Yb, we can employ π-polarized spectroscopy light to address only the $^1S_0|F = 0, m_F = 0\rangle \rightarrow {}^1P_1|F' = 1, m'_F = 0\rangle$ transition, for which we observe a significant reduction of the excited state confinement [Fig. 2.20(a)]. Strikingly, we find that the strecthed $^1S_0|F = 0, m_F = 0\rangle \rightarrow {}^1P_1|F' = 1, m'_F = \pm 1\rangle$ transitions feature a vanishing differential light shift, indicating a near-magic trapping condition [Fig. 2.20(b)]. The situation is therefore reversed compared to the $^1S_0 \rightarrow {}^3P_1$ transition at the same wavelength. We extend our investigations to ^{171}Yb, finding a positive small differential light shift for the $^1S_0|F = 1/2, m_F = \pm 1/2\rangle \rightarrow {}^1P_1|F' = 3/2, m'_F = \pm 1/2\rangle$ transitions, due to their intermediate character between the stretched and the $^1S_0|F = 0, m_F = 0\rangle \rightarrow {}^1P_1|F' = 1, m'_F = 0\rangle$ transition of ^{174}Yb [Fig. 2.20(c)]. As the near-magic condition for the stretched transitions does not depend on the specific isotope, fluorescence detection schemes based on these transitions are beneficial also for ^{171}Yb. We report in Fig. 2.20(d) a spectroscopic curve obtained for σ-polarized probe light, same as our imaging light. This light excites all possible transitions and we cannot decouple the stretched transitions from $^1S_0|F = 1/2, m_F = \pm 1/2\rangle \rightarrow {}^1P_1|F' = 3/2, m'_F = \pm 1/2\rangle$ excitations.

We summarize our measurements in Fig. 2.20(e). We measure differential light shifts $\Delta\alpha =$

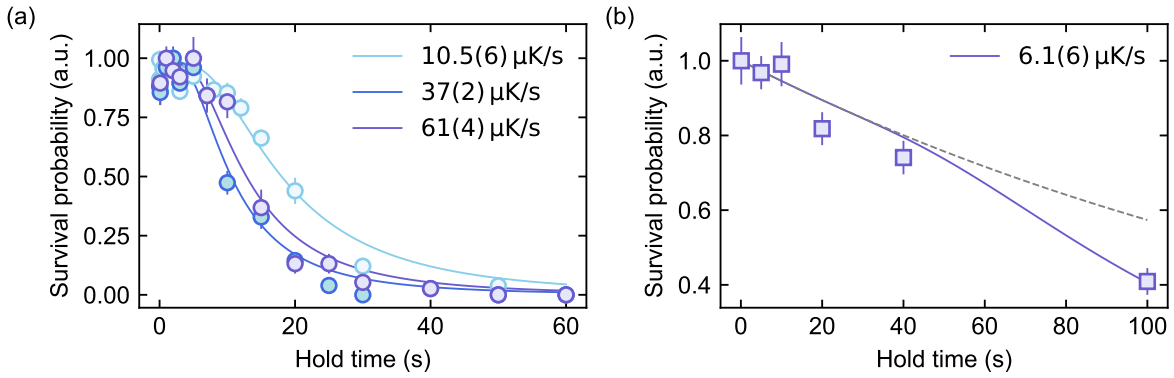

Figure 2.21| Tweezers dark lifetime. (a) Normalized atom number versus holding time for a 10-tweezer array at different trap depths: $U_0 \simeq 0.57$, 1.1, 2.3 mK, indicated by darker shades of blue. Solid lines are fit with a heating-induced loss model [see Sec. 1.3 and Ref. [133]], yielding the reported heating rates. (b) Lifetime at $U_0 \simeq 2.3$ mK with interleaved cooling pulses for ^{174}Yb. For each second of holding time we apply a 2 ms cooling pulse on the magic $^1S_0 \rightarrow {}^3P_1$ transition to undo the effect of trap-induced heating. The solid line is a fit with the heating rate model while the dashed line represents our 180 s vacuum-limited lifetime. All data refer to a 10-tweezer array.

59(2)%, 22(2)% for the ^{174}Yb $|m'_F = 0\rangle$ and ^{171}Yb $|m'_F = \pm 1/2\rangle$ states respectively. Most importantly, we observe a very small differential light shift $\Delta\alpha = 1.1(8)\%$ for the stretched transitions. All our measurements are in good agreement with our polarizability model presented in Sec. 1.2.1.

2.3.5 Tweezers lifetime

Another crucial property of tweezer-trapped atoms is their lifetime. In particular, the dark lifetime of the sample, i.e. when only the trapping light is applied, can provide valuable information on the noise properties of the traps themselves. Moreover, the dark lifetime is essentially a higher bound to the duration of experiments and detection schemes. As discussed in Sec. 1.3, the main mechanisms limiting the lifetime of single trapped atoms are off-resonant scattering, intensity noise and intermodulation noise.

In Fig. 2.21(a) we show a measurement of the dark lifetime of a 10-tweezer array for different trap depths. We find lifetimes between 10 and 20 s for traps in the investigated 0.57-2.3 mK range. Notably, the shape of the lifetime curve is not a simple exponential, as it shows an initial plateau followed by a decay at longer times. This is caused by the mechanism underlying heating-induced atom losses. In fact, atoms are lost when their energy overcomes the depth of the confining potential. Laser-cooled atoms in sufficiently deep traps have energies that are typically much lower thant the trap depth, and therefore require a relatively long time to acquire a sufficient amount of energy to escape the trap. After this initial plateau, instead, the survival probability decreases steeply. Knowing the trap depth and the initial atomic temperature we can fit our lifetime data with the loss model described by Eq. (1.48) [133]. From the fit, we extract the trap-induced heating rates α, finding $\alpha = 10.5(6)$, 37(2), 61(4) μK/s for $U_0 \simeq 0.57$, 1.1, 2.3 mK respectively. The higher heating rate explains the shorter lifetime observed for deeper traps, despite the larger confinement.

The measured rates are much larger than what we would expect from off-resonant scattering alone, for which we find $\alpha_{sc} \simeq 9.6$, 4.8, 2.4 μK/s for the investigated traps. Moreover, the measured heating rates do not scale linearly with the trap depth, further indicating that off-

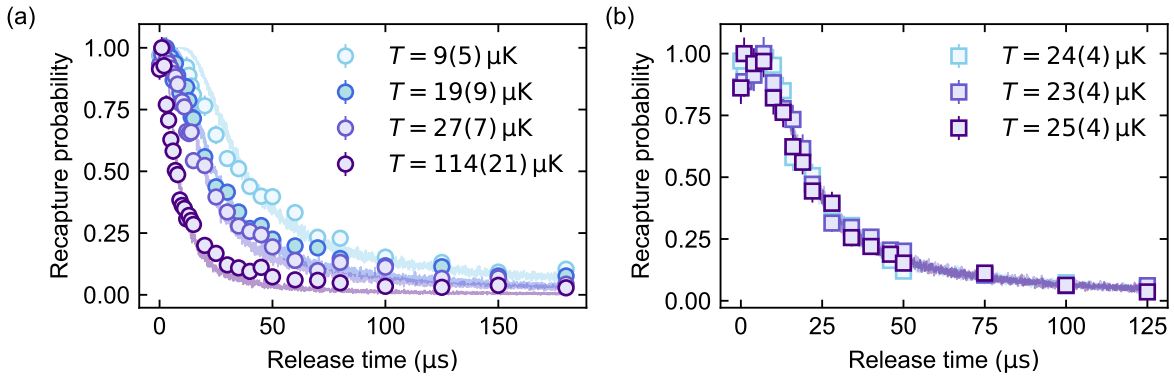

Figure 2.22| Temperature extraction via release and recapture. (a) Release and recapture curves for a 10-tweezer array at $U_0 \simeq 2.3\,\mathrm{mK}$ performed after variable holding time. Darker shades of blue indicate holding times of 1 ms, 0.5, 1 and 5 s. (b) Release and recapture curves for a 10-tweezer array at $U_0 \simeq 2.3\,\mathrm{mK}$ after variable holding time (0.2, 1, 5 s) with a 100 ms Doppler cooling pulse before release. Shaded lines indicate the simulated recapture probabilities for the extracted temperature. Each point is obtained from 50 experimental repetitions.

resonant scattering is not the dominant heating source. Parametric heating due to technical noise strongly depends on the trap depth. In fact, for a given intensity noise spectrum, the response of atoms to noise at different frequencies shifts when changing the trap depth and therefore the trapping frequencies. We conclude that our lifetime is likely limited by intensity noise, originating either from fluctuations of the global laser power in the array or from intermodulation noise. In particular, we know that we are affected by strong intermodulation noise as we observe a significant reduction of the heating rate in shorter arrays [see Sec. 4.6.1] and, conversely, a reduction of the lifetime in longer arrays.

Regardless of its origin, we can remove the excess energy introduced by heating through repeated cooling pulses. In Fig. 2.21(b) we show the lifetime of a 10-tweezer array of ^{174}Yb atoms at $U_0 \simeq 2.3\,\mathrm{mK}$, where we apply 2 ms of cooling every 1 s of holding. We perform Doppler cooling on the magic $^1\mathrm{S}_0 \rightarrow {}^3\mathrm{P}_1$ transition employing the MOT beams below saturation intensity and closely detuned from the atomic resonance. Fitting the lifetime curve with our loss model we find a very small 6.1(6) μK/s heating rate indicating that we can almost completely remove the detrimental effects of trap-induced heating and prolong the lifetime of our trapped atoms [132].

Temperature extraction via release and recapture

Being a thermodynamic quantity, temperature is well suited to describe many-particle ensembles and not individually-trapped atoms. In fact, in tweezer arrays it would be more appropriate to discuss the occupation of different harmonic oscillator levels rather than the atomic temperature. Even more so, temperature can be tuned without any cooling or heating by adiabatically ramping the trap depth while remaining in the same harmonic oscillator level [133]. As we do not have a detection protocol for the oscillator states, such as resolved sideband spectroscopy, we employ an average temperature, at a considered trap depth, as a proxy of the distribution of the atomic energies in the trap across different realizations. We emphasize that this definition of temperature is obtained by averaging the energy over many realizations of the same experiment with a single atom.

Such temperature can be measured through the release and recapture technique introduced in Ref. [133]. In brief, the idea behind this scheme is that it is possible to obtain information about the energy distribution of a single atom in a trap by releasing it for a variable time

and determining the probability of recapturing it. Once a recapture probability against release time curve is obtained, we extract the atomic temperature with Monte Carlo simulations of the single-atom trajectories. For each trajectory, we start from a Maxwell-Boltzmann distribution in a trapping potential and we randomly generate a position and velocity. We let the atom evolve during the release time and determine its energy once the trap is turned on again, considering it captured if its energy is lower than the trap depth. We simulate this for many trajectories, varying the temperature of the initial distribution until the simulated recapture probability curve matches the experimental one.

In Fig. 2.22(a) we show the measured temperatures for a 10-tweezer array with $U_0 \simeq 2.3\,\mathrm{mK}$ for different holding times (1 ms, 0.5, 1 and 5 s). We observe a linear increase of the measured temperature as we expect from a constant heating rate during the holding time. However, the measured heating rate $\simeq 20\,\mu\mathrm{K/s}$ is much smaller than the one extracted from our loss-model fit. Besides ascribing this to changes in the intensity stabilization loop parameters or to variations in the laser noise properties due to e.g. operation at different currents or drifts in the ambient temperature, we have no explanation for this discrepancy. We instead confirm that with a single cooling pulse at the end of the holding time we can completely undo the trap-induced heating [Fig. 2.22(b)]. To this end, we hold our trapped atoms for times between 0.2 and 5 s and we then perform a 100 ms Doppler cooling pulse, finding a constant temperature $\simeq 25\,\mu\mathrm{K}$ for all holding times.

2.4 Single-atom imaging

Single-atom imaging relies on collecting the fluorescence of individual atoms through a high-NA objective lens and focusing it on a scientific camera. High detection-fidelity is achieved when the collected photons are sufficient to clearly distinguish the single-atom signal from the camera background. This is typically obtained by cooling the atoms during imaging in order to compensate the recoil-induced heating caused by scattering of imaging photons. Indeed, an atom escaping its trapping potential during imaging results in a reduced number of collected photons, and therefore a diminished fidelity. Moreover, atom losses hinder repeated measurements, which are key to experimental techniques such as tweezers rearrangement and to many quantum information schemes. Imaging and cooling lights can be combined in a single red-detuned beam [52, 54, 65, 82, 84] or they can address different transitions [27, 53, 55, 76, 114], which is particularly beneficial for non-magic trapping conditions. Both these schemes have been applied to image ^{174}Yb [52, 114] and ^{171}Yb [53, 54, 65, 82, 84] atoms but no single-atom imaging of ^{173}Yb have been so far demonstrated. In this section we will describe our imaging setup, how we measure the detection fidelity and survival probability of our imaging schemes and we will report on the two-color imaging scheme we have employed to image single ^{173}Yb atoms in optical tweezers.

2.4.1 Fluorescence collection setup

In our setup, we employ the same microscope objective to project the optical tweezer array and collect the atomic fluorescence. Our objective is custom-made[64] to meet the specific requirements of our setup. It has a numerical aperture of 0.6, with a working distance (WD) of 17.5 mm and a 300 µm field of view (FOV) diameter. Importantly, the objective is diffraction limited over the whole visible range and it is corrected for axial color shift for 399, 532, 556 and 759 nm, allowing us to employ tweezers of different wavelengths and to collect fluorescence from both ytterbium cooling transitions.

[64] Special Optics

Prior to its installation in the experimental setup, we verified that the objective matches the desired specifications. In particular, we employed a 250 nm pinhole, well below the resolution of our imaging system, to generate point source which we imaged on a cMOS camera with a $\simeq \times 20$ magnification. For these measurements we also placed a test window with the same thickness as our glass cell viewports between the pinhole and the objective, as the latter is intended to work with such viewport within its WD. For a point source, we expect the following intensity distribution of the image formed on the camera:

$$I(r) = I_0 \left[\frac{2J_1(\frac{2\pi}{\lambda} r\mathrm{NA})}{\frac{2\pi}{\lambda} r\mathrm{NA}} \right]^2 \tag{2.7}$$

where $J_1(x)$ is the Bessel function of the first kind of order one. This distribution corresponds to the point spread function (PSF) of the imaging system and it is characterized by an intensity minimum for

$$r_R = 0.61\lambda/\mathrm{NA} \tag{2.8}$$

This distance is typically used to estimate the imaging system resolution according to the Rayleigh criterion. Fitting the measured PSFs we obtained an NA of 0.58(3) and 0.62(3) at 399 nm and 532 nm, respectively. We also verified the lack of noticeable aberrations in a FOV diameter of $\sim$ 300µm, with large aberrations, and in particular astigmatism, appearing out of the expected FOV.

After testing the objective, we installed it above our glass cell. We employ a custom-designed objective holder to attach it to a tiltable mount[65] which is held by a XYZ tranlsator stage[66] equipped with a picomotor piezo actuator for fine-tuning of the objective vertical position. The XYZ stage holding the objective is installed on a stainless steel breadboard above the glass cell. Please refer to Ref. [122] for a detailed description of the objective mount and on the procedure we employed for its first alignment.

In Fig. 2.23(a) we sketch a scheme of the combined single-atom imaging and tweezers setup. Tweezer light at 532 nm is linearly polarized along the $\hat{y}$ direction and is projected on the atomic plane by our microscope objective. We employ two beams addressing the $^1\mathrm{S}_0 \rightarrow {}^1\mathrm{P}_1$ transition to excite atomic fluorescence. The beams propagate along the $\hat{y}$ direction, parallel to the quantization axis and perpendicular to the array direction. In the figure we show both the imaging beams configurations employed throughout in this work. We continuously illuminate atoms with both imaging beams simultaneously when we perform the two-color imaging scheme at the end of this chapter and when we explore the possibility of performing fast imaging with continuous beams [see Sec. 4.2.3]. In both these cases, we employ a retro-reflected beam in the lin-perp-lin configuration in order to avoid interference effects. Instead, we use a horizontal polarization for both the imaging beams when we alternate them for the flash imaging scheme described in Chapter 4. In order to minimize the possibility of acquiring directional momentum during imaging, we balance the flash imaging beams intensity and align them such that each beam is coupled back into the others' optical fiber.

Fluorescence light at 399 nm is decoupled from the tweezers light through a dichroic mirror[67] and it is focused on a scientific camera by a $f = 200$ mm 2" achromatic tube lens [see Fig. 2.23(b)]. Considering the objective EFL at 399 nm ($\sim$ 25.5 mm), our imaging systems features a theoretical $\times 8$ magnification factor M and a measured $M = 7.98$. This has been obtained by fitting the distance between different tweezers traps, assuming knowledge on the

[65] Standa 5KVDOM
[66] Newport TSDS-655SL-M6
[67] Optoman HRu 399 nm, HTp 460 + 532-759 nm

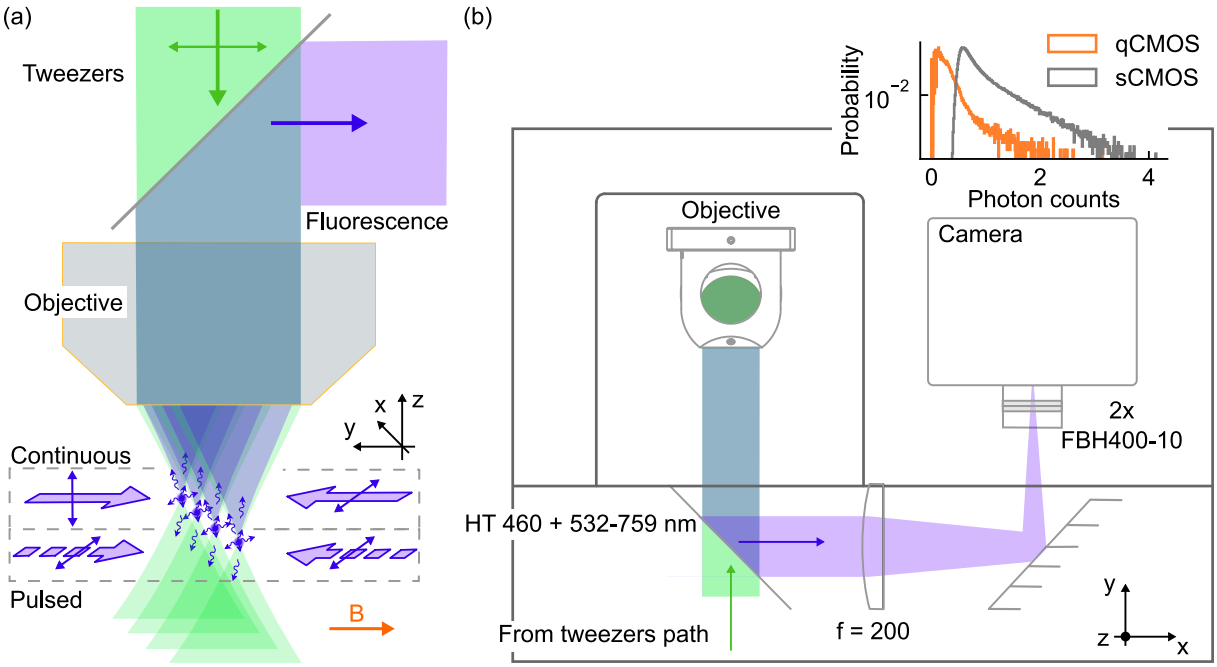

Figure 2.23| Single-atom imaging setup. (a) Sketch of the imaging setup. The objective projects the trapping light at 532 nm and collects the atomic fluorescence at 399 nm. We illuminate the atoms with counter-propagating beams, directed perpendicularly to the tweezer array and parallel to the magnetic field and tweezers polarization direction. We represent both the imaging beams configurations employed in this work: continuous beams with perpendicular polarization or pulsed beams with horizontal polarization. (b) Layout of the single-atom imaging optical setup. Fluorescence light is focused by a $f = 200$ mm achromatic lens on a scientific camera. We use two bandpass filters centered at 400 nm to reduce the stray light on the camera sensor. Inset: readout noise histograms of the qCMOS and sCMOS camera.

tweezers spacing on the atom plane. We estimate this value from the frequency difference between AOD tones and the magnification of the tweezer-projection telescope, previously measured in a test setup. The choice of a relatively low magnification is motivated by the desire to concentrate most of the single-atom signal on few pixels. In fact, single-atom detection is performed by integrating the photon counts over a well-defined region of interest (ROI) and discriminating the presence or absence of an atom according to the measured counts. If the ROI is too large, the noise of camera pixels leads to a reduced separation between the sum of the background photon counts and the one corresponding to the single-atom signal. Our low magnification allows us to focus most of the atomic signal on a single pixel and we thus typically employ 3×3 ROIs for photon integration. However, this also results in a lack of resolution and low information on the spatial profile of the atomic signal, which would be desirable when imaging atoms in tightly-spaced arrays [see Sec. 4.5].

In order to minimize the size of the atomic signal it is necessary to precisely tune the position of the tube lens with respect to the camera. To this end, we initially employed an auxiliary large and collimated beam mimicking the atomic fluorescence after the objective and we focused the tube lens minimizing the waist on the camera. We then performed a finer tuning of the tube lens position by directly minimizing the average spot size of the single-atom signal. When analyzing the shape of the experimental PSF, we also noticed the presence of significant astigmatism, even though our trap frequency measurements were indicating otherwise. We found that this aberration was introduced only in the imaging system by the dichroic mirror separating the

fluorescence from the tweezers light. We therefore unscrewed the mirror and gently rotated it, monitoring changes in the shape of the atom signal. After a couple of iterations, corresponding to an estimated rotation between $\sim 45°$ and $\sim 60°$, we found that astigmatism had disappeared and we therefore very gently tightened the screw fixing the dichroic mirror in its mount.

For our first experiments, we acquired images with a sCMOS[68] camera. With this camera we have performed single-atom detection with a two-color scheme combining imaging and cooling to achieve high-fidelity and good survival probability and with fast cooling-free imaging both with continuous and alternated beams. However, upgrading our camera to a qCMOS[69] has allowed us to really push the performances of our detection schemes and achieve the results on fast imaging presented in this thesis.

The qCMOS brings three fundamental improvements over the sCOMS. First, the qCMOS has a much higher (83%) quantum efficiency (QE) at 399 nm compared to the sCMOS (65%). Second, the readout noise of camera pixels is much smaller for a qCMOS compared to a sCMOS camera. We have measured the readout noise histograms for our two cameras and report it in the inset of Fig. 2.23(b). To obtain these histograms we acquire N dark images with the camera sensor completely blocked and compute the difference between the i-th and $i+1$-th image, obtaining $N-1$ difference-images. We then compute the pixel-wise standard deviation of such images to obtain a single image in which the value of each pixel corresponds to the standard deviation of the values of that precise pixel over many repetitions. The histograms reported in Fig. 2.23(b) and in the datasheets of many cameras are in fact the histogram of the standard deviation of different pixels. We compute the median(RMS standard deviation) of the pixel-by-pixels readout noise finding a 0.21(0.3) and 0.89(1.03) for the qCMOS and cMOS, respectively. Finally, the qCMOS pixels display a so-called deep trench isolation structure which prevents photon leakage between adjacent pixels. This effect leads to a larger signal spread in sCMOS cameras which require larger ROIs (and an increased the background noise) to integrate the full atomic signal. The combination of higher QE, lower noise and absence of signal leakage makes the single-atom imaging performances of qCMOS cameras much superior compared to those of sCOMS.

For both our cameras, we employ two bandpass filters centered at 400 nm[70] to prevent any stray light form reaching the sensor. Finally, we estimate the collection efficiency of our imaging system, i.e. the ratio between the detected fluorescence photons and total number of photons scattered by the atoms. Taking into account the QE, the geometric collection efficiency [see Sec. 4.2.2], the transmission through the objective at 399 nm and the losses associated to the dichroic, the two filters and the other optical components we estimate a $4\simeq 4.5\%$ total collection efficiency, which is confirmed by the experimental number of collected photons given our expected scattering rate.

2.4.2 Detection fidelity and losses estimation

The two main figures of merit for evaluating the performances of single-atom imaging schemes are the detection fidelity and the survival probability. The first is essentially an estimation of the confidence in determining the presence or absence of an atom in a single shot, while the second expresses the likelihood that the atom has survived the imaging process and is therefore available for successive stages of the experimental sequence. Typically, the presence of an atom is determined by setting a photon-count threshold in the integrated photon-counts within a ROI: if the counts are above the threshold the atom is present. Detection infidelities correspond to wrong labeling of experimental images. These can occur when the background signal is too high,

[68] Teledyne Photometrics Kinetix22
[69] Hamamatsu Orca Quest
[70] Thorlabs FBH400-10

due to e.g. fluctuations in the pixels noise, and an empty image is mistaken as full, or when the signal of an atom is too low, due to e.g. an early loss or excitation to a dark state, and its presence goes undetected.

To estimate the fidelity and losses associated to our imaging schemes we follow the model-free approach presented in Refs. [55, 121, 208]. In particular, we acquire two successive equal images and perform a Bayesian analysis on the correlations between atom occupancy in the first and second image. We set the dark time between images according to the frame rate of the camera used, namely 50 ms for the sCOMS and 25 ms for the qCMOS. By acquiring over many images, we set a trial photon-count threshold to distinguish between atoms and void. For each site of the array we determining the probability of measuring an atom in both the images (P_{11}), a void in both the images (P_{00}), an atom and then a void (P_{10}) or a void and then an atom (P_{01}). The probability of each outcome is given by:

$$\begin{aligned} P_{11} &= f(1-F_0)F_1(1-S) + (1-f)(1-F_0)^2 + fF_1^2S \\ P_{10} &= fF_1S(1-F_1) + fF_1(1-S)F_0 + (1-f)(1-F_0)F_0 \\ P_{01} &= f(1-F_0)(1-F_1)(1-S) + (1-f)(1-F_0)F_0 + f(1-F_1)F_1S \\ P_{00} &= 1-(P_{11}+P_{10}+P_{01}) \end{aligned} \tag{2.9}$$

where f is the filling fraction, S is the survival probability after one image and F_1 and F_0 are the fidelities of correctly identifying an atom or a void, respectively. The total single-atom detection fidelity is defined as $F = fF_1 + (1-f)F_0$. For each trap, we solve the equations above for different trial threshold values and we choose the value that maximizes the total fidelity.

2.4.3 Imaging of ^{173}Yb atoms with a two-color imaging scheme

High-fidelity single-atom imaging is often achieved by actively cooling the atoms during detection, in order to minimize the probability of photon-recoil induced atomic losses. In presence of efficient cooling, this scheme allows to achieve extremely high detection fidelity and survival probability as atoms remain confined within their traps for long illumination times, allowing to collect many photons and to retain the atoms for successive operations [12, 52, 54, 55, 65, 76, 81, 82, 84, 132].

For alkalis, the same optical red-detune light is used to provide cooling and at the same time scatter fluorescence photons [18, 132, 209–211]. A similar scheme can also be applied to image lanthanide atoms (ytterbium, erbium and dysprosium) employing a narrow-line transition, provided that a magic trapping condition is available to guarantee efficient cooling [52, 54, 65, 84, 135, 136]. Alternatively, single-atom imaging can be achieved with a two-color scheme, where fluorescence photons are scattered on a broad-line transition, such as the $^1\mathrm{S}_0 \rightarrow {}^1\mathrm{P}_1$, while simultaneously cooling on a narrow-line transition such as the $^1\mathrm{S}_0 \rightarrow {}^3\mathrm{P}_1$. This allows to achieve a sufficient scattering rate without compromising too much on cooling efficiency. This scheme is particularly well-suited for imaging Sr atoms, where the few-kHz line of the $^1\mathrm{S}_0 \rightarrow {}^3\mathrm{P}_1$ transition does not guarantee a sufficiently high photon scattering rate for imaging, but provides an excellent line for cooling [12, 55, 76, 81]. Moreover, in strontium the long lifetime of the excited $^3\mathrm{P}_1$ state gives access to a Sisyphus sub-Doppler cooling scheme based on differential confinement of the ground and excited state in non-magic traps [12, 76, 81]. This kind of cooling is hardly accessible in ytterbium, due to the relatively short $\simeq 884$ ns lifetime of the excited $^3\mathrm{P}_1$ state. Therefore, in the case of ytterbium the best imaging performances are typically achieved with magic trapping conditions for the $^1\mathrm{S}_0 \rightarrow {}^3\mathrm{P}_1$ transition. However, two-color imaging of single ^{171}Yb atoms in non-magic traps with high-fidelity and good survival probability has been recently demonstrated [53], after the two-color imaging scheme had already

been applied to ^{174}Yb [52, 114]. On the other hand, no single-atom imaging of ^{173}Yb had been previously demonstrated.

In the following, we show that the two-color imaging scheme enables single-atom detection of ^{173}Yb in non-magic traps, achieving fidelities and survival probabilities comparable to those obtained for the two-color scheme in ^{174}Yb and ^{171}Yb. To excite fluorescence, we illuminate the atoms with a retro-reflected beam, near resonant with the $^1\mathrm{S}_0|F = 5/2\rangle \rightarrow {}^1\mathrm{P}_1|F' = 7/2\rangle$ transition, while simultaneously cooling on the $^1\mathrm{S}_0 \rightarrow {}^3\mathrm{P}_1$ transition with our MOT beams. For cooling we employ a weak intensity $\simeq 3\, I_{\mathrm{sat}}$, where I_{sat} is the saturation intensity of the $^1\mathrm{S}_0 \rightarrow {}^3\mathrm{P}_1$ transition, and a detuning of $-8.5\,\mathrm{MHz}$ from the light-shifted $^1\mathrm{S}_0|F = 5/2\rangle \rightarrow {}^3\mathrm{P}_1|F' = 7/2, m'_F = \pm 1/2\rangle$ transitions. We note that due to our five-beam geometry, we employ slightly different values for the intensity and detuning of the vertical beam ($\simeq 1.6\, I_{\mathrm{sat}}$ and $-6.5\,\mathrm{MHz}$). Probably due to the large detuning, we find that the measured imaging performances are weakly sensitive to the exact cooling beam detuning in a few-MHz range around the optimal point. During imaging, we apply a low magnetic field of 0.2 G along the tweezers polarization direction.

Due to the quadratic differential light shift for $^3\mathrm{P}_1$ sub-levels with large $|m'_F| > 1/2$, we expect that states with larger $|m_F|$ will feature reduced cooling efficiency. In particular, atoms in the $|m_F = \pm 5/2\rangle$ states will feel a much larger red-detuning of the cooling beams due to the large positive shift of the $|m'_F = \pm 3/2,\ \pm 5/2 \pm 7/2\rangle$ states. However, the observed low imaging losses indicate sufficient cooling across all nuclear-spin states. We ascribe this to two possible reasons, both enabled by the presence of the blue imaging light. First, the blue light is essentially resonant with all the available transitions, due to the near-magic condition at 532 nm and the broad linewidth. Therefore, the imaging light acts as a continuous repumper, redistributing the ground state population from the $|m_F = \pm 5/2\rangle$ states into the $|m_F = \pm 1/2,\ \pm 3/2\rangle$ states which are efficiently cooled. On the other hand, the $\sigma^{\pm}$ polarization of the imaging light favors pumping towards the stretched transitions, which seems to oppose the described mechanism. We therefore think that another element might come into play for cooling the stretched states, enabled by the reduced confinement of the $^3\mathrm{P}_1$ excited state in our non-magic traps. When an atom acquires energy due to photon recoil-induced heating, it starts to explore a larger region of the confining potential, accessing areas where the differential light shift is reduced due to the lower light intensity. It is possible that our large red-detuning compared to the light-shifted resonance at the center of the trap becomes much smaller for atoms that have been pumped in the $|m_F = \pm 5/2\rangle$ states, have not been efficiently cooled and have thus acquired sufficient energy to explore regions of the trap where the differential light shift is reduced. In this case, atoms in the $|m_F = \pm 5/2\rangle$ states will then become near-resonant with the cooling light, be cooled and roll down towards the center of the trap. While this is not a Sisyphus-like mechanism, the non-magic trapping condition allows to put an energy cap on the maximum energy that can be acquired by atoms during imaging.

In Fig. 2.24(a) we show the average infidelity and survival probability for a 10-tweezer ^{173}Yb array as a function of the imaging beam intensity. For these measurements we fix the illumination time to 50 ms, a relatively long duration which is required to collect enough photons, given the low imaging intensity employed. In fact, the two-color imaging scheme relies on a delicate balance between the heating induced by the imaging light and the simultaneous cooling. For the deep employed traps ($U_0 \simeq 2.3\,\mathrm{mK}$) we achieve an average fidelity of 99.96(1)% and a survival probability of 98.5(2)% for an imaging intensity $I \simeq 1.3 \times 10^{-2}\, I_{\mathrm{sat}}$, where I_{sat} is the saturation intensity of the $^1\mathrm{S}_0 \rightarrow {}^1\mathrm{P}_1$ transition. At high intensities, the survival probability decreases while the infidelity saturates around 4×10^{-4}, approaching the lower limit set by the number of recorded images. We characterize the imaging performances with the two-images scheme outlined above and we show the correlation between the photon counts in the first and second

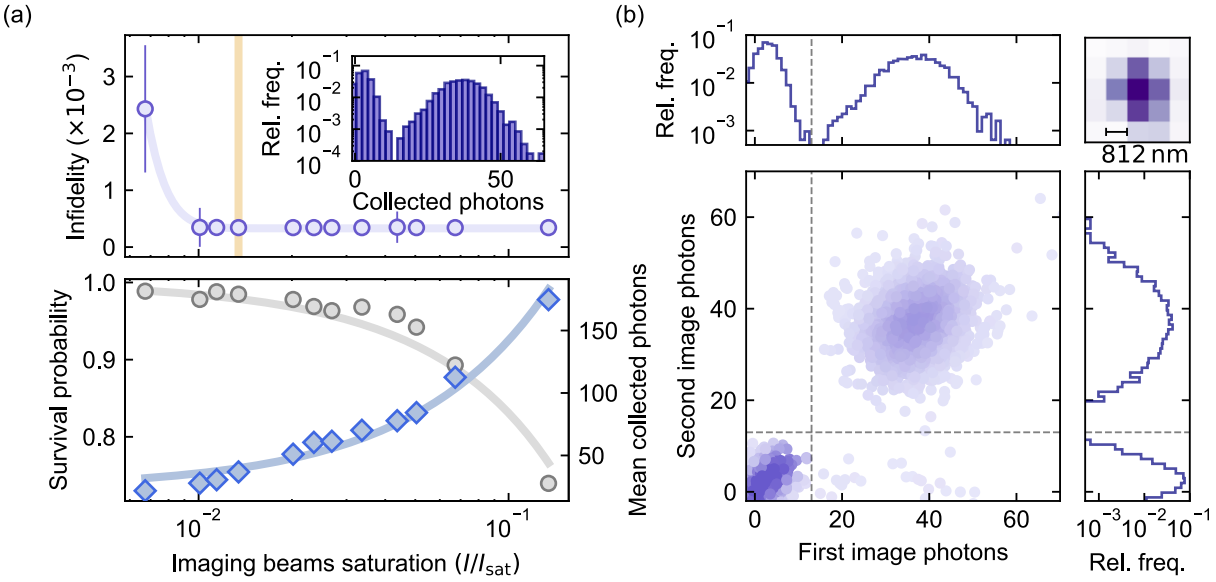

Figure 2.24| Two-color imaging of single ^{173}Yb atoms. (a) Imaging infidelity, survival probability and mean photon number per ROI as function of imaging beam intensity for a 50 ms illumination. The vertical yellow line indicates the intensity at which 99.96(1)% fidelity, 98.5(2)% survival probability, and 36.8(1) mean photons/ROI are obtained. Lines under the data are guides to the eye. The inset shows the photon count histogram corresponding to the vertical line, obtained for 3×3 pixel ROIs. Each point is extracted from about 300 images of a 10-tweezer array. Error bars for the fidelity and survival probability are obtained with a bootstrapping procedure [212]. (b) Correlation between photon counts in the first and second images at the intensity marked by the vertical line in (a). The gray dashed lines indicate the photon count threshold which maximizes the global fidelity. In the top right we show the average single-atom signal. All data are obtained with the sCOMS camera.

image for our optimal imaging intensity in Fig. 2.24(b).

It would be relatively easy to improve on the obtained performances. First, reducing the illumination time for increasing imaging intensity will allow to retain a high fidelity $> 99.9\%$ while strongly reducing losses and at the same time shortening the imaging duration. Second, the described characterization has been performed with our sCMOS camera, and repeating the same experiments with the qCMOS will lead to a lower noise and higher collection efficiency, boosting the fidelity, allowing for shorter illumination times and weaker driving of the imaging transitions, both of which strongly benefit the survival probability. Finally, as discussed in Sec. 4.2.2, the lin-perp-lin configuration employed for the imaging beams leads to a reduced collection efficiency and thus to a large number of scattered photons that enhance the loss probability without contributing to the fidelity. Exploring schemes combining cooling and alternated pulses of imaging light will maximize the collection efficiency and possibly result in a significant improvement of single atom imaging performances.

3

Preparation of a dense laser-cooled sample

The preparation of a cold atomic sample is a crucial step in all neutral-atom based platforms. Be it a single-atom array or a degenerate quantum gas, the sample needs to be produced in the fastest and most efficient way. Before being loaded into optical traps, atoms need be captured and cooled in a MOT in order to achieve the require phase-space density. Narrow-line MOTs of alkaline-earth-like atoms can reach few-µK temperatures, which are sufficiently low to directly load atoms into tightly focused traps such as optical tweezers. After extinguishing the MOT beams, each trap is typically filled with a stochastic number of particles, and successive steps are needed to achieve single-atom occupancy.

Single-atom resolved experiments employ high numerical aperture (NA) optics, which saturate the optical access on at least one side on the atomic sample and often conflict with the six beams required for typical MOT configurations. To solve this, it is possible to produce the MOT in a separate chamber and then transport the atoms in the science cell [139, 142, 149] or to employ intricate MOT beam arrangements [53]. Another option is to work in an open-top configuration, where the downward MOT beam is omitted and entirely replaced by gravity to provide the necessary confinement along the vertical direction. Such five-beam MOT (5B MOT) approach had been so far demonstrated only for erbium and dysprosium atoms [213] but can be extended to other species sharing similar properties, including strontium and ytterbium.

In this chapter we will present the first realization of a 5B MOT of ytterbium atoms and how we employ it to load optical traps for the next stages of our experiments. We will discuss the 5B MOT working principle, employing Monte Carlo simulations of atomic trajectories to gain further insight into its properties. We will then characterize the 5B MOT performances in our experiment, comparing it to a conventional six-beam (6B) geometry and analyzing results for different isotopes. We will also outline how we compress the MOT to achieve the high phase-space densities required to load atoms into an optical tweezer array and into a larger optical dipole trap. We will the describe the experimental sequences employed to reach single atom occupancy in the tweezers and comment on the loading of the optical dipole trap for different ytterbium isotopes. Finally we will show how we can prepare samples with different spin populations through optical pumping.

3.1 An ytterbium five-beam MOT

Most state-of-the-art neutral-atom based platforms capitalize on the capability to detect and manipulate individual atoms. This requires to employ one or more high-NA microscope lenses for addressing and imaging atoms with sub-micron resolution. Such large optics saturate the optical access on at least one of the science cell and often conflict with typical MOT configurations, where three-dimensional confinement is provided by shining counter-propagating beams

along each direction. Therefore, in state-of-the-art experimental setups it is necessary to either produce the MOT in a dedicated chamber and then transport the atoms to the science cell or to accept the challenge of combining the six MOT beams with bulky high-resolution optical elements. While there have been demonstrations of MOTs working with a single input beam in a pyramidal configuration [214, 215] or employing optical gratings [216, 217] to obtain the necessary reflections, the in-vacuum optics required for such configurations add further experimental complexity and hinder the employment of other addressing or trapping beams. A more diffused approach is to arrange the three pairs of MOT beams such that two of them cross at a shallow angle, allowing to avoid interference with the high-NA optics [121]. This is the configuration that is typically utilized in experimental setups with rectangular glass cells but it is not compatible with other cell geometries, such as the octagonal one employed in our setup, as microscope objectives fully saturate the cell's viewports. Moreover, the anti-reflection coatings of science cells are usually designed to work with small incident angles, and the shallow angles required to avoid the objective lead to unwanted reflections from the glass surfaces. To preserve the typical orthogonal-beams configuration in high-resolution setups it is instead necessary to shine one beam-pair, often the vertical one, through the microscope objective, which introduces several experimental challenges. MOT beams passing through an objective need to be focused in the back focal plane of the objective to ensure collimation inside the science cell. Then, they need to be decoupled from any other light passing through the objective, which can require additional dichroic mirrors and beam splitters [55, 170], or custom-made mounts and small mirrors to be placed in the objective back focal plane [53]. While these are all viable solutions, in most cases they have a negative effect on the performances of the high-resolution setup, e.g. by reducing the overall collection efficiency or introducing optical aberrations.

A different approach in experimental setups having vertically-aligned objectives is to forego the top MOT beam, and take advantage of gravity to balance the push from the bottom beam. This open-top configuration allows to free space for the microscope objective on top of any science cell and eliminates the need for intricate beam arrangements[1] without excessively compromising the loading performance. So far, the five-beam approach had been only demonstrated for erbium and dysprosium atoms, for which 5B MOTs acting on narrow-line intercombination transitions are now employed in different research groups [136, 213, 218]. However, this technique can be extended to other atomic species displaying narrow-line cooling transitions such as other lanthanides and AEAs as ytterbium and strontium.

3.1.1 Five-beam MOT working principle

In typical MOT configurations the net force on the atoms along each direction is balanced by pairs of counter-propagating beams. In a 5B MOT, instead, the force applied by the bottom beam is balanced by gravity alone. Therefore, the acceleration imprinted on the atoms by the bottom beam needs to be strong enough to hold atoms against gravity without pushing them out of the MOT due to an excessive force. The acceleration induced by the scattering force produced by a single vertical beam on an atom in a MOT is [71]:

$$a = \frac{1}{m}\,\hbar k \frac{\Gamma}{2} \frac{s}{1 + s + 4\left(\Delta - kv + 2\pi\mu_B g_J m'_J \frac{\partial B}{\partial z} z\right)^2 / \Gamma^2} \tag{3.1}$$

where m is the atomic mass and Γ is the linewidth of the addressed atomic transition; k, s and Δ are the beam's wavevector, saturation parameter and detuning, respectively. The last term in the denominator of Eq. (3.1) takes into account that the effective detuning depends on the

[1] As long as a single objective is employed.

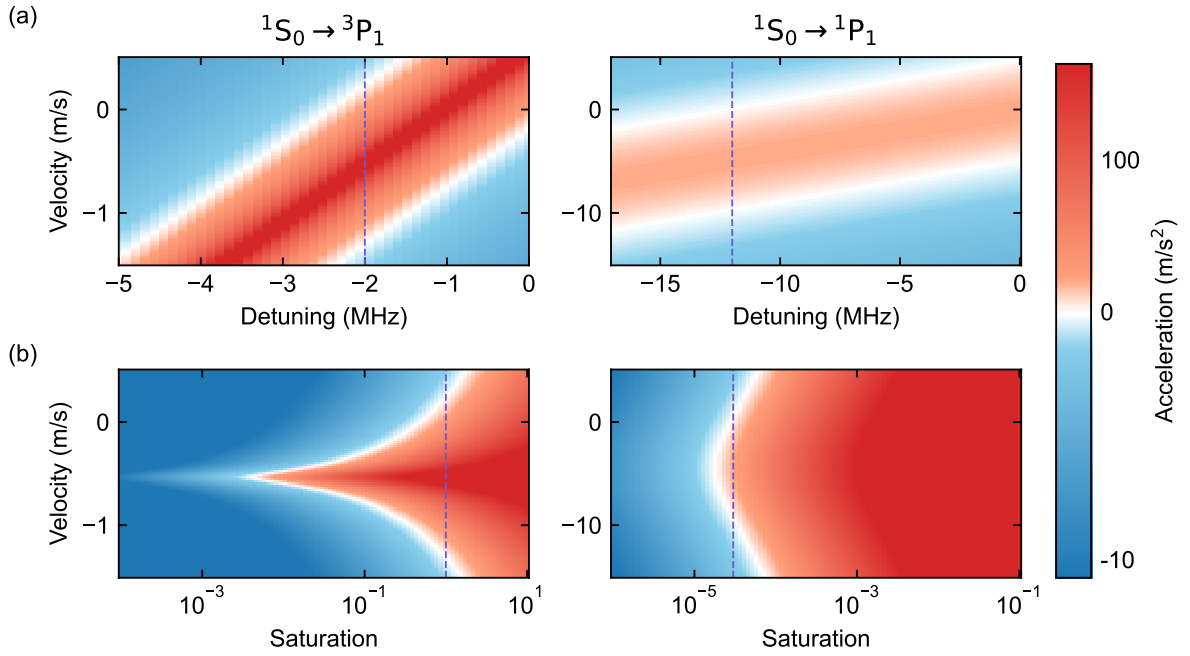

Figure 3.1| Vertical acceleration of an atom under the action of gravity and of a single MOT beam addressing different Yb transitions. (a) Acceleration as a function of beam's detuning and atomic vertical velocity for fixed saturation. (b) Acceleration as a function of beam's saturation and atomic vertical velocity for fixed detuning. Left and right columns correspond to a MOT beam acting on the $^1S_0 \rightarrow {}^3P_1$ and $^1S_0 \rightarrow {}^1P_1$ transition respectively. Violet dashed lines in panel (a)[(b)] correspond to the detuning[saturation] employed in panel (b)[(a)]. The imprinted acceleration is computed with Eq. (3.1) considering a ^{174}Yb atom in the center of the magnetic field gradient and adding the contribution of gravity.

atomic vertical velocity v as well as on the Zeeman shift induced by the vertical magnetic field gradient $\frac{\partial B}{\partial z}$ at the atomic position z.

By choosing the appropriate set of parameters, a can always be tuned to perfectly balance the gravitational acceleration g for a given position and velocity. However, as atoms move, accelerate and decelerate in the MOT, this condition is quickly lost. Therefore, a single beam cannot exactly compensate gravity at each point of the atomic trajectory but it has to balance gravity on average across the whole atomic motion. In particular, the bottom beam needs to hold atoms when they are falling ($v < 0$) without pushing them out of the trap when they are already moving upward. This velocity-selectivity requirement is the fundamental reason behind the employment of narrow-line transitions for MOTs operating in a 5B configuration. This is displayed in Fig. 3.1, where we plot the vertical acceleration of a ^{174}Yb atom fixed in the center of the magnetic field gradient ($z = 0$) under the action of gravity, comparing the effect of a single vertical beam addressing the $^1S_0 \rightarrow {}^3P_1$ and the $^1S_0 \rightarrow {}^1P_1$ transition. For the narrow-line transition, the upward acceleration compensates and overcomes gravity only for a relatively narrow class of velocities, which can be selected by changing the beam's detuning. This allows to address atoms that start to fall without affecting those that have $v \geq 0$ employing realistic experimental parameters of few-MHz detuning and $s \sim 1$, On the other hand, balancing gravity with a beam acting on a broad-line transition presents numerous challenges. First, it requires to work at an extremely low saturation ($s \sim 10^{-5}$), reducing robustness to experimental drifts. Then, the addressed velocity class is so wide that to avoid pushing out atoms with $v \geq 0$ the

detuning has to be increased to address atoms with large negative velocities. To acquire such large velocity in free fall, atoms would need to travel for distances much larger than any realistic MOT size and would therefore be lost before being pushed up by the vertical beam.

As atoms fall, the vertical magnetic field gradient starts to play a role. In particular, the gradient makes the effective detuning, and therefore the addressed velocity class, position-dependent. Indeed, if $z < 0$, the resonant condition is shifted to less-negative velocities [see Eq. (3.1)], resulting in an upward translation along the y-axis in the plots in Fig. 3.1. This leads to an effective restoring force for falling atoms, which are pushed upwards when the combination of their velocity and position matches the resonant condition. Even for low saturation and taking into account a large magnetic field gradient, so that that the bottom beam is largely detuned for all atoms sitting above the quadrupole center, we suspect that a broad-line transition would imprint so much upward acceleration to the atoms with $z < 0$ that they would fly out of the MOT before being decelerated by gravity.

While the narrow-line character of the employed transition is crucial to the functioning of the 5B MOT, the large mass of the lanthanide atoms for which it has been so far demonstrated is a beneficial but not crucial ingredient. In fact, atomic mass is just a numerical coefficient in the imprinted acceleration [see Eq. (3.1)]. While a large mass allows to achieve the necessary acceleration with higher saturation, making the experimental parameters more accessible and robust, by reducing the vertical beam's intensity, e.g. through Neutral Density Filters, the 5B MOT approach can be extended to much lighter atoms displaying narrow-line transitions.

3.1.2 Five beam MOT simulations

The functioning of the 5B MOT relies on a combination of many elements and its optimal working parameters are not trivial to guess a-priori. To investigate the 5B MOT feasibility for ytterbium atoms and guide our experimental efforts we therefore developed a code for Monte Carlo simulation of the three-dimensional atomic trajectories in the MOT. This code has been helpful in determining the experimental parameters for producing our first MOTs, both for the five and six-beam configurations, and it has provided valuable insight into the 5B MOT working principles and properties when analyzing experimental data.

The simulations work as following. An atom is typically initialized with zero velocity at the intersection of the MOT beams corresponding to the center of the quadrupole field, and it evolves under the combined influence of the MOT beams, the magnetic field gradient and gravity. The trajectory is divided into time steps of duration $\tau = 1/\Gamma$, where Γ is the linewidth of the relevant atomic transition, during which an atom can scatter a photon from one of the MOT beams. In particular, at each step we evaluate the scattering probability for each MOT beam as $P_{\mathrm{i}} = \tau\,\Gamma_{\mathrm{sc,i}}$, where $\Gamma_{\mathrm{sc,i}}$ is the scattering rate of beam i and depends on the beam's parameters as well as on the atomic three-dimensional coordinates:

$$\Gamma_{\mathrm{sc,i}}(\vec{x},\vec{v}) = \frac{\Gamma}{2}\frac{s_{\mathrm{i}}(\vec{x})}{1+s_{\mathrm{i}}(\vec{x})+4\left(\Delta_{\mathrm{i}}-\vec{k_{\mathrm{i}}}\cdot\vec{v}+2\pi\mu_B g_J m'_J B(\vec{x})\right)^2/\Gamma^2} \tag{3.2}$$

We assume a textbook electronic structure, as the one of ^{174}Yb, and consider a spinless ground state and an excited state with $J' = 1$. To take into account the opposite circular polarization of counter-propagating MOT beams, we select $m'_J = +1(-1)$ for the forward (backward) propagating beam. We stochastically determine if the scattering event is successful, i.e. if the atom has absorbed and re-emitted a photon for each beam independently, If more than one beam yields a scattering event, we randomly choose one of them with uniform probability. We stress that in this situation a uniform probability distribution is indeed the correct one: weighting the choice of beam on the scattering probability would "doubly" penalize beams with low scattering

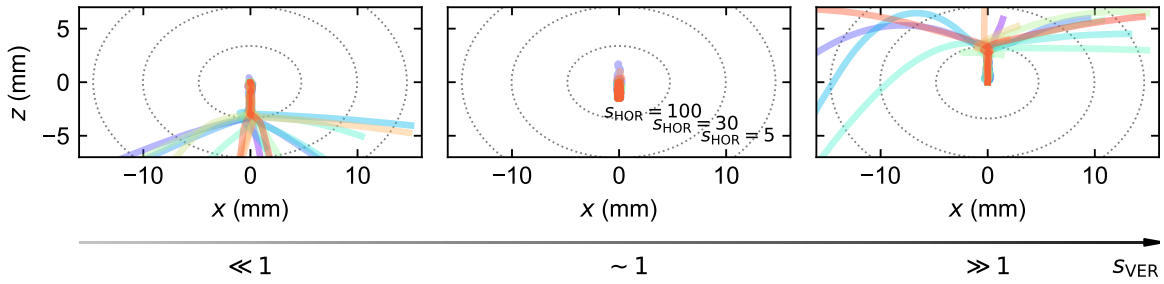

Figure 3.2| Monte Carlo simulation of single-atom trajectories in the five-beam MOT. Atoms are initialized at the intersection of the MOT beams and the dynamics is tracked for 200 ms. The MOT beam waists are 8 mm and 5 mm in the horizontal and vertical directions, respectively. Tuning the vertical beam saturation parameters $s_{\mathrm{VER}} = I_{\mathrm{VER}}/I_{\mathrm{s}}$ we identify a regime where the average radiation pressure balances gravity holding the atoms without pushing them out of the MOT region. Dotted ellipses represent the intensity profile of one of the horizontal beams, described by its saturation parameter s_{HOR}. The elliptical shape results from projecting on the $x - z$ plane of the horizontal beam, which propagates at a 45 deg angle compared to the plane.

probability in an un physical way, since the scattering probability is already taken into account by the first extraction. After determining whether the atom has scattered a photon, and from which beam, we update its velocity taking into account absorption and isotropic spontaneous emission and evolve its coordinates with an equation of motion in free space before proceeding to the next time step. Our choice of τ is such that the maximum scattering probability is 1/2, with a corresponding scattering rate $\Gamma/2$, for a resonant beam with infinite saturation, while it is much lower for realistic MOT beams. This ensures that atoms do not scatter photons in most of the simulation steps, indicating that their duration is short enough to densely sample the atomic trajectory and correctly represent the stochastic nature of photon scattering events.

Simulations results

By varying the relevant parameters and looking at the resulting trajectories we can gain insight on how each of them affects the MOT performance. Not surprisingly, a crucial parameter for the functioning of a 5B MOT is the power of the vertical beam, propagating along the z axis [Fig. 3.2]. For typical few-MHz detuning, when the vertical beam intensity is too low ($s_{\mathrm{VER}} = I_{\mathrm{VER}}/I_{\mathrm{s}} \ll 1$, where $I_{\mathrm{s}} = 0.139\,\mathrm{mW/cm^2}$ is the saturation intensity of the $^1\mathrm{S}_0 \rightarrow {}^3\mathrm{P}_1$ transition) the radiation pressure from the vertical beam is not sufficient to hold atoms against gravity, causing them to fall out of the MOT region. On the other hand, when $s_{\mathrm{VER}} \gg 1$ the MOT is unstable because atoms escape upwards due to an excessive push from the bottom beam. At $s \sim 1$, the average force balances gravity, allowing atoms to remain trapped in the MOT. As mentioned before, this condition is achieved at an intensity around I_{s} thanks to the narrow-linewidth of the employed transition and the large mass of ytterbium. Indeed, lighter atoms would experience a stronger acceleration, thus requiring a weaker intensity to produce a stable MOT.

The radiation pressure of the vertical beam also depends on its detuning from resonance. In the left panel of Fig. 3.3(a) we show the effect of both the vertical beam intensity and detuning on the 5B MOT stability. As figure of merit for the stability, we repeat the simulation many times and consider the fraction of atoms remaining in the MOT region, defined by the MOT

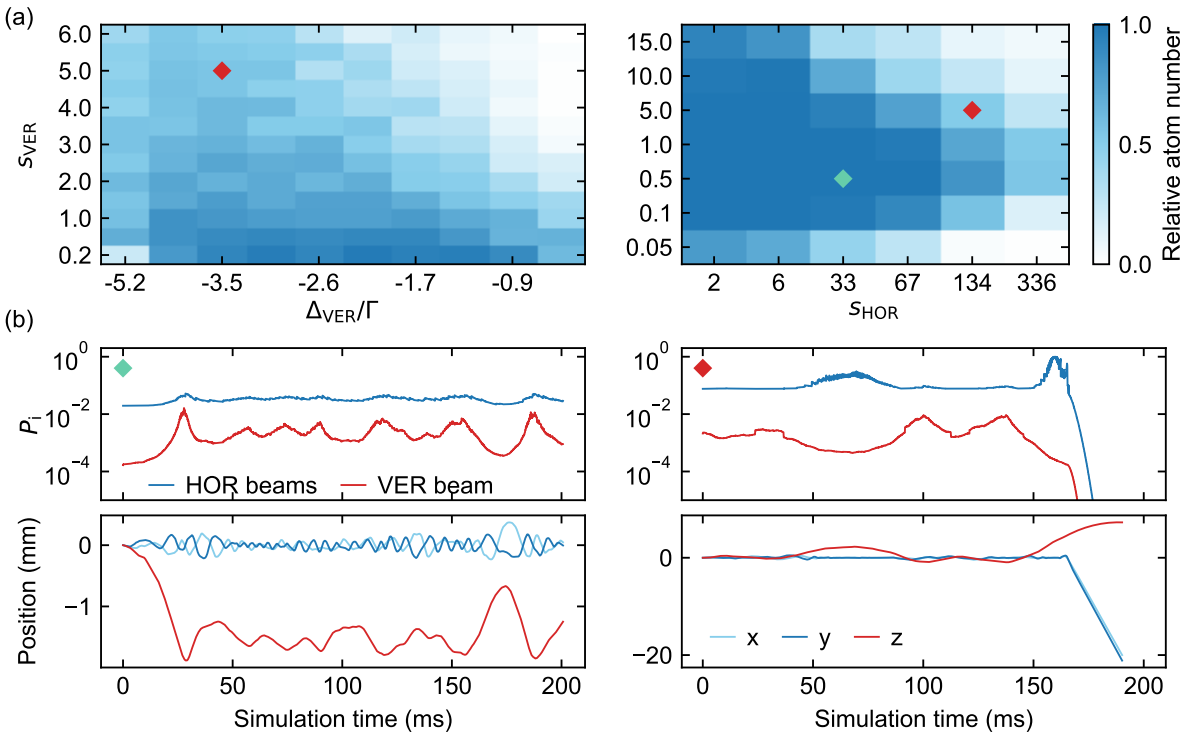

Figure 3.3| Effect of intensity and detuning on the 5B MOT stability. (a) Fraction of atoms trapped in the MOT as a function of vertical beam intensity and detuning (left) and vertical and horizontal beams intensities (right). Atoms are initialized at the intersection of the MOT beams with zero velocity and then evolve under the action of the MOT beams and gravity. An atom is considered trapped if it is retained in the MOT region after 200 ms of time evolution. Each point is obtained from 100 individual trajectories. The green and red diamonds indicate representative points of the 5B MOT operation, corresponding to high and low stability respectively. (b) Illustrative scattering probability (top) and associated atomic trajectory (bottom) as a function of time for the two scenarios marked by diamonds in panel (a). Blue (red) curves represent the photon scattering probability from any of the horizontal beams (the vertical beam). In the high-stability region (green diamond), the atom experiences repeated bounces in the vertical direction caused by sudden variations in the vertical beam scattering probability. For the second condition (red diamond), corresponding to lower stability, the atom is pushed upward by the vertical beam and eventually escapes horizontally.

beams' size, after a 200 ms time evolution. We observe the expected correlation between the bottom beam intensity and detuning, as larger intensities require larger detunings to produce the radiation pressure necessary to hold the atoms [Fig. 3.3(a), left panel]. More surprisingly, we find a correlation between the intensities of the vertical and horizontal beams [Fig. 3.3(a), right panel], which we naively expected to be completely independent. This arises from the interplay of different mechanisms. For low s_{VER}, a too-large intensity of the horizontal beams leads to an excessive imbalance in the scattering probability between the vertical and horizontal directions and atoms fall as they scatter essentially only from the horizontal beams which saturate the transition. For $s_{\mathrm{VER}} \leq 1$ instead, we observe that an overall increase of the intensities leads to a larger number of captured atoms. The behavior reverses for larger s_{VER} values, where lower horizontal intensities are again more favorable.

To gain insight on the reasons behind this we look at individual atomic trajectories, such

as the one displayed in the right panel of Fig. 3.3(b). When the vertical intensity is too high, atoms have a higher probability of escaping as they are pushed upward, and reach a region above magnetic quadrupole center, where horizontal confinement is less robust. Lowering s_{HOR} in this case is beneficial, as it reduces the horizontal scattering rate, giving the atom more time to fall back in a stable region of the MOT before scattering from the horizontal beams.

Individual trajectories offer also valuable insight on the stable region of the 5B MOT. In this case [Fig. 3.3(b), left panel] the scattering probability of the vertical beam is much lower than the one of the horizontal beams and atoms do not scatter many photons from the bottom beam until the resonant condition is matched. This is marked by a peak in the scattering probability and a sudden inversion of motion along the vertical direction. The resulting trajectory displays a peculiar shape in the vertical direction, characterized by a series of free falls and bounces which keep the atoms inside the MOT region. Interestingly, the equilibrium z position does not correspond to the center of the quadrupole field, but rather to the position where the resonant condition is matched. This can be tuned by varying the magnetic field gradient as well as the vertical beam parameters which can effectively shift the atom cloud along the vertical direction, albeit with possible changes in the MOT stability. We note that the period of the vertical bounces is much shorter than the one of horizontal oscillations. This happens because the elastic restoring force in a MOT is proportional to the saturation parameter s, which is much lower for the vertical beam.

All the simulations in Fig. 3.3 are performed with the following parameters (when not indicated in the plot):

$\partial B/\partial z$	HOR beams diameter	s_{HOR}	$\Delta_{\mathrm{HOR}}/\Gamma$	VER beam diameter	$\Delta_{\mathrm{VER}}/\Gamma$
9 G/cm	16.5 mm	134	-4.8	10 mm	-3.5

3.2 Capturing atoms in the five-beam MOT

Incoming atoms can be captured in a MOT only if they enter the MOT region with a velocity that is smaller than the capture velocity v_{c}. As $v_{\mathrm{c}} \propto \sqrt{\Gamma}$, this parameter is particularly relevant for loading narrow-line MOTs, which have capture velocities of the order of few-m/s. Even though such low velocities can be obtained through a Zeeman slower (ZS), in modern experiment this is rarely the preferred solution. In fact, to avoid excessive falling and spreading of slowed atoms, the end of the ZS should be as close as possible to the MOT region, adding experimental complexity and precluding this option for setup employing glass cells. Alternative approaches include first capturing atoms in a broad-line MOT before loading the narrow-line MOT [219], combining the two colors in a core-shell configuration [220] or loading from a 2D-MOT with a push beam [75].

In our setup, we adopt a recently developed scheme based on further slowing of the atomic beam exiting the ZS with a pair of crossed beams acting on the broad $^1\mathrm{S}_0 \rightarrow {}^1\mathrm{P}_1$ transition. This approach allows to decelerate atoms from few-tens to few-m/s in a short space right before the MOT and it has been employed to load narrow-line MOTs of ytterbium [170, 196], erbium [221] and dysprosium [195] atoms. In particular, with the crossed beams (CB) described in Sec. 2.1.5 we reduce the speed of the atoms exiting our atomic beam source from $\sim 40\,\mathrm{m/s}$ to values below the narrow-line MOT capture velocity $v_{\mathrm{c}} \sim 8\,\mathrm{m/s}$. We stress to retain the advantages of the 5B MOT configuration it is necessary to employing either a CB slowing or a push beam as a broad-line MOT is incompatible with the 5B geometry.

In a 5B MOT the primary role of the vertical beam is to counteract gravity, while the horizontal beams must slow and capture the incoming atoms. Consequently, a 5B MOT greatly

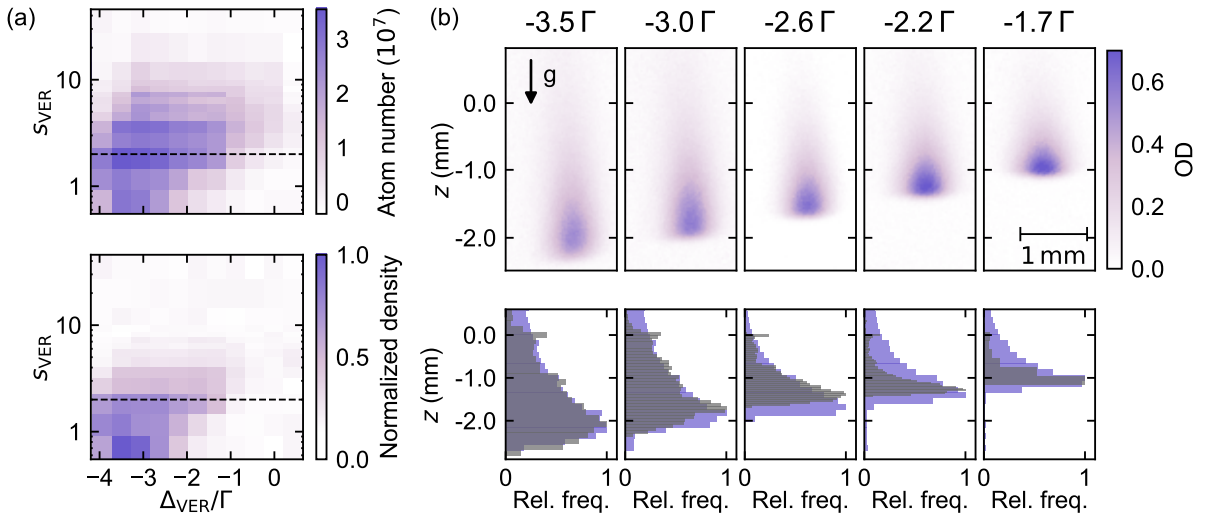

Figure 3.4| Dependence of the five-beam MOT loading on the vertical beam parameters. (a) Atom number captured by a ^{171}Yb 5B MOT (top) and normalized atom peak density (bottom) after 2 s loading time as a function of the saturation parameter and detuning of the vertical beam. The magnetic field gradient is set to 5 G/cm, while the horizontal beams have a detuning of $\Delta_{HOR} = -3.4\,\Gamma$ and a saturation of $s_{HOR} = 60$ for each beam. (b) Top: in situ absorption images of the ^{171}Yb 5B MOT for different detuning after 1 s of loading. The vertical beam intensity is fixed at $s_{VER} = 2$, corresponding to the dashed horizontal line in panel (a). The black arrow indicates the direction of gravity. Bottom: histograms of the experimental optical density (purple) and of simulated trajectories (grey) sampled on the z axis. Experimental histograms are obtained by integrating the optical density along the horizontal direction. Each simulated histogram is the result of 20 independent trajectories. The zero of the z axis in experimental images is set to optimally align them with simulations

benefits from an unconstrained control on the horizontal and vertical beam intensities and detuning. In light of this, we designed our 556 nm laser system with two separate MOT AOMs[2]: one for the horizontal beam-pair and one for the single vertical beam. As in simulations, also real experiments require a fine tuning of the vertical beam parameters for the realization of a stable 5B MOT. In the top panel of Fig. 3.4(a) we show the dependence of the atom number captured in a ^{171}Yb 5B MOT after 2 s of loading as a function of the vertical beam intensity and detuning. While we do not observe the expected intensity-detuning correlation evident from the simulations [see Fig. 3.3(a)], we confirm that in an ytterbium 5B MOT the vertical beam needs to be tuned at a few-MHz detuning and have an intensity of the order of the saturation intensity. We find that our optimal parameters are consistent with the simulated ones, and we ascribe their small difference to the nuclear-spin structure of ^{171}Yb, which is not accounted for in the simulations, and to changes in fiber coupling efficiency when changing the AOM driving frequency. Notably, the atom number and peak density [Fig. 3.4(a), bottom] do not reach their maxima for the same conditions, since variations in the vertical beam parameters also affect the shape of the atomic cloud.

We show the dependence of the MOT shape after 1 s of loading on the vertical beam detuning in Fig. 3.4(b). At fixed intensity, when the detuning is increased, the cloud shifts downwards to a position where the radiation pressure from the upward beam balances gravity. At the same time, the cloud develops into a drop-like shape, maintaining a roughly constant atom number

[2]G&H 3080-125

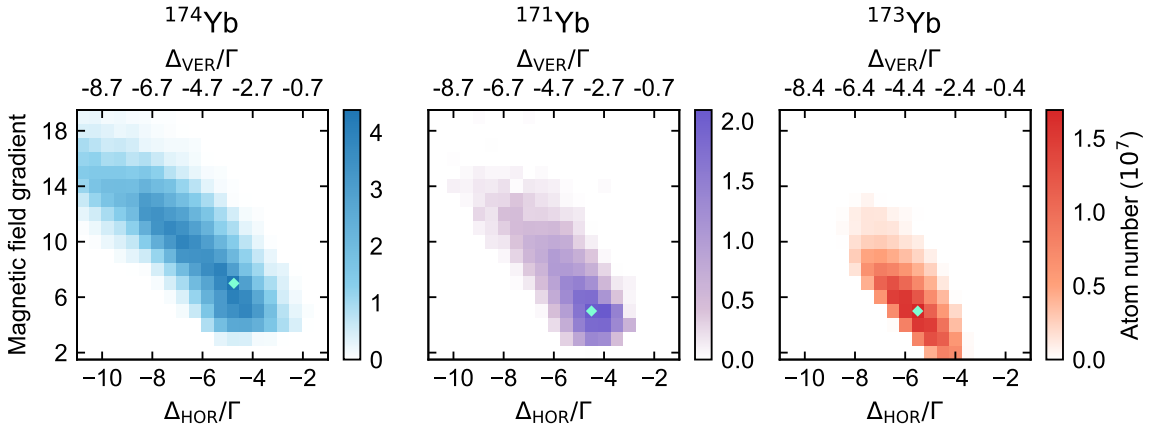

Figure 3.5| MOT dependence on detuning and gradient for different isotopes. Trapped atom number as a function of the horizontal and vertical beams detuning and vertical component of the magnetic field gradient for ^{174}Yb (left), ^{171}Yb (center) and ^{173}Yb (right). The difference between vertical and horizontal detuning is kept constant across different measurements and the loading time is 2 s. The green diamonds indicate the typical working parameters for the different isotopes. The intensities of the each horizontal beam and the vertical one are 180 I_s and 3 I_s for ^{174}Yb, 60 I_s and 4 I_s for ^{171}Yb and 180 I_s and 6 I_s for ^{173}Yb.

but slightly reducing its peak density. We note that this behavior seems to be different for 2 s of loading, where the peak density depends very weakly on the detuning, possibly because the longer loading time leads to a saturation of the atom number in the denser region of the MOT [see Fig. 3.6(a) for the MOT loading rates]. The change in MOT shape with detuning is confirmed in our Monte Carlo simulations. In the bottom panel of Fig. 3.4(b) we compare the horizontally-integrated experimental atomic densities with simulated distributions, obtained by binning the vertical positions across 20 independent atomic trajectories for each detuning. We can assume that each atom samples all accessible states in a single trajectory as the atomic motion proceeds on timescales on the order of $h/E_{\mathrm{rec}} = 270\,\mu$s (where E_{rec} is the atomic recoil energy from a 556 nm photon), much shorter than the total simulation time of 200 ms. We thus compare the position across an entire simulated trajectory of a single atom with an experimental image of the MOT cloud observed at a specific time. The simulations match the experimental data and reproduce both the vertical shift of the atomic cloud position and the asymmetric density profile broadening as a function of the vertical beam detuning.

While the vertical beam intensity needs to be low to sustain atoms without pushing them upwards too much, the horizontal beams need to work at high saturation and detuning to slow and capture and the incoming atoms. In Fig. 3.5 we show the number of captured atoms for fixed intensity, varying the magnetic field gradient and the overall detuning of the MOT beams. For these plots, we keep the frequency shift between the horizontal and vertical beams constant and vary the detuning of the MOT beams by changing the overall laser frequency with a double-pass AOM in the ULE lock path [see Sec. 2.2.1]. We find that the 5B configuration allows to efficiently load MOTs of the most relevant ytterbium isotopes (^{174}Yb, ^{171}Yb, ^{173}Yb) and that the optimal working parameters and overall dependence on frequency and magnetic gradient are very similar across different isotopes. However, we observe that the fermionic isotopes, in particular ^{173}Yb, display a reduced robustness to parameter changes, which we attribute to the hyperfine and nuclear sub-structure of the $^1S_0 \rightarrow {}^3P_1$ transition. In particular, the probability of scattering photons on the stretched $|F, m_F = \pm F\rangle \rightarrow |F' = F+1, m'_F = \pm F'\rangle$ transitions, which are the most advantageous for atom slowing and capture, is reduced with respect to the

	6B (^{174}Yb)	**5B (^{174}Yb)**	**5B (^{171}Yb)**	**5B (^{173}Yb)**
τ_L (s)	14(1)	2.6(2)	2.60(7)	5.0(3)
N_s (10^8)	11.9(7)	0.81(2)	0.433(3)	0.40(1)
R (10^8 s^{-1})	0.84(5)	0.32(1)	0.166(1)	0.080(2)

Table 3.1| MOT loading rate parameters. Mean loading time τ_L, stationary atom number N_s and loading rate R, obtained from exponential fits of $N(t)$ for different isotopes and beam configurations. The temperature of the atomic source oven was kept constant at 380 °C across all measurements.

case of ^{174}Yb ($I = 0$). Moreover, the presence of nearly-degenerate $\sigma^{\pm}$-transitions, as those connecting $|m_F = \pm 1/2\rangle$ to $|m'_F \mp 1/2\rangle$ states leads to position-dependent competing optical forces, including anti-restoring forces that push atoms out of the trap [222, 223]. This effect is especially pronounced in ^{173}Yb, where the large nuclear spin results in a more complex hyperfine structure and a denser manifold of near-degenerate $\Delta m_F = \pm 1$ transitions with respect to ^{171}Yb. The issue is well-known in narrow-line MOTs of ^{87}Sr, where the combination of an even larger nuclear spin ($I = 9/2$) and a narrower line ($\Gamma/2\pi = 7.5$ kHz) compared to ytterbium, often requires to employ a so-called stirring beam to minimize its negative impact.

3.2.1 Five-beam MOT loading and stability

We compare the loading curves of 5B MOTs for different isotopes and that of a ^{174}Yb 6B MOT in Fig. 3.6(a). We fit the loaded atom number with the exponential function

$$N(t) = N_{\mathrm{s}} \left(1 - e^{-t/\tau_{\mathrm{L}}}\right) \tag{3.3}$$

where N_{s} is the steady state atom number and τ_{L} is the loading time constant. The loading efficiency can be described by a loading rate $R = N_{\mathrm{s}}/\tau_{\mathrm{L}}$. We report the values of R, N_{s} and τ_{L} for the 5B MOTs of different isotopes and the 6B MOT of ^{174}Yb in Table 3.1. Comparing the different isotopes, we find that the 5B MOTs of ^{171}Yb and ^{173}Yb reach a lower steady state number compared to ^{174}Yb, with ratios that are consistent with their isotopic abundances. While the two fermionic isotopes have roughly the same N_{s}, the loading time of ^{173}Yb is almost twice the one of ^{171}Yb, with consequently halved loading rate. We ascribe this to inefficiencies in the 399 nm slowing of the large-spin isotope, which lead to a reduced flux of slowed atoms towards the MOT. In particular, the $^1\mathrm{S}_0 \rightarrow {}^1\mathrm{P}_1$ transition of ^{173}Yb displays a small hyperfine shift of approximately 70 MHz between the $F' = 3/2$ and $F' = 7/2$ states. This complicates efficient 2D MOT operation and CB slowing which operate on the red-detuned side of the $^1\mathrm{S}_0\,|F = 5/2\rangle \rightarrow {}^1\mathrm{P}_1|F' = 7/2\rangle$ transition.

For all isotopes, we find that the 5B MOT saturates faster and at a lower steady state value compared to the 6B case, suggesting a reduced stability of this configuration. We ascribe the reduced performance of the 5B MOT to an intrinsic residual loss mechanism, associated with the presence of an escape channel for atoms along the vertical direction. Specifically, fluctuations in the upward scattering force lead to atoms exiting the trapping region vertically and being lost. This effect should be even more pronounced for ^{173}Yb, where transitions associated with each nuclear-spin state of the ground-state manifold feature widely different line strengths, which could explain the slight reduction in N_{s} compared to ^{171}Yb, despite the slightly larger isotopic abundance. The reduced stability of the 5B MOT compared to the 6B geometry is confirmed by the lifetime measurement presented in Fig. 3.6(c). In particular, we find a lifetime of 186(4) s and 54(1) s for the ^{174}Yb 6B and 5B MOT, respectively. While we expect the 6B lifetime to

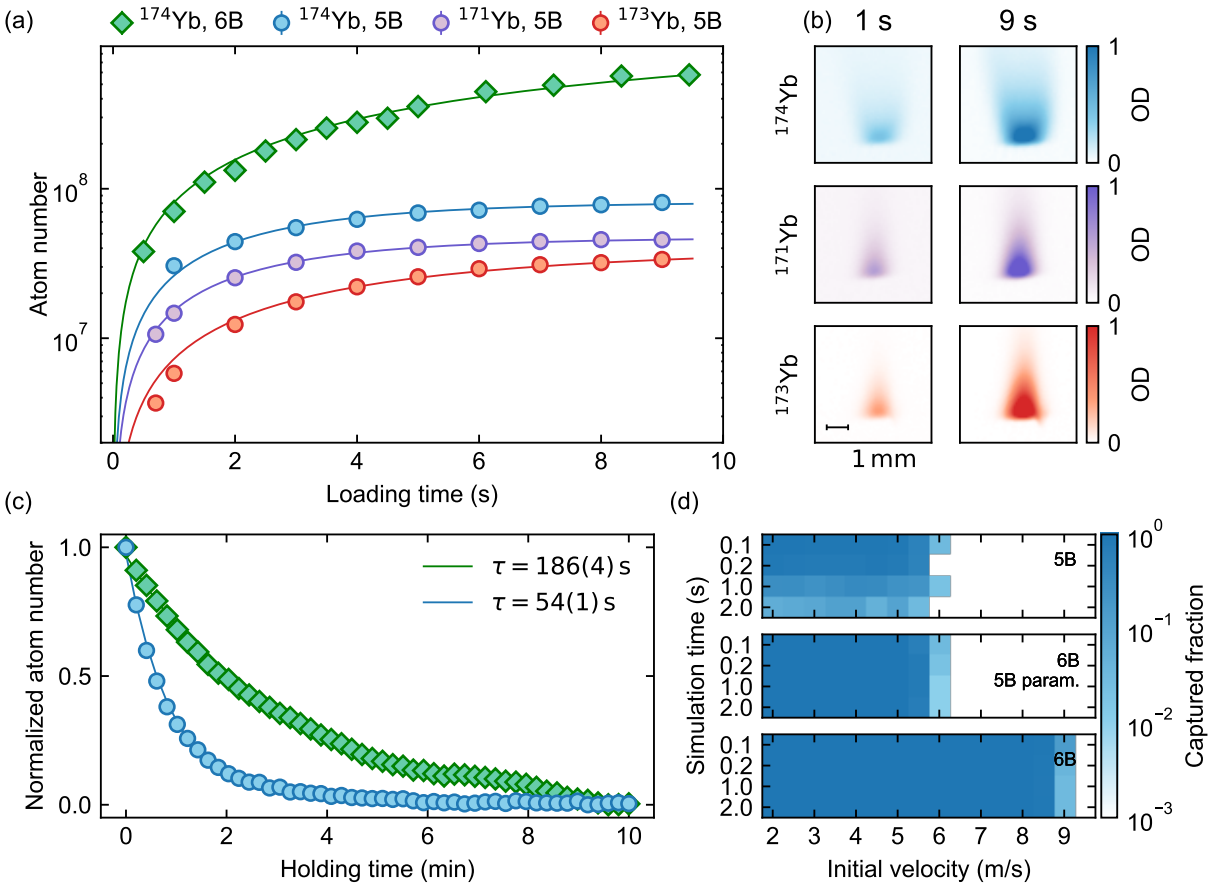

Figure 3.6| MOT loading and stability. (a) Trapped atom number as a function of loading time for different isotopes and beam geometries. Solid lines are exponential fits to the data. (b) Absorption images of 5B MOTs for different isotopes and loading times. (c) Relative MOT atom number as a function of holding time for a 6B (green diamonds) and 5B (blue circles) MOT of ^{174}Yb. Solid lines are exponential fits. (d) Monte Carlo simulations of the capture and stability of a 5B MOT (top), a 6B MOT operating with the 5B MOT parameters (middle) and a 6B MOT operating with optimal parameters (bottom). For each situation, we simulate the capture process for 100 independent atoms entering the MOT region with variable initial velocity. We estimate the captured fraction from the number of atoms remaining in the MOT region after a variable simulation time.

be dominated by vacuum background collisions, the much shorter lifetime of the 5B MOT is another marker of its intrinsic instability.

To investigate the difference in loading and stability between the two MOT geometries we take advantage of our Monte Carlo simulations and simulate the capture and holding of atoms in the MOT. We initialize atoms entering the MOT region with different longitudinal velocities, as they would after the CB slowing, and we determine the number of trapped atoms after a variable simulation time. In Fig. 3.6(d) we compare three different scenarios: a 5B MOT with optimal parameters (top panel), a 6B MOT with the same parameters as the 5B MOT (middle panel) and a 6B MOT with optimized parameters (bottom panel). We find that the 5B MOT has a capture velocity of around 5.5 m/s, however captured atoms are progressively lost as they have a probability of escaping the trap, mainly due to rare events where they scatter too many photons from the bottom beam and are pushed out from the MOT. We note that the decay of

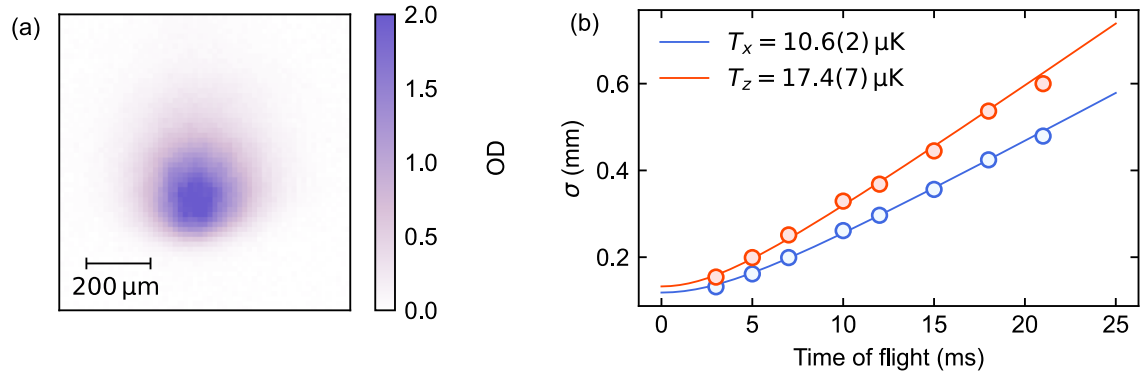

Figure 3.7| Compressed MOT. (a) In-situ absorption image of a ^{171}Yb cMOT after 700 ms of loading. (b) Temperature measurement through time of flight (TOF) expansion. We plot the fitted Gaussian size of the cMOT along the horizontal (blue) and vertical (red) directions as a function of the TOF duration. Solid lines are fits with a ballistic expansion.

the trapped number over time is caused by the nature of our simulations, which do not include the continuous loading of new atoms. We also remark that our simulations account only for losses arising from atomic motion out of the trap and do not consider e.g. background gas collisions or density-induced losses, which should not depend on the MOT geometry. For the 6B geometry, in fact, we do not see any decay of the trapped atom number over time, as the scattering force is well-balanced in every direction. We observe that the 6B MOT operating with the 5B parameters has the same capture velocity of the 5B, while the 6B operating with optimal parameters has a larger capture velocity of almost 9 m/s. In the 5B case, the reduced vertical beam's intensity leads to preferential scattering from the horizontal beams and when the horizontal intensity is too high, this imbalance causes atoms to fall out of the trap [see Fig. 3.3]. Therefore, to improve stability the horizontal beams' intensity must be reduced compared to the 6B case, resulting in a lower capture velocity. Despite the reduced capture velocity and the shorter lifetime, the 5B MOT remains effective in rapidly capturing a sufficient number of atoms for ytterbium isotopes discussed in this work.

3.2.2 MOT compression

After loading, the MOT needs to be compressed to achieve the phase-space density required to load atoms into optical traps. To this end, we first interrupt the atomic flux in the glass cell by switching off the 2D MOT beams. We also extinguish the CB while we can keep the ZS on for the whole experimental cycle to our beam source geometry. To compress the MOT we then progressively reduce the beams' power and detuning while increasing the magnetic field gradient.

This is done in two stages. In the pre-compression stage (pre-cMOT) the detuning of all the MOT beams is reduced simultaneously acting on an AOM in the 556 nm laser lock path and the magnetic field gradient is increased from $\simeq 5$ G/cm to $\simeq 15$ G/cm. During the final compression (cMOT), instead, we tune the frequency of the horizontal and vertical beams independently and increase the gradient to the final value of $\simeq 30$ G/cm. The overall compression typically lasts around 150-250 ms, divided roughly equally between the two stages. The main difference between a 6B and 5B compression lies in the vertical beam adjustment: since its power is already low during the loading stage, only a minimal reduction is required during compression. Similarly, its frequency is moved towards resonance only in the pre-cMOT as the vertical beam is $\simeq 1.5$ MHz closer to resonance than the horizontal beams already during loading. For our final cMOTs

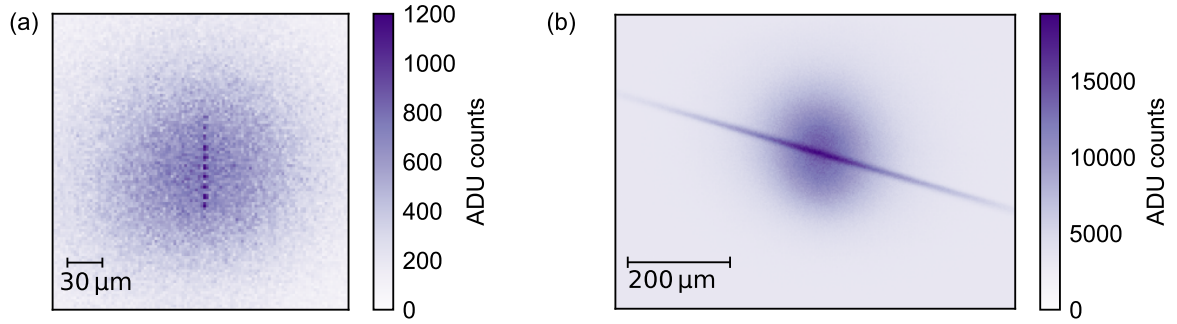

Figure 3.8| Direct loading of optical traps from the cMOT. (a) Fluorescence image of a 10-tweezer array overlapped with the cMOT. The image is obtained by driving the $^1S_0 \rightarrow {}^1P_1$ transition with an extremely low power for 100 ms. (b) Fluorescence image of the ODT and the cMOT. The image is obtained with an extremely short (1 µs) flash imaging pulse.

we typically employ detunings of $\Delta_{\mathrm{HOR,\,VER}} \simeq -2.5\,\Gamma$ with saturation parameters $s_{\mathrm{HOR}} \simeq 2$ and $s_{\mathrm{VER}} \simeq 0.2$. After this compression, we achieve typical temperatures of $\sim 20\,\mu\mathrm{K}$ for all ytterbium isotopes studied in this work and, for 2 s of loading, densities as high as $\sim 10^{11}\,\mathrm{cm}^{-3}$. We find that such high-densities are not needed to load a tweezer array as we reach an array filling fraction limited by light-assisted collisions (LACs) and independent on the MOT loading time for loadings as short as 100 ms.

From the cMOT we can also load atoms into a 759 nm optical dipole trap, as we will discuss more in detail in the next section. While the filling fraction in a tweezer array is dominated by the efficiency of the LACs, the number of trapped atoms in the ODT is very sensitive to the cMOT properties. When optimizing the cMOT for loading in the ODT we therefore find a different optimum compared to the one obtained for loading the tweezers. In particular, the ODT loading strongly benefits from trapping a larger number of atoms and reaching lower temperatures, albeit in a larger volume. We therefore maintain a smaller magnetic field gradient of 10 G/cm during the whole compression stage and reduce the MOT beams detuning to $\Delta_{\mathrm{HOR,\,VER}} \simeq -0.9\Gamma$. In order to allow for such a small detuning we also strongly reduce the beams intensity to $s_{\mathrm{HOR,VER}} \simeq 0.1$. We find that for these parameters we do not need to differentiate between the horizontal and vertical MOT beams. We show an exemplary absorption image of a ^{171}Yb cMOT obtained with these parameters after 700 ms of MOT loading in Fig. 3.7(a). Notably, during compression we lose only $\sim 25\%$ of the initially captured atoms, ending up with $\sim 1.8\times10^6$ atoms from $\sim 2.5 \times 10^6$ atoms in the MOT. We extract the cMOT temperature by fitting its ballistic expansion in time of flight, finding temperatures of $\simeq 10\,\mu\mathrm{K}$ when fitting the horizontal expansion direction [Fig. 3.7(b)]. We obtain slightly higher temperatures for the vertical expansion, likely due to a reduced cooling efficiency along that direction caused by the lack of the top beam.

3.3 Loading of optical traps

When loading atoms into an optical trap, the typical rule of thumb is that atoms that have an energy $\sim 1/10$ of the trap depth are successfully trapped. More quantitatively, we can see the meaning of this rule with Eq. (1.47). By setting $\eta = U_0/k_BT = 10$ we find a survival probability of 99.7%, indicating that an atom confined in a potential that is 10 times deeper than its energy is almost certain to remain trapped. Interestingly, we find a 87% confinement probability already for $\eta = 5$, suggesting that the factor 10 is typically a conservative estimate.

Owing to the narrow-line character of the $^1S_0 \rightarrow {}^3P_1$ transition, we achieve cMOT temperatures in the 10-20 µK range and we can directly load atoms into optical traps of moderate depth.

To load both our tweezer array and our ODT, we ramp up the traps after or during the compression, making sure that they are spatially overlapped with the cMOT, and hold them for a variable time, until enough atoms have been captured. After extinguishing the MOT beams and magnetic field gradient, we are left with our trapped atoms and can go on with the experimental sequence. In Fig. 3.8 we show fluorescence images of the cMOT overlapped with a tweezer array and with the ODT.

3.3.1 Preparation of single-atom arrays

We show a typical sequence for loading a tweezer array in Fig. 3.9. The figure refers to the case of ^{171}Yb but the conceptual stages of the sequence and most of the reported values are valid also for ^{174}Yb and ^{173}Yb, with the most notable difference being the parameters of LACs stage.

We load our 1D tweezer arrays by turning on the traps during the pre-cMOT stage, with a typical trap depth $U_0 \simeq 570\,\mu$K. We do not find any significant improvement in the obtained single-atom filling fraction when delaying the trap ramps to the final cMOT stage. On the other hand, we see that finely tuning the cMOT position after compression along all three directions with the bias coils helps to improve the spatial overlap with the array and therefore the tweezer loading probability. This movement typically lasts $\sim 50\,$ms, which is sufficiently slow to avoid heating of the cMOT due to sudden displacements and provides ample time for the atoms to be captured in the tweezers.

After extinguishing the MOT beams and the magnetic field gradient, we are left with an array of traps, each containing a stochastic number of particles. The number of trapped atoms is set by two competing processes: the loading from the cMOT, and the two-body losses caused by red-detuned LACs [134, 224, 225]. Notably, directly after the MOT we never find empty tweezers, indicating that the rate of loading from the MOT is larger than the two-body loss rate. To reach single-atom occupancy we actively drive LACs collisions with the MOT beams until we see that the photon count histograms show a clear single-atom signal, without tails at higher counts. For the LACs stage we employ significantly different parameters for ^{171}Yb compared to ^{173}Yb and ^{174}Yb.

For ^{174}Yb and ^{173}Yb we drive red-detuned LACs, leading to pairwise losses and a corresponding $\sim 50\,\%$ filling fraction [Fig. 3.10(a, b)]. For both isotopes we typically perform LACs at a large trap depth $U_0 \simeq 2\,$mK. While this is not strictly necessary, we have found this to be a good working point during our first optimization. In fact larger trap depths result in a generally lower loss probability, consistent with the picture that atoms are lost when the kinetic energy acquired during a light-assisted collision is larger than the trap depth. Working with deep traps results in lower loss probability, favoring multiple occupancy rather than empty sites when the LACs parameters are not optimized. This can be helpful to have a good signal if e.g. the parameters need to be optimized after a drift or to find the first single-atom signal. For ^{174}Yb, we typically drive the $^1\mathrm{S}_0 \rightarrow {}^3\mathrm{P}_1$ transition very weakly ($s_{\mathrm{HOR,\,VER}} \simeq 0.6$), with small detunings ($\Delta_{\mathrm{HOR,\,VER}} \sim -\Gamma$) with respect to the unshifted $^1\mathrm{S}_0 \rightarrow {}^3\mathrm{P}_1|J' = 1, m'_J = 0\rangle$ resonance. For ^{173}Yb, instead we employ a small blue detuning ($\Delta_{\mathrm{HOR,\,VER}} \sim +\Gamma$) from the free-space transition, which however corresponds to a significant red-detuning due to the large differential light shift. We find that for ^{173}Yb the filling fraction is maximized by high-intensity LACs pulses with ($s_{\mathrm{HOR,\,VER}} \simeq 180$), achieving an almost 60% filling. For both isotopes, we keep a small 0.2 G magnetic field aligned with the tweezers polarization direction.

On the other hand, we achieve a much larger filling fraction for ^{171}Yb, taking advantage of the near-deterministic loading scheme demonstrated in Ref. [53]. In particular, we reach a 87% single-atom filling fraction through a combination of grey-molasses cooling and LACs in blue-detuned molecular potentials [Fig. 3.10(c)]. As discussed in detail in Sec. 5.2.1, the near-deterministic scheme is realized by splitting the $|m'_F\rangle$ states of the ${}^3\mathrm{P}_1|F' = 3/2\rangle$ manifold

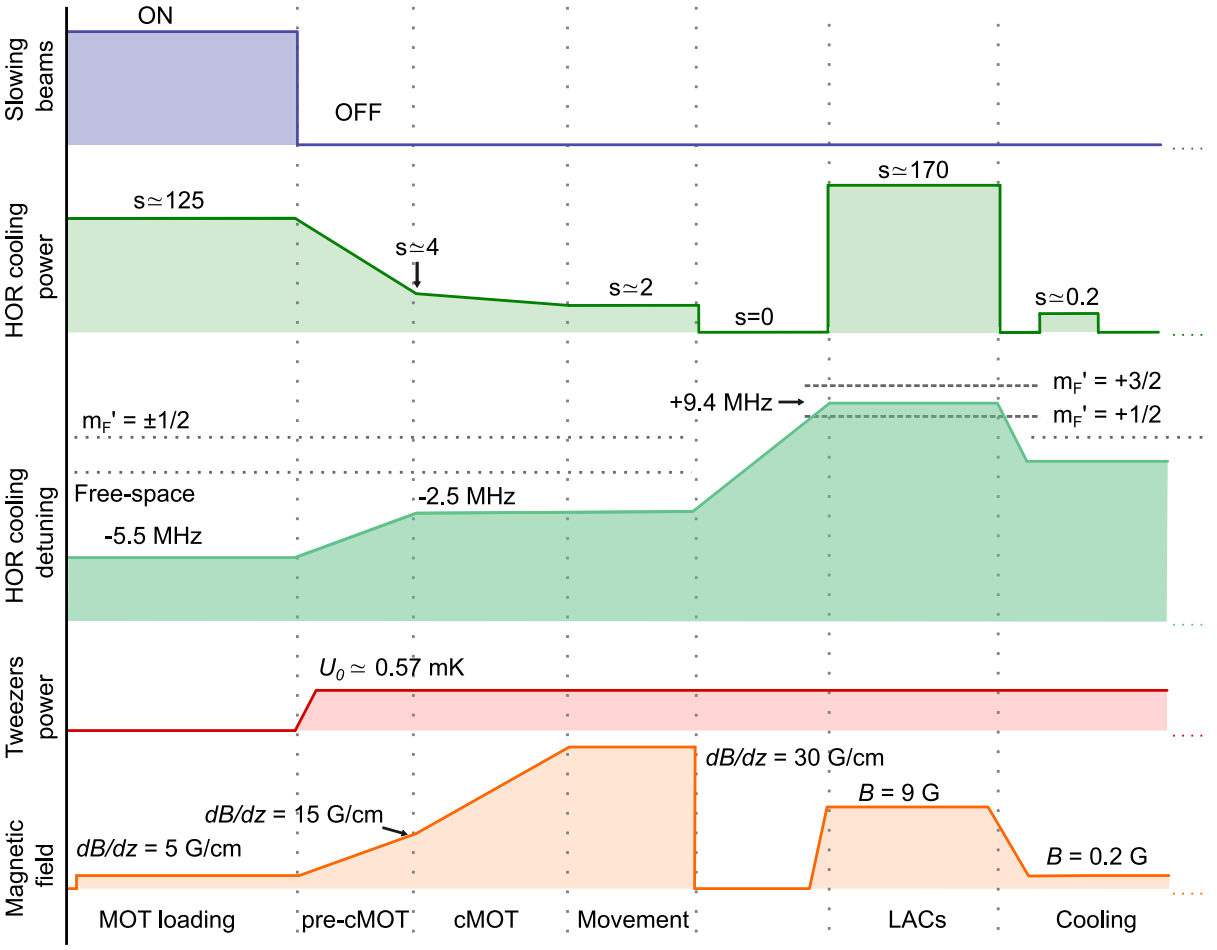

Figure 3.9| Scheme of the experimental sequence for preparing an optical tweezer arrays of single ^{171}Yb atoms. After the MOT loading stage ($\sim$ 100 ms) the MOT is compressed in $\sim$ 150 ms while simultaneously ramping up the tweezers power. After compression, the position of the cMOT is shifted to optimize the overlap with the tweezer array before extinguishing the MOT. We achieve single-atom occupancy in tweezers by driving LACs with the MOT beams and we perform a stage of Doppler cooling to further reduce the temperature of trapped atoms. The dotted horizontal lines in the cooling detuning correspond to the free-space and light shifted $^1S_0 \rightarrow {}^3P_1$ transition resonances, while the two dashed lines in correspondence of the LACs stage also include the Zeeman splitting. Axes are not to scale. Note: the LACs stage of ^{174}Yb and ^{173}Yb displays very different parameters [see text].

with a combination of differential light shifts and magnetic fields. To this end, we employ a 9 G magnetic field aligned with the tweezers polarization direction and drive LACs for around 80 ms with a high intensity ($s_{\mathrm{HOR}} \simeq 170\, I_{\mathrm{sat}}$) pulse at a detuning $\Delta_{\mathrm{HOR,\,VER}} \simeq +9.4$ MHz from the $^1S_0 \rightarrow {}^3P_1$ free-space resonance. While grey-molasses cooling prevents losses due to blue-detuned light during the LACs, we find that we can further reduce the atomic temperature after the LACs with a 20 ms Doppler cooling pulse. After this pulse, we are left with an array of single atoms at $\simeq$ 15 µK and we can proceed with our experiments.

3.3.2 Loading the ODT

Our goal for the near future is to prepare a degenerate fermionic sample trapped in a single optical tweezer. To this end, we need to start with as many trapped atoms as possible. However,

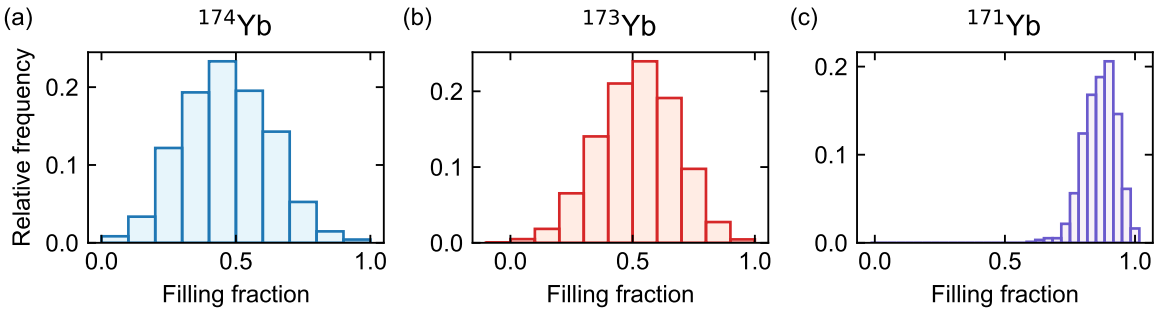

Figure 3.10| Tweezer-array filling fraction for different ytterbium isotopes. (a, b) Single-atom occupancy is obtained by driving red-detuned light-assisted-collisions for ^{174}Yb and ^{173}Yb, achieving a single-atom filling faction of 51% and 58% respectively. (c) The enhanced loading scheme based on blue-detuned light-assisted-collisions available for ^{171}Yb allows to reach a 87% filling fraction. Data in (a, b) are obtained for a 10-sites tweezer array while we employ a 30-sites array for (c). Each histogram is the result of thousands of experimental realizations.

the number of atoms that can be loaded into a tweezer directly from the MOT is limited by the competition between the loading rate and the LACs induced by the cooling light. We find that we can capture up to $\sim 100-200$ atoms in a single tweezer. This however requires careful optimization of the cMOT and tweezer parameters, including the waist of the tweezer which we can increase by inserting an aperture before the tube lens. In particular, increasing the waist helps in reducing the atomic density within the trap thus reducing also the loss rates associated to LACs. We note that our estimation of the atom number is rather qualitative in this regime as it is obtained assuming a constant photon-count signal per atom, which is likely to be false due to the presence of collective optical effects in atomic ensembles with very high densities [96–98]. To strongly enhance the number of atoms loaded in the tweezer we decided to implement the ODT described in Sec. 2.1.6.

In Fig. 3.11 we show the typical sequence employed for loading the ODT in the case of ^{171}Yb. After the MOT compression described in Sec. 3.2.2, we ramp up the ODT at its maximum power ($\sim 2\,$W) in 40 ms. During the ramp, we paint the profile of the trap with a 20 kHz arcocosine frequency modulation of the last AOM in the ODT path [see Sec. 2.1.6]. This allows to effectively enlarge the horizontal waist of the trap by roughly a factor 4 and enhance the capture volume, albeit with a reduced trap depth. We maintain the overlap between the painted ODT and the cMOT for 80 ms, after which we quickly reduce the painting amplitude with a 7 ms ramp. Owing to the reduction in the horizontal waist, the trap depth increases during the ramp, reaching its maximum value $U_0 \simeq 300\,\mu$K when the painting is off. After this ramp, we extinguish the MOT and proceed with our experiments.

We monitor the ODT both with fluorescence imaging, by applying extremely short flash imaging pulses [see Fig. 3.8(b)], and with absorption imaging, as shown in Fig. 3.12(a). While with fluorescence imaging we can observe the spatial profile of the atomic distribution, which has been extremely helpful in focusing the ODT in the correct location, absorption imaging allows us to measure the number of trapped atoms. In Fig. 3.12(b) we show the atom number as a function of the ratio between the painted and unpainted waists of the ODT and on the duration of the ramp-down of the painting amplitude. We clearly see a beneficial effect of increasing the capture volume by painting the trap. With optimized parameters, we find that the atom number saturates to $\simeq 7.7\times10^5$ for MOT loading times larger than 5 s [Fig. 3.12(c)]. Finally, by performing TOF-expansion measurements we extract the temperature of the atoms in the ODT, finding $T = 33.5(5)\,\mu$K [Fig. 3.12(d)]. This value is only marginally larger than the one of the cMOT, indicating that the presence of the trap and the painting do not induce too large

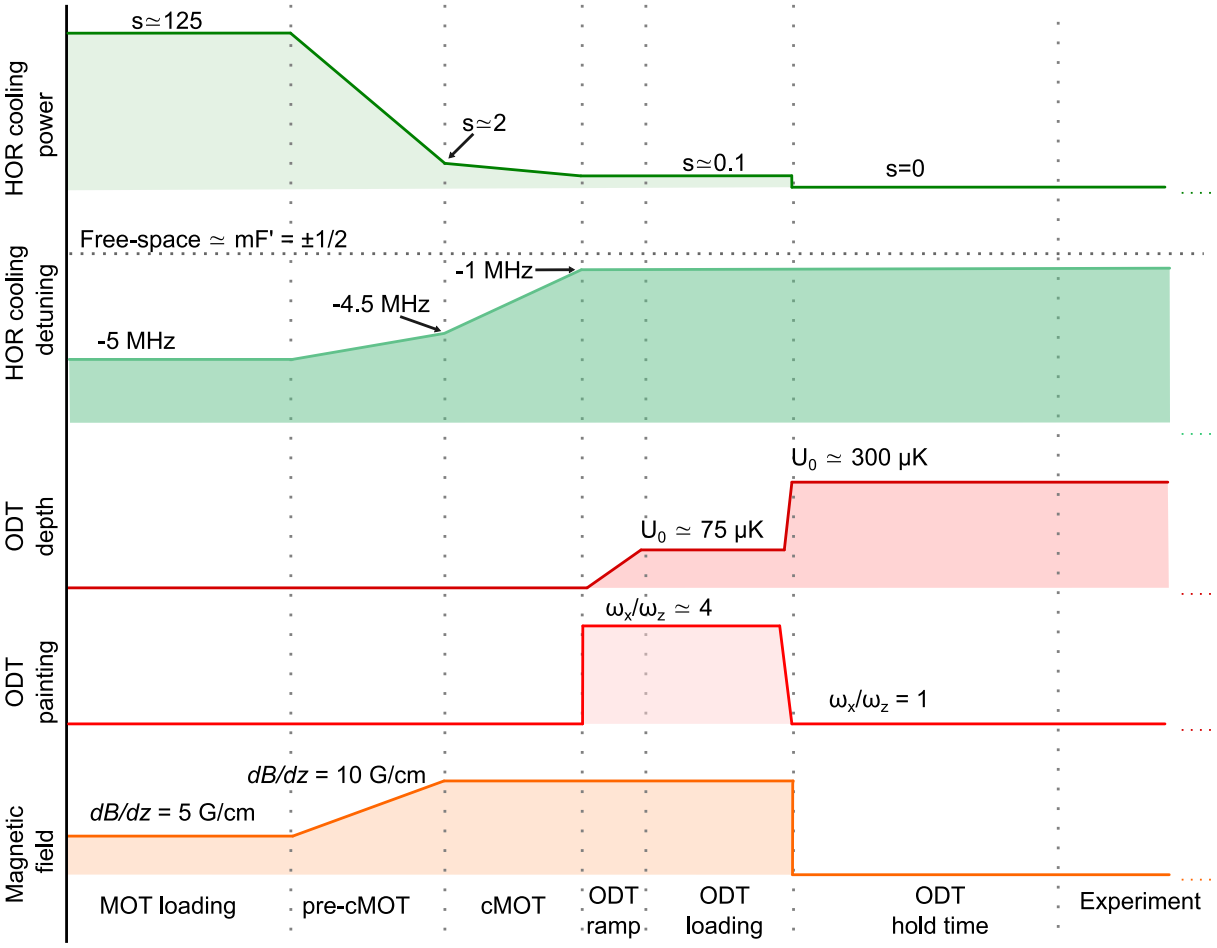

Figure 3.11| Scheme of the experimental sequence for loading ^{171}Yb atoms in the ODT. The sequence starts by loading and compressing the MOT, tuning the compression parameters in order to minimize the cMOT temperature while maintaining a high atom-number. We then ramp up the ODT to its maximum power ($\sim 2\,$W) in 40 ms. During this ramp we paint the trap profile, resulting in a $\times 4$ increase of the horizontal waist. We maintain the overlap between the cMOT and the painted trap for other 80 ms to finish the ODT loading before quickly extinguishing the painting in 7 ms and switching off the cMOT. As the horizontal waist is reduced, the trap depth is increased by roughly a factor 4 and the sample is ready for the next stages of the experiment. The dotted horizontal line in the cooling detuning section indicates the free-space $^1\mathrm{S}_0 \rightarrow {}^3\mathrm{P}_1|F' = 3/2, m'_F = \pm 1/2\rangle$ resonance which is only moderately light shifted by the 759 nm trapping wavelength.

heating.

With $\sim 5 \times 10^5$ atoms confined in the small volume of the ODT, we have a dense sample which we can use as a reservoir to load atoms into one or more optical tweezers, drastically increasing the number of trapped atoms. In particular, ramping up a tweezer trap at the center of the ODT profile introduces a dimple in the potential, where atoms tend to accumulate [13, 178, 226].

The results presented so far are obtained for ^{171}Yb, which displays a very small scattering length between ground state atoms and degeneracy is typically obtained through sympathetic cooling with ^{174}Yb [174]. However, we believe that with our dimple it will be possible to produce a degenerate gas of ^{171}Yb without any sympathetic cooling. In fact, a sufficiently high atom

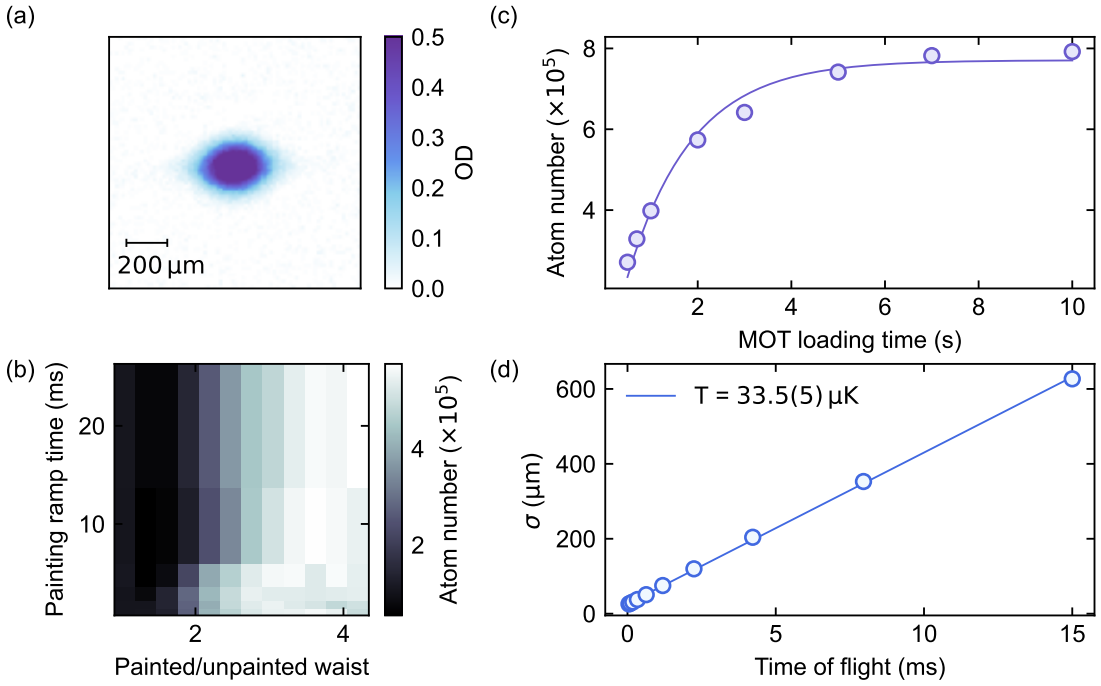

Figure 3.12| Optical dipole trap for ^{171}Yb atoms. (a) Absorption image of the ODT after 1 ms of TOF. (b) Trapped atom number versus painted-to-unpainted waist ratio and duration of the painting ramp-down. (c) Trapped atom number as a function of MOT loading time. Solid line is a fit with the exponential function Eq. (3.3). (d) Gaussian RMS size of the ODT expanding in time of flight. Solid line is a fit with a ballistic expansion model, yielding a measured temperature $T = 33.5(5)\,\mu$K. Panels (a, b, d) are obatined for 2 s of MOT loading time.

number in the dimple would allow to reach very low T/T_F values, owing to the high atom density increasing the Fermi temperature T_F. We will discuss this in more detail in Sec. 5.3.2.

On the other hand, ^{173}Yb can be easily evaporated [171], thanks to its larger scattering length and the enhancement of collision rates provided by its SU(N) symmetry of interactions [178]. However, its complicated nuclear-spin structure and the effect of differential light shifts caused by the 759 nm trapping light may pose challenges to the ODT loading. Prior to optimizing the ODT loading of ^{173}Yb we therefore investigate the differential polarizability of the $^3\mathrm{P}_1|F' = 7/2, m'_F\rangle$ states.

Light shifts in the ODT

To measure the differential light shifts, we start by loading ^{173}Yb atoms in the ODT with a similar sequence to the one described for ^{171}Yb. We then perform a blow-out spectroscopy of the $^1\mathrm{S}_0 \rightarrow {}^3\mathrm{P}_1$ transition, similarly to what we do for single atoms in tweezers [see Sec. 2.3.4]. We show the measured polarizabilities in Fig. 3.13, comparing them to the predictions of our theoretical model.

We first measure the light shifts for π-polarized trapping light, i.e. when $\theta = 0°$, where θ is the angle between the ODT polarization and the quantization axis, which is defined by a sufficiently large magnetic field. Contrarily to what observed at 532 nm, we find that the excited states are more confined than the $^1\mathrm{P}_1$ ground state and thus display a negative differential polarizability. Moreover, the confinement is larger for states with larger $|m'_F|$. We measure differential polarizabilities $\Delta\alpha \simeq -8(2)\%$, $-27(4)\%$, $-51(2)\%$, $-80(2)\%$ for $|m'_F = \pm 1/2, \pm 3/2, \pm 5/2, \pm 7/2\rangle$

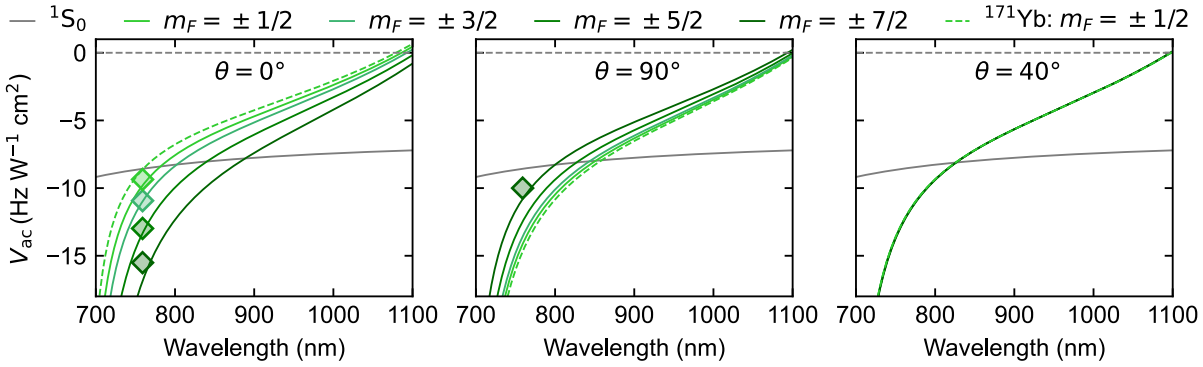

Figure 3.13| Light shifts of the $^1P_1$ and $^3P_1$ states in fermionic isotopes at the ODT trapping wavelength. We show the expect light shifts for the different nuclear spin states of ^{173}Yb (solid lines) and ^{171}Yb (dashed-dotted line) obtained through our polarizability model. By tuning the angle θ between the trapping light polarization and the quantization axis we can tune the relative magnitude of differential lights shifts of the excited $|m'_F\rangle$ states. Diamonds indicate experimentally measured values for ^{173}Yb through blow-out spectroscopy in the ODT.

respectively, finding good agreement with our theoretical polarizability model.

The negative sign of the differential polarizability may cause detrimental effects on the ODT loading. In fact, the most efficient loading schemes for combined dipole traps and cooling light rely on trapped atoms being essentially dark to the cooling thanks to a large blue-shift of the cooling transition caused by the trap itself or by an appropriate light-shifting beam [178, 226]. In this case, trapped atoms are hidden from the cooling light which might induce detrimental effects such as LACs. We expect that this mechanism is also, at least partially, taking place when we load our 532 nm tweezer traps from the MOT. The observed larger trapping of the excited states at 759 nm results in the opposite effect: atoms that are colder and closer to the center of the trap, in this case to the maximum intensity of the ODT, will see a red-shift of the $^1S_0 \rightarrow {}^3P_1$ transition and thus a reduced detuning of the cooling light. This could lead to losing the atoms with the lowest energy and pose a strong limit to the attainable phase space densities in dipole trap at 759 nm directly loaded from the MOT. The situation might be better for ^{171}Yb, which displays an almost magic condition for the $^1S_0 \rightarrow {}^3P_1|F' = 3/2, m'_F = \pm 1/2\rangle$ states [see first panel of Fig. 3.13], and indeed we observe a satisfactory number of trapped atoms in the ODT.

We also explore the effect of a linearly polarized $\sigma^{\pm}$ trapping light ($\theta = 90°$) by changing the quantization axis through a 4 G magnetic field perpendicular to the tweezers polarization direction. For this scenario, we measure only the differential polarizability of the $|m'_F = \pm 7/2\rangle$ states, finding $\Delta\alpha = -17(1)\%$. We note that for $\sigma^{\pm}$-polarized trapping light, the order of the light shifts is reversed, with the stretched transitions featuring the smallest differential light shift. This inversion for a 90° rotation of the quantization axis suggests that for an appropriate angle θ, it should be possible to equalize the differential light shifts of all $|m'_F\rangle$ states and we theoretically estimate this value as $\theta = 40°$. While an experimental confirmation of this result might be extremely interesting, further validating our polarizability model and helping in understanding how to tune differential light shifts to reach e.g. magic conditions, we suspect that the magnitude of the magnetic field necessary to rotate the quantization axis will result in a significant Zeeman shift, reducing the utility of this angle tuning.

3.3.3 Optical pumping

Control on the initial population of different spin states is key to several experiments, as it is a fundamental qubit initialization in quantum information schemes and provides a crucial tuning knob in the investigation of SU(N) symmetric interactions [87, 161, 178]. For both fermionic isotopes, we observe a roughly balanced spin population after the MOT, with a possibly larger population of states with $m_F < 0$ caused by the σ^- polarization of the vertical beam in our 5B geometry. We implement optical pumping (OP) and gain control on the spin populations with the schemes presented in Fig. 3.14.

For ^{171}Yb, we perform OP in an array of individually trapped atoms. During OP, we reduce the tweezer depth to $U_0 \simeq 280\,\mu$K to mitigate the effect of differential light shifts and off-resonant scattering and we employ a 12 G magnetic field to split different $|m'_F\rangle$ sub-levels of the excited $^3\mathrm{P}_1|F' = 3/2\rangle$ manifold. This results in splitting of $\simeq 16.7\,$MHz $= 14.6\,\Gamma$, where Γ is the $^1\mathrm{S}_0 \to {}^3\mathrm{P}_1$ transition linewidth. We drive the $^1\mathrm{S}_0|F = 1/2, m_F = +1/2\rangle \to {}^3\mathrm{P}_1|F' = 3/2, m'_F = -1/2\rangle$ transition with our σ^- polarized vertical MOT beam with intensity much lower than the saturation intensity for 10 ms. After the OP pulse, we determine the spin-state population by selectively blowing out one spin state and measuring the remaining atom number. We observe that when the OP beam frequency matches the $^1\mathrm{S}_0|F = 1/2, m_F = +1/2\rangle \to {}^3\mathrm{P}_1|F' = 3/2, m'_F = -1/2\rangle$ transition we transfer almost the atoms in the $|m_F = -1/2\rangle$ state with a 90% fidelity, defined as the ration between atoms in $|m_F = -1/2\rangle$ to the total atom number [Fig. 3.14(b)]. This 10% infidelity could stem from spin flips due to off-resonant scattering from the trap or caused by the blow-out pulse on the other spin state.

We extend our OP scheme to ^{173}Yb, employing a sequence of 5 OP pulses on the $^1\mathrm{S}_0 \to {}^3\mathrm{P}_1|F' = 7/2\rangle$ transition with σ^- light [Fig. 3.14(c)]. In this way we can bias the spin population towards negative m_F values and eventually produce a spin-polarized $|m_F = -5/2\rangle$ sample. In Fig. 3.14(d) we show the result of a blow-out spectroscopy of ^{173}Yb atoms in the ODT before optical pumping, measured with the ODT fluorescence. We employ a ODT depth of $U_0 \simeq 60\,\mu$K to reduce differential light shifts and use a field of 6 G to split the $|m'_F\rangle$ states. We observe 7 resonant peaks, corresponding to $|m'_F = -5/2, -3/2, -1/2, +1/2, +3/2, +5/2, +7/2\rangle$ states, while the resonance of the $|m'_F = -7/2\rangle$ state is not visible in the plot. We note that peaks corresponding to $|m'_F < 0\rangle$ states display a larger amplitude, suggesting an initial imbalance of the spin population likely due to our 5B MOT configuration. We observe that with a single OP pulse we can enhance this imbalance towards $|m'_F < 0\rangle$ states as we suppress the $|m'_F = +3/2, +5/2, +7/2\rangle$ peaks. However, the observed pumping is larger than what expected from a single OP pulse and we therefore conclude that a 6 G splitting is not sufficient to selectively drive $|m_F\rangle \to |m'_F = m_F - 1\rangle$ transitions. We therefore employ a larger 10 G magnetic field and implement the 5-pulses scheme to transfer all the population to the $|m_F = -5/2\rangle$ state. Fig. 3.14(e) shows the result of a blow-out spectroscopy at 10 G on a spin-polarized sample.

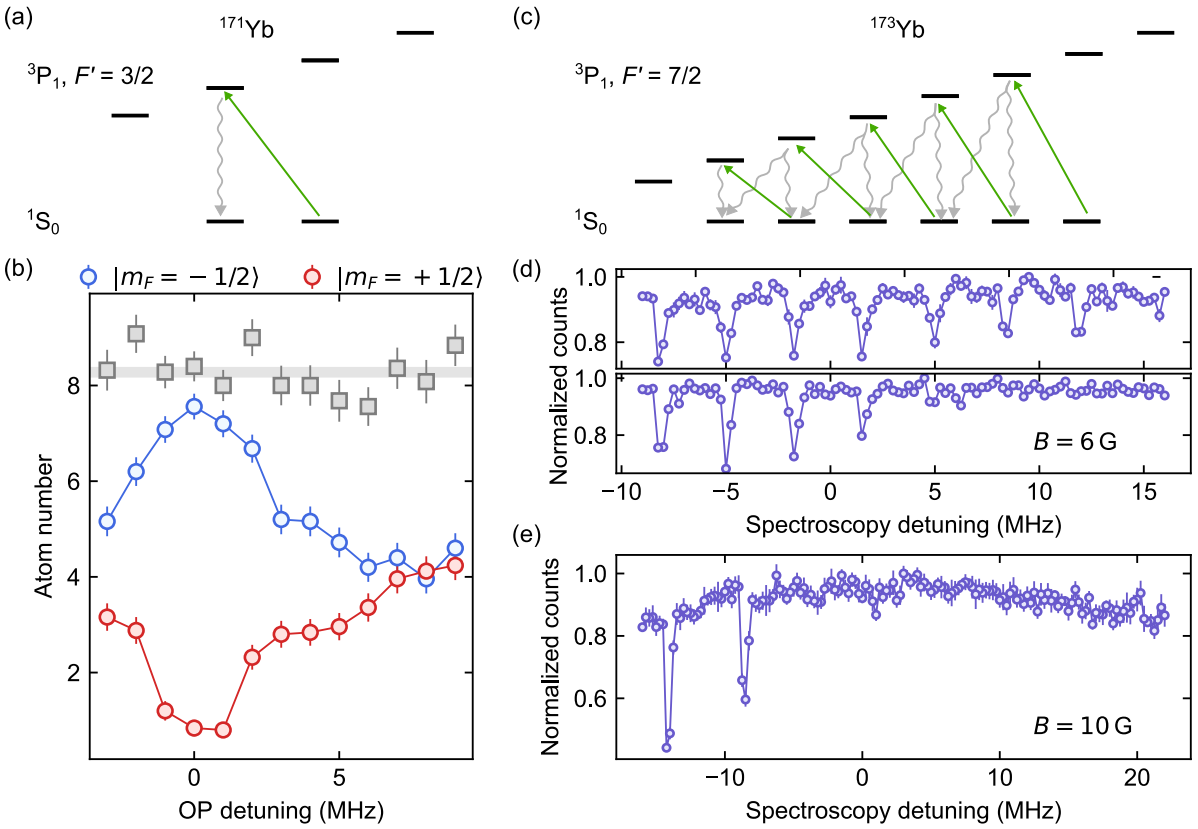

Figure 3.14| Optical pumping in ^{171}Yb and ^{173}Yb. (a) Sketch of the OP scheme to prepare atoms in the $|m_F = -1/2\rangle$ state in ^{171}Yb. We use a 12 G magnetic field to split $|m'_F\rangle$ sub-levels of the excited $^3\mathrm{P}_1|F' = 3/2\rangle$ manifold and drive the σ^- transition until atoms are transferred in the $|m_F = -1/2\rangle$ state. (b) Optical pumping on a 10-site tweezer array of ^{171}Yb atoms. We plot the population of the two spin states, measured as the remaining atom number after blow-out of the other state, as a function of the OP detuning from the $^1\mathrm{S}_0 \rightarrow {}^3\mathrm{P}_1|F' = 3/2, m'_F = -1/2\rangle$ resonance. The grey squares indicate the total atom number after OP and the grey band is the average atom number. (c) Sketch of the OP scheme to prepare a spin-polarized sample in ^{173}Yb. We use a 10 G magnetic field to split $|m'_F\rangle$ sub-levels of the excited $^3\mathrm{P}_1|F' = 7/2\rangle$ manifold and apply 5 successive OP pulses driving σ^- transitions. (d) Spectroscopy of ^{173}Yb atoms in the ODT before (top) and after a single OP pulse (bottom) employing a 6 G magnetic field. The 7 peaks correspond to transitions to $|m'_F = -5/2, -3/2, -1/2, +1/2, +3/2, +5/2, +7/2\rangle$, while the $|m'_F = -7/2\rangle$ is further to the left. We see that after a single OP pulse we suppress the $|m'_F = +3/2, +5/2, +7/2\rangle$ peaks, indicating excessive pumping due to a too low Zeeman splitting. (e) Spectroscopy after 5 OP pulses at 10 G. The two peaks correspond to transitions to $|m'_F = -5/2, -3/2\rangle$, with the $|m'_F = -7/2\rangle$ being more on the left. The presence of only two peaks indicates that we have a polarized sample in the $|m_F = -5/2\rangle$ state. In panels (a, c) we do not depict decays on the driving transitions to not overcrowd the schemes. In panels (d, e) the detuning is referred to the free-space resonance.

4

Low-loss microsecond-scale imaging of single atoms

Detecting individual atoms with high-fidelity is key to several applications in quantum science, from quantum simulation to metrology and computing [7, 8, 15, 17, 18, 23, 27–29, 31, 48, 49, 65, 82, 159, 160, 227–231]. Most single-atom imaging schemes rely on collecting fluorescence light while simultaneously cooling the atoms, allowing to achieve high single-particle detection fidelity with very low associated losses. However, efficient imaging and cooling often requires careful control of trapping light shifts and long imaging durations, from few to hundreds of milliseconds, which limit the experimental repetition rate and mid-circuit measurements capabilities [12, 18, 52, 54, 65, 76, 82, 84, 114, 139, 209, 210]. A fundamentally different strategy is to operate in a non-equilibrium, cooling-free regime where atoms scatter a burst of photons in a short time [48, 49, 136, 175, 199, 232–234]. This enables orders-of-magnitude faster detection, at the cost of atom survival. Low-loss fluorescence imaging without cooling becomes possible for atoms like ytterbium, where a strong, closed optical transition facilitates efficient photon scattering, while the large atomic mass reduces recoil-induced heating.

In this chapter, we will describe our fast single-atom imaging scheme (*flash imaging*), through which we achieve microsecond-scale low-loss imaging of single ytterbium atoms. The scheme is greatly inspired by the approach developed in the group of Selim Jochim in Heidelberg, where single lithium atoms are imaged in free-flight by addressing them with alternated high-intensity pulses [175]. This pulsed scheme has been recently extended to lanthanides [136, 233, 234] and, even more recently, to alkaline-earth-like atoms [50, 51]. We will first describe the imaging setup we have realized to implement the flash imaging scheme, focusing on the motivation for the alternated-pulses approach. We will then analyze the performances of our single-atom imaging scheme regarding the detection fidelity and atom survival probability, discussing the physical origin of our loss-sources and possible improvements. Leveraging the low-loss nature of our imaging technique, we can perform repeated measurements on the same atoms. However, the lack of cooling results in atoms accumulating motional excitations and leads to a roughly quadratic increase in loss probability for each detection [see Eq. (1.48)]. We will describe how we overcome by applying a cooling pulse to restore the motional state after each image, allowing us to perform repeated fast detections with high and constant survival probability per image. We will then explore the possibility of applying our imaging technique to dense atom-arrays, similar to those employed in lattice gas microscopy. In particular, we will discuss how the low-loss nature of our scheme does not compromise the optical resolution, approaching the diffraction limit and allowing to resolve single atoms also in tightly-spaced arrays. For situation where the signal of different atoms starts to overlap we increase the detection fidelity by employing a reconstruction algorithm based on maximum likelihood estimation (MLE). Finally, we will discuss flash imaging of single atoms in free-flight and how this can be applied to gain information on the thermodynamic properties of our system.

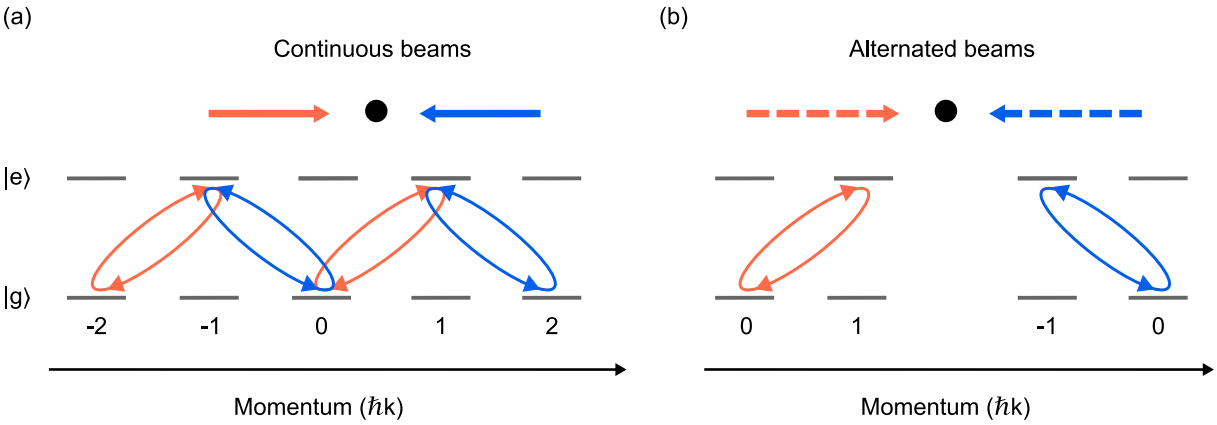

Figure 4.1| Sketch of the momentum-space evolution under continuous and alternated illumination. (a) An atom illuminated by two high-intensity beams performs a quantum walk in momentum space, exploring states with larger momenta and leading to larger momentum spread. (b) When the two beams are alternated, only states with 0 and $\pm\hbar k$ momentum are coupled and the momentum remains confined to $\pm\hbar k$ before spontaneous emission. Figure adapted from Ref. [234].

4.1 Fast imaging with alternated pulses

Fast imaging requires to collect as many photons as possible in the shortest amount of time. To this end, it is necessary to resonantly address a broad cooling transition, providing high photon-scattering rate. This is maximized by saturating the imaging transition with high-intensity beams, allowing to reach the $\Gamma_{\mathrm{sc}} \simeq \frac{\Gamma}{2}$ scattering rate limit, where atoms spend half of the time in the ground and half in the excited state.

For a single beam, the high scattering rate, and correspondingly large radiation pressure, leads to high atom-loss and large position spread, as atoms are pushed along the beam's propagation direction. To avoid this, it is necessary to image the atoms with two identical counter-propagating beams such that the net momentum transfer is zero. Employing retro-reflected beams allows to achieve fast single-atom imaging, but the resulting atom-loss probability and position spread of the atoms remain high [48, 49, 234]. The key to achieve low-loss fast imaging, and at the same time improve optical resolution, is instead to illuminate the atoms with alternated high-intensity pulses, avoiding simultaneous illumination from the two beams [175, 234]. The physical motivation behind this is related to the effect of quantum walks in momentum space, which lead to an increase of momentum spread when both beams are illuminating the atoms simultaneously [234].

For a single high-intensity ($s = I/I_{\mathrm{sat}} \gg 1$) beam addressing a transition of linewidth $\Gamma = 1/\tau$, the Rabi frequency is larger than the spontaneous decay rate: $\Omega = \Gamma\sqrt{s/2}$. Therefore, the illuminated atom undergoes coherent Rabi oscillations between the electronic ground state, with zero initial momentum ($|g, 0\rangle$) and the electronic excited state with momentum $\hbar k$ along the beam's direction ($|e, +\hbar k\rangle$). The atom performs on average $\sqrt{s/2}$ coherent oscillations between these two states until a spontaneous decay projects it back to $|g\rangle$, adding an approximately isotropic momentum kick due to photon emission. When two beams are present at the same time, the atom can undergo quantum walks in momentum space, which can be modeled as a Su-Schrieffer-Heeger (SSH) model [234, 235]. This models described as one-dimensional lattice with two sites per unit cell, where atoms can hop within the unit cell, i.e. oscillate between $|g, n\,\hbar k\rangle \leftrightarrow |e, (n \pm 1)\hbar k\rangle$, or hop to the adjacent cell, corresponding to $|g, n\,\hbar k\rangle \leftrightarrow |e, (n \pm 2)\hbar k\rangle$. As $\Omega > \Gamma$, the atom can explore states with larger momenta before a spontaneous decay projects

it to a specific state, resulting in significant momentum spread [Fig. 4.1(a)]. Moreover, if the Rabi frequencies of the two beams are not exactly the same, the quantum walk will be biased by the larger Ω, resulting in a net momentum transfer. On the other hand, if the two beams are alternated, coherent oscillations are limited to $|0\rangle \leftrightarrow |\pm \hbar k\rangle$ momentum states and the momentum acquired before a spontaneous emission event is confined to $\pm\hbar k$ [Fig. 4.1(b)]. If both beams are highly saturated, an imbalance between the two does not cause significant momentum transfer. In this case atomic motion during imaging is primarily governed by diffusive random walks from spontaneous emission events and the kinetic energy increase is well described by Eq. (1.45), which is advantageous for both low-loss and free-space imaging. Therefore, flash imaging based on highly-saturated alternated pulses is the most favorable scheme to achieve fast and high-fidelity single-atom imaging for a different range of applications.

4.2 Flash imaging implementation

Existing implementations of fast imaging, both with alternated and continuous pulses, have been so far either fully destructive [48–51], with atoms being lost from the trap upon excessive heating, or have been performed on atoms in free-flight [175, 232, 234]. Atoms escaping their trapping site also deteriorate the imaging spatial resolution, as they undergo diffusion due to photon recoils and deposit fluorescence on a large detector area, leading to an increased spread of the signal [175]. Nonetheless, the favorable atomic properties of ytterbium allow to employ the flash imaging scheme to achieve high-fidelity low-loss imaging of single atoms in timescales as short as few-microseconds.

To implement the flash imaging scheme, we designed and realized a dedicated laser setup. In order to have sufficient power, we opted to fully dedicate an independent laser source (Toptica DLpro, $\sim$100 mW output power). The laser source is offset-locked to our master 399 nm seed laser [see Sec. 2.2.3]. The offset frequency is typically chosen to compensate for the shift introduced by AOMs in the optical path and to keep the flash imaging beams resonant with the $^1S_0 \rightarrow {}^1P_1$ transition . However, it can also be tuned to perform spectroscopy on the blue transition in a large frequency-range and, most importantly, to image the atoms in high magnetic fields. The offset lock also allows to quickly jump with the laser frequency ($\sim$ 400 MHz in 100 µs), a fundamental ingredient to perform spin-sensitive imaging at high-fields.

We sketch a scheme of the main components of the laser setup in Fig. 4.2 and refer to Sec. 2.4.1 for a description of the imaging path on the main breadboard. The elliptical output beam of the laser source is rendered circular by a cylindrical telescope and a small portion of it is deflected towards the offset-lock section described in Sec. 2.2.3. The main laser beam is then deflected by an AOM[1] which acts as a common switch[2] for the flash imaging beams: as all downstream optical elements are aligned on the +1 order of this AOM, switching off its RF drive ensures that no light is directed towards the atoms. The first order is then split in roughly equal parts by a 50:50 beamsplitter[3] to produce the two flashing beams. A common lens focuses the two beam into the crystals of a pair of AOMs[4] which are employed to perform the alternated pulses. Both beams are then recollimated and coupled to optical fibers which transport the light to the atoms' table. The paths of the two beams are designed to be symmetric, sharing the same optical components placed at the same distances. Nonetheless, we find that a 50:50 splitting of the beams does not result in equal powers on the atoms, we suspect due to different outputs from the optical fibers and the effect of polarization cleaning PBSs. To compensate this imbalance,

[1] G&H 3110-125
[2] The RF is turned on and off with a switch (ZX80-DR230-S+, 2 µs switching time)
[3] Thorlabs BSW20
[4] G&H 3200-129

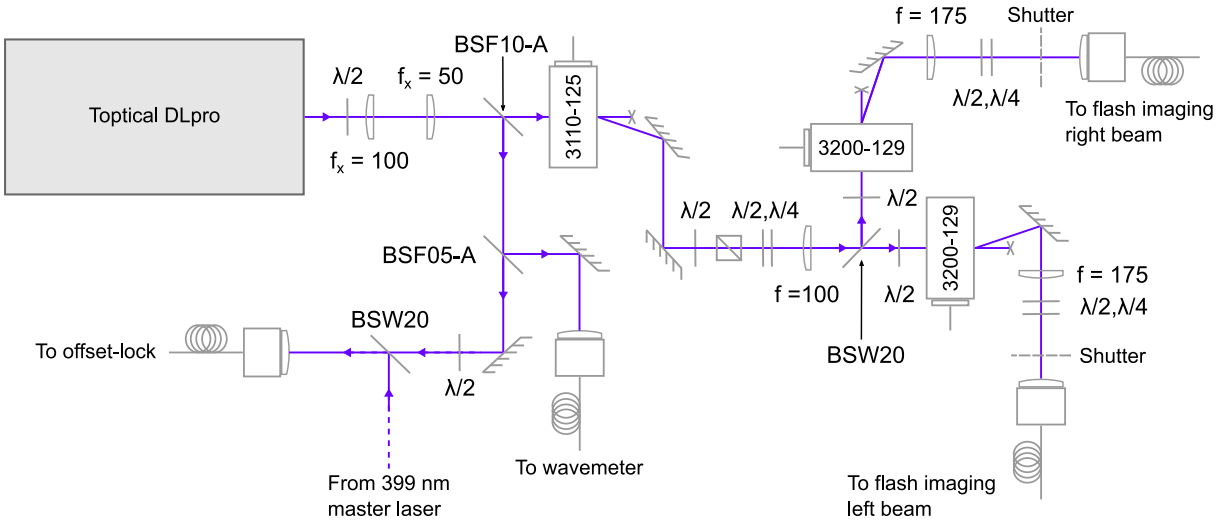

Figure 4.2| Schematic layout of the flash imaging setup. The scheme illustrates the most relevant components of the laser setup employed for realizing and controlling the alternated flash imaging pulses. A small portion of the laser output is combined with light coming from our 399 nm master laser to produce the beat note for the offset-lock of the flash imaging source.

we finely tune the polarization of the light before the 50:50 beamsplitter, taking advantage of the polarization dependence of the beamsplitter reflectivity and transmittivity to equalize the final power of the two beams. Every time we tune the polarization before the beamsplitter we need to recover polarization stabilization in the fibers, which could be avoided by replacing the 50:50 beamsplitter with a PBS cube. After all the optical components, including optical fibers and polarization cleaning on the main breadboard, we have $\simeq 13\,\mathrm{mW}$ in each beam. With our $1.2\,\mathrm{mm}$ output beams $1/e^2$ waist radius, this corresponds to a saturation parameter $s \simeq 40$ for the ${}^1\mathrm{S}_0 \rightarrow {}^1\mathrm{P}_1$ transition.

Too long transients in the AOMs switching are detrimental to flash imaging as they put a lower limit to the duration of the single pulses. The purpose of the common $f = 100\,\mathrm{mm}$ aspheric lens is to minimize the flashing AOMs rise time by focusing the beams inside the crystals. For each beam, we expect a waist diameter of $\simeq 60\,\mu\mathrm{m}$ inside the crystal, and we measure a rise and fall time of $30\,\mathrm{ns}$, defined as the total time to go from zero to maximum efficiency and vice versa. To further optimize the timing of our pulses, we have carefully aligned the AOMs such that the distance between the beam and the piezoelectric transducer is the same for both paths. This allows to reduce the difference in delay time between the response of the two AOMs down to a few nanoseconds.

We find that, probably as a result of this careful alignment and of internal reflections in the crystals, even when the flashing AOMs are completely off, some light is still coupled into the optical fibers. While we block this light with beam shutters for most of the experimental sequence, the atoms will be affected by it during the few milliseconds required for the shutters to open and close before and after imaging. We therefore employ the common AOM described above as a further, much faster, switch for both the imaging beams. We have not found an evident gain in terms of survival probability when using this switch compared to the shutters only, likely due to the low power ($\simeq 150\,\mathrm{nW}$ in each beam) of the stray light on the atoms and the large detuning ($200\,\mathrm{MHz}$). On the other hand, the reduction in power due to the finite efficiency of the common AOM results in a very moderate reduction in scattering rate, which is an acceptable price to avoid stray light on the atoms.

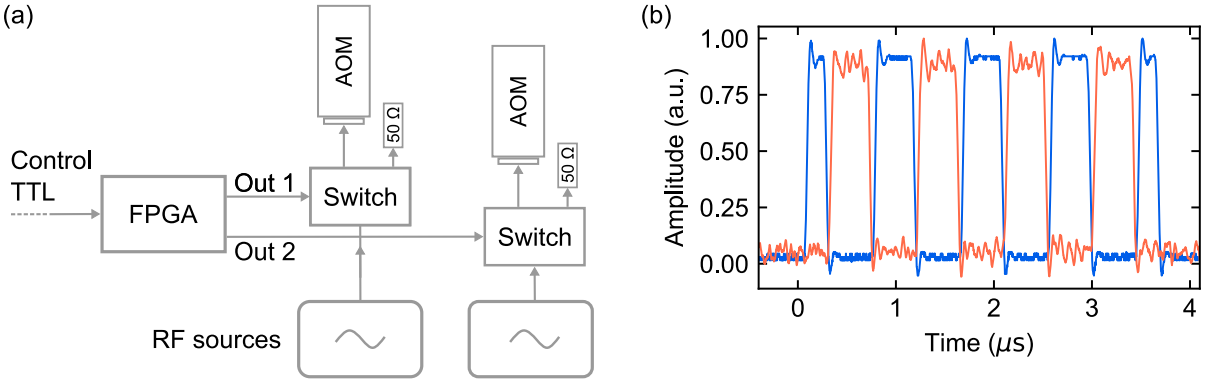

Figure 4.3| Realization of alternated pulses. (a) Scheme of the electronic components employed for the generation of alternated imaging pulses. A TTL signal from our experimental control starts the production of alternated pulses from the two outputs of the FPGA. Each output controls a fast switch, directing the RF signal towards the two AOMs in an alternated fashion. The RF amplifiers before the AOMs are not represented. (b) Signal of the monitor photodiodes for the two fast imaging beams showing a representative sequence of alternated pulses. The higher noise on the orange curve is caused by the lower absolute value of the oscilloscope reading.

4.2.1 Realization of alternated pulses

The trains of alternated RF pulses are generated by a FPGA (Red Pitaya STEMlab 124-14) with a custom firmware which works as follows. An external logical-high signal (produced by our control system) starts the imaging sequence and the FPGA manages the generation of the alternated pulses by generating strobed TTL signals from two outputs. When the control signal falls to a logical-low, the FPGA computes the number of remaining pulses required to equalize the number of pulses from the two beams and completes the sequence. In this way we always have a balanced number of pulses from the two beams. For a given single-pulse duration, this results in discrete steps of the effective illumination times we can set. The duration of each pulse is set to 400 ns as a compromise between the limit imposed by the AOMs rise time and the large momentum transfer from a single beam associated to longer pulses [234]. For the same reason, the first and last pulse of the train are set to 200 ns, half as all the others. With these settings atoms are effectively illuminated for 8/9 of the total illumination time. We have investigated the effect of the single pulse duration, finding no evident advantage in increasing or decreasing this duration in the 200 ns − 1 µs range. The FPGA firmware also allows to finely tune the dark time between pulses, in order to avoid overlap between the two imaging beams, as well as the delay between the two pulse-trains to compensate for remaining small differences between the AOMs delay times.

The AOMs are controlled by independent channels of an RF source[5] and the two RF outputs strobed by two fast switches[6], which are controlled by the train of pulses generated by the FPGA. Each switch directs the RF signal towards an amplifier and the AOM when its control signal is high, while it directs it to a 50 Ω terminated output when it is low. All the electronics components and cables are chosen to be symmetric between the two paths. In Fig. 4.3 we show a scheme of the electronic components and a representative signal of the alternated pulses from the two monitor photodiodes of the flash imaging beams.

[5]Siglent SDG6022X
[6]ZYSWA-2-50DR, 20 ns switching time

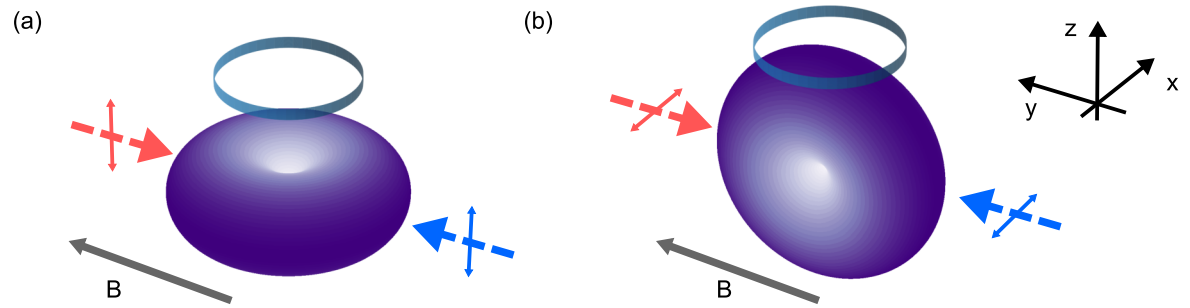

Figure 4.4| Dipole emission pattern for linearly polarized exciting light. Axes are defined as in our experimental setup: the excitation pulses (dashed arrows) propagate along the $\hat{y}$ direction, coinciding with the quantization axis defined by the tweezers polarization and a small magnetic field. Colored solid arrows indicate vertical [(a)] and horizontal [(b)] polarization of the imaging light. The microscope objective is represented as a transparent cylinder above the emission pattern.

4.2.2 Angular distribution of emitted radiation

The flash imaging scheme allows to freely choose the polarization of both fluorescence beams without incurring in optical interference, which strongly hinders single-atom detection due to the discussed quantum walks and to the development of a standing wave with intensity minima in the imaging beams. Such free choice of the imaging beams polarization is particularly beneficial for maximizing the photon collection efficiency, which strongly depends on it through the angular distribution of fluorescence emission.

To quantitatively treat this dependence, we follow the approach presented in Ref. [234]. The probability of emitting a photon per unit time per unit solid angle is $(d\omega/d\Omega)_\mu$, where μ is the polarization of the emitted photon. By dropping the solid angle $d\Omega = \sin\theta d\theta d\phi$ we can write $d\omega \propto \sum_\mu [d^1_{q,\mu}(\theta)]^2$, where $d^1_{q,\mu}(\theta)$ is the D-matrix in Euler angle form and q is the change of m state of the atom. For different cases we have [236, 237]:

$$d^1_{q,\mu}(\theta) = \begin{pmatrix} \frac{1}{2}(1+\cos\theta) & -\sin\theta/\sqrt{2} & \frac{1}{2}(1-\cos\theta) \\ \sin\theta/\sqrt{2} & \cos\theta & -\sin\theta/\sqrt{2} \\ \frac{1}{2}(1-\cos\theta) & \sin\theta/\sqrt{2} & \frac{1}{2}(1+\cos\theta) \end{pmatrix} \tag{4.1}$$

Taking into account the angular aperture of our microscope objective, we can write the geometrical collection efficiency as:

$$C_{\text{geom}} = \frac{1}{I}\int_0^{\theta_{\max}}\int_0^{2\pi}\sum_\mu [d^1_{q,\mu}(\theta)]^2 \sin\theta d\theta d\phi \tag{4.2}$$

where $I = \int_0^\pi \int_0^{2\pi} \sum_\mu [d^1_{q,\mu}(\theta)]^2 \sin\theta d\theta d\phi$ is a normalization factor and $\theta_{\max} = \arcsin(\text{NA})$ is the maximum acceptance angle of the objective. For each value of q we collect both $\mu \pm 1$ photons polarization and we can directly perform the summation in Eq. (4.2).

For ^{174}Yb, the resulting distribution is $d\omega \propto ([d^1_{0,1}(\theta)]^2 + [d^1_{0,-1}(\theta)]^2) = \sin^2\theta$ in the case of linearly polarized exciting light. This is the typical donut-shaped emission profile of a linear oscillating dipole [Fig. 4.4]. For our geometry, the quantization axis ($\hat{y}$) coincides with the beams propagation direction and the linear oscillations are decomposed in a combination of right and left circular components driving both $\sigma^\pm$ transitions. In our geometry, we can write the excited

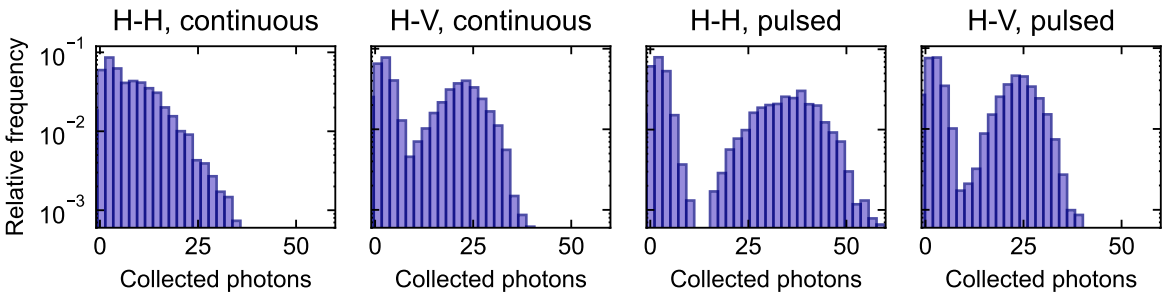

Figure 4.5| Comparison between imaging configurations. Photon-count histograms of a ^{174}Yb array obtained for 20.7 µs illumination time for different polarization combinations of the two imaging beams (H: horizontal, V: vertical), and for pulsed or continuous illumination. Each histogram is obtained from 400 images acquired with a sCMOS camera.

states in the $\{J, m_J\}$ basis as sums of Cartesian orbitals:

$$\begin{aligned} |J' = 1, m'_J = 0\rangle &= |P_y\rangle \\ |J' = 1, m'_J = \pm 1\rangle &= |P_z\rangle \pm i|P_x\rangle \end{aligned} \tag{4.3}$$

The coherent driving of both $\sigma^{\pm}$ transitions by a beam linearly polarized along $\hat{x}(\hat{z})$ excites the corresponding $|P_x\rangle(|P_z\rangle)$ orbital, inducing oscillations along the same axis. As most of the photons are directed out of the oscillation axis, it is strongly beneficial to align the polarization to be perpendicular to the microscope objective axis. We employ Eq. (4.2) to compute the geometric collection efficiency for the two scenarios depicted in Fig. 4.4, including the change of variable described in Ref. [234] to rotate the integration axis when it is is not aligned with the beams polarization. For our 0.6 NA we find a geometric collection efficiency of 2.8% and 13.6% when the light polarization is parallel and perpendicular to the objective axis, respectively[7].

In experiments, this results in a much higher photon-count signal obtained for horizontally polarized imaging light compared to vertical. We report a comparison between the photon-count histograms obtained for different polarization orientations and for pulsed and continuous illumination in Fig. 4.5. For continuous illumination and same horizontal polarization for both beams, interference prevents single-atom detection. On the other hand, interference can be avoided by employing beams with orthogonal polarization, which allows to achieve acceptable single-atom detection fidelity also for continuous illumination. However, this constrains one of the two beams to have be vertically polarized, which results in lower collection efficiency as evident from the comparison between horizontal-horizontal and horizontal-vertical configurations for pulsed illumination. As mentioned above, in our setup the quantization axis is defined by the tweezers light polarization and by a small 0.2 G magnetic field aligned with the propagation direction of the imaging beams. Our exciting light therefore addresses the stretched $^1\mathrm{S}_0|J = 0, m_J = 0\rangle \rightarrow {}^1\mathrm{P}_1|F' = 1, m'_J = \pm 1\rangle$ transitions both for horizontal and vertical polarization, the only difference between the two configurations being the oscillation direction of the dipole and thus the angular distribution of the emitted photons. In particular, the H-V pulsed configuration yields $\sim 65\%$ of the photon-counts obtained for the pulsed H-H, which is roughly compatible with the $\sim 60\%$ we expect from the average between the geometric integrals for horizontally and vertically polarized light.

[7] We note that the same geometric collection efficiency can be achieved by rotating the quantization axis along the $\hat{x}$ direction and exciting π transitions, which however feature lower Clebsch-Gordan coefficients in fermionic isotopes.

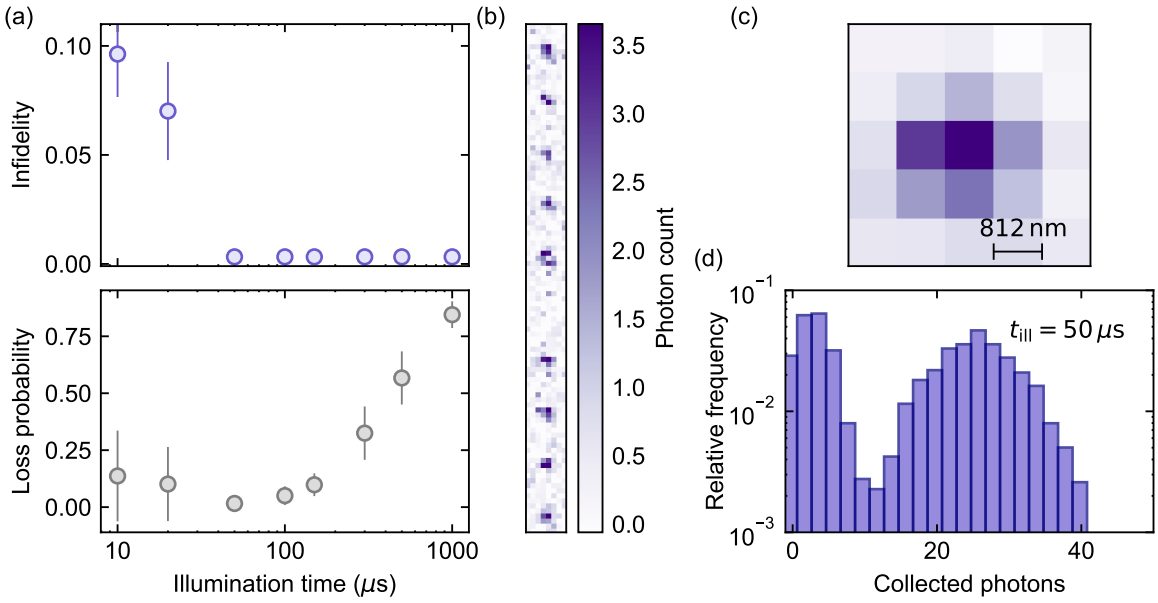

Figure 4.6| Fast imaging with continuous beams. (a) Infidelity (top) and loss probability (bottom) versus illumination time for a ^{173}Yb atom array. The best compromise between infidelity and loss probability is obtained for $t_{ill} = 50\,\mu s$, yielding a fidelity of 99.7(1)% and a survival probability of 98(2)%. The infidelity saturation for long illumination is caused by the limited statistics. (b) Single-shot image of a 10-tweezer array of ^{173}Yb atoms obtained with $t_{ill} = 50\,\mu s$. (c) Average image of a single atom for $t_{ill} = 50\,\mu s$. (d) Photon-count histogram obtained for $t_{ill} = 50\,\mu s$ and a 3×3 ROIs. All data in this figure are obtained at $U_0 \simeq 2.3\,mK$ trap depth from around 300 experimental images acquired with a sCMOS camera.

Extending this treatment to fermionic isotopes is more challenging due to the different Clebsch-Gordan coefficients and decay channel for the various $|m'_F\rangle$ states. These states are not eigenvalues of the electronic angular momentum J_z and should be decomposed in sums of $|J', m'_J\rangle$ states as in Sec. 1.2.1. A notable exception are excited states connected by stretched transitions, for which $|F' = F+1, m'_F = \pm F'\rangle = |J' = J+1, m'_J = \pm J'\rangle$. Therefore, in fermionic isotopes the photons scattered from stretched transitions display the same emission profile as those of ^{174}Yb. Moreover, these transition feature the largest optical coupling to the ground state, making them the most favorable to address during imaging.

4.2.3 Fast imaging with continuous beams

The high ytterbium mass and closed $^1S_0 \rightarrow {}^1P_1$ transition allow single-atom detection also for continuous illumination, even though with reduced performances compared to the alternated pulses configuration. Fast single-atom imaging with continuous illumination from retro-reflected beams has been demonstrated both for ytterbium [48] and strontium [49], achieving $\sim$ 99% single-atom detection fidelity but very high atom-loss. In Fig. 4.6 we show our results for fast imaging with continuous beams in a 10-tweezer array of ^{173}Yb atoms. For these experiments, we employ a retro-reflected imaging beam resonant with the $^1S_0|F = 5/2\rangle \rightarrow {}^1P_1|F' = 7/2\rangle$ transition. The forward and retro-reflected beams have horizontal and vertical polarization respectively, to avoid optical interference. During imaging, we keep our tweezer traps on at a trap depth $U_0 \simeq 2.3\,mK$ and use a high imaging light intensity corresponding to a saturation $s \simeq 8$ and Rabi frequency $\Omega/(2\pi) \simeq 58\,MHz$. Fluorescence light is focused on our sCMOS camera [Teledyne Photometrics Kinetix22, see Sec. 2.4.1] and we integrate the collected photons

on 3×3 ROIs centered on each tweezer.

To measure the single-atom detection fidelity and losses associated to our imaging we acquire two successive images separated by around 50 ms of dark time and perform the analysis described in Sec. 2.4.2. As expected, an increasing illumination time leads to an increased fidelity and to a decrease of survival probability. We find that an illumination time $t_{\text{ill}} = 50\,\mu\text{s}$ provides a good compromise between a statistics-limited high detection fidelity of 99.7(1)% and a good survival probability of 98(2)%. We note that the large error on the survival probability, computed as the standard deviation across the array, results from a systematically reduced survival probability of the last two tweezers in the array and by excluding these outliers from the analysis we achieve an improved average survival probability of 99.2(5)%. The overall positive performances achieved by our continuous imaging are the result of our deep trapping potential, which provides strong confinement also for the $^1\text{P}_1$ excited state [see Sec. 2.3.4], mitigating losses and the consequent spread and reduction of atomic signal. Lowering the trap depth during imaging, we observe a steep increase in atom-losses, with survival probabilities below 70% for $U_0 \simeq 1.1\,\text{mK}$ and below 40% for $U_0 \simeq 570\,\mu\text{K}$. On the other hand we achieve $> 99\%$ fidelity for $t_{\text{ill}} \geq 100\,\mu\text{s}$ for all the investigated trap depths. While these results are obtained for ^{173}Yb, fast imaging relies on physical properties shared by all ytterbium isotopes and similar performances are expected for ^{174}Yb and ^{171}Yb, as shown for the flash imaging configuration [see Fig. 4.7(d)].

Our findings indicate that continuous illumination with orthogonally-polarized beams is a viable technique for fast imaging of single ytterbium atoms and can, for appropriately deep confinement, result in acceptable atom-loss. Moreover, our results are obtained with a sCMOS camera, displaying lower overall performances compared to EMCCD or qCOMS cameras, and a camera upgrade can indeed enhance the performances of this imaging scheme. On the other hand, the reduced collection efficiency, caused by the angular distribution of scattered photons due to the polarization component aligned with the objective axis, demands for longer illumination times to achieve good detection fidelity, resulting in diminished survival probability compared to the alternated pulses configuration. Nonetheless, the straightforward experimental realization of the continuous illumination scheme can make it particularly appealing for experiments without stringent requirements on atom survival, such as for erasure conversion for fault tolerant quantum circuits [48, 49, 144].

4.3 Low-loss microsecond-scale detection

Flash imaging allows to detect trapped ytterbium atoms in few microseconds, achieving state-of-the art fidelity and high survival probability. As mentioned above, for flash imaging we employ counter-propagating beams at high-intensity ($s \simeq 40$), alternating them with 400 ns-long pulses. The beams are tuned to be resonant with the $^1\text{S}_0|F\rangle \rightarrow {}^1\text{P}_1|F' = F+1\rangle$ transition. Both imaging beams are linearly polarized along the $\hat{x}$ axis and propagate along the $\hat{y}$ axis, coinciding with the quantization axis, in order to address $\sigma^{\pm}$ transitions and maximize photon collection efficiency. Photons are collected by our 0.6 NA microscope objective and are focused on a qCMOS camera (Hamamatsu Orca Quest), concentrating an atom's signal over few pixels [see Sec. 2.4.1]. As displayed in the inset of Fig. 4.7(a), we keep our optical tweezers on during detection. For sufficiently short illumination times and deep optical traps, atoms remain confined even when they increase their energy due to photon-induced recoils. We note that our 532 nm tweezer wavelength is particularly beneficial for this scheme as it allows to achieve smaller waists, and larger confinement for same amount of power, compared to e.g. infrared traps. Moreover, our polarizability model [see Sec. 1.2.2] and spectroscopic measurement [see Sec. 2.3.4] show that, for all ytterbium isotopes, all the $^1\text{P}_1|F' = F+1, m'_F\rangle$ states are confined by 532 nm tweezers, which also provide magic trapping conditions for the stretched $^1\text{S}_0|F, m_F\rangle \rightarrow {}^1\text{P}_1|F' = F+1, m'_F = \pm F'\rangle$

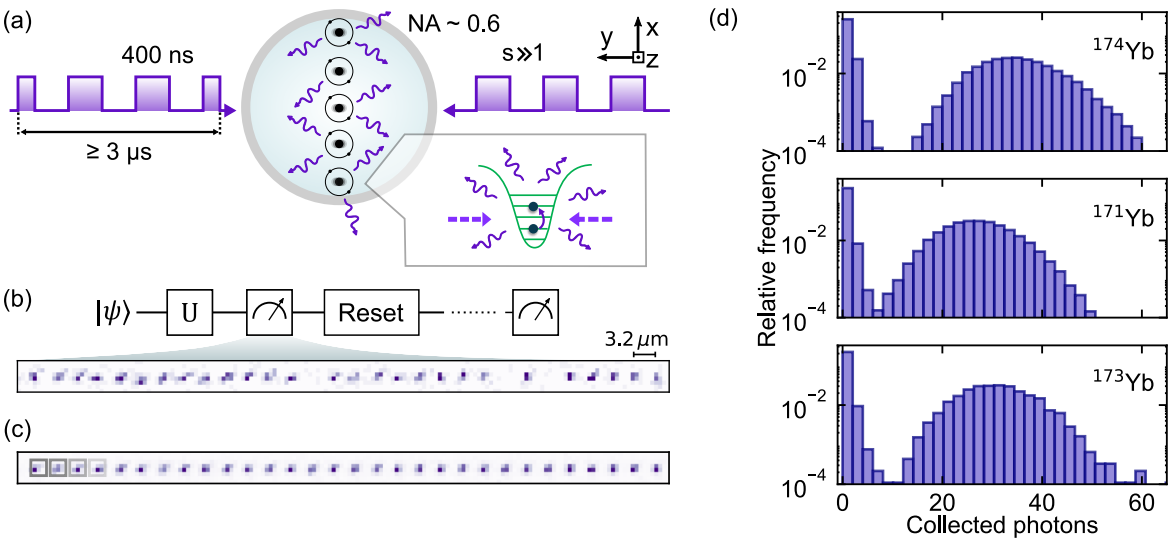

Figure 4.7| Flash imaging. (a) An array of ytterbium atoms is illuminated with high-intensity ($s \simeq 40$) counter-propagating pulses (400 ns single-pulse duration) for few-microseconds. The scattered photons are collected by our microscope objective (NA = 0.6). The inset shows a sketch of the low-loss imaging working principle: atoms increase their energy due to photon-induced recoils but remain confined in deep optical traps. (b) Proposed application of the scheme for mid-circuit measurements and single-shot image of the tweezer array. (c) Average image over 1000 realizations. Both the single-shot and the average image are obtained for $t_{\mathrm{ill}} = 10.8\,\mu\mathrm{s}$. The gray squares indicate the 3×3 ROIs for photon integration. (d) Photon-count histograms for different ytterbium isotopes with $t_{\mathrm{ill}} = 10.8\,\mu\mathrm{s}$.

transitions.

As our imaging scheme relies on general properties of ytterbium, it can be employed for high-fidelity detection of all the ytterbium isotopes discussed in this thesis. We show a comparison between photon-count histograms for same illumination time for ^{174}Yb, ^{171}Yb and ^{173}Yb in Fig. 4.7(d). We find that ^{174}Yb yields the highest signal between all investigated isotopes, with ^{171}Yb and ^{173}Yb showing a $\sim 20\%$ and $\sim 10\%$ reduction in mean photon count. We ascribe this to the simpler $J = 0 \rightarrow J' = 1$ structure of the $^1\mathrm{S}_0 \rightarrow {}^1\mathrm{P}_1$ transition in ^{174}Yb. In this case, our $\sigma^{\pm}$-polarized imaging light addresses only the stretched transitions, which provide the expected collection efficiency [see Sec. 4.2.2]. For ^{171}Yb and ^{173}Yb instead, our imaging light also excites non-stretched transitions, with weaker optical coupling and modified emission pattern. Compared to ^{171}Yb, ^{173}Yb yields a photon-count signal more similar to that of ^{174}Yb as atoms are quickly pumped to the extreme $|m_F = \pm 5/2\rangle$ states and then scatter mostly on the stretched transitions due to the very large (21:1) Clebsch-Gordan coefficients ratio. In the following, we focus on ^{171}Yb, an atom of central importance in quantum metrology, simulation and computing [4, 47, 48, 53, 54, 65, 82], where fast low-loss imaging is highly desirable.

Combining flash imaging, deep traps, and the favorable properties of ytterbium leads to numerous improvements over to previous demonstrations of fast imaging with continuous beams. First, atoms remain confined within their trapping sites for longer illumination times, and, even when they are lost, they experience small position spread. In fact, we observe that the mean number of collected photons in our few-pixels ROIs keeps increasing linearly with illumination time, indicating that atoms keep depositing photons on the same pixels for up to tens of microseconds [Fig. 4.8(a)]. Moreover, for long illumination the bright peaks in the photon-count histograms develop only a moderate tail and remain clearly separated from the background sig-

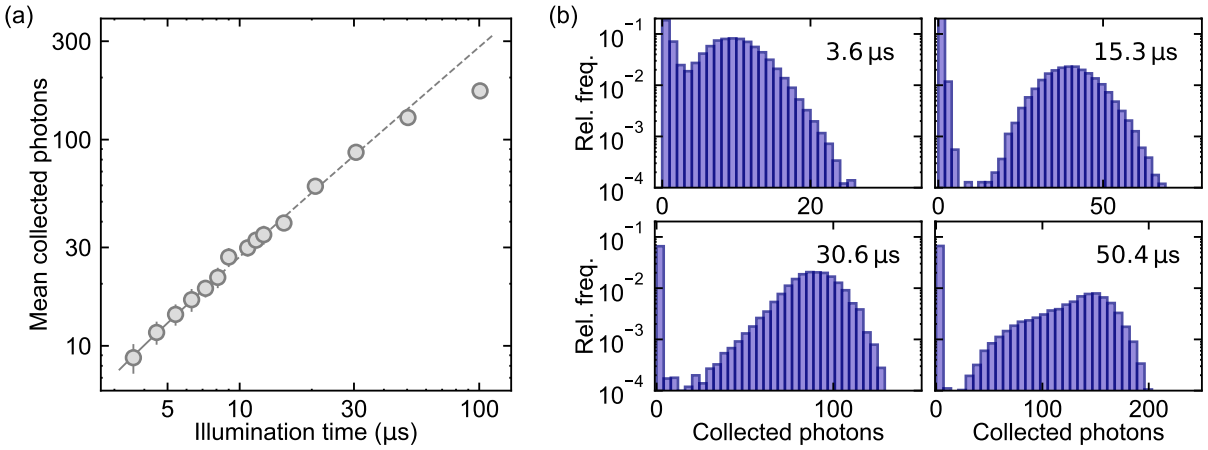

Figure 4.8| Collected photons and illumination time for a ^{171}Yb atom array. (a) Mean photon counts per atom versus illumination time. Points are the array-average value and error bars are the standard deviation. We fit the first 6 data points (solid line), where the behavior is clearly linear, and extend the fitted curve to longer illuminations (dashed line). (b) Photon-count histograms for selected illumination times. All points and panels are obtained from 5000 experimental repetitions at a trap depth $U_0 \simeq 2.3\,\mathrm{mK}$

nal [Fig. 4.8(b)]. This suggests that the fidelity can be pushed to extremely high values by just extending the illumination time.

Imaging performance

We characterize the detection fidelity and the associated losses by acquiring two consecutive images of equal duration and analyzing their photon-count correlation, following the approach outlined in Sec. 2.4.2. In Fig. 4.9(a) we show the result of this analysis for $t_{\mathrm{ill}} = 6.3\,\mu\mathrm{s}$, for which we achieve a fidelity of 99.96(4)% and survival probability of 99.52(7)% at a trap depth of 2.27 mK. We find that that the average infidelity is dominated by a few underperforming tweezers, and we report the median of the array as a more representative figure of merit. In particular, we observe that a few trapping sites yield reduced photon counts, and therefore lower fidelity, due to lower quantum efficiency of the underlying camera pixels. This effect is more evident for larger and more tightly-spaced arrays, as shown in Fig. 4.9(b). While we have optimized the location of the 10-sites array on the camera sensor to avoid the most underperforming pixels, doing it for the longer and tighter-spaced 30-sites array is more challenging and, for simplicity, we decide to maintain the same position for all our arrays. The underperforming tweezers lead to a moderate reduction of the array-average fidelity compared to the median for $t_{\mathrm{ill}} \leq 7\,\mu\mathrm{s}$, while we see no effect for longer illumination times, for which the number of collected photons is sufficiently high to cover this effect. In contrast to the fidelity, the atom loss probability is uniform across the array, and we thus report the array-averaged value.

In Fig. 4.9(c) we show the dependence of the imaging performance on the illumination time. The shortest illumination employed ($t_{\mathrm{ill}} = 3.6\,\mu\mathrm{s}$) yields 99.0(9)% fidelity and 99.77(6)% survival probability, whereas longer illuminations improve the fidelity at the cost of a reduced survival. For $t_{\mathrm{ill}} \geq 7.2\,\mu\mathrm{s}$ the fidelity saturates at 99.98(1)%, limited by our 5000 experimental repetitions per point. For this high-number of collected photons we expect the infidelity to be dominated by decays to dark states from the excited $^1\mathrm{P}_1$. Owing to the almost perfectly closed nature of the $^1\mathrm{S}_0 \rightarrow {}^1\mathrm{P}_1$ transition, these decays have branching ratios of the order of $\sim 1 \times 10^{-7}$ [72, 79, 238, 239], resulting in infidelities at the 0.01% level for up to thousands of scattered photons.

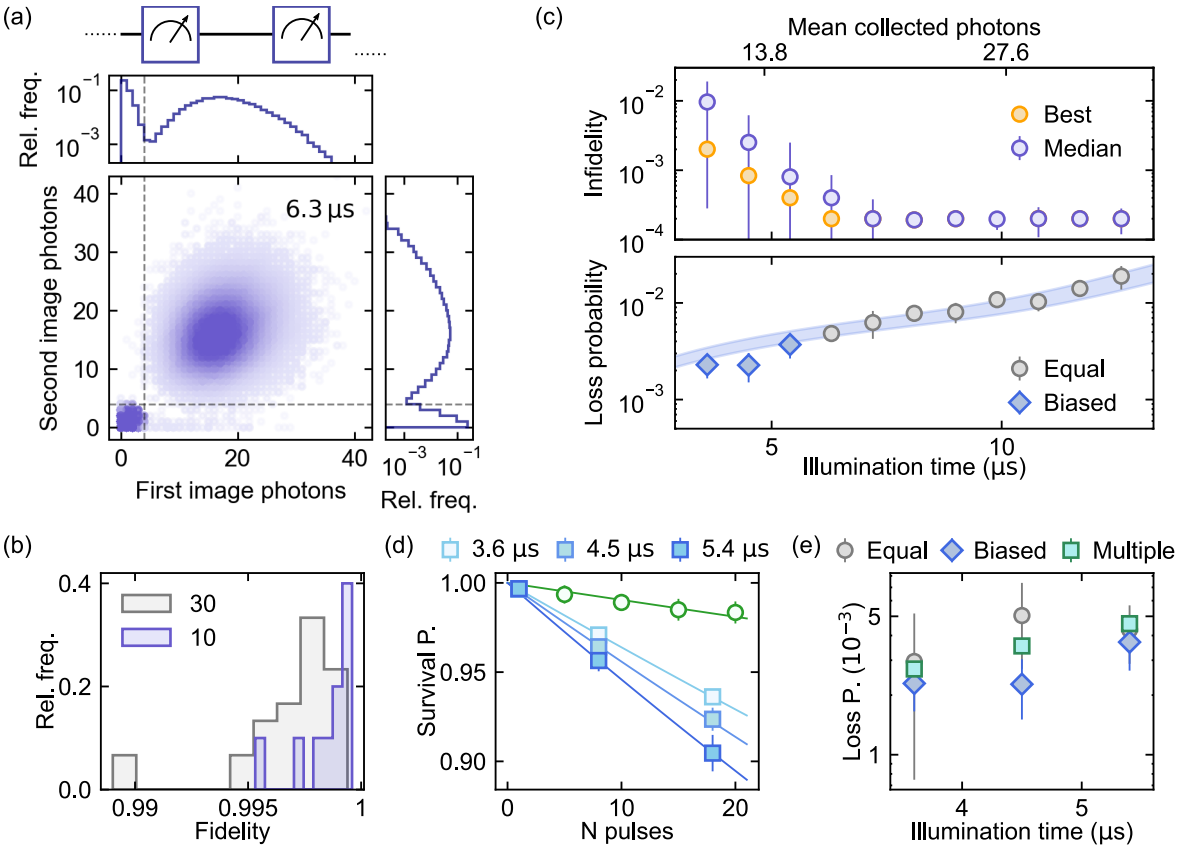

Figure 4.9| High-fidelity low-loss single-atom detection of ^{171}Yb atom arrays. (a) Top: scheme of the experimental sequence used to measure imaging losses and detection fidelity. Bottom: correlation of photons collected in two consecutive images with illumination time $t_{\mathrm{ill}} = 6.3\,\mu\mathrm{s}$. (b) Histograms of the single-site fidelity over a 30 (grey) and 10 (purple) tweezer array for $t_{\mathrm{ill}} = 5.4\,\mu\mathrm{s}$. We employ a trap spacing of $3.15\,\mu\mathrm{m}$, and $8.4\,\mu\mathrm{m}$ for 30- and 10-sites array respectively. (c) Infidelity (top) and loss probability (bottom) versus illumination time and mean photon counts. Purple and orange circles show the array median and best-tweezer infidelity. Gray circles and blue diamonds indicate the array-averaged loss probability from the equal-images and the fidelity-bias method, respectively. Shaded region: fit to a loss model with 2σ confidence interval (see text). (d) Survival probability after a variable number of pulses. Green circles: effect of the reset pulses only. Blue squares: interleaved detection and reset pulses; darker colors indicate longer illumination time. Solid lines are fits to the data assuming a constant loss probability per pulse. (e) Comparison between loss probabilities extracted with different methods for the shortest illumination times. Teal squares indicate the extracted single image loss from the fits in (d). All methods yield compatible losses. In all panels, each point is obtained from around 5000 experimental images for $U_0 \simeq 2.27\,\mathrm{mK}$, except (b) for which the trap depth is $U_0 \simeq 1.13\,\mathrm{mK}$.

For short illumination, the infidelity becomes comparable to or larger than the loss probability, making it increasingly difficult to reliably estimate the losses themselves. To overcome this issue, we adopt an asymmetric imaging sequence: we extend the illumination time of the second image to $12.6\,\mu\mathrm{s}$ to enhance its fidelity and we bias the threshold of the first image to higher values to suppress mislabeling of empty tweezers as occupied. We then compute the loss probability simply as the probability of detecting an atom in the first image and a void in the

second. As a further cross-check, we measure the atom-loss by employing the repeated imaging scheme presented in the next section. We acquired multiple repeated detection-reset sequences and fit the per-image loss probability, correcting for the losses caused by the reset pulse alone [Fig. 4.9(d)]. We obtain the per-pulse losses by fitting the data with:

$$S_N = (1 - P_{\text{loss}})^N \tag{4.4}$$

where S_N is the survival probability after N pulses and P_{loss} is the per-pulse loss probability. In Fig. 4.9(e) we compare the loss probabilities for the shortest illumination times obtained with the three methods described above, finding good agreement across different measurement schemes.

As our detection scheme injects motional excitations into the system, the initial state of the atoms in the second image is indeed different compared to the first. However, we do not observe any significant effect of the first detection on the second image photon-count histogram for most of the investigated illumination times, with only minor effects for the longest illumination times ($t_{\text{ill}} \geq 10\,\mu\text{s}$). We also verify that introducing an interleaved cooling pulse between the images does not lead to significant improvements in the measured fidelity and survival probability when only two images are considered. Without an interleaved cooling pulse, atoms have a higher probability of being lost in the second image due to the energy acquired in the first. However, our scheme is capable of imaging atoms in free space an thus it is not sensitive to atoms that are lost during detection. Therefore, to measure the performances of the first image only we do not need to remove the excess energy, as we do for performing repeated detections [see Sec. 4.4].

4.3.1 Losses sources

To gain insight into the mechanisms leading to the measured imaging losses, we compare experimental data with a theoretical model taking into account different atom-loss sources. In particular, we estimate the total loss probability as a sum of the following contributions:

$$P_{\text{loss}} = P_{\text{img}} + P_{\text{wait}} + P_{\text{triplet}} + P_{\text{exc}} \tag{4.5}$$

where P_{img} and P_{wait} are the heating and vacuum-induced losses during and between images; P_{triplet} is the loss probability associated to decays to long-lived triplet states and P_{exc} accounts for losses caused by optical excitations from the $^1\text{P}_1$ stat to higher-lying anti-trapped states as well as for photionization events.

We compute the first two terms of Eq. (4.5) with the loss model presented in Sec. 1.3. In particular, we define $P_{\text{img}} = P_{\text{h,v}}(U_{\text{eff}}, T_{\text{img}}, t_{\text{ill}})$, where U_{eff} is the average effective trap depth experienced by atoms spending part of the illumination time in the ground and part in the excited state, T_{img} is the atomic temperature after one image and $P_{\text{h,v}}(U, T, t)$ is computed with Eq. (1.48). As mentioned when discussing the model [Sec. 1.3] and the heating rates in our traps [Sec. 2.3.5], we observe that a thermal description of the energy distribution of a single atom is justified as long as temperature is thought of as the value corresponding to the average energy of multiple experimental realizations. Our 532 nm traps, provide almost the same confinement for the $^1\text{S}_0$ and $^1\text{P}_1$ states, with only the $|m'_F = \pm 1/2\rangle$ having a small differential light shift of 4.6(1) MHz/mK [see Sec. 2.3.4]. Considering the 3:1 ratio between the probability of exciting the stretched or the $|m_F = \pm 1/2\rangle \rightarrow |m'_F = \mp 1/2\rangle$ transitions, we estimate an excited state trap depth of around $0.95\,U_0$, where U_0 is the ground state trap depth. During imaging, the atomic temperature increases linearly due to the combined effect of trap-induced heating and photon recoils: $T_{\text{img}} = T_0 + (\alpha_{\text{trap}} + \alpha_{\text{img}})\, t_{\text{ill}}$, where $T_0 \simeq 20\,\mu\text{K}$ is the initial atomic temperature. When evaluating P_{img} we also take into account the vacuum lifetime $\tau_{\text{v}} \simeq 180\,\text{s}$

and the trap-induced heating rate $\alpha_{\text{trap}} \simeq 60\,\mu\text{K/s}$, even though their contribution to the loss probability is rather marginal due to the short illumination time.

Losses between images are similarly defined as $P_{\text{wait}} = P_{\text{h,v}}(U_0, T_{\text{wait}}, t_{\text{wait}})$, where T_{wait} is the atomic temperature after the wait time t_{wait} between consecutive images. During this time, trap-induced heating is the only mechanism that increases the atomic temperature, which is however already higher due to effect of the first image: $T_{\text{wait}} = T_{\text{img}} + \alpha_{\text{trap}} t_{\text{wait}}$.

The P_{triplet} term takes into account for losses caused by spontaneous ${}^1\text{P}_1 \to {}^3\text{D}_{1,2}$ decays. From the ${}^3\text{D}_{1,2}$ states, atoms can either decay to the metastable ${}^3\text{P}_{0,2}$ states, exiting the imaging cycle and resulting in an effective atom-loss, or decay first to the ${}^3\text{P}_1$ state and then back to the ground state with a typical timescale of $\tau_{{}^3\text{P}_1} \simeq 0.86\,\mu\text{s}$, leading to a detection infidelity. Compared to other species possessing a similar electronic structure, such as other alkaline-earth-like atoms or lanthanides, the ${}^1\text{P}_1 \to {}^3\text{D}_{1,2}$ decay rates of ytterbium are extremely low [72, 79, 239], leading to a very low probability $P_{\text{triplet}} \approx 10^{-7}\, N_{\text{ph}}$ of decaying into long-lived triplet states, where N_{ph} is the number of scattered imaging photons, which we estimate from the number of collected photons and our $\simeq 4.5\%$ overall collection efficiency.

The further loss probability P_{exc} is proportional to the number of scattered photons and needs to be introduced for the model to match By fitting our model to the measured P_{loss}, we extract an imaging-induced heating rate of $18.5(4)\,\mu\text{K/}\mu\text{s}$, consistent with an independent measurement and photon recoil estimations, and we find $P_{\text{exc}} \simeq 6.5\,10^{-6}\, N_{\text{ph}}$. In the following we will describe our imaging heating-rate measurement as well as our findings regarding the losses due to excitations from the ${}^1\text{P}_1$ state.

Heating rate measurement

Neglecting coherent effects, during imaging atoms increase their energy due to absorption and spontaneous emission of fluorescence photons. We can estimate the expected heating rate with the simple model outlined in Sec. 1.3. In particular, for each scattering event the atomic energy increases by $2E_{\text{rec}}$, where $E_{\text{rec}} \simeq 0.34\,\mu\text{K}$ is the ytterbium recoil energy for a 399 nm photon. By plugging in our highly-saturated scattering rate $\Gamma_{\text{sc}} \simeq \Gamma/2 \simeq 2\pi \times 14.5\,\text{MHz}$, in Eq. (1.45) we estimate an heating rate of $20.5\,\mu\text{K/}\mu\text{s}$. This value is roughly consistent with the heating rate obtained from our losses model and we can directly measure it taking advantage of tweezer thermometry via realize and recapture [133] [see Sec. 2.3.5].

To measure the imaging heating rate we acquire a first image with variable illumination time and we then perform a release and recapture measurement to measure the atomic temperature after the first image as a function of the illumination time. We compare the recapture probability before and after a $t_{\text{ill}} = 10.8\,\mu\text{s}$ imaging pulse in Fig. 4.10(a). From the obtained probabilities, we compute the temperature in the two situations and find that the imaging pulse induces a $\sim 200\,\mu\text{K}$ temperature increase. We directly measure the imaging heating rate by measuring the final temperature after a variable illumination time [Fig. 4.10(b)]. The temperature displays a linear dependence on illumination time for up to $t_{\text{ill}} < 20\,\mu\text{s}$, after which we observe deviations from a linear behavior. This can be ascribed to the reduced validity of the model employed for temperature estimation of highly energetic particles exploring anharmonic regions of the traps. Considering the imaging duration as the full illumination time, we find an heating rate of $18.6(4)\,\mu\text{K/}\mu\text{s}$, slightly lower than our expectations. However, we have to consider that atoms interact with light for 8/9 of the total illumination due to the dark time between the alternated pulses. Taking this into account, we obtain a measured heating rate of $20.9(4)\,\mu\text{K/}\mu\text{s}$. This value is in excellent agreement with both our theoretical estimate and the result from the loss model fit, after rescaling it for 9/8 to take into account the real atom-light interaction time.

We note that, despite a linear increase of temperature over time, the loss probability does not have a linear dependence on illumination time. In fact, as described in Sec. 1.3, losses

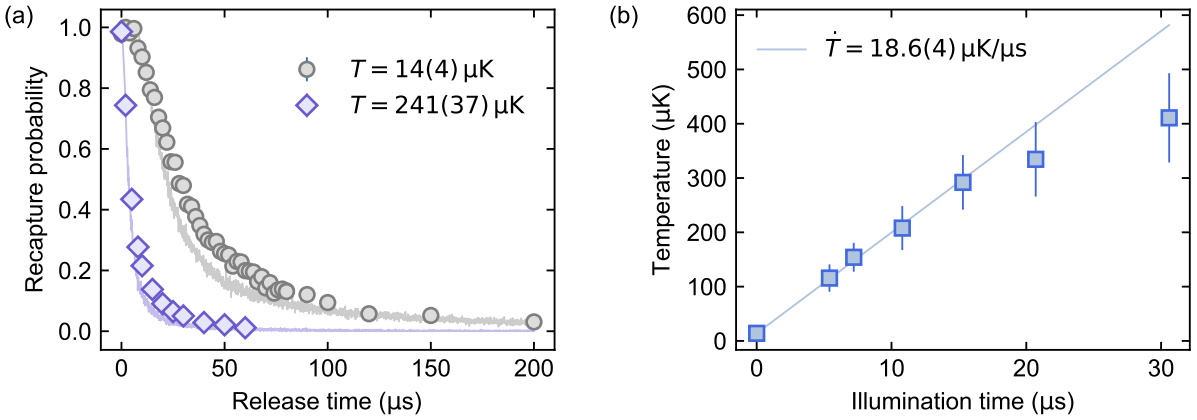

Figure 4.10| Imaging heating rate. (a) Release and recapture measurement before (grey circles) and after an imaging pulse with $t_{\mathrm{ill}} = 10.8\,\mu\mathrm{s}$ (purple diamonds). The shaded lines indicate the simulated recapture probability for the extracted temperature. Data points are obtained from 300 experimental realizations. (b) Atomic temperature as a function of illumination time. The zero illumination time point corresponds to the 14 µK measured in panel (a). The solid line is a linear fit to the data, excluding the two points with longer illumination time. For each point, we repeat 50 full release and recapture curves. All data in this figure are obtained for a 10-tweezer array of ^{174}Yb atoms.

depend on the probability of having an atom with energy larger than the trap depth, given the atomic energy distribution. As long as the average energy is negligible compared to the trap depth, the loss probability remains very small. This is the key mechanisms allowing low-loss fast detection: the short imaging duration combined with the small heating rate results in a moderate amount of injected energy during detection. We also note that this is a key advantage of the flash imaging scheme compared to continuous illumination, where the lower number of collected photons requires longer illumination times to achieve an acceptable fidelity. Longer imaging durations lead to a larger amount of injected energy, and a roughly quadratic increase in loss probability.

Excitations from the $^1\mathrm{P}_1$ state

The P_{exc} term in Eq. (4.5) becomes particularly relevant for the shortest illumination times, when recoil-induced heating is not sufficient to justify the measured losses. To gain insight into the origin of these losses, we explore the dependence of the survival probability on the imaging light intensity and on the trap depth.

We first investigate the effect of the imaging light saturation. We vary the imaging saturation and illumination time together, keeping the number of scattered photons constant and corresponding to those scattered for $t_{\mathrm{ill}} = 5.4\,\mu\mathrm{s}$ at maximum saturation and yielding 99.9(1)% fidelity and 99.63(1)% atom survival [Fig. 4.11(a)]. To measure losses, we opt for the biased-threshold scheme, taking a first image with variable illumination and intensity and increasing both in the second image to further enhance the fidelity. We do not measure any dependence of the atom survival on the imaging light intensity for any of the investigated parameters and we therefore exclude that two-photon excitation processes driven by imaging photons play a significant role in our losses [Fig. 4.11(b)].

On the other hand, we find a strong dependence of the survival probability on trap depth [Fig. 4.11(c)]. For this measurement, we keep a fixed illumination time of $t_{\mathrm{ill}} = 5.4\,\mu\mathrm{s}$, yielding

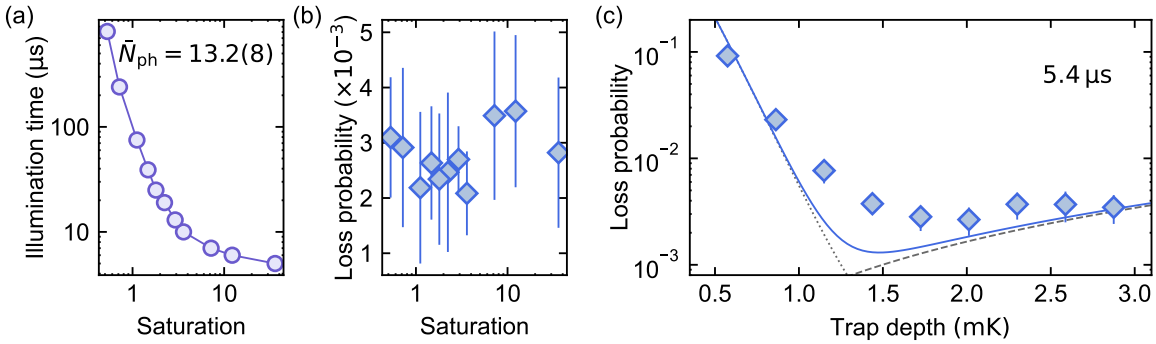

Figure 4.11| Imaging losses sources. (a) Relation between the imaging light saturation and the illumination time required to keep a fixed number of scattered photons, corresponding to a mean-photon count of $\simeq 13$. Solid line is a guide to the eye. (b) Loss probability as a function of imaging light intensity. We keep the average number of collected photons fixed at 13.2(8) as in panel (a). The trap depth $U_0 \simeq 2.3\,\mathrm{mK}$ is also constant. (d) Loss probability versus trap depth for $t_{\mathrm{ill}} = 5.4\,\mu\mathrm{s}$ and maximum imaging light intensity. The gray dotted and dashed lines show expected losses from heating and off-resonant scattering, respectively; the solid blue line combines both effects. All data in this figure are obtained from 5000 experimental realizations of a 10-sites array of ^{171}Yb atoms.

a high and trap-independent fidelity, and vary the trap depth between $U_0 \simeq 570\,\mu\mathrm{K}$ and $U_0 \simeq 2.8\,\mathrm{mK}$. For the shallowest traps, we observe a strong reduction of the survival probability as the energy injected by the imaging light is sufficient to extract atoms from the traps, in qualitative agreement with our heating-rate model. However, we find that the loss probability saturates around $P_{\mathrm{loss}} \simeq 0.3\%$ for traps deeper than $\sim 1.5\,\mathrm{mK}$, deviating from expectations of recoil heating and known decays to long-lived triplet P-states. We attribute these excess losses to the off-resonant scattering of 532 nm trap photons, which induce excitations from the $^1\mathrm{P}_1$ state. Employing excited level lifetimes from Ref. [240] as inputs, we estimate the expected 532 nm scattering rate for an atom in the $^1\mathrm{P}_1$ state in a 1 mK-deep trap as $a_{1\text{-ph}} \simeq 115\,\mathrm{s}^{-1}\mathrm{mK}^{-1}$, dominated by a relatively broad ($\Gamma \simeq 2\pi \times 3.2\,\mathrm{MHz}$) transition to the $6\mathrm{s}7\mathrm{d}\,^1\mathrm{D}_2$ state at 518.4 nm. As this state is anti-trapped by the tweezers light, we estimate the loss probability due to off-resonant trap-photons scattering as $P_{\mathrm{exc},\,1} = N_{\mathrm{ph}}\, a_{1\text{-ph}}\, U_0\, \tau_{^1\mathrm{P}_1}$, where $\tau \simeq 5.46\,\mathrm{ns}$ is the lifetime of the $^1\mathrm{P}_1$ state. As even this contribution is not enough to explain our measured losses, we also take into account the possibility of two-photon photoionization events from the $^1\mathrm{P}_1$ state as $P_{\mathrm{exc},2} = N_{\mathrm{ph}}\, a_{2\text{-ph}}\, U_0^2\, \tau_{^1\mathrm{P}_1}$. We estimate the photoionization rate per mK from our experimental data, finding $a_{2\text{-ph}} \simeq 180\,\mathrm{s}^{-1}\mathrm{mK}^{-2}$, on the same order of magnitude of two-photon photoionization rates from triplet states in 487 nm traps [48]. By summing both these off-resonant scattering contributions in $P_{\mathrm{exc}} = P_{\mathrm{exc},1} + P_{\mathrm{exc},2}$ we obtain qualitative agreement with our measured losses.

Our findings indicate that for 5.4 µs illumination time, it is possible to achieve state-of-the-art fidelity (99.9%) and good survival probability ($> 99\%$) for all trap depths greater than $\sim 1\,\mathrm{mK}$. This is particularly relevant for the scalability of our scheme, as laser power and decoherence effects often limit the maximum accessible trap depths. If instead deeper trapping is available, our 532 nm traps are not ideal as the loss probability becomes quickly dominated by off-resonant scattering, mostly caused by the $6\mathrm{s}7\mathrm{d}\,^1\mathrm{D}_2$ state, which we believe can also act as an intermediate state and favor two-photon photoionization. Even though any trapping wavelength shorter than $\sim 800\,\mathrm{nm}$ is sufficient to induce two-photon photoionization events, they, together with single-photon off-resonant scattering, can be strongly suppressed by employing trapping wavelengths near or above $\sim 760\,\mathrm{nm}$, given that the nearest transition ($^1\mathrm{P}_1 \rightarrow 6s6d\,^1\mathrm{D}_2$) has a wavelength

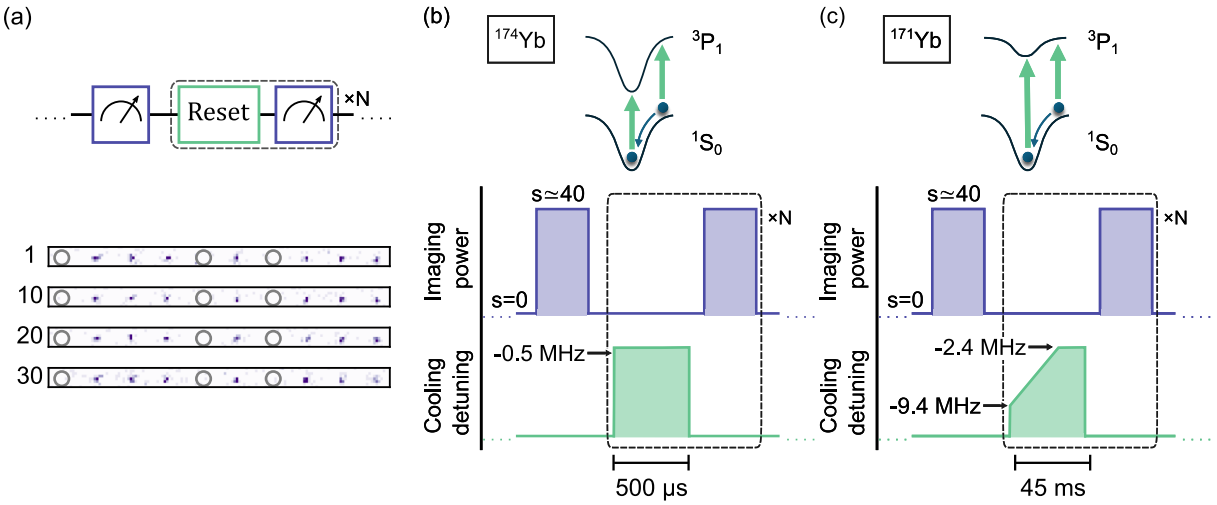

Figure 4.12| Repeated imaging scheme. (a) Top: repeated imaging sequence with interleaved reset pulse between detections. Bottom: single-shot images after 1, 10, 20, and 30 detection cycles for $t_{\mathrm{ill}} = 6.3\,\mu\mathrm{s}$. Grey circles indicate empty sites. (b) Cooling pulses for ^{174}Yb: owing to the magic condition for the $^1\mathrm{S}_0 \rightarrow {}^3\mathrm{P}_1|J' = 1, m'_J = 0\rangle$ transition, we can tune the cooling beams frequency to approach the free-space resonance and reduce the pulse duration down to 500 µs. (c) Cooling pulses for ^{171}Yb: due to the reduced confinement of the $^3\mathrm{P}_1$ excited state, we chirp the cooling frequency during the reset pulse, requiring larger detuning and increasing the reset pulse duration. Reported detunings refer to the unshifted $^1\mathrm{S}_0 \rightarrow {}^3\mathrm{P}_1|J' = 1, m'_J = 0\rangle$ free-space resonance for ^{174}Yb and to the light-shifted $^1\mathrm{S}_0 \rightarrow {}^3\mathrm{P}_1|F' = 3/2, m'_F = \pm 1/2\rangle$ transitions for ^{171}Yb.

of 667 nm. This wavelength range should also provide deep confinement of the $^1\mathrm{P}_1$ state [see Fig. 1.7] provided enough optical power to compensate for the larger beam waist is available. In particular, 759 nm could be an extremely appealing choice due to the combination of magic and near-magic conditions for the $^1\mathrm{S}_0 \rightarrow {}^3\mathrm{P}_0$ and $^1\mathrm{S}_0 \rightarrow {}^3\mathrm{P}_1$ transition .

4.4 Repeated low-loss imaging

Our imaging scheme can be employed to perform fast repeated detection of the same atoms. However, each detection injects significant energy to the atoms, and motional excitations keep adding up leading to higher and higher losses. The increase in loss probability is more than linear with number of images, as each detection increases the average temperature, pushing the center of the atomic energy distribution closer to the loss-threshold represented by the trap depth [see Sec. 1.3]. To mitigate this, we apply a reset pulse, driving the $^1\mathrm{S}_0 \rightarrow {}^3\mathrm{P}_1$ cooling transition to restore the atomic motional state after each image. This allows to remove the energy injected during fast detection and acquire tens of successive low-loss images [Fig. 4.12(a)].

Owing to the magic condition for the $^1\mathrm{S}_0 \rightarrow {}^3\mathrm{P}_1|J' = 1, m'_J = 0\rangle$ transition at 532 nm, we can cool trapped ^{174}Yb atoms in a fast and effective way [Fig. 4.12(b)]. In particular, we can tune the cooling beams frequency close to the free-space resonance ($\Delta/(2\pi) \simeq 0.5\,\mathrm{MHz}$) and employ relatively high intensity of $\simeq 1.5\,I_{\mathrm{sat}}$, where I_{sat} is the $^1\mathrm{S}_0 \rightarrow {}^3\mathrm{P}_1$ transition saturation intensity. This allows us to maximize the cooling rate and reduce the reset pulse duration down to 500 µs. On the other hand, for ^{171}Yb the lack of a magic trapping condition at 532 nm hinders our cooling efficiency. In particular, differential light shifts render the $^1\mathrm{S}_0 \rightarrow {}^3\mathrm{P}_1$ cooling resonance energy-dependent, as atoms with different energies explore different areas of the potential. We thus

sweep the cooling-laser frequency towards resonance during each reset pulse, enabling efficient cooling across different motional states [Fig. 4.12(c)]. Our frequency chirp can be thought of as a moving cap on the atomic energy, progressively cooling atoms with lower energies as the frequency is swept towards resonance. Interestingly, this is reminiscent of the energy cap mechanism underlying repulsive Sisyphus cooling observed in strontium [12, 81]. However, the shorter lifetime of the $^3P_1$ state in ytterbium strongly limits the possibility of observing any Sisyphus cooling effect. We find that the cooling is optimized when we sweep the laser frequency from $\Delta/(2\pi) \simeq -9.4\,\mathrm{MHz}$ to $\Delta/(2\pi) \simeq -2.4\,\mathrm{MHz}$, where the Δ is the detuning from the light-shifted $^1S_0|F = 1/2, m_F = \pm 1/2\rangle \rightarrow {}^3P_1|F' = 3/2, m'_F = \pm 1/2\rangle$ resonance. In our setup, frequency-sweep rates are limited to $\sim$ 5MHz/ms due to the 556 nm laser frequency-locking bandwidth. This slows the whole reset pulse, with a typical duration of 45 ms.

In Fig. 4.13(a-b) we show how we can restore the initial atomic temperature with our reset pulses, focusing on ^{174}Yb, where magic trapping facilitates the pulse optimization. We start by acquiring a preliminary image with long illumination $t_{\mathrm{ill}} = 20.7\,\mu\mathrm{s}$ to significantly increase the atomic temperature from $\simeq 14\,\mu\mathrm{K}$ to $\simeq 400\,\mu\mathrm{K}$. We then apply a reset pulse for a variable time and perform a full release and recapture measurement to extract the atomic temperature. For fixed cooling pulse intensity of $0.2\,I_{\mathrm{sat}}$ we find that, despite the high starting temperature, we can restore the initial state after around 5 ms of cooling [Fig. 4.13(b)]. The reset pulse duration can be shortened by reducing the starting temperature and increasing the cooling power. In Fig. 4.13(c) we show the recapture probability after a $t_{\mathrm{ill}} = 6.3\,\mu\mathrm{s}$ preliminary image for fixed 5 µs release time. Upon increasing the cooling beams intensity, we find that longer durations lead to enhanced losses but good recapture probabilities can be obtained with below-millisecond reset pulses, indicating efficient temperature restoring even after short cooling. By comparing measured recapture probabilities to release and recapture simulations at different temperatures, we can estimate the atomic temperature after the reset pulse and the cooling rates obtained for different intensities. We obtain cooling rates of 130, 150 and 180 µK/ms for cooling pulse intensities of 0.2, 0.6 and $1.5\,I_{\mathrm{sat}}$ respectively.

We apply our repeated detection scheme to perform many successive images. Considering the loss probability after 10 images as figure of merit, we find that for ^{174}Yb we can reduce the reset pulse duration to 500 µs, completing the full detection-reset sequence in essentially 0.5 ms [Fig. 4.13(d)]. By extending the number of successive detections, we observe a linear increase of the loss probability, indicating constant per-image losses [Fig. 4.13(e)]. In Fig. 4.13(f) we show the survival probability after each image for a ^{171}Yb atom-array, where we apply our chirped cooling pulses to compensate for non-magic trapping. Assuming a uniform loss probability across repeated detections [see Eq. (4.4)], for $t_{\mathrm{ill}} = 6.3\,\mu\mathrm{s}$ we observe a per-image survival probability of 99.43(1)%, only slightly lower than that of a single image. This small reduction is due to losses associated with each reset pulse, estimated as 0.096(8)% from an independent measurement where we apply only a variable number of reset pulses [green curve in Fig. 4.9(d)]. For the shortest illumination times, we verify that losses remain constant and compatible with those associated to a single detection for up to tens of repetitions [blue curves in Fig. 4.9(d)], while deviations from constant-loss behavior appear for $t_{\mathrm{ill}} > 8\,\mu\mathrm{s}$-likely due to suboptimal cooling rather than fundamental limitations.

In conclusion, we can employ our imaging scheme to perform repeated fast detection of both ^{171}Yb and ^{174}Yb achieving very similar results between the two isotopes. We report a comparison between the parameters and results obtained for the two isotopes in Table 4.1. For a single image we observe a slightly higher photon-count, and fidelity, for ^{174}Yb, owing to the larger collection efficiency observed for this isotope. Despite the big difference of the reset pulse parameters, we obtain the same per-image survival probability when performing repeated detections. In both cases, the reset pulse duration is the limiting time for the repeated detection rate. In particular,

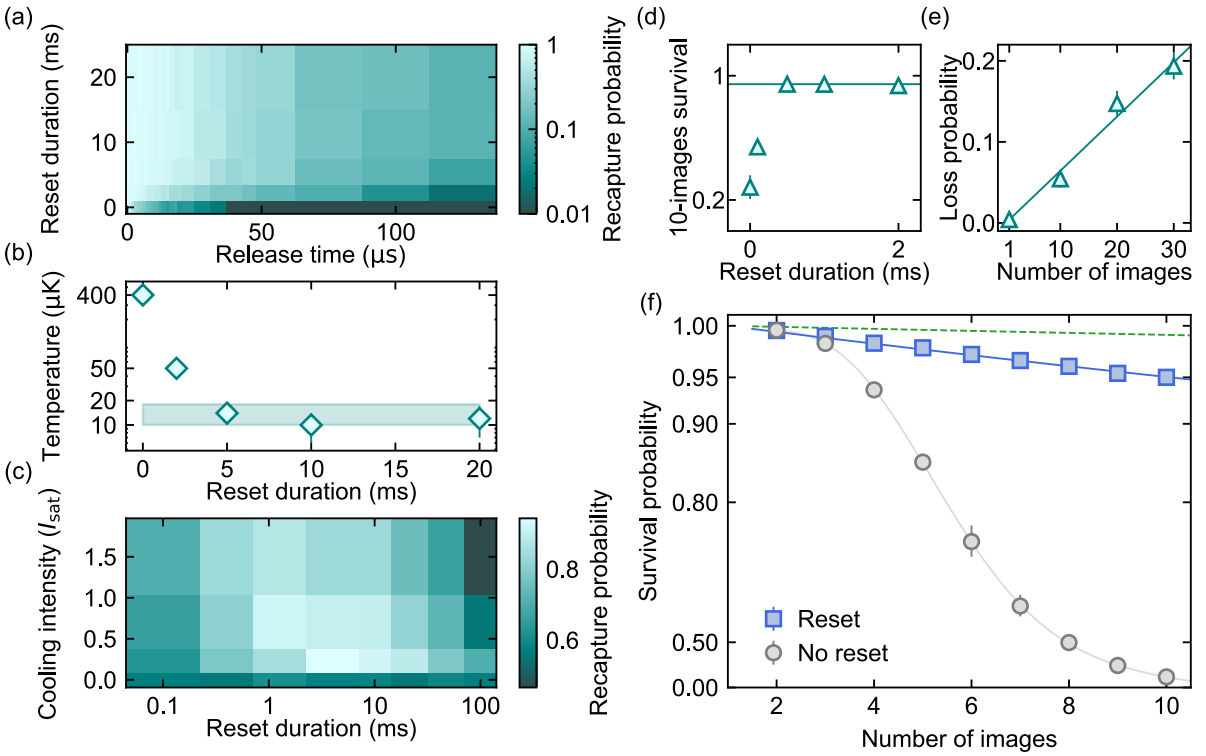

Figure 4.13| Repeated imaging for ^{174}Yb and ^{171}Yb arrays (a) Release and recapture measurement after a preliminary image ($t_{\mathrm{ill}} = 20.7\,\mu\mathrm{s}$) as a function of reset pulse duration. The probability is normalized to have recapture probability 1 when the release time is zero. (b) Extracted atomic temperature as a function of reset pulse duration. The shaded band indicates the 14(4) μK temperature measured in absence of a preliminary image. All data are obtained for a ^{174}Yb tweezer array employing a reset pulse intensity $I \simeq 0.2\,I_{\mathrm{sat}}$. (c) Recapture probability after a preliminary image ($t_{\mathrm{ill}} = 6.3\,\mu\mathrm{s}$) for fixed 5 μs release time as a function of reset pulse duration and intensity. All points of panels (a-c) are obtained for ^{174}Yb acquiring hundreds of experimental realizations with a reset pulse detuning $\Delta/(2\pi) \simeq -0.55\,\mathrm{MHz}$. (d) Survival probability after 10 images ($t_{\mathrm{ill}} = 6.3\,\mu\mathrm{s}$) versus reset pulse duration for ^{174}Yb. The solid line corresponds to a survival probability of 94.6%. (e) Survival probability after a variable number of detection-reset pulses ($t_{\mathrm{ill}} = 6.3\,\mu\mathrm{s}$) for ^{174}Yb. Here we use 500 μs long cooling pulses with $\simeq 1.5\,I_{\mathrm{sat}}$ intensity. Solid line is a linear fit to the data. (f) Survival probability versus number of images for $t_{\mathrm{ill}} = 6.3\,\mu\mathrm{s}$ without (gray) and with (blue) reset pulse for a ^{171}Yb array. The blue solid (green dashed) line is a fit of the measured survival after repeated detection-reset (reset alone) pulses, assuming uniform survival probability across repetitions. Gray line is a guide to the eye. Here we employ a cooling intensity of $\simeq 0.5\,I_{\mathrm{sat}}$ and the frequency chirp described in the text to efficiently cool in non-magic traps. Data points in panels (d-f) are obtained from thousands or experimental realizations. In all panels the trap depth is fixed at $\simeq 2.27\,\mathrm{mK}$ both during imaging and cooling.

the magic trapping condition for ^{174}Yb, enables a detection rate of $\sim$ 2000 images/s with a $\simeq 0.5\%$ loss-probability per image in $\sim 2\,\mathrm{mK}$ traps. On the other hand, the slow frequency chirp strongly reduces the attainable detection rate for ^{171}Yb. We believe this could be solved by exploring cooling schemes alternative to simple Doppler cooling or employing magic trapping conditions also for ^{171}Yb.

	^{171}Yb	^{174}Yb
Mean photon counts	17(2)	19(2)
Detection fidelity	99.96(4)%	99.98(1)%
Survival probability	99.52(7)%	99.67(1)%
Reset pulse duration	35 ms (sweep) + 10 ms	0.5 ms
Reset pulse detuning	$-9.4\,\mathrm{MHz} \rightarrow -2.4\,\mathrm{MHz}$	-0.55 MHz
Reset pulse intensity	$0.5\,I_{\mathrm{sat}}$	$1.5\,I_{\mathrm{sat}}$
Per-image survival (10 images)	99.43(1)%	99.4(1)%

Table 4.1| Imaging parameters and performance for ^{171}Yb and ^{174}Yb. The results refer to 6.3 µs illumination time $\simeq$ 2.27 mK traps.

4.5 Imaging in dense arrays

An important question is whether our flash imaging approach is restricted to tweezer arrays, or if it can also be extended to lattice experiments. While flash imaging has already been applied to image erbium atoms initially trapped in an optical lattice, for the imaging phase atoms were observed in free space after the inter-particle spacing was increased to a few micrometers with an accordion lattice [233, 234]. This had been necessary due to the extremely small spacing of the science lattice (266 nm) and to the choice of performing free-space imaging, during which fluorescence signal spreads as atoms undergo momentum-space diffusion. In our case, the low-loss nature of the detection scheme ensures that atoms remain confined during imaging, which substantially reduces image-blurring and enhances spatial resolution. This opens up the possibility of performing fast single-atom detection in dense arrays and dramatically reduce the imaging times in quantum gas microscopes [18, 114, 209, 210, 227].

The short wavelength of the $^1\mathrm{S}_0 \rightarrow {}^1\mathrm{P}_1$ transition allows to reach a very high spatial resolution, with a diffraction-limited resolution, as defined by the Rayleigh criterion [see Eq. (2.8)] However, aberrations and experimental imperfections, as well as atomic movement during imaging, often prevent from reaching the ideal, diffraction-limited resolution. Moreover, several scientific motivations, including requirements on high tunneling rates, investigation of long-range interactions [233] and observation of sub-wavelength optical effects [241], lead to the realization of arrays with very short lattice spacing, for which site-by-site detection is challenging also for diffraction-limited systems. In such situations, it is possible to either increase the lattice-spacing before imaging [234] or to take advantage of matterwave optics to magnify the atomic signal [192, 242]. An alternative approach is to employ advanced methods, such as deconvolution algorithms [148, 243, 244] and neural networks [211, 245], to reconstruct site occupancy in single-shot experimental images.

In the following, we investigate the spatial resolution properties of our flash imaging scheme and explore its applicability to tightly-spaced arrays. To this end, we directly employ our imaging scheme to detect single atoms in arrays with the shortest spacing achievable in our tweezer setup, taking advantage of a reconstruction algorithm based on maximum likelihood estimation (MLE) to distinguish single atoms also when the signals of different sites start to overlap.

4.5.1 Optical resolution and atom-signal size

Owing to the large ytterbium mass, which limits the recoil energy and the exploration of the trap during detection, and to the low-loss nature of our imaging scheme, we expect that atoms experience very little position-spread during imaging, a fundamental requirement to reach a

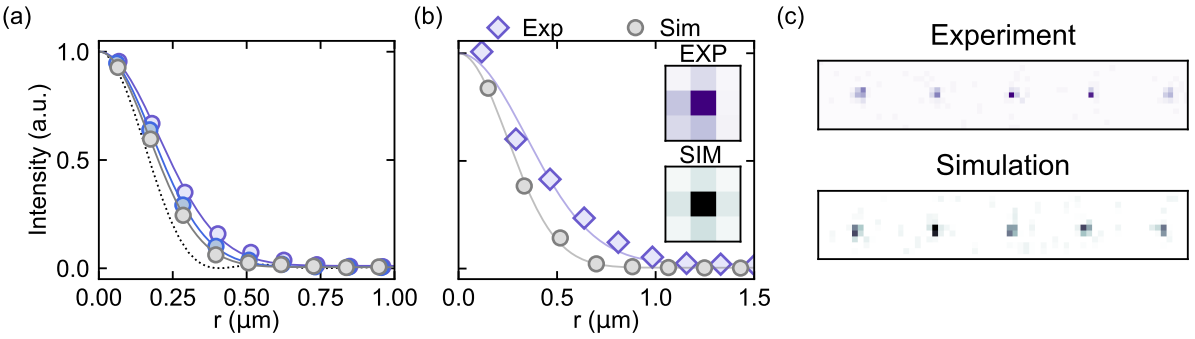

Figure 4.14| Size of the atomic signal. (a) Size of the atomic signal from Monte Carlo simulations for different imaging conditions: $t_{\mathrm{ill}} = 5\,\mu\mathrm{s}$, $U_0 = 1.1\,\mathrm{mK}$ (gray); $t_{\mathrm{ill}} = 20\,\mu\mathrm{s}$, $U_0 = 2.3\,\mathrm{mK}$ (blue); $t_{\mathrm{ill}} = 20\,\mu\mathrm{s}$, $U_0 = 1.1\,\mathrm{mK}$ (purple). Solid colored lines are Gaussian fits; black dotted line is the analytic PSF. The imaging magnification is set to $\times 80$ to enhanced the resolution of the simulations. (b) Size of the atomic signal for experimental and simulated images. Solid colored lines are Gaussian fits. Insets: experimental (top) and simulated (bottom) average signal from a single atom. We employ a $\times 8$ magnification for the simulated images, to match the experimental conditions. (c) Single-shot experimental image and simulation of a 5-site array. For both simulation and experiment in panels (b-c) we use a $\simeq 12\,\mu\mathrm{s}$ illumination time and a $\simeq$2.3 mK trap depth. Simulation and experimental data are obtained by averaging 100 and 500 independent realizations, respectively.

diffraction-limited signal. We first investigate the spatial resolution of our imaging scheme through Monte Carlo simulations, in order to disentangle fundamental limits from experimental imperfections. We simulate the full imaging process, accounting for stochastic photon scattering and the associated atomic motion, by adapting and extending the MOT trajectory simulation code [see Sec. 3.1.2]. The simulations start by drawing a random position and momentum from a Boltzmann distribution at the experimental temperature and considering a 3D harmonic confinement. We then simulate the atomic trajectory under pulsed illumination (400 ns single-pulse duration), taking into account stochastic photon scattering and the associated momentum kicks as well as the restoring force of the optical trap. We instead neglect all coherent effects.

For every emitted photon, we simulate the full detection process to reconstruct the image obtained on the camera. We collect only photons that are emitted within the solid angle of the objective aperture and we apply stochastic losses to account for the finite transmission of the objective at 399 nm (76%). The 3D position where each photon has been emitted is then converted into a two-dimensional position on the imaging plane by considering the point spread function (PSF) of the imaging system, which also accounts for the $\times 8$ magnification of our imaging system. This is done by Monte Carlo sampling a 2D cut of the PSF for each emitted photon in the imaging plane. As the PSF depends on the three-dimensional position in space where the photon has been emitted, this approach includes the out-of-focus blurring associated with atoms exiting the focal plane of the objective. Finally, the resulting photon distribution is integrated over the $4.6\,\mu\mathrm{m} \times 4.6\,\mu\mathrm{m}$ pixels of our qCMOS camera. The final image is generated by further accounting for the finite quantum efficiency and readout noise of camera pixels.

First, we verify that the simulation of a fixed motionless atom correctly reproduces the theoretical PSF of our imaging system, given by Eq. (2.7). However, the finite size of the camera pixels strongly affects the effective imaging resolution. In fact, with our relatively low magnification, the PSF size is comparable to that of a single pixel and the convolution between the PSF and the square window function corresponding to the pixel dimensions leads to a significant increase in the effective size of the signal. For this reason, even for a diffraction-

limited imaging system, it is not possible to obtain images that match the theoretical PSF with our current magnification. This also reduces the impact of atomic motion on the spot size, since the blur due to atomic motion is typically smaller than the effect of pixel convolution. To overcome this, we simulate images acquired with a $\times 10$ finer pixel grid, corresponding to a $\times 80$ magnification. In this way, we find that the signal of a fixed atom exactly reproduces the expected PSF [dotted line in Fig. 4.14(a)].

For this large magnification, we achieve near diffraction-limited images for a set of illumination times and trap depths [Fig. 4.14(a)]. As expected, lower trapping and longer illumination lead to a wider spot size as atoms undergo larger position spread in less confining traps. We analyze images by first averaging over many independent simulated images of a 10-site tweezer array and then overlapping the signals from different sites to obtain a single representative spot. This recentering is also beneficial to effectively increase the resolution of our pixel grid by allowing sub-pixel values. Once we have a single spot, we perform an azimuthal average and fit it with a 1D Gaussian function. We find a Gaussian $1/e^2$ waist radius of 340 nm, 360 nm and 400 nm for ($t_{\mathrm{ill}} = 5\,\mu\mathrm{s}$, $U_0 = 1.1\,\mathrm{mK}$), ($t_{\mathrm{ill}} = 20\,\mu\mathrm{s}$, $U_0 = 2.3\,\mathrm{mK}$), ($t_{\mathrm{ill}} = 20\,\mu\mathrm{s}$, $U_0 = 1.1\,\mathrm{mK}$), respectively.

Finally, we set the simulated magnification and parameters to match the experimental ones and we compare simulated and experimental images [Fig. 4.14(b-c)]. For $\simeq 12\,\mu\mathrm{s}$ illumination times and $\simeq 2.3\,\mathrm{mK}$-deep traps, we obtain Gaussian $1/e^2$ waists of 495 nm and 685 nm for the simulated and experimental images, respectively. We ascribe this difference to small residual aberrations in the imaging system or to the neglected coherent effects. In case the larger size of the experimental spot is due to some fundamental limitation, the attainable resolution can still be pushed to $< 500\,\mathrm{nm}$ by increasing the magnification and approaching the conditions presented in Fig. 4.14(a).

4.5.2 Maximum-likelihood estimation algorithm

Leveraging the high spatial resolution of our imaging scheme, we directly explore its applicability to tightly-spaced arrays. In our setup, we tune the tweezer spacing by changing the difference in the RF tones driving our AOD. We find that we cannot produce arrays with a spacing smaller than 1.5 µm, corresponding to a 750 kHz frequency difference between AOD tones. In fact, when we try to reduce the spacing even further we observe extremely low filling probability and short lifetime, probably due to cross-talk between different traps causing modulation of the traps and heating the atoms. Even though this value is quite larger than typical spacings in optical lattices, owing to our low magnification we observe that already at this distance the signal of different sites start to overlap, as it is often the case in quantum gas microscopy. We show an average and single-shot image of our 30-site array with 1.5 µm spacing in Fig. 4.15(a).

For this tightly-spaced array, defining non-overlapping ROIs around each tweezer becomes unfeasible. We partially overcome this by employing rectangular 1×3 pixels ROIs, where the reduced dimension along the array length mitigates leakage of signal between neighboring sites. However, the single-pixel length of the ROIs and the incommensurate ratio between tweezer-spacing and camera pixel grid results in cases for which ROIs do not appropriately cover their corresponding trap. Under these conditions, conventional ROI photon-counts thresholding fails and more advanced reconstruction methods are required.

Here, we adopt a reconstruction algorithm based on maximum likelihood estimation, which was initially developed in the group of Selim Jochim (Heidelberg University) to reconstruct atomic positions in free-flight and which has been extended to trapped atoms in a collaboration with Ralf Klemt (Stuttgart University). This approach is based on a statistical analysis of the single-shot photon distribution, which is compared to a set of hypotheses in order to obtain the most likely reconstruction. A fundamental requirement of this technique is a detailed knowledge

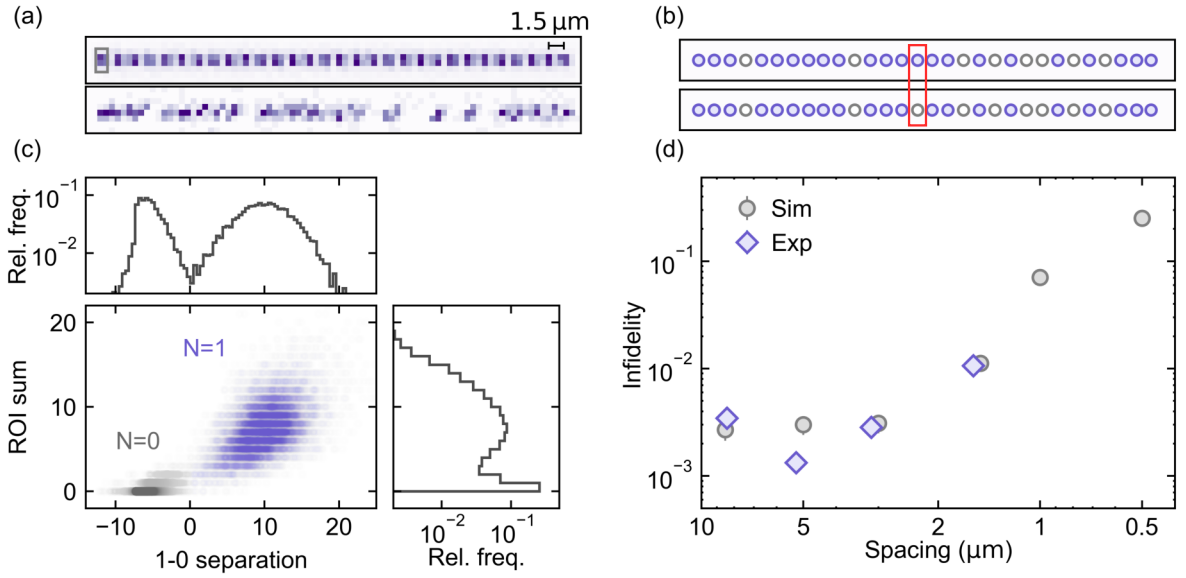

Figure 4.15| Imaging in dense arrays and maximum likelihood reconstruction. (a) Average (top) and single shot (bottom) image of a 30-site ^{171}Yb tweezer array with a 1.5 µm spacing. The rectangular grey square on the left represents the 1×3 pixels ROIs we employ for photon-count integration. The illumination time is set to $t_{\text{ill}} = 10.8\,\mu\text{s}$ and the trap depth is $U_0 \simeq 1.1\,\text{mK}$. (b) Schematic representation of the log-likelihood separation: we compute the logarithm of the difference between the likelihood of the most likely configuration (top) and that of alternative configurations (bottom) in the occupation of a single site (marked by the red rectangle) is flipped. (c) Comparison of photon counts in 1×3 ROIs and logL separation between filled and empty configurations for 1.5 µm-spacing arrays with $t_{\text{ill}} = 5.4\,\mu\text{s}$. (d) Infidelity versus spacing for $t_{\text{ill}} = 5.4\,\mu\text{s}$. Purple diamonds and grey circles indicate experimental and simulated data respectively, obtained from $> 10^4$ data points.

of the expected signal distributions. This can be obtained through numerical or Monte Carlo simulations of the imaging process or, as we do, by acquiring a large number of single-shot images and analyzing them to obtain a precise description of the single-atom signal. We do this by acquiring sets of consecutive images in our larger-spacing arrays prior to analyzing the tightly-spaced case. For the first image we employ the illumination time whose atom-signal we want to reconstruct, while we use a longer illumination for the second image to reach extremely high fidelity and, through post-selection, limit our analysis to certified atomic signals. We also acquire a separate set of empty images to characterize the distribution of noise and background counts recorded by the camera.

Having a deep knowledge of the expect dark and single-atom signal, we proceed with the analysis of tightly-spaced images. We start by formulating a set of global hypotheses h on the occupation of the full N-sites tweezer array: $|h\rangle = |n_1\rangle|n_2\rangle\cdots|n_N\rangle$, where n_i denotes the occupation of the i^{th} tweezer. Based on prior information on the range of expected occupation numbers (e.g. based on the LACs pulse duration in our setup), we can restrict $n_i \in [0,1]$ (or $n_i \in [0,1,2]$). From our knowledge on the shape of the atom spread function and photon distribution we can formulate a probability distribution $P_1(n_{\text{photon}}(x_i)|h)$ describing the expected number of photons n_{photon} impinging on a given pixel (indexed by x_i), conditioned on the hypothesis h. Knowing the noise-distribution and background counts of the camera we can also express the probability that a certain number of counts $n_{\text{counts}}(x_i)$ is recorded on pixel x_i, if

$n_{\text{photon}}(x_i)$ are impinging on that pixel: $P_2(n_{\text{counts}}(x_i)|n_{\text{photon}}(x_i))$. Given the experimentally measured counts $n^{\text{exp}}_{\text{counts}}(x_i)$, we can therefore trace back the conditioned probability of measuring $n^{\text{exp}}_{\text{counts}}(x_i)$ for $n_{\text{photon}}(x_i)$ impinging photons and the conditioned probability that $n_{\text{photon}}(x_i)$ photons are effectively impinging, given the reconstruction hypothesis h. We estimate the global logarithmic likelihood of a hypothesis by comparing the experimentally measured counts in each pixel to the expected distribution for that hypothesis:

$$\begin{aligned} \text{LogL}(h) &\propto \sum_i \sum_{n_{\text{photon}}} \log\left(P_2(n^{\text{exp}}_{\text{counts}}(x_i)|n_{\text{photon}}(x_i)) \cdot P_1(n_{\text{photon}}(x_i)|h)\right) \\ \text{LogL} &= \max_h \text{LogL}(h). \end{aligned} \tag{4.6}$$

For each experimental image, we compute the likelihood of all possible occupation-number hypotheses across the array and select the most likely one. We note that this is a global reconstruction scheme and therefore naturally takes leakage of signal from neighboring tweezers into account. Moreover, the spatial information on the atomic signal is fully utilized in the reconstruction, making this algorithm suitable for analyzing images where aberrations or position-spread during imaging play a significant role. On the other hand, the huge computational cost of computing the likelihood of all possible hypotheses strongly hinders its applicability to systems where there is little prior information on the possible occupation numbers and the expected atomic positions, as uncertainties in these quantities dramatically increase the number of hypotheses to be checked.

As figure of merit for single-atom detection, we compute the logarithm of the difference between the likelihood (logL separation) of the most likely configuration and that of alternative configurations in which the occupation of a single site is flipped. This is sketched in Fig. 4.15(b): we flip the occupation of each tweezer one-at-a-time and compute the logL separation between the filled and empty configuration. This results in a single output value (1-0 separation) from every tweezer, similarly to the ROI photon-count sum. We compare the 1-0 logL separation to the ROI sums for $t_{\text{ill}} = 5.4\,\mu\text{s}$ in Fig. 4.15(b). While the dark and bright peaks in the ROI sums are partially overlapped, indicating reduced detection fidelity, we observe a much clearer distinguishability in the logL separation. In particular, we can distinguish a peak with negative 1-0 separation, corresponding to empty sites where the likelihood of having zero atoms is larger than that of having one, and a peak of positive 1-0 separation, corresponding to filled sites.

The better results obtained by the MLE approach compared to simple photon counting is motivated by its accounting for the spatial information of the atomic signal, enabling high-fidelity detection in regimes where thresholding is not applicable. We assess the performance of this method by recording two equal images and evaluating the reconstruction fidelity with our Bayesian approach [see Sec. 2.4.2]. We investigate the dependence of the detection infidelity on tweezer spacing, applying the algorithm to simulated data for spacings beyond our experimental range [Fig. 4.15(d)]. The reconstruction fidelity exceeds 99%, for all spacings larger than 1 µm, and can be further enhanced by increasing the illumination time, at the cost of higher losses. For sub-µm spacing, the fidelity quickly degrades due to the lack of spatial information in our current imaging system, where the we focus most of the atomic signal on few pixels. We note that for large spacing the photon-count threshold performs better than the maximum likelihood approach, possibly due to mislabeling induced by the lack of spatial information on our images.

In conclusion, we have shown that our flash imaging scheme can be applied to tightly-spaced arrays even when the signal of neighboring sites is overlapping. In this case, with appropriate reconstruction algorithms, which are typically required in lattice microscopy, it is still possible to achieve high detection fidelity. This can be further enhanced by employing larger optical magnification in order to enhance the information encoded in the spatial signatures of single-atom signals. Another possible advancement could be to acquire several images with minimal illumi-

nation time and to analyze the time correlations between photon counts in different detections to discriminate the signal of an atom from the background noise.

4.6 Free-space imaging

The flash imaging technique was originally developed to image single atoms in free flight [175], where both fast detection and reduced position-spread are particularly crucial. In this case, imaging needs to be fast enough to yield significant photons before freely-evolving atoms move out of their original position [246]. Atomic movement also introduces a blurring of the signal, leading to uncertainties in determining the original position, and to a strong reduction of the signal for atoms flying out of the objective focal plane. To avoid the latter situation, it is often necessary to add a trapping potential providing vertical confinement during the free evolution and detection. Such potential can also be exploited to let the atoms expand in the trap, taking advantage of matterwave magnification techniques to access both atomic position and momenta [192, 242]. A complementary approach consists in introducing a 2D pinning lattice, which is ramped up during the free expansion and enables to reproduce typical fluorescence imaging conditions after an evolution in continuous space. This so-called continuum quantum gas microscopy has been recently introduced to investigate continuous many-body systems with single-atom resolution [229–231].

A large atomic mass is extremely beneficial to free-space imaging, as it results in both a small initial velocity upon release from a trap and in reduced position spread during imaging [234]. This, together with the short wavelength of the imaging transition, makes ytterbium a particularly favorable choice for free-space imaging, compared to lighter atomic species. In particular, upon release from trapping, single atoms undergo ballistic expansion, just as when they are released from a MOT [246]:

$$\sigma(t_{\mathrm{TOF}}) = \sqrt{\sigma_v^2 t_{\mathrm{TOF}}^2 + \sigma^2(0)} \tag{4.7}$$

where σ is the root-mean-square (RMS) spread of the atomic position after an expansion time t_{TOF} and $\sigma_v^2 = k_{\mathrm{B}}T/m$ is related to the atomic temperature in the trap and is essentially the initial velocity. During imaging, the atom position spread is instead given by [246]:

$$\sigma(t_{\mathrm{ill}}) = \frac{1}{3} v_{\mathrm{rec}} \sqrt{\Gamma_{\mathrm{sc}}}\, t_{\mathrm{ill}}^{3/2} + \frac{1}{\sqrt{3}} \sigma_v\, t_{\mathrm{ill}} \tag{4.8}$$

where $v_{\mathrm{rec}} = \hbar k/m$ is the photon recoil velocity and Γ_{sc} is the scattering rate.

Taking advantage of the large mass, we can detect single ytterbium atoms in free-flight with high spatial resolution and relatively long time-of-flight (TOF) without employing any trapping potential [Fig. 4.16(a)]. In particular, for our typical $\sim 20\,\mu\mathrm{K}$ temperatures we can allow for tens of microseconds of TOF expansion before exiting the objective focal plane. We investigate the atom spread during detection by imaging freely evolving atoms after a minimal $t_{\mathrm{TOF}} = 1\,\mu\mathrm{s}$ for variable illumination time [Fig. 4.16(b)]. To estimate the atomic position spread, we acquire many single-shots, select only those that contain one atom, and fit the Gaussian RMS size of the average image. Already for the shortest illumination, we observe an asymmetric shape of the position distribution, with atoms spreading more, and faster, along the propagation direction of the imaging light ($\hat{y}$-axis). This asymmetry is likely caused by the directional photon recoils induced by the imaging beams. For increasing illumination, atoms spread in both directions, saturating after around $20\,\mu\mathrm{s}$. This saturation could origin from a number of reasons. For long illumination atoms could exit the imaging focal plane due to the acquired momentum along the vertical direction, and stop to contribute to the measured photon signal. Alternatively, the profile could deviate from a Gaussian, resulting in an unreliable fit, or the experimental

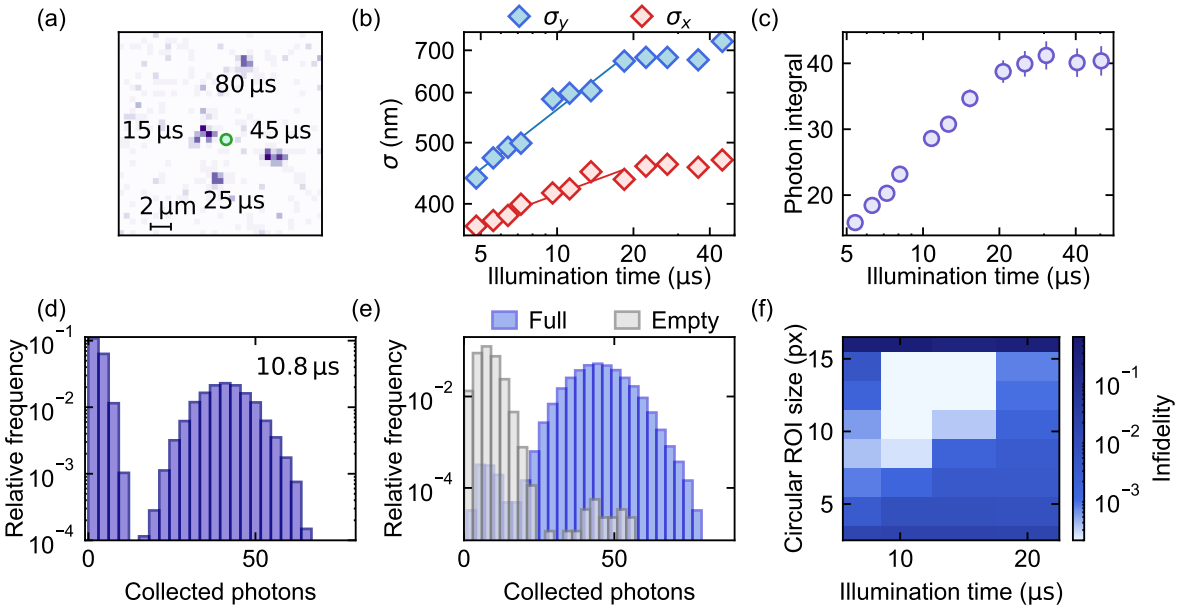

Figure 4.16| Free-space imaging. (a) Sum of 4 single-shots images of a single ^{174}Yb atom imaged in free space after being released from a tweezer trap, represented by the green circle. Imaging is performed with $t_{\mathrm{ill}} = 10.8\,\mu\mathrm{s}$ after a variable time-of-flight indicated above each spot. (b) Gaussian RMS size of an average image after 1 µs time-of-flight as a function of illumination time. Solid lines represent linear fits of the first data points points to extract the power-law exponent α (see text). (c) Integral of the collected photons from the Gaussian fits obtained in (b). (d) Photon-count histogram for free-space imaging and $t_{\mathrm{ill}} = 10.8\,\mu\mathrm{s}$. We employ circular ROIs with 9-pixels diameter to maximize the signal-to-noise ratio. (e) Photon-count histogram for $t_{\mathrm{ill}} = 10.8\,\mu\mathrm{s}$, pre-conditioned with a preliminary in-trap image. (f) Infidelity as a function of illumination time and circular ROI diameter. Each point results from 5000 experimental realizations. Panels (d-f) are obtained for a 10-tweezer ^{174}Yb array with minimal (1 µs) time-of-flight.

statistics could simply be insufficient to sample the position distribution when single atoms are dispersed over a large region. We fit the dependence on position spread over time and extract the exponent α of a $\sigma \propto (t_{\mathrm{ill}})^{\alpha}$ power law, finding $\alpha = 0.15$ and $\alpha = 0.31$ for the $\hat{x}$ and $\hat{y}$ direction, respectively. This is somewhat surprising as from Eq. (4.8) (discussed in Ref. [246]) we would have expected $\alpha \simeq 1.5$. Another possibility would be that of diffusive motion, for which, we would expect $\alpha \simeq 0.5$. We believe that this difference from expectations could be related to coherent effects, such as those discussed in Ref. [234] which we have never considered in this work. We also verified that changing the single-pulse duration of our flash imaging pulses in the $200\,\mathrm{ns} - 1\,\mu\mathrm{s}$ range has no significant effect on the position spread during imaging.

By analytically computing the area under the fitted Gaussians, we can estimate the average number of photons deposited on the camera by a single atom [Fig. 4.16(c)]. Similarly to the RMS size, we observe a saturation after $t_{\mathrm{ill}} \simeq 20\,\mu\mathrm{s}$, which we ascribe to atoms being lost due to e.g. flying out of the focal plane or to deviations from a Gaussian profile. Nonetheless, the relatively small position spread and the high photon-integral indicate that we can achieve detection fidelities comparable to the ones in trap also for detection in free-space.

In Fig. 4.16(d) we show the photon-count histogram obtained for 10-tweezers array of ^{174}Yb atoms with minimal (1 µs) TOF. To maximize the signal-to-noise ratio we integrate the photon counts over circular camera ROIs and enlarge the ROI size. This allows to detect photons that

are spread on a larger area due to atomic motion, while avoiding to include unnecessary pixels which would enhance the overall noise[8]. For 9-pixels diameter circular ROIs and $t_{\text{ill}} = 10.8\,\mu\text{s}$ we collect tens of photons from a single atom and achieve a very high separation between the dark and bright peaks of the photon-count histogram.

We measure the fidelity of our free-space imaging by taking advantage of our low-loss in trap detection. We perform a preliminary in-trap image with $t_{\text{ill}} = 6.3\,\mu\text{s}$, we then apply a cooling pulse to restore the initial temperature and release the trapping to perform a free-space image. By pre-conditioning on the initial occupancy, we can obtain separate histograms for the free-space detection of full and empty traps. In Fig. 4.16(e) we show a pre-conditioned histogram for a 10-site tweezer array of ^{174}Yb with $t_{\text{ill}} = 10.8\,\mu\text{s}$, $t_{\text{TOF}} = 1\,\mu\text{s}$ and integrated over 15-pixels diameter ROIs. We compute the infidelity by measuring the probability of detecting a discrepancy between the two images and correcting by the loss probability of the first image:

$$F = 1 - (P_{10} + P_{01}) + P_{\text{loss},1} \tag{4.9}$$

Even though we observe a few 0-1 and 1-0 events, they have a $\sim 10^{-4}$ probability and are compensated by the few-10^{-3} loss probability of the first image. We therefore find a 99.98(1)% fidelity limited only by statistics of the 5000 acquired images. By removing the loss-probability correction from Eq. (4.9), we can set a very pessimistic lower bound of 99.81(5)% to our free-space imaging fidelity.

We explore the dependence of the fidelity on illumination time and circular ROIs diameter in Fig. 4.16(f). Not surprisingly, shorter illuminations do not benefit from larger ROIs, as the photons are anyway distributed over few pixels and increasing the ROIs size only increase the background noise. On the other hand, longer illuminations benefit from larger ROIs up to a 15-pixel diameter, after which the fidelity drops dramatically. This happens when ROIs are so large that we observe leakage between the signal of neighboring atoms in our array. As we are using a negligible TOF, the atomic distance is essentially fixed by our tweezer array spacing, which sets a constant size-threshold, corresponding to 15 pixels, to this signal leakages. However, real experiments with multiple atoms evolving for longer TOFs will display variable inter-particle distances, making the choice of illumination time and ROI size more critical and likely requiring to employ algorithms not based on ROI photon-count integration.

Indeed, in real applications the fidelity of our free-spacing is not limited by the number of collected photons, but rather by the identification of the atomic positions out of the traps. In fact, before defining the ROIs for photon-counting we need to find the center of the atomic signal in the full camera ROI. While this is easily done by e.g. low-passing the images to find the peaks corresponding to the one-atom signal, the possibility of going out of focus or of finding multiple overlapping atoms complicates the situation. For such scenarios, we believe that more refined techniques such as reconstruction schemes and machine learning approaches will provide a powerful tool to increase the overall detection fidelity.

4.6.1 Free-space thermometry

Temperature is a fundamental quantity in many ultracold atoms experiments and it can be measured in a number of different ways. These notably include in-situ density profiles fitting [247], fluctuation thermometry [248, 249] and time-of-flight expansion [250]. The latter can be also used to probe the temperature of single atoms by performing repeated TOF measurements [246]. In this case, we stress that temperature is thermodynamic quantity and its value for a single atom is not well defined. On the other hand, many repetitions of a single-atom experiment

[8] Of course the positive effect of the circular ROIs is more evident for longer illuminations and noisier detectors.

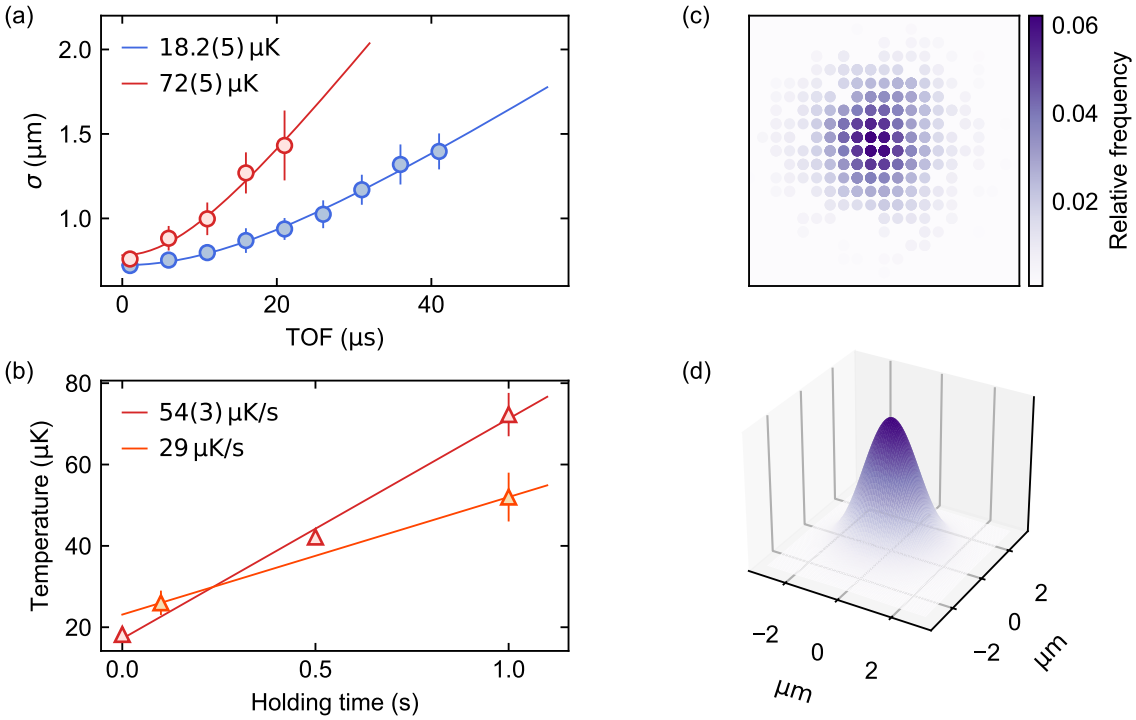

Figure 4.17| Free-space thermometry. (a) RMS size of the average position of an atom after variable time-of-flight. Blue and red data correspond to TOF measurement performed with a holding time of few-ms and 1 s in a 10-tweezer array. Solid lines are fits with a ballistic expansion, yielding the reported temperatures. (b) Measured temperature after variable holding time. Red and orange triangles correspond to a 10- and 2-tweezer arrays, respectively. Solid lines are linear fits to the data. (c) Reconstruction of the atomic positions after 40 μs of time-of-flight from a single tweezer. Each spot corresponds to a camera pixel of 575 nm size. (d) Gaussian fit of the resulting distribution yielding a 930 nm RMS size. Each panel is obtained from many hundreds of experimental repetitions.

allow to extract a value for the temperature by averaging the energy over many independent realizations [133].

As a first application, we employ free-space imaging to measure the temperature of tweezer-trapped single atoms. We prepare a 10-tweezer array of laser-cooled ^{174}Yb atoms and release them for variable TOF. As before, we perform many repetitions of the same experiment and fit a 2D Gaussian to the average image to determine the RMS position spread. We note that the effective average "cloud" displays the same features of a single-shot image of a non-interacting gas. In order to avoid overlap between signals from different traps and to reduce the probability of atoms exiting the objective focal plane we limit the investigated TOFs to few tens of microseconds. Moreover, we consider only the RMS along the $\hat{x}$ direction, orthogonal to our imaging beams, as we have seen that it is less affected by photon-recoil during imaging. As shown in Fig. 4.17(a), we fit the evolution of the position spread with a ballistic expansion [see Eq. (4.7)] and extract a temperature of 18.2(5) μK, in agreement with independent release and recapture measurements [see Sec. 2.3.5]. Assuming a Boltzmann temperature distribution, we can related the temperature measured from the radial expansion to the average radial occupation number. In particular we can write $k_B T = 2\langle n_\mathrm{r}\rangle \hbar\omega_r$, where ω_r is the radial trap frequency and $\langle n_r\rangle = (\langle n_x\rangle + \langle n_y\rangle)/2$. Using this expression we find $\langle n_\mathrm{r}\rangle = 1.35$.

Holding the atoms in our tweezer traps results in heating due to off-resonant scattering and technical noise. Understanding the trap-induced heating rate can be useful to gain insight into its origin, try to mitigate it, or at least take it into account during experiments. By performing TOF thermometry after variable holding time we are able to extract an heating rate of 54(3) µK/s for a trap depth of ≃2.3 mK, consistent with our release and recapture measurements [Fig. 4.17(b)]. To disentangle intermodulation noise between RF tones from other heating sources, we perform the same experiments in a 2-tweezer array, where such noise is absent. In this case we obtain a heating rate of $\simeq 29\,\mu K/s$, confirming that intermodulation noise is a major heating source in our setup. This could be improved by fine-tuning of the RF tones driving the AOD, to avoid overlap between the fundamental tones and their sums and differences.

Even though we have performed single-atom TOF experiments, so far we have only looked at average images. To harness the full potential of single-atom resolution we instead need to detect the presence, and the position, of single atoms in every experimental shot. This strongly expands the amount of available information, allowing to access correlations, if more particles are present, and full counting statistics of the atomic distribution.

To detect the positions of individual atoms in free space, we employ the following algorithm. We normalize, clip and filter our experimental images in order to identify the pixel-region with the highest probability of containing an atom. We identify the central pixel of this region and draw a ROI around it. We then sum the collected photons in the ROI to determine the presence of the atom with thresholding and take the central pixel as its location. As already mentioned, this method is sufficient for high-fidelity imaging when either a single atom is present or when the number of atoms is known and we are only interested in their positions. For more complicated scenarios, more refined machine learning techniques can be explored.

In Fig. 4.17(c), we show the histogram over hundreds of repetitions of the positions of a single atoms after $t_{\mathrm{TOF}} = 40\,\mu s$ from a single tweezer. The obtained position distribution reflects the density profile of the original single-atom wavepacket. Through free-space imaging we can therefore directly reconstruct the probability distribution of an atomic wavefunction through repeated sampling, where each image corresponds to a single projective measurement. The same technique has also been employed in continuum quantum gas microscopes [251], which however suffer from the additional complexity of requiring a pinning lattice compared to free-space imaging. In our case, the wavepacket is that of a particle in a harmonic potential and has a simple Gaussian profile. As we are observing the radial distribution of the atomic position, we can relate its variance to the average radial quantum number $\langle n_r \rangle$ as [251]:

$$\sigma(t_{\mathrm{TOF}})^2 = (2\langle n_r \rangle + 1)\,\frac{\hbar}{2m\omega_r}(1 + \omega_r^2 t_{\mathrm{TOF}}^2) \tag{4.10}$$

This approach is complementary and equivalent to the ballistic expansion fit as it also assumes a ballistic evolution after release. We show the reconstructed wavefunction in Fig. 4.17(d), corresponding to $\langle n_r \rangle = 3.7(2)$. This results in an average temperature of $T \simeq 19.5(8)\,\mu K$ for the reduced trap depth $U_0 \simeq 210\,\mu K$, with a corresponding radial trap frequency $\omega_{\mathrm{r}} \simeq 2\pi \times 55\,\mathrm{kHz}$. The higher $\langle n_r \rangle$ measured here is due to the very different sequence employed in this experiment, where we do not perform LACs and laser-cooling in the tweezer but rather try to employ evaporation to reduce the atomic temperature and reduce the trap depth until only one atom is left.

Single-atom wavefunction reconstruction is not limited to thermometry of Gaussian harmonic oscillator states. In fact, it can be employed to perform tomography of more exciting quantum states, such as Fock states between neighboring tweezers, which has so far relied on average images [252]. Moreover, this technique also allows to detect fluctuations on top of the atomic distribution, enabling studies of fluctuation thermometry with full counting statistics [179]. Even though the large mass of ytterbium enables high-fidelity free-space imaging without the need

of additional traps, introducing a vertical confinement will be very beneficial, allowing longer TOF expansion and the implementation of matterwave magnification techniques. Finally, while the study of single atoms has its own level of merit, free-space imaging find its most exciting application in the detection of multi-atom ensembles, where it can be employed to count and pin-point each particle, allowing to access both atom-number fluctuations and correlations in real and momentum space.

5

Multi-atom ensembles

When multiple atoms are confined within the same trap, detecting their number becomes challenging. Typical fluorescence imaging is not suited to number-resolved detection, as the cooling light induces parity projection through light-assisted collisions in the trap [134, 225, 253, 254], and imaging is too slow to count atoms in free space. While there have been demonstrations of detection of two particles in the same site by spatially separating them [10, 146, 249, 255–258] these techniques come at the cost of additional experimental complexity. Flash imaging offers a compelling alternative approach for number-resolved detection in atom-arrays. The short imaging timescale allows to detect multiple atoms in a trap before parity-projection occurs [136] or, in free space, after a short time-of-flight [234]. Besides counting, flash imaging allows to image atomic ensembles in free-flight, enabling measurements of particle number, position and momentum by pin-pointing the location of each atom [15, 175, 259].

In this chapter we will discuss number-resolved detection of systems of few ytterbium atoms through our flash imaging scheme. First we will show how we can count the number of atoms in a multiply-filled trap, taking advantage of the faster timescale of our detection compared to the LACs dynamics. Owing to our good optical resolution, we can also detect multiply-filled sites in tightly-spaced arrays without the need to dynamically readjust the inter-particle spacing. We will then employ our number-resolved imaging to track the near-deterministic loading dynamics of single ^{171}Yb atoms in tweezers, obtained through a combination of gray molasses cooling and repulsive molecular potentials [53, 66]. Fitting the population evolution with a rate equations model, we extract the relevant loss rates and shed light on the mechanisms underlying enhanced tweezer loading. Finally, we will show how we can employ flash imaging to observe multiple atoms released in free space from a single trap and discuss our first steps towards the realization of cold few-fermion samples.

5.1 Number-resolved imaging

Knowing the exact number of particles confined in a single trap is essential for a wide range of experiments. In mesoscopic ensembles, the particle number strongly influences the global properties of the system, and considerable effort is devoted to understanding how many-body effects emerge from just a few particles [14, 16, 19]. The number of emitters is also a key parameter in the development of collective optical phenomena, and precise knowledge of the atom count at sub-wavelength distances would greatly benefit studies of collective atom–light interactions [97, 98]. In lattice microscopes, measurements involve the detection of filled sites. However, achieving on-site number resolution would provide a powerful tool for studying itinerant many-body systems, where the competition between interactions and tunneling determines lattice-site occupations [10, 234, 249, 256]. Such capability is particularly relevant for exploring multi-orbital or SU(N)-symmetric Hubbard-like Hamiltonians [47, 90, 109, 111, 164, 165]. On-site atom-counting would also benefit studies of optical lattice clocks, where interactions

between particles sitting on the same site induce frequency shifts of the clock transition [260, 261]. Finally, number-resolved imaging could enhance the precision of tweezer clocks platform by enabling detection in multiply-filled traps.

For these applications, number-resolved detection is hardly achieved by fluorescence imaging relying on cooling. In fact, cooling light induces pairwise losses through light-assisted collisions in the traps [134, 225, 253, 254], and imaging is too slow to count atoms in free space. This limitation has been overcome by spatially separating multiple particles in a trap, either through a combination of magnetic field gradients and light-sheets [10, 146, 249, 255–257], a scheme which would not be suitable for non-magnetic atoms like ytterbium, or through optical superlattices [258]. These techniques have allowed to detect up to two particles per site, but have a large cost in terms of additional experimental complexity.

On the other hand, the short timescale of flash imaging allows to resolve the number of atoms trapped within a single trap before LACs-induced parity projection [136]. Atom-number resolution can similarly be achieved through a short TOF, during which the signal of multiple atoms remains overlapped as if they were in a single trap [234]. This scheme has allowed to detect up to three erbium atoms in a trap with high fidelity and it has been employed for the investigation of itinerant Hubbard systems with long-range interactions [233].

5.1.1 Multi-atom counting

Taking advantage of the separation of timescales between our fast detection and the LACs dynamics, we employ flash imaging to resolve the number of atoms in each trap in multiply-filled tweezer arrays. For this study, we focus on ^{171}Yb and we remove the LACs stage of the experimental sequence to allow multiple occupations of the same traps. By employing large circular camera ROIs (14-px diameter) and increasing the illumination time we resolve up to 7 distinct peaks in the photon-count histograms [Fig. 5.1(a)].

We fit our histograms with a multi-peak function to extract the thresholds for atom-counting as well as the detection fidelity and occupation probabilities for different atom numbers. Our fitting function consists in the sum of Gaussian peaks, each corresponding to an atom number N, and a Poissonian distribution which accounts for the dark peak ($N = 0$). In addition, we employ and exponential tail to account for high-count events, where individual peaks are no longer well-resolved. The full fitting function reads:

$$\begin{aligned} f_{N_{\max}}(n) = A_0 \, \frac{x_0^n}{n!} e^{-x_0} \; + \sum_{N=1}^{N_{\max}-1} A_N \, \exp\left(-\frac{(n-x_N)^2}{2\sigma_N^2}\right) + \\ + A_{N_{\max}} \, (n - x_{N_{\max}})^2 \, e^{-\gamma(n-x_{N_{\max}})} \, \theta(n - x_{N_{\max}}) \end{aligned} \tag{5.1}$$

where $N_{\max}$ is the total number of considered peaks, n are the photon counts, x_N, σ_N and A_N are the centers, widths and amplitudes of the Gaussian peaks; γ is a decay constant and θ is the Heaviside step function. The last term of Eq. (5.1) is designed to optimize the fit of the last peak before the exponential tail. Accurate fitting requires careful setting of the initial guess for the various parameters (e.g., peak positions and amplitudes), which we implement via a preliminary peak-search on a smoothed version of the histogram.

From the amplitude of the fitted peaks we can obtain the occupation probability for each atom number with good precision. In Fig. 5.1(b) we show the occupation probabilities obtained from the histogram in (a), corresponding to the result of the loading from the MOT. The atom-number distribution in the traps results from the interplay between two competing processes: the loading from the MOT, and the losses induced by light-assisted collisions [134]. In our setup, the combination of a narrow-line MOT and non-magic trapping results in a roughly Poissonian probability distribution [224] with average per-trap atom number $N_{\text{avg}} = 3.6(2)$, obtained for

a MOT loading time of 100 ms and a tweezer loading depth $U_0 \simeq 570\,\mu K$. We do not find any significant effect of increasing the duration of the tweezer-loading stage, while N_{avg} can be enhanced by increasing the MOT density, through e.g. longer loading.

Besides the occupation probabilities, we extract from the multi-peak fitting function the photon-count thresholds th_N used to distinguish between N and $N+1$ atoms in single shots. Each threshold is obtained by minimizing the overlap between peaks corresponding to different atom numbers. Following Ref. [136], we extract the counting fidelity for each atom number N as the ratio between the correct classification events, i.e. the integral of the N-th peak between thresholds th_N and th_{N+1}, and all events within the thresholds:

$$F_N = \frac{\int_{th_N}^{th_{N+1}} \exp\left(-\frac{(n-x_N)^2}{2\sigma_N^2}\right) dn}{\int_{th_N}^{th_{N+1}} f_{N_{\max}}(n) dn} \tag{5.2}$$

where $f_{N_{\max}}(n)$ is defined in Eq. (5.1). For $t_{ill} = 20.7\,\mu s$ we obtain fidelities of 99.6%, 97.6%, 94.3%, 90.4%, 86.9% and 82.8% for counting $N = 1, 2, 3, 4, 5, 6$ atoms, respectively. The fidelity decreases for larger atom numbers due to the broadening of the Gaussian distributions for higher numbers of collected photons. Even in the ideal case of a Poissonian distribution, the width of the N-th peak increases with N, requiring a larger photon count per atom to distinguish it from neighboring peaks. To enhance the fidelity of the higher atom numbers it is therefore necessary to increase the illumination time [Fig. 5.1(c)]. For $N \leq 6$ case, we can use our photon-count thresholds to reliably distinguish different trap occupancies, as shown in Fig. 5.1(d, e). While our current scheme is limited to $N \leq 6$, we believe that this could be improved in the case of a single tweezer. In this case, a larger ROI and longer illumination time, possibly combined with a small TOF and an additional vertical confinement to keep atoms in focus, could help to increase the detection range.

We also test the performances of multi-atom detection with our double-imaging scheme to explore the possibility of taking successive number-resolved images. In Fig. 5.1(f) we show the correlation of photon counts between two equal successive images with $t_{ill} = 10.8\,\mu s$. In general, we observe larger than expected single-atom imaging losses, as visible from the significant transfer of counts from N to $N-1$ between images. Even for $N = 1$, we find a very large $\simeq 38\%$ loss probability, simply estimated as the probability of detecting one atom in the first image and zero in the second. We mainly ascribe this to a higher initial atomic temperature. In fact, the experimental sequence employed to prepare multiply-filled traps does not include any cooling stage after the MOT, to avoid LACs. Therefore, we expect the atomic temperature in the tweezers to be higher than in the single-atom case, leading to higher losses even for $N = 1$. While the survival probability for the $N = 2$ is rather low ($\simeq 35\%$), losses are dominated by $2 \to 1$ events and the $2 \to 0$ probability ($\simeq$14%) is compatible with the probability of losing the two atoms independently. Our findings indicate that the flash imaging light does not lead to significant pairwise losses for the investigated illumination times and that the survival probability, even for multiple atoms, is dominated by single-atom losses. This suggests that repeated multi-atom detection could be within reach, provided that shorter illumination times can be afforded and that the initial temperature can be lowered even in multiply-occupied traps. Finally, the Bayesian approach described in Sec. 2.4.2 could be extended to $N > 1$ in case a more refined analysis of the imaging losses and fidelity is required.

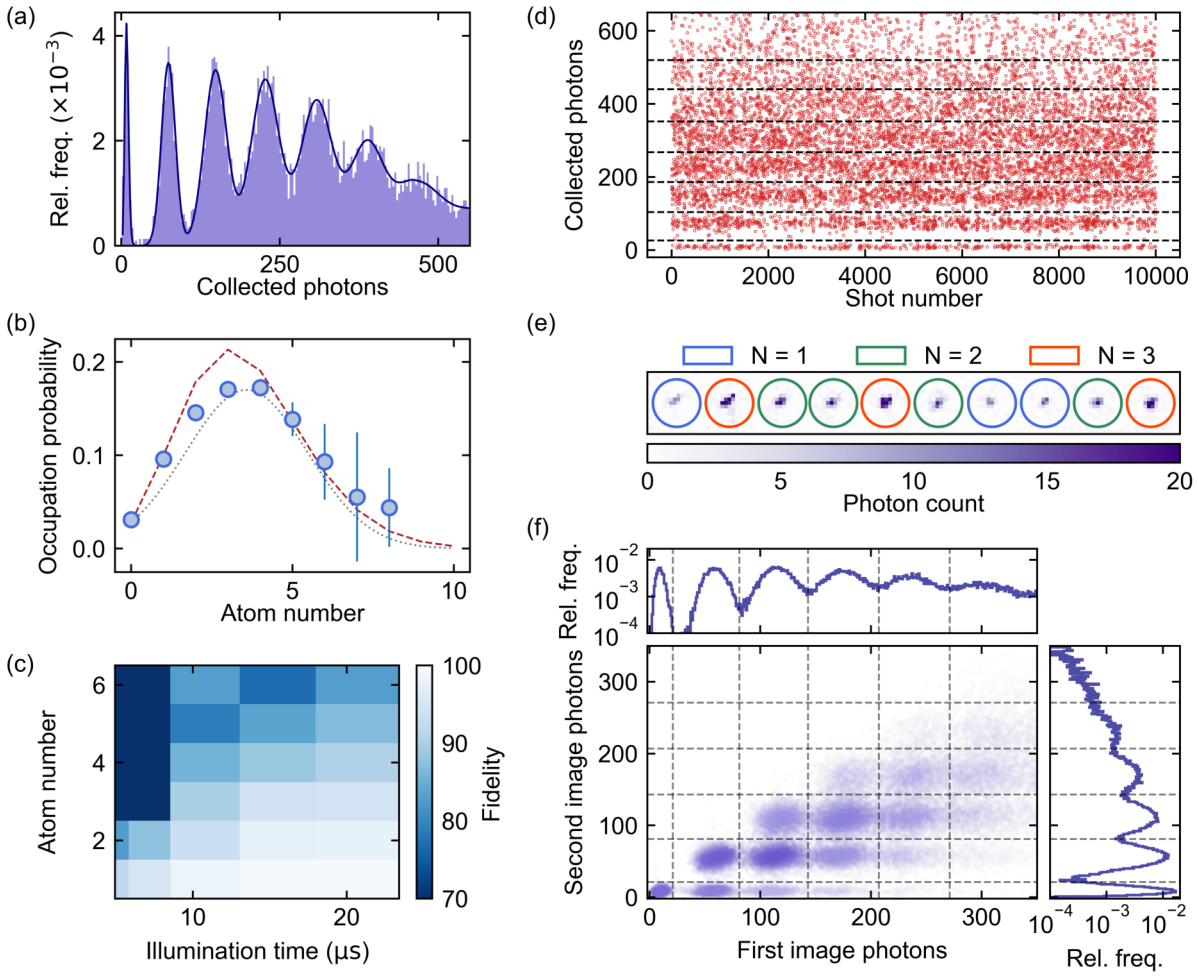

Figure 5.1| Number-resolved imaging. (a) Multi-atom photon-count histogram for $t_{\mathrm{ill}} = 20.7\,\mu\mathrm{s}$. Solid line is a multi-peak fit. (b) Occupation probability of different atom numbers. Blue circles indicate the probabilities extracted form the fit in (a), giving an average atom number $N_{\mathrm{avg}} = 3.6(2)$; the red-dashed line is a Poissonian distribution centered on N_{avg} and the black dotted line is a Gaussian with mean $\mu = \sigma^2 = N_{\mathrm{avg}}$. Error bars indicate the errors on the fit amplitudes, with the last three points having larger error bars due to lower distinguishability of the peaks corresponding to $N \geq 6$. (c) Fidelity of detecting different atom numbers as a function of illumination time. (d) Multi-atom photon counts as a function of experimental repetition for $t_{\mathrm{ill}} = 20.7\,\mu\mathrm{s}$. Dashed lines indicate the thresholds for atom-number counting. (e) Single-shot image with $t_{\mathrm{ill}} = 20.7\,\mu\mathrm{s}$. Colored circles indicate the photon-integration ROIs and the obtained atom number in each trap. (f) Photon-count correlations between two successive multi-atom images with $t_{\mathrm{ill}} = 10.8\,\mu\mathrm{s}$. All data are obtained for a 10-tweezer array of ^{171}Yb atoms in $\simeq 2.27\,\mathrm{mK}$-deep traps. Photon counts are integrated over 14-px diameter ROIs and each point is the result of thousands of experimental repetitions.

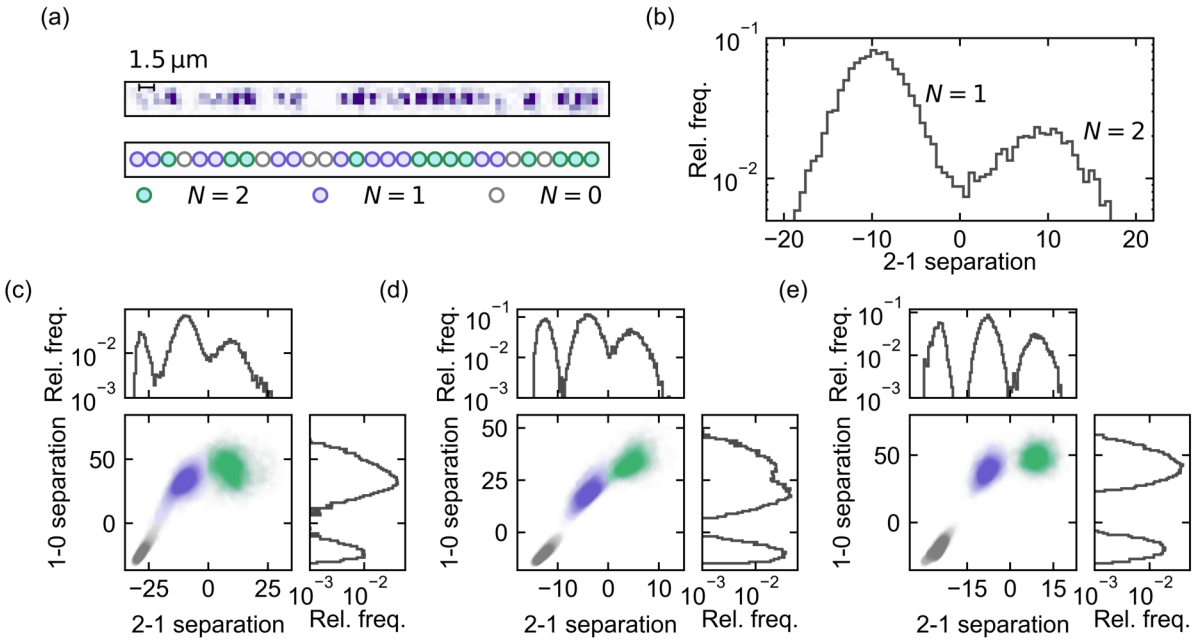

Figure 5.2| On-site counting in dense arrays. (a) Single-shot and MLE reconstruction with $N = 0, 1, 2$ for $t_{\text{ill}} = 20.7\,\mu\text{s}$. (b) Log-likelihood separation of the 2-1 atoms hypotheses for occupied sites in a multiply-filled array with 1.5 µm spacing and $t_{\text{ill}} = 20.7\,\mu\text{s}$. (c) 2-1 and 1-0 separation allowing us to distinguish empty (grey), singly-occupied (purple) and doubly-occupied (green) tweezers in 1.5 µm spacing arrays with $t_{\text{ill}} = 20.7\,\mu\text{s}$. (d) and (e) 2-1 and 1-0 separation for simulated data with $t_{\text{ill}} = 10\,\mu\text{s}$ and $t_{\text{ill}} = 20\,\mu\text{s}$ respectively. All experimental points are obtained from thousand of repetitions at a trap depth $U_0 \simeq 1.1\,\text{mK}$.

5.1.2 On-site counting in dense array

We explore the possibility of extending our on-site atom-counting capability to tightly-spaced arrays, making the first steps towards in-trap number-resolved microscopy. We start by preparing 30-sites array with a 1.5 µm spacing [see Sec. 4.5.2] and tune the LACs duration to restrict atom occupancy to $N = 0, 1, 2$. We then image the atoms employing a relatively long (20.7 µs) illumination time to enhance the distinguishability between singly and doubly occupied traps. By applying the MLE reconstruction algorithm described in Sec. 4.5.2 we can successfully determine the occupancy of each tweezer trap [Fig. 5.2(a)].

To discriminate between single and double occupancies, we first distinguish between empty and filled traps and then compare the probability of having one or two atoms in each filled trap. For our experimental data we achieve a good separation between the negative 2-1 separation peak, corresponding to single occupations, and the positive 2-1 peak referring to double occupancies [Fig. 5.2(b)]. We note that our choice of LACs duration, optimized to have a negligible $N = 3$ probability, also results in a lower probability of double compared to single-atom filling. For the most likely reconstruction, we compute both the 1-0 and 2-1 separation by changing the occupation of each site to zero, one or two and determining the likelihood difference with the remaining tweezers kept at the their most likely occupation. We observe a very large separation between the empty and occupied hypotheses as the model discriminates very well between these two scenarios, while it struggles more to discriminate between single and double occupations [Fig. 5.2(c)]. We note that for the multi-atom case we find small discrepancies between the observed signal shape and model used in the reconstruction (based on the shape of a single

atom). We ascribe this to the larger atomic losses of multi-atom imaging, which result in a larger signal spread. Indeed by applying the reconstruction algorithm to simulated data, were no loss mechanism is present, we obtain a much clearer separation between the one- and two-atom hypotheses [Fig. 5.2(d,e)]. Our findings indicate that flash imaging could be a possibility for number-resolved microscopy.

5.2 Light-assisted collisions dynamics

Scalability—the ability to increase the size of the system—is a highly desirable feature of any platform for quantum science and technology. In this respect, atom arrays exhibit outstanding performances, with both optical lattices and tweezer arrays enabling single-particle trapping and detection of up to thousands of atoms [12, 139, 140, 142]. However these numbers might be not sufficient for the any useful realization of quantum computing. In fact, fault tolerant computation requires logical qubits composed of many physical ones for error correction, thus pushing the demands to even higher numbers.

Typically, single-atom occupancy in optical traps is achieved through red-detuned parity-projective light-assisted collisions [134, 225, 254]. This approach yields a $\sim 50\%$ filling fraction and necessitates tweezer rearrangement to obtain defect-free arrays [262]. Furthermore, under these conditions, roughly half of the traps remain unused during the actual experiment, resulting in inefficient use of both laser power and optical field of view.

The probability of loading single atoms in an optical trap can be significantly enhanced by driving blue-detuned light-assisted collisions, through which filling factors of about 90% have been obtained both for alkalis [66–68] and ytterbium atoms [53]. Such near-deterministic loading allows to drastically increase the filling fraction, simplifying rearrangement schemes and increasing the overall loading speed and efficiency. A precise description of the LACs dynamics, and specifically of the atom loss rates, could provide a benchmark for theoretical works aimed at finding the optimal regimes for single-atom loading. Quantitative studies have been performed for rubidium atoms in the parity-projective regime [225, 254, 263] and, very recently, also in the enhanced loading regime [264]. Similar loss-rates measurements have also been performed for tweezer-trapped erbium atoms [136, 265], albeit only for parity-projective LACs. Equipped with our number-resolved detection, we can quantitatively investigate the dynamics of LACs leading to the near-deterministic loading demonstrated for ^{171}Yb [53].

5.2.1 Atomic collisions in repulsive molecular potentials

The LACs process can be understood by considering an atomic pair undergoing a collision under non-resonant illumination [7, 66]. We show a sketch of the red- and blue-detuned LACs mechanism in Fig. 5.3(a). For a homonuclear pair separated by a distance R much larger than the repulsive range of the Van der Waals interactions, the ground-state S+S inter-atomic potential varies as $-1/R^6$. When the inter-particle distance is such that the driving light becomes resonant with one of the many available molecular potentials, the pair is excited to a S+P electronic state. These states feel a $1/R^3$ potential whose sign and amplitude are determined by the specific properties of the addressed molecular potential [264]. Atom pairs in the S+P state roll down the molecular potential, acquiring kinetic energy before spontaneously decaying back to the S+S ground state. The amount of kinetic energy acquired results in loss of one, both, or none of the atoms involved. For red-detuned LACs light, atoms are excited to an attractive molecular potential, resulting in large acquired kinetic energy and loss of both the atoms. Typically, these are the kind of LACs that are employed to achieve single-atom occupancy in optical traps and the induced pairwise losses are responsible for parity-projection and the $\sim 50\,\%$ filling fraction [134,

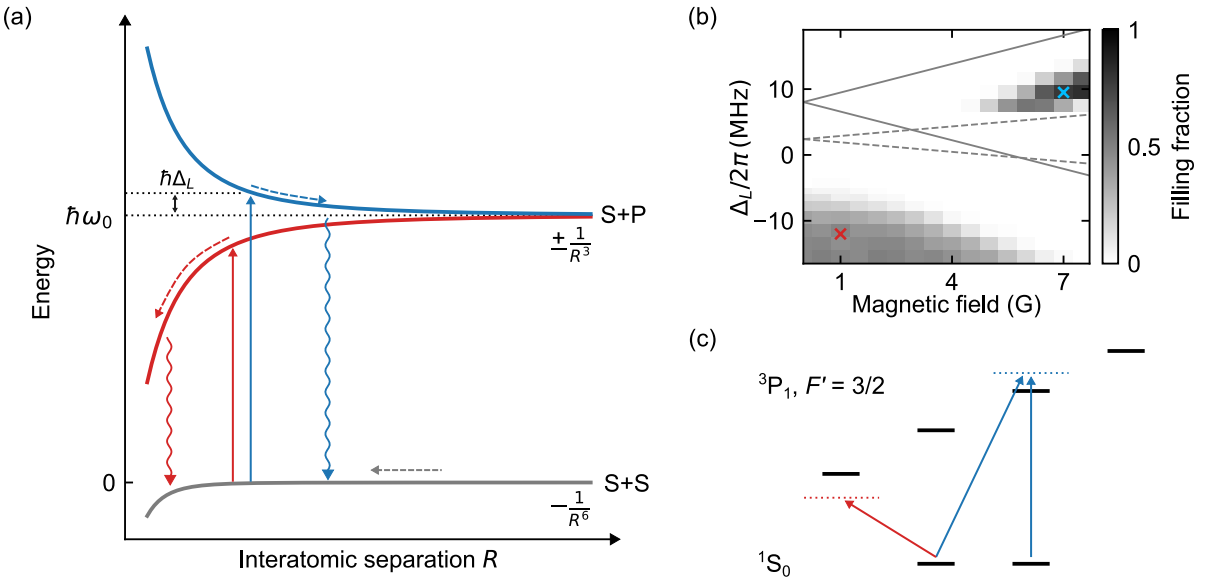

Figure 5.3| Enhanced loading through blue-detuned LACs. (a) Sketch of the LACs mechanism for red and blue-detuned light. A colliding atomic pair can be excited by a red- or blue-detuned photon (solid arrows) to an attractive or repulsive S+P molecular potential, respectively. The atoms then roll down the potential (dashed arrows), acquiring kinetic energy until a spontaneous emission event brings them back to the S+S ground state (wavy arrows). For blue-detuned light, the acquired kinetic energy is limited by the detuning Δ_L with respect to the single-atom resonance ω_0. Only two of the many available molecular potentials are drawn [264]. Energy axis is not to scale. (b) ^{171}Yb filling fraction versus magnetic field and detuning for a 80 ms LACs-pulse with intensity $I_L \simeq 215\, I_{sat}$ in $\simeq 570\,\mu$K-deep traps. Dashed (solid) lines show the splitting of $m'_F = \pm 1/2$ ($m'_F = \pm 3/2$) states. The blue cross marks our working point for near-deterministic loading ($\Delta_L/(2\pi) \simeq 9.4$ MHz, $B = 7$ G) and the red cross indicates representative red-detuned LACs parameters yielding $\sim 50\%$ filling fraction. (c) Scheme of the involved levels in the red-detuned and blue-detuned LACs for ^{171}Yb. Red and blue arrows indicate the relevant transitions of red- and blue-detuned LACs respectively.

225, 254]. On the other hand, blue-detuned light leads to the excitation of a repulsive molecular potential, where atoms acquire only a limited amount of kinetic energy before a spontaneous emission event. This energy cap is set by the LACs pulse detuning Δ_L and it can be tuned such that only a single atom is expelled from the trap after an inelastic collision. Therefore, blue-detuned LACs allow to achieve near-deterministic single-atom loading as atoms are expelled from the trap one at a time, until only one is left [53, 66, 68].

While blue-detuned LACs pulses in repulsive molecular potentials allow to achieve single-atom occupancy in an almost deterministic way, the applied blue-detuned light expels the remaining single-atoms from the trap rendering the process practically ineffective. This limitation can be overcome by combining red-detuned cooling light, which induces parity projection, with the blue-detuned light driving $2 \to 1$ losses. By making sure that the $2 \to 1$ rate dominates the pairwise losses and employing deep optical traps, this technique has allowed to reach $\simeq 90\%$ filling fractions for tweezer-trapped rubidium atoms [66, 266, 267]. A more efficient approach to achieve enhanced tweezer loading with blue-detuned LACs consists in taking advantage of sub-Doppler mechanisms to provide cooling with the same light that drives the LACs [68]. This simplifies the beams configuration, solves the conflict between $2 \to 1$ and $2 \to 0$ loss rates and

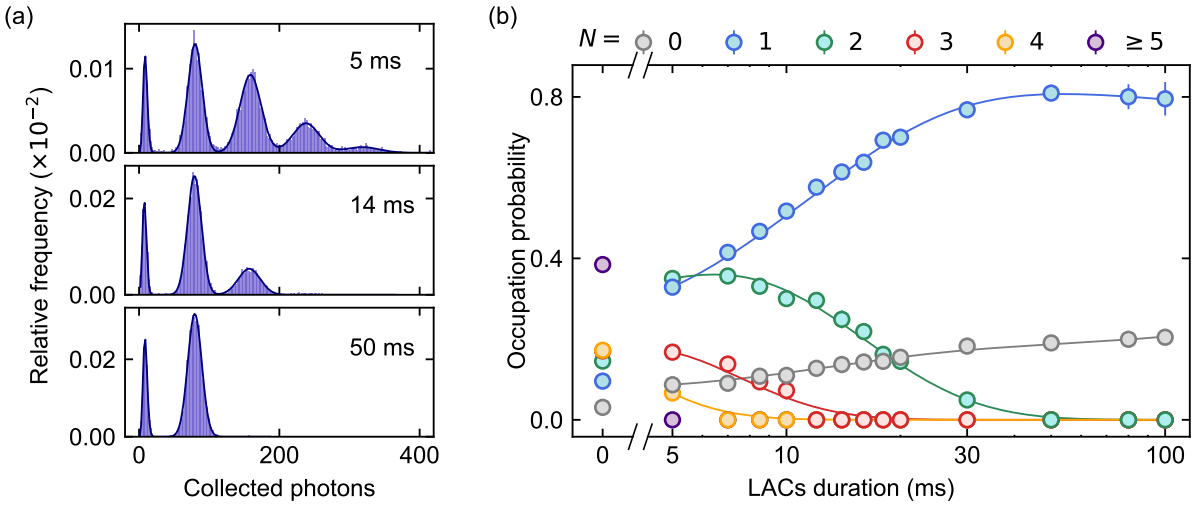

Figure 5.4| Enhanced loading dynamics. (a) Multi-atom photon-count histograms recorded after different LACs-pulse durations (5, 14 and 50 ms), using $t_{\mathrm{ill}} = 20.7\,\mu\mathrm{s}$ and integrating over circular ROIs with 7-px radius. Solid lines are multi-peak fits. (b) Filling probability versus blue-detuned LACs-pulse duration with intensity $I \simeq 170\, I_{\mathrm{sat}}$; detuning and magnetic field are those indicated by the blue cross in Fig. 5.3(b). Solid lines are fits with the rate-equation model. Each point corresponds to around 1000 shots in a 10-tweezer ^{171}Yb array.

typically requires much shallower traps as atoms are cooled during the process. For ^{87}Rb, this is possible thanks to a sub-Doppler Λ-enhanced gray-molasses cooling scheme [268, 269].

Recently, a similar feature has been observed in ^{171}Yb, where $\simeq 90\%$ loading efficiency has been achieved through blue-detuned LACs in 790 µK-deep tweezer [53]. By investigating the filling fraction dependence on applied magnetic field and detuning of the LACs pulse, we are able to reproduce the feature observed in Ref. [53] and achieve near-deterministic loading of single ^{171}Yb atoms [Fig. 5.3(b)]. In particular, we obtain a filling factor of 86.6(2)% for a 30-sites tweezer array by driving a LACs pulse with $\Delta_{\mathrm{L}}/(2\pi) \simeq 9.4\,\mathrm{MHz}$ and intensity $I_{\mathrm{L}} \simeq 170 I_{\mathrm{sat}}$, where the detuning is defined from the free-space $^1\mathrm{S}_0 \rightarrow {}^3\mathrm{P}_1|F' = 3/2\rangle$ transition and I_{sat} is the saturation intensity of the $^1\mathrm{S}_0 \rightarrow {}^3\mathrm{P}_1$ transition. We drive the LACs for 80 ms in $\simeq 570\,\mu\mathrm{K}$-deep traps applying a magnetic field $B = 7\,\mathrm{G}$ aligned with the tweezers polarization direction. The magnetic field is necessary to further split the excited m'_F states, which are already separated by the tensor light-shift of the optical trap, in order to isolate the three-level system depicted in Fig. 5.3(c). In such system, the $\simeq 12\,\mathrm{MHz}$ splitting between the $^3\mathrm{P}_1|F' = 3/2, m'_F = 3/2\rangle$ and $^3\mathrm{P}_1|F' = 3/2, m'_F = 1/2\rangle$ states is large compared to the $^1\mathrm{S}_0 \rightarrow {}^3\mathrm{P}_1$ transition linewidth. This allows to drive LACs on repulsive molecular potentials and grey-molasses cooling with the same laser light, blue-detuned of few-MHz from the $^1\mathrm{S}_0 \rightarrow {}^3\mathrm{P}_1|F' = 3/2, m'_F = 1/2\rangle$ transition.

5.2.2 Near-deterministic loading dynamics

We employ our number-resolved detection to investigate the dynamics of the LACs leading to the observed enhanced loading in ^{171}Yb. We start from a 10-tweezer array filled with multiple atoms from the MOT and apply a LACs pulse for a variable duration before acquiring a number-resolved image. For optimal LACs pulse parameters, we observe a transfer of population from the higher atom numbers to $N = 1$ with only a moderate increase of the 0-atom peak [Fig. 5.4(a)]. By fitting the resulting photon-count histograms, we are able to track the LACs dynamics and measure the evolution of the N-atom occupation probability, as shown

in Fig. 5.4(b). The occupation probability for the highest atom numbers drops in the first few milliseconds of evolution, as LACs are highly more likely to occur when many atoms are present within a trap. On the other hand, achieving single atom occupancy and suppressing the $N = 2$ state requires tens of milliseconds. Notably, the much longer timescale of LACs dynamics compared to the flash imaging duration is the key feature enabling number-resolved detection. We note that even though LACs induced by the $^1\mathrm{S}_0 \rightarrow {}^1\mathrm{P}_1$ transition might display a faster timescale compared to the ones investigate in this work, the evidence of number-resolved detection indicates that their timescale is still longer compared to the few-microseconds required for imaging. Moreover, as we employ resonant imaging light, the amount of kinetic energy acquired by an atom pair is strongly reduced, as the excitation to a molecular potential can happen only for large inter-atomic distances [see Fig. 5.3(a)].

Rate equations model

To obtain quantitative information on the LACs dynamics, we employ a rate-equations model where we consider three possible loss channels induced by the LACs light. We show a sketch of the atom-loss mechanism in Fig. 5.5(a). A single atom can be lost due to heating caused by e.g. blue-detuned light, with a corresponding one-body loss rate γ_{1b}. When two atoms are present, light can drive red-detuned LACs, leading to pairwise two-body losses with rate γ_{2b}, or blue-detuned LACs, resulting in the two-to-one rate $\gamma_{2\to1}$ [264]. The signature of near-deterministic loading is the dominance of $\gamma_{2\to1}$, which transfers population from $N \geq 2$ to $N = 1$ without significantly increasing $N = 0$.

To fit the time evolution of the occupation probabilities under the effect of the LACs pulse, we use a system of coupled rate equations considering up to four atoms. As we want to assign an occupation probability to each N-state, we slightly modify our histogram multi-peak fitting function [Eq. (5.1)]. In particular, we employ a normalized function and we restrict our analysis to histograms displaying a negligible $N > 4$ population. For our illumination time of choice (20.7 µs), the $N \leq 4$ peaks are well separated and our imaging fidelity exceeds 90%, ensuring reliable fitting. Knowing the occupation probability $P_N(t)$, we write the following set of coupled rate equations:

$$\begin{cases} \dot{P}_0(t) = \gamma_{1b}\, P_1(t) + \gamma_{2b}\, P_2(t) \\ \dot{P}_1(t) = -\,\gamma_{1b}\, P_1(t) + (\,\gamma_{2\to1} + 2\,\gamma_{1b})\, P_2(t) + \,3\,\gamma_{2b}\, P_3(t) \\ \dot{P}_2(t) = -(\,\gamma_{2b} + \gamma_{2\to1} + 2\,\gamma_{1b})\, P_2(t) + \,3\,(\gamma_{2\to1} + \gamma_{1b})\, P_3(t) + 6\,\gamma_{2b}\, P_4(t) \\ \dot{P}_3(t) = -3\,(\gamma_{2b} + \gamma_{2\to1} + \gamma_{1b})\, P_3(t) + \,(6\,\gamma_{2\to1} + 4\,\gamma_{1b})\, P_4(t) \\ \dot{P}_4(t) = -(6\,\gamma_{2b} + 6\,\gamma_{2\to1} + 4\,\gamma_{1b})\, P_4(t) \\ P_4(t) = 1 - [P_0(t) + P_1(t) + P_2(t) + P_3(t)] \end{cases} \tag{5.3}$$

where the last equation accounts for the normalization condition. The integer prefactors account for the number of equally-likely ways to loose one or two atoms among the N available. We limit our model to 4 atoms per site as the peak fitting becomes less reliable for higher occupations and we therefore limit our analysis to times for which the probability $P_{\geq5}(t)$ of having $N \geq 5$ atoms is negligible. We exclude that three body losses play any relevant role in the observed dynamics as adding a corresponding rate to our models results in order of magnitude higher fit cost function value compared to the case for which we neglect this effect. Moreover, by performing a LACs dynamics study on post-selected $N = 3$ images we can directly exclude the presence of a relevant three-body loss rate (see next section).

We map the loss rates as a function of LACs-pulse detuning and intensity at a fixed magnetic field of 7 G. We show the dependence of the three loss rates on the LACs-pulse detuning for

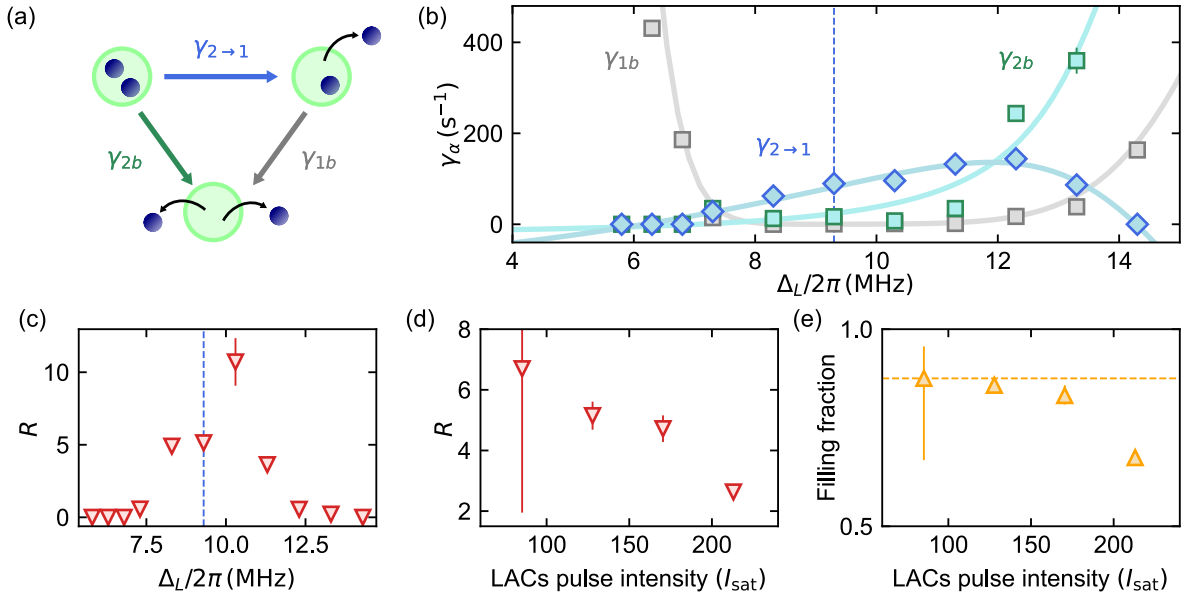

Figure 5.5| Light-assisted collisions loss rates. (a) Sketch of the relevant loss rates during LACs. Two-body (γ_{2b}) and two-to-one ($\gamma_{2\to1}$) losses are induced by red- and blue-detuned LACs respectively. Single atoms can also be lost from the traps due to one-body losses (γ_{1b}). (b) Loss rates versus LACs-pulse detuning from the $^1S_0 \to {}^3P_1|F' = 3/2\rangle$ free-space resonance at fixed LACs pulses intensity $I_L \simeq 170\, I_{sat}$. Solid lines are guides to the eye and the vertical dashed line marks the detuning employed in panels (d, e) (c) Good-to-bad collisions ratio $R = \gamma_{2\to1}/(\gamma_{1b} + \gamma_{2b})$ as a function of LACs-pulse detuning. (d) Good-to-bad collisions ratio R as a function of LACs-pulse intensity. (e) Optimal filling fraction versus LACs-pulse intensity extracted from the rate-equations fits. The dashed lines marks the maximum filling $\simeq 0.87$. Each point is obtained for the LACs-pulse duration that maximizes the filling fraction. For all panels, error bars are obtained from the errors of the rate-equation fit; the large error bar for the lowest-intensity point in (d, e) is caused by the large uncertainty on the negligible one-body loss rate. All points are obtained from around 1000 experimental repetitions.

fixed intensity $I_L \simeq 170\, I_{sat}$ in Fig. 5.5(b). We investigate the detuning range between the two $^1S_0 \to {}^3P_1|F' = 3/2, m'_F = +1/2\rangle$ and $^1S_0 \to {}^3P_1|F' = 3/2, m'_F = +3/2\rangle$ resonances, where Λ-enhanced grey molasses cooling can occur. Approaching the $^1S_0 \to {}^3P_1|F' = 3/2, m'_F = +1/2\rangle$ transition from the blue side, atoms are expelled from the trap due to the blue-detuned light and the dominant term is γ_{1b}. On the other hand, approaching the red-side of the $^1S_0 \to {}^3P_1|F' = 3/2, m'_F = +3/2\rangle$ resonance we observe a dominant γ_{2b} loss rate caused by red-detuned LACs associated with cooling, while the one-body loss rate increases only for very small detuning from resonance. Between these two limits, we identify a few-MHz wide region where the dominant loss rate is $\gamma_{2\to1}$, corresponding to the presence of a near-deterministic loading feature. We quantify the efficiency of such process with the ratio between the good $2 \to 1$ rate and the sum of the bad two-body and one-body loss rates: $R = \gamma_{2\to1}/(\gamma_{1b} + \gamma_{2b})$. In Fig. 5.5(c) we show the dependence of the good-to-bad ratio on the LACs-pulse detuning, showing a clear peak centered on roughly 10 MHz detuning from the free-space resonance, corresponding to $\simeq$+4 MHz and $\simeq$-8 MHz detuning from the shifted $m'_F = +1/2$ and $m'_F = +3/2$ states respectively. We note that our typical working point [indicated by a blue dashed line in Fig. 5.5 (b, c)] is close but does not coincide with the maximum R, indicating that further improvements on the filling fraction are possible. We believe that quantitative knowledge on the different loss rates could help in

future optimizations of LACs pulses for all atomic species, helping to push the filling fraction to higher values.

To this end, we investigate the dependence of the good-to-bad ratio on the LACs-pulse intensity [Fig. 5.5(d)]. We observe that the maximum R is achieved for lower-intensity pulses, requiring longer times to reach single-atom occupancy. The filling fraction extracted from the measured rates shows a similar behavior and it is maximized for low-intensity, long pulses [Fig. 5.5(e)]. While reducing the LACs-pulse intensity leads to a reduction of $\gamma_{2\to1}$, it results in a much stronger suppression of the one- and two-body loss rates, which become negligible for the lowest intensity point (hence causing the large error bar). This indicates that the highest filling fractions are not achieved when $\gamma_{2\to1}$ is maximized, but rather when the other loss rates are minimized, so that atoms can solely be lost due to a blue-detuned LAC until only one is left in the trap. As we are working at a blue-detuning smaller than the trap depth ($U_0 \simeq 12\,\mathrm{MHz}$), the energy imparted in each LAC is typically less than the trap depth, and the likelihood of both atoms remaining in the trap after a collision is high. Our findings are consistent with the interpretation reported in Ref. [53], where it is suggested that enhanced loading results from a large number of low-energy collisions, each with a small probability of losing an atom and a negligible probability of losing two.

5.2.3 LACs dynamics with post-selection

An alternative approach for the investigation of LACs dynamics consists in preparing a deterministic number-state and observe its evolution under LACs. In this case, knowledge on the initial atom number provides a further tool to explore the loss rates associated to different atom numbers. This study has been done for rubidium atoms by preparing two optical tweezers, each filled with one atom, and merging them into a single trap [264]. Leveraging our fast number-resolved imaging, we can acquire an image of the array before LACs take place to know the initial atom number. Then we apply a LACs pulse, image the atoms and post-select on a specific initial atom number to observe the evolution of that state during LACs illumination.

However, a few complications related to repeated multi-atom imaging arise. First, we have seen [see Fig. 5.1(f)] that a single multi-atom detection induces significant losses due to the longer illumination time required to resolve multiple atoms, the lack of an initial cooling stage and the higher probability of losing one atom when $N > 1$. Second, atoms that survive the first image have acquired energy during the detection process and explore different part of the confining potential compared to colder atoms. In our non-magic traps, this results in an effective shift of the $^1\mathrm{S}_0 \to {}^3\mathrm{P}_1$ transition and thus in a change of the detuning required for near-deterministic loading.

We partially overcome these complications by adopting the sequence displayed in Fig. 5.6, where we employ a chirped-multi atom cooling to reduce the temperature at the cost of few two-body losses. We first verify that applying a chirped Doppler-cooling pulse does not induce too large parity projection for low enough atom numbers. For this pulse we employ a low intensity ($I \simeq 0.4\, I_{\mathrm{sat}}$) and consider only states with $N = 2, 3$, for which the LACs timescale is longer due to the lower density. While the frequency ramps limit our cooling pulse duration to a minimum of $\sim 40\,\mathrm{ms}$, it is possible that the frequency chirp in non-magic traps also plays a role in mitigating parity projection. After this first cooling pulse, we ramp the trap depth to $U_0 \simeq 2.3\,\mathrm{mK}$ and acquire a preliminary multi-atom image with $t_{\mathrm{ill}} = 10.8\,\mu\mathrm{s}$, shorter compared to the one employed for detecting larger atom numbers. We then restore the atomic temperature with another chirped cooling pulse before lowering the trap depth and increasing the magnetic field to the LACs pulse parameters. After a variable LACs duration, we acquire a final image to measure the remaining atoms. Notably, we find that the detuning required for near deterministic loading is not shifted compared to the single-image case, indicating that the cooling pulse after

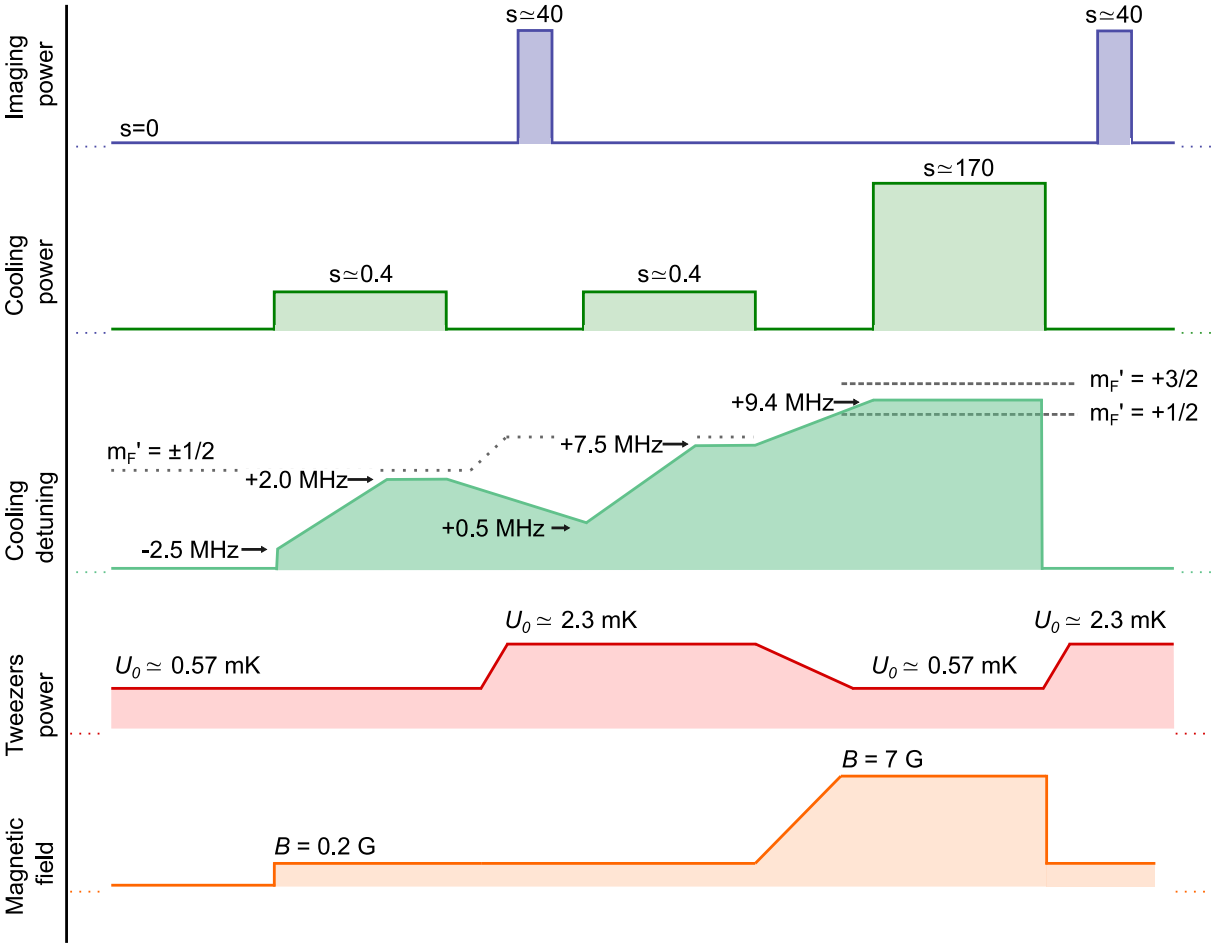

Figure 5.6| Experimental sequence for interleaved LACs pulse and repeated multi-atom detection. Starting from a multiply-filled trap at $U_0 \simeq 570\,\mu\text{K}$ we perform a chirped cooling at low intensity. We then ramp up the tweezer depth to $U_0 \simeq 2.3\,\text{mK}$ and acquire the first image. After imaging we perform another chirped cooling to restore the initial temperature. We then increase the magnetic field and reduce the trap depth applying a high-intensity LACs pulse for a variable time, after which we acquire a second image of the array to check the remaining population. The dotted line in the cooling detuning axis indicates the light-shifted $^1\text{S}_0 \rightarrow {}^3\text{P}_1|F' = 3/2, m'_F = \pm 1/2\rangle$ resonance while the two dashed lines indicate the resonances for the $^3\text{P}_1|F' = 3/2, m'_F = 3/2\rangle$ and $^3\text{P}_1|F' = 3/2, m'_F = 1/2\rangle$ states shifted by the 7 G magnetic field applied during the LACs stage. Axes are not to scale.

the first detection has effectively undone its effect.

In Fig. 5.7 we show the dynamics of the $N = 2$ and $N = 3$ states after post-selecting with a preliminary image. We observe that the first image and the interleaved cooling pulse do induce significant losses as we measure a < 1 occupation probability for $N = 2$ and $N = 3$ states even when the LACs duration is set to zero [Fig. 5.7(a, c)]. However, the evolution of the occupation probabilities is well described by our rate equations model and we obtain loss rates that are consistent with those measured with the single-image approach. In particular, for our typical LACs parameters we extract $\gamma_{1b} = 0.1(2)\,\text{s}^{-1}$, $\gamma_{2b} = 18(2)\,\text{s}^{-1}$ and $\gamma_{2\rightarrow1} = 76(3)\,\text{s}^{-1}$ by post-selecting on $N = 2$ and $\gamma_{1b} = 0.05(17)\,\text{s}^{-1}$, $\gamma_{2b} = 17(1)\,\text{s}^{-1}$ and $\gamma_{2\rightarrow1} = 71(1)\,\text{s}^{-1}$ by post-selecting on $N = 3$. In the case of post-selection on $N = 3$, we can also add a three-body losses term to the model with a rate γ_{3b}. We find a very small value for such rate ($\sim 10^{-7}\,\text{s}^{-1}$),

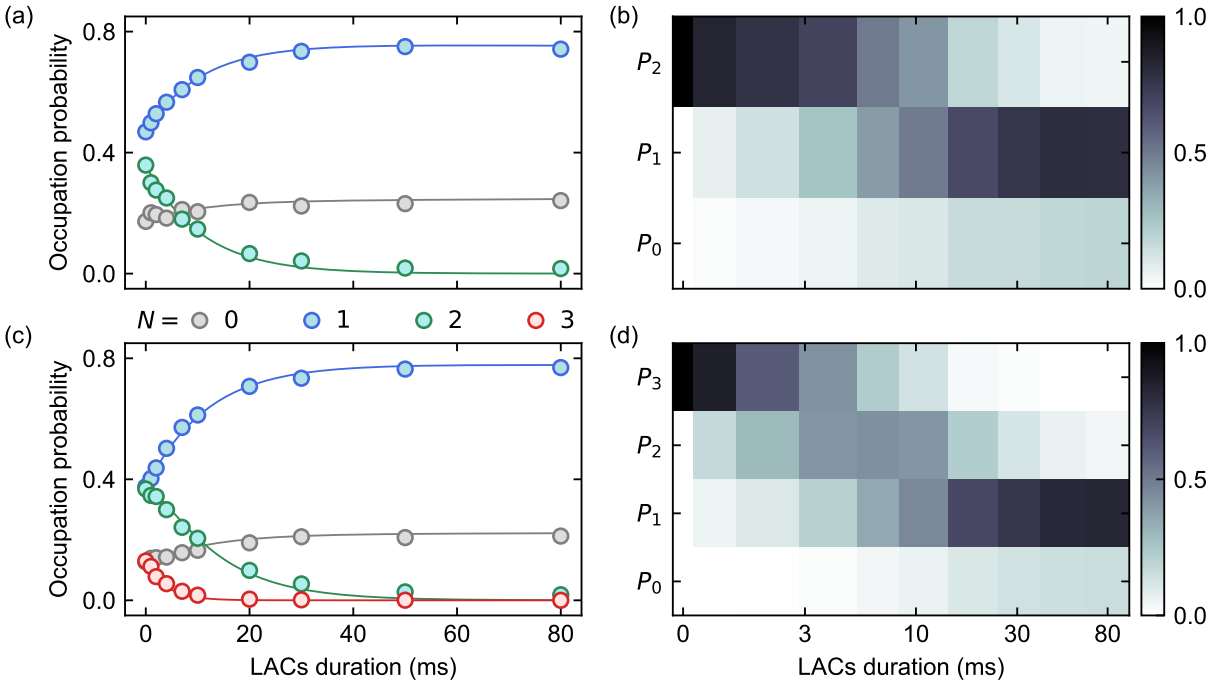

Figure 5.7| LACs dynamics with post-selection. Occupation probability dynamics in blue-detuned LACs after post-selecting for $N = 2$ [(a, b)] and $N = 3$ [(c, d)] with a preliminary image. Solid lines in (a) and (c) are fits with the rate equations model and different colors correspond to different atom numbers in the second image. Data in (b) and (d) are corrected to take into account the losses induced by the first detection. Each point is obtained from more than 2000 experimental realizations.

consistent with the absence of such loss mechanism. By comparing data and the rate equations model for post-selected $N = 2$ and $N = 3$, the final filling is slightly larger for the latter case, indicating that loading tweezers with $N \gg 2$ (to keep the probability of starting with $N = 2$ as low as possible) is beneficial to achieve the largest fraction of single-atom occupations.

Taking into account the measured loss rates both with single and double images, we can rescale the measured atom number in the second image and correct for the losses associated to the first detection. By doing so, we can set the initial $P_{N=2,3}(t = 0) = 1$ an directly observe the transfer of probability from $N > 1$ to $N = 1$ during near-deterministic loading [Fig. 5.7(b, d)]. We note that for the selected $N = 2, 3$, the required correction is just a rescaling, while for lower atom numbers the LACs pulse induces non-trivial transfers between the different probabilities and information on the loss rates is required to correct for the initial losses.

In conclusion, we have employed our number-resolved detection to investigate the dynamics of LACs in gray molasses via repulsive molecular potentials, a fundamental mechanism underlying near-deterministic loading of neutral-atom arrays. We have also performed repeated multi-atom detection, which could become an extremely valuable tool, provided that the complications related to the imaging losses can be overcome. Both simple and repeated multi-atom detection can be employed to track population dynamics in a broad class of experiments such as the investigation of three-body losses and contact interactions in degenerate fermionic or bosonic systems and the extension of tweezer clocks to multi-atom ensembles.

5.3 Preparing and imaging cold mesoscopic samples

The number of particles in a system dramatically affects the properties of the system as a whole. Understanding the transition from a single-particle description to a many-body state, and the intermediate few-particle behavior, is one of the open challenges of modern physics [19]. Owing to their high degree of control at the single particle level, neutral-atom based quantum simulators are a powerful platforms for the investigation of few-particles mesoscopic systems. In particular, pioneering works in the group of Selim Jochim (Heidelberg University) have introduced experimental techniques to deterministically prepare and control few-fermion systems both in one and two dimensions [13, 14]. Combining deterministic preparation of degenerate systems, flash imaging and the properties of lithium atoms has allowed to investigate the emergent properties of few-fermion ensembles in different interaction regimes [14–16].

So far, studies have been typically limited to spin-1/2 fermions belonging to the same dispersion band, thus realizing single-orbital SU(2)-symmetric Hamiltonians. However, models from both condensed matter and high-energy physics are often characterized by multiple orbitals and enlarged SU(N > 2) symmetry. Extending the experimental techniques developed for lithium to ytterbium atoms will allow to tackle the many open questions about the properties of such models at the mesoscopic scale. In this section, we will describe our first steps towards the preparation and detection of degenerate few-fermion systems of ytterbium atoms.

5.3.1 Detecting multiple atoms in free space

Flash imaging in free space is not limited to single atoms and can be directly applied to detect multiple atoms released from a single trap. When many atoms are interacting within one trap, free-space detection is often favorable compared to the in-trap counting described in the previous sections. In fact, when the signal of multiple atoms is spatially overlapped, as is the case for in-trap imaging, the fidelity and maximum counting range are limited by the broadening of the peaks corresponding to different atom numbers, which even for an ideal Poissonian distribution scales as $\propto \sqrt{N}$. On the other hand, after free-space evolution the likelihood of finding multiple overlapping atoms is reduced, allowing to extend the counting range and detect the spatial location of each atoms. In particular, for sufficiently long ballistic expansion the position of each particle is a direct probe of its initial momentum. Therefore, imaging multiple atoms released from a single trap allows to access the momentum correlations present in the system before the expansion. This has allowed to measure momentum correlations in bosonic and fermionic systems [176, 229, 230, 259], including the presence of Cooper pairs in a few-fermion BCS superconductor [15].

In our experiment, we employ flash imaging to detect multiple atoms propagating in free space after being released from a single tweezer [Fig. 5.8]. We note that the results presented here refer to ^{171}Yb, where the small scattering length between ground state atoms ensures that interactions do not play a significant role during the expansion. To count the number of atoms and detect their positions we apply the algorithm described in Sec. 4.6.1: we filter and clip the experimental images to determine the regions where it is most likely to find an atom, draw a ROI around the most likely pixel and then perform thresholding to determine its presence. While this allows to reconstruct the atomic positions with a decent fidelity for simple scenarios, the algorithm requires the photon-integration ROI size, the single-atom photon-count threshold and the minimum distance between atoms as inputs. The optimal choice for these parameters is, in general, extremely unclear and the algorithm is prone to numerous errors when many atoms are present. For example, larger ROIs typically lead to higher detection fidelity but if the ROI size is too large it might cover the signal of more than one atom. In this case, employing large ROI covering multiple atoms and applying multiple thresholds corresponding to different atom

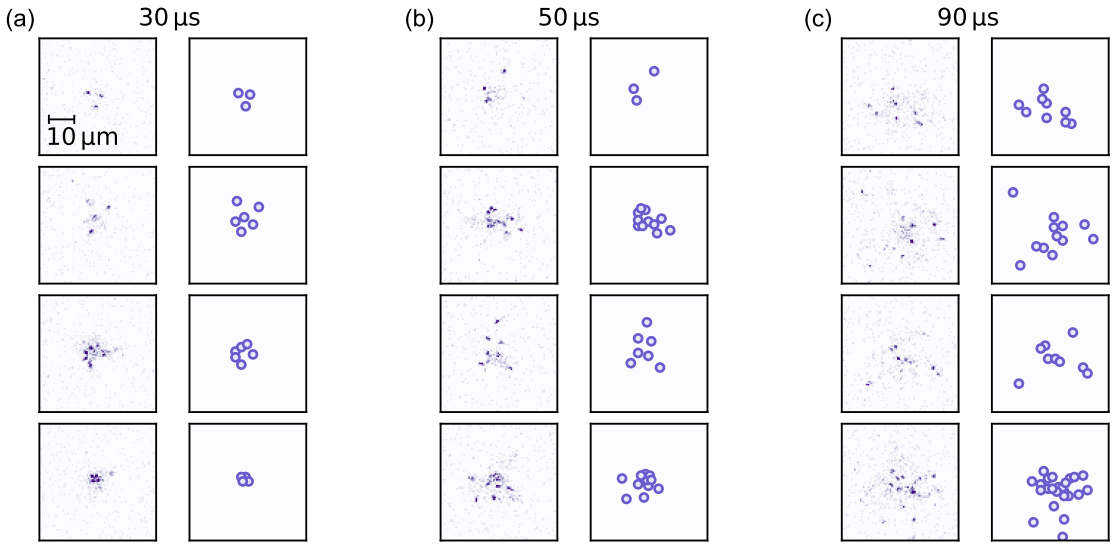

Figure 5.8| Free-space imaging of multiple atoms. Collections of single-shot images of ^{171}Yb atoms released in free-space from a single trap for 30 µs [(a)], 50 µs [(b)], 90 µs [(c)]. Columns on the right represent the reconstructed atomic positions. Images in (c) are obtained after longer MOT loading time (300 ms instead of 100 ms) and thus contain on average more atoms. Free-space detection is performed with $t_{\mathrm{ill}} = 10.8$ µs [(a, b)] and $t_{\mathrm{ill}} = 7.2$ µs [(c)].

numbers might be a solution, but leakage of signal in and out of the ROIs remain a significant problem. The same problems appear when when choosing the minimum distance at which atoms can be found, as large values lead to missing closely-spaced atoms while small values might lead to over counting.

The problem of reconstructing atomic positions in multi-atom free-space images could be tackled through more refined techniques such as the MLE reconstruction algorithm employed for high-fidelity detection in tight arrays. However, the extremely high number of hypotheses to be checked, regarding both the atom number and positions, would require a huge amount of computational resources, making MLE-based approaches more challenging. A possibility could be to employ a combination of thresholding and MLE reconstruction by, e.g. applying the MLE only for uncertain situations. Nonetheless, we believe that the most promising approach to solve this problem is to take advantage of machine learning techniques based on convolutional neural networks. After supervised training on a set of certified multi-atom images, such as the ones that we can produce through Monte Carlo simulations, we expect that a neural network will be able to reconstruct both the atom number and position of multiple atoms propagating in free space. Alternatively, an unsupervised network could be used, as this kind of network has already been successfully applied to reconstruct images of an extremely short-spacing quantum gas microscope [211].

Regardless of the algorithm employed, longer TOFs lead to more efficient reconstruction, as the probability of having multiple overlapping particles is reduced. Moreover, a direct mapping from momentum to position coordinates after ballistic expansion is only reached in the so-called far-field limit, corresponding to $t_{\mathrm{TOF}} \to +\infty$. Typically, this is achieved by letting the atoms expand in a harmonic confinement, taking advantage of matterwave Fourier optics to achieve the far-field condition while at the same time ensuring that atoms remain in the focal plane of the objective [175, 270]. Owing to the favorable properties of ytterbium, we can perform tens of

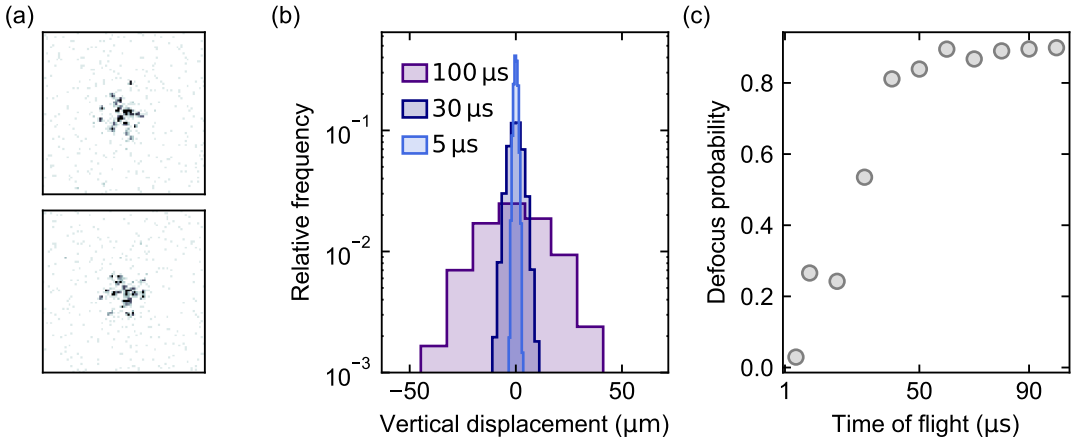

Figure 5.9| Long time-of-flight simulations. (a) Single-shot simulated images of 30 ^{171}Yb atoms after 90 µs of time-of-flight and imaged with $t_{\mathrm{ill}} = 7.2$ µs. (b) Histograms of the final vertical positions of 300 atoms for variable TOF. Larger TOFs lead to a significant spread with a high probability of exiting the objective depth of focus ($\simeq 2$ µm), corresponding to the center of the vertical axis. (c) Probability of defocusing due to large vertical displacement as a function of time of flight duration.

microseconds expansions without external potentials and still maintain a moderate probability of defocusing. However, already after ~ 30 µs expansion we observe the defocusing of some atoms, resulting in a fainter and broader single-atom signal [see e.g. the top right dot in the bottom image of Fig. 5.8(a)]. Defocusing becomes more evident for longer TOFs, with some atoms contributing to a diffuse fluorescence halo contaminating the image and complicating the identification of all atoms [e.g. second image in Fig. 5.8(c)].

We verify the TOF-induced defocusing by performing Monte Carlo simulations of the free-space imaging process. We simulate the detection of 30 atoms in each shot, finding that some of the atoms lead to a blurred and fainter signal while others seem to be completely missing [Fig. 5.9(a)]. These correspond to atoms that have traveled out of the objective focal plane ($\simeq 2$ µm). In Fig. 5.9(b) we show the histograms of the final vertical position of 3000 atoms for variable t_{TOF}. Not surprisingly, we find that longer expansion times lead to a higher vertical position spread. In particular, we find that already at $t_{\mathrm{TOF}} = 30$ µs we have a $\sim 50\,\%$ defocus probability, defined as the probability of having a vertical displacement larger than 2 µm [Fig. 5.9(c)]. While this does not mean that we lose the signal of half the atoms after only 30 µs, as there is not a sharp threshold for this process to occur, it is clear that a vertical confinement is needed to enable for longer time of flight. This can be provided by the optical dipole trap employed to increase the atomic density within the tweezer.

Finally, we note that our current imaging capability is limited to the detection of atoms, and lacks sensitivity to their internal spin state. Access to spin-state information would be particularly valuable for studying phenomena where spin-exchange [161] interactions between ground and clock state atoms play a key role, such as in orbital impurity models [47, 58]. Typically, spin sensitivity on the $^1\mathrm{S}_0 \rightarrow {}^1\mathrm{P}_1$ transition is achieved by mapping the nuclear spin to the clock state and shelving one state to render it dark to the imaging light [65]. However, high-fidelity excitation of the clock transition for freely-propagating atoms seems a rather challenging task. On the other hand, free-space spin sensitivity could be achieved by employing high magnetic fields of $800 - 1000$ G to split the nuclear spin sub-levels of the $^1\mathrm{P}_1$ state, reaching the Paschen-Back regime in order to minimize spin-flip probability during imaging. In this case a vertical confinement would be mandatory to allow for sufficient time between images. This

would effectively reproduce the technique employed for lithium atoms [175], however at a much larger magnetic field due to the large hyperfine constant for the $^1P_1$ of ytterbium. In case our available fields are not sufficient to prevent undesired spin flips, an alternative approach could be to extend the optical Stern-Gerlach (OSG) scheme [85] to single atoms in order to map their spin state into their momentum, and then to position after a time of flight.

5.3.2 Towards a few-fermion degenerate sample

The discussed extensions of flash imaging to longer TOFs and spin-sensitive detection will provide a versatile tool for exploring many-body effects in few-particle systems. However, to access regimes where quantum many-body effects play a significant role, we need to first prepare a degenerate sample. In the following, we will describe our first steps and possible strategies to realize a degenerate mesoscopic system of fermionic ytterbium atoms.

Our approach is greatly inspired by pioneering techniques developed for lithium atoms in the group of Selim Jochim (Heidelberg University) [13, 14]. There, atoms are initially prepared in a relatively large optical dipole trap reaching moderate degeneracy at $T/T_F \simeq 0.5$, where the Fermi temperature is defined as $T_F = \frac{E_F}{k_B} = \frac{1}{k_B}\frac{\hbar^2}{2m}\left(3\pi^2 n\right)^{2/3}$ and n is the atomic density. Atoms are then transferred into a tightly focused trap, i.e. an optical tweezer, that is overlapped with the larger trap, providing a dimple in the optical potential. The tweezer locally enhances the chemical potential while the absolute temperature of the gas remains the same, resulting in a strong enhancement in density in the dimple, and a corresponding much lower $T/T_F \simeq 0.05$ value. Such of lower T/T_F, and thus high degeneracy, leads to an increased occupation of the lower harmonic oscillator levels. One advantage of this scheme is that, even if the initial degeneracy in the dimple is not sufficient, the tight confinement in the tweezer leads to high collision and thermalization rates, allowing to complete the evaporative cooling stage within the tweezer itself. When the system is deeply degenerate and all first levels are filled, the number of particles is tuned with a spilling procedure. This is done by tilting the trapping potential through a superimposed linear potential, which in the case of lithium consists in a magnetic field gradient. With such tilt, lowering the trap depth in a precisely controlled way allows to reduce the number of bound states and control the number of trapped fermions in a deterministic way.

The described scheme hinges on the favorable properties of lithium, for which interactions can be tuned with broad Feshbach resonances. This facilitates evaporation in the preliminary optical dipole trap and in the tweezer, and, once the degenerate regime has been reached, it allows to prepare a non-interacting Fermi gas for the spilling stage. Moreover, the significant magnetic moment of ground-state lithium atoms allows to tilt the confining potential with only moderate magnetic field gradients. On the other hand, AEAs atoms like ytterbium display very different atomic properties: they lack an intra-orbital Feshbach resonance and they have a negligible magnetic moment in long-lived electronic states. This poses challenges to the extensions of few-fermion systems preparation scheme to ytterbium.

The first difficulty lies in performing efficient evaporative cooling down to the degenerate regime in a system lacking a Feshbach resonance. We identify two possible approaches to overcome this limitation. First, evaporation of fermionic ^{173}Yb has already been demonstrated [171] and degenerate gases of this isotopes have been employed as quantum simulators in different experimental setups [109, 110, 161, 163, 165]. Evaporative cooling of ^{173}Yb is enabled by the significant ground-state scattering length ($a_{gg} \simeq 200\, a_0$) and it is favored by the large nuclear spin, resulting in an enhanced number of collision channels and thus an effective increase of interactions. Indeed, studies performed on ^{87}Sr ($I = 9/2$) have demonstrated the role of SU(N) symmetric interactions in facilitating fast and efficient evaporative cooling [178]. In our setup, we could therefore evaporate ^{173}Yb atoms both in the ODT or directly in the tweezer trap to reach the degenerate regime.

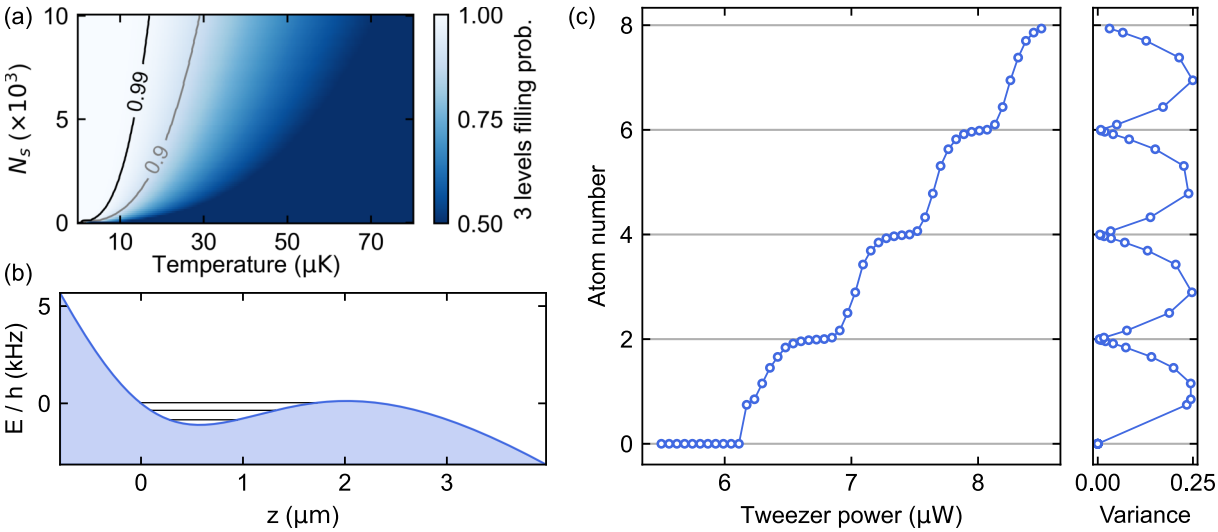

Figure 5.10| Preparing a ^{171}Yb few-fermion system. (a) Probability of completely filling the first 3 energy levels in a harmonic trap with $(\nu_r, \nu_z) = (90\,\text{kHz}, 20\,\text{kHz})$ as a function of the temperature and the per-spin state number of ^{171}Yb atoms. Loading thousands of atoms at $\sim 10\,\mu\text{K}$ allows to reach a 99% fidelity of preparing the target state. (b) Profile of the axial potential for an optical tweezer trap in presence of gravity. We assume a harmonic confinement with a trap frequency ratio $\nu_r/\nu_z \simeq 4.8$, roughly matching our experimental parameters. (c) Simulated atom number and expected variance as a function of tweezer power for our experimental trap geometry. The presence of plateaus at 2, 4, 6 atoms, with corresponding minima in the atom-number variance, signals deterministic preparations.

On the other hand, the situation would be rather different for ^{171}Yb, where evaporative cooling is strongly hindered by the extremely small ground-state interaction strength ($a_{gg} \simeq -2\,a_0$) between the two available spin states. For this reason, ^{171}Yb is typically brought to degeneracy through sympathetic cooling with another ytterbium isotope [174]. However, we speculate that the high atomic densities attainable in an optical tweezer might enable evaporative cooling also for this isotope. We have recently started to investigate whether starting from a very high number of ^{171}Yb atoms confined in an optical tweezer could lead to a sufficient collision rate to perform runaway evaporation, allowing to reach degeneracy with an acceptable evaporation time.

However, evaporative cooling can be avoided completely if a sufficient number of cold atoms is loaded in the tweezer from the ODT as Pauli blocking results in a freezing of the excitations of the lowest energy levels. To understand this mechanism we can consider the situation of spin-1/2 fermions loaded in an harmonic trap: at $T = 0$ Pauli exclusion principle demands that fermions fill all the harmonic oscillator levels in pairs, starting from the lowest energy state up to the last filled level, corresponding to the Fermi energy. In a real-life scenario at finite temperature, atoms can be excited to available states above the Fermi energy, producing holes in the Fermi sea. In this case, a large level-spacing and a high number of trapped fermions suppress excitations in the lower energy levels, as the first available states are found at much higher energies. Therefore, by loading thousands of ^{171}Yb atoms at a moderate temperature in a single tweezer we can realize a state that, while having many defects and excitations close to the Fermi energy, has the first quantum levels completely filled and frozen by the large energy cost of producing a hole deep in the Fermi sea. In Fig. 5.10(a) we show the probability of having the first 3 harmonic oscillator levels completely filled as a function of the temperature and the number of ^{171}Yb atoms per spin state. For a trap with radial and axial frequencies of $(\nu_r, \nu_z) = (90\,\text{kHz}, 20\,\text{kHz})$ we find a

$> 99\%$ probability in an accessible region of temperatures and atom numbers. We note that for this ratio of trap frequencies, corresponding to the current aspect ratio of our 532 nm traps, the first three harmonic oscillator levels correspond to energy levels along the less-confining axial direction.

Having the lowest energy levels completely filled, the next stage of the deterministic preparation scheme is to cut the Fermi sea by spilling out atoms in a controlled way, thus removing the excess entropy of high-lying and not completely filled energy levels. This is done by tilting the confining potential to unbind a controlled number of energy levels through an external potential gradient. Due to the small magnetic moment of ground-state ytterbium atoms, producing a significant tilt with a magnetic field gradient would require gradients of the order of 10^4 G/cm, making it practically unfeasible. On the other hand, ytterbium has a large mass and nature provides us with a linear potential conveniently aligned along the axial direction of our tweezers: gravity. For ytterbium, the gravitational force produces a gradient of $dU/dz = mg/h = 4.28\,\mathrm{kHz/\mu m}$[1]. For appropriate traps, the separation between the harmonic oscillator levels can be tuned to be such that this gradient is enough to unbind all states above a certain energy, as shown in Fig. 5.10(b). For the geometry of our traps, this allows to deterministically prepare systems of 2, 4 and 6 atoms by lowering the tweezer power to cut the energy distribution above the first, second or third harmonic oscillator level, respectively [see Fig. 5.10(c)]. On the other hand, changing the aspect ratio of the traps enables deterministic preparation of also other harmonic oscillator states. We note that, in general, this scheme requires a very precise tuning of the tweezer power, at the µW level, due to the low tilt introduced by gravity. While we plan to achieved this with appropriate low-noise stabilization loops, a more fundamental limitation might arise in the case of ^{173}Yb. In fact, the presented picture of well-separated harmonic oscillator levels is strictly valid only for a non-interacting Fermi gas. While this is almost the case for ^{171}Yb, as for lithium atoms close to the zero-crossing of the Feshbach resonance, for the strongly interacting ^{173}Yb we expect that inter-atomic repulsion between atoms in different spin states will significantly change the available energy levels and possibly completely wash out the atom-number steps required for deterministic preparation. Even though this would hinder deterministic preparation, it could lead to interesting experiments exploring the interplay between harmonic oscillator levels, Pauli blocking and strong SU(N)-symmetric interactions.

Recent developments

In the last months and during the writing of this thesis we have taken the first steps towards the implementation of the described scheme for the preparation of few-fermion systems with ytterbium atoms. In particular, we have installed the optical dipole trap presented in Sec. 2.1.6 and started to explore the loading of different fermionic ytterbium isotopes in the ODT [see Sec. 3.3.2] and from the ODT to the tweezer.

The role of the ODT is threefold. First, it provides a reservoir from which we can load thousands of atoms in the optical tweezer as it is denser than the MOT and does not induce light-assisted collision. Second, it can be employed to perform evaporative cooling in a large sample, allowing to further enhance the phase-space density before loading the tweezer and, possibly, to perform quantum simulation of extended systems in the ODT itself. Finally, it provides vertical confinement when imaging the atoms released from the tweezer, enabling longer time of flights. Interestingly, we also explored the possibility of single-atom imaging directly in the ODT. As the unpainted ODT is too dense to distinguish single atoms, before imaging we paint the trapping beam to dilute the confined cloud, which we then image with our flash imaging scheme; we show an exemplary single-shot obtained with this procedure in Fig. 5.11(a). Even

[1] h is Planck's constant and not a vertical position.

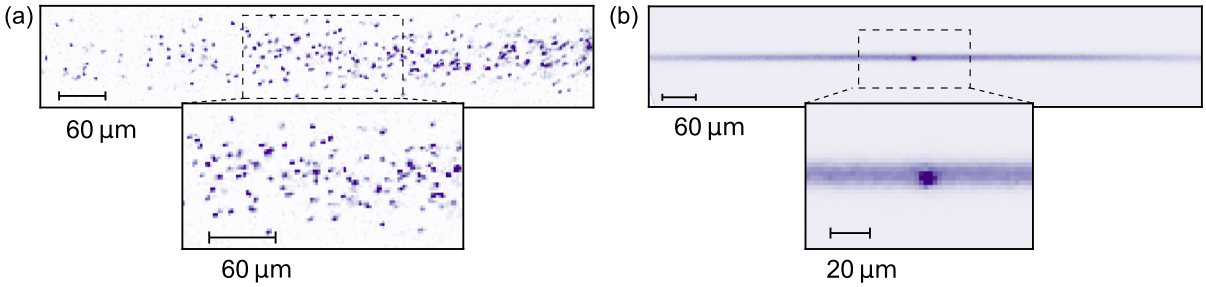

Figure 5.11| Single-atom imaging in tweezer loading in the ODT. (a) Single-shot fluorescence image of atoms trapped in the painted ODT. Here we employ an illumination time $t_{\mathrm{ill}} = 20.7\,\mu\mathrm{s}$ and we paint the horizontal direction of the trap to reduce the cloud density. (b) Average in-situ fluorescence image of a single optical tweezer overlapped at the center of the ODT.

though we have not quantitatively characterized the properties of this imaging scheme as of yet, and plenty of optimization is still required, especially concerning the alignment of the ODT with the focal plane of the objective, these kind of images suggest that flash imaging of ytterbium atoms enables single-atom detection also in dilute continuous gases. Leveraging the favorable properties of ytterbium, this technique could complement recent demonstrations of continuous quantum gas microscopy [229–231], without the need of a pinning lattice.

By overlapping a single optical tweezer with the ODT, we introduce a dimple in the potential where atoms tend to accumulate, as shown in Fig. 5.11(b). We find that for both fermionic isotopes we can dramatically increase the number of atoms in the tweezer by loading them from the ODT, compared to loading directly from the MOT. In particular, we can load $\sim 10^3$ atoms in our tight tweezer with 580 nm waist and we can gain an order of magnitude in the number of trapped atoms by enlarging the tweezer's waist. With these numbers, we are in a good position to attempt evaporative cooling in the tweezer and explore the possibility of gravity-assisted spilling, employing atom number-squeezing as a signature of quantum degeneracy.

Conclusions and outlook

In this thesis, we demonstrated novel schemes for the preparation and detection of ytterbium atom arrays. We have shown that cold and dense atomic samples can be prepared with a simplified MOT geometry and we have successfully loaded and imaged single-atom tweezer arrays of the most common ytterbium isotopes. Capitalizing on favorable atomic properties, we have established the flash imaging scheme as a versatile, fast and minimally destructive detection technique for many different scenarios in ytterbium-based platforms.

We have demonstrated the operation of a 5B MOT for the three most common ytterbium isotopes (^{174}Yb, ^{171}Yb, ^{173}Yb), a configuration that had only been employed with erbium and dysprosium atoms so far [213]. This geometry allows the preparation of cold and dense samples with short loading times, making it a viable and practical solution for platforms employing high-NA objective lenses. The 5B MOT relies on precise tuning of the radiation pressure exerted by the bottom beam and benefits from operating on a narrow cooling transition. This makes it easily adaptable to strontium atoms, where we expect that a higher saturation parameter $s \sim 10^3$ will be required to sustain atoms against gravity. On the other hand, strontium experiments typically employ a preliminary broad-line MOT, whose operation requires all six beams, reducing the advantages of a full 5B approach such as the one presented in this work. Still, transferring atoms from a broad-line 6B MOT to a narrow-line 5B geometry could be useful to avoid focusing both MOT colors through the high-NA objective as well as to reduce the number of dichroic mirrors and optical components in the delicate high-resolution setup. Extensions to experiments featuring two microscope objectives and other atomic species, including alkalis, could be explored with the support of Monte Carlo simulations to guide experimental implementations.

From our 5B MOT, we have successfully loaded one-dimensional tweezer arrays of ^{174}Yb, ^{171}Yb and ^{173}Yb atoms. With a two-color imaging scheme, we have demonstrated single-atom detection of ^{173}Yb atoms with high-fidelity (99.96(1)%) and good survival probability (98.5(2)%). These values are comparable to those obtained with the two-color scheme in ^{171}Yb [53], indicating that the more complex nuclear-spin structure of ^{173}Yb does not pose a strong limitation to this detection protocol. This scheme could be adapted to other fermionic AEAs which lend themselves to high-dimensional quantum encodings [271–273] and to optical lattice experiments, enabling investigation of SU(N)-symmetric models with single-particle resolution [47, 62].

In optical traps, differential confinement between electronic states plays a crucial role in manipulating and detecting individual atoms [52, 55, 65, 76] as well as in metrology [4] and simulation [109–111]. We have employed a previously-developed approach [104, 105, 170] to compute the polarizability of the most relevant electronic states of ytterbium, finding excellent agreement with data from literature and with newly performed measurements of differential light shifts in 532 nm and 759 nm optical traps. Moreover, we have established 532 nm as a new magic wavelength for the stretched transitions with the $^1\mathrm{S}_0 \rightarrow {}^1\mathrm{P}_1$ transition with π-polarized trapping light.

Leveraging such magic trapping condition and the favorable properties of ytterbium, we have achieved microsecond-scale low-loss single-atom detection through the flash imaging scheme developed for lithium atoms [175] and recently extended to lanthanides [234]. In particular, for 6.3 µs illumination time we have measured a 99.96(4)% detection fidelity and a 99.52(7)% survival probability for ^{171}Yb atoms. While our imaging requires deep optical traps, the necessary mK-scale confinement can be obtained across $\sim$ 1000 sites in two-dimensional optical lattices or

tweezer arrays with Watt-level laser power. This imaging scheme allows high-fidelity detection of all ytterbium isotopes studied in this work and could be adapted to other atomic species, with other AEAs and lanthanides as the most natural candidates, albeit with possibly reduced performances. Through interleaved imaging and cooling pulses we have performed multiple repeated detections with a high and constant survival probability per image. In particular, for magic trapping conditions we employ cooling pulses as short as 500 µs, allowing for $\sim$ 2000 low-loss detections per second. This imaging scheme could provide a valuable tool for fast mid-circuit detection, possibly benefiting a wide class of experiments [24, 31, 48–51, 65, 82, 84, 144, 145].

Capitalizing on the very short time required for detection, we have employed flash imaging to count the number of atoms in multiply-filled traps, avoiding the parity projection induced by light-assisted collisions. Leveraging number-resolved imaging, we have investigated the dynamics leading to near-deterministic loading through LACs in blue-detuned molecular potentials for ^{171}Yb [53, 264]. From the population dynamics, we extracted the relevant loss rates, which could help guide future optimization of LACs pulses and theoretical works aimed at understanding the optimal regimes for deterministic trap loading, an important step to facilitate the realization of large-scale atom arrays. Moreover, number-resolved imaging has already been applied to lattice-based quantum simulators [233, 274] and could benefit future developments in tweezer clocks by allowing detection of multiple clock-atoms confined within a single trap.

Finally, we have explored the application of flash imaging to many different scenarios, including tightly-spaced arrays and freely-propagating atoms. By supplementing imaging with an appropriate reconstruction algorithm we have successfully detected trap occupancies in tightly-spaced arrays, also in the case of multiply-filled traps. Even though our smallest trap-spacing is considerably larger than the ones employed in lattice microscopes, our findings suggest that, with appropriate optical magnification and reconstruction algorithms, flash imaging could be employed in lattice-based experiments, enabling much faster detection and on-site atom counting. We have also employed flash imaging to detect single and multiple atoms propagating in free space, a technique that gives access to information on the thermodynamic properties of single particles and interacting systems [16, 178, 179, 251] also in the case of continuous gasses [229–231].

Outlooks

The presented results constitute the first outcomes of the experimental apparatus developed over the course of this thesis, and they open the way to several promising extensions. In the following, we will comment on a potential extended and quantitative study of ytterbium light shifts at various wavelengths as well as on the numerous possible extensions of the flash imaging scheme. Finally, we will provide an outlook towards the realization of degenerate fermionic systems, aimed at investigating orbital-impurity physics with single particle resolution.

A precise characterization of the differential confinement between states involved in cooling transitions in AEAs would benefit a wide class of experiments. Recent works have mapped the magic and tune-out wavelengths of the ytterbium clock transition [56, 57], paving the way to the investigation of lattice gauge theories [59, 60, 170] and orbital impurity models [58] in newly-developed quantum simulators. The importance of differential trapping during cooling and imaging of individual AEAs calls for a similar study focused on the $^1S_0 \rightarrow {}^3P_1$ and $^1S_0 \rightarrow {}^1P_1$ transitions. Indeed, several experiments aimed at quantum information processing with ^{171}Yb have already identified two magic wavelengths for the $^1S_0 \rightarrow {}^3P_1$ transition around 480 nm [54, 82]. However, laser sources providing power to create large arrays of deep traps are hard to find at those wavelengths, even though this limitation is partially mitigated by the higher confinement provided by smaller beam waists and larger values of the ground-state polarizability

compared to longer trapping wavelengths [see Fig. 1.7]. Moreover, the two $(6s^2)^1P_1 \rightarrow (6s7d)^1D_2$ and $(6s^2)^1P_1 \rightarrow (6s8d)^1D_2$ transitions at 518.4 nm and 468.7 nm result in a weak trapping of the $^1P_1$ excited state at 480 nm, possibly hindering low-loss fast detection. We have also observed that vicinity of the $(6s^2)^1P_1 \rightarrow (6s7d)^1D_2$ transition to our 532 nm trapping wavelength favors off-resonant scattering of trap photons from the $^1P_1$ state, limiting our imaging survival probability. We therefore believe that deep optical traps at similar wavelengths will feature the same problem, even though options like strobing of the traps during imaging could help in mitigating this effect. On the other hand, the $^3P_1$ and $^1P_1$ polarizabilities are largely unexplored for trapping wavelengths > 650 nm. In this region, we expect strong trapping of both the $^3P_1$ and $^1P_1$ states, with lower off-resonant scattering rates due to the larger detuning from the closest transitions. Moreover, the light shifts of the $^3P_1$ at these wavelengths might also play an important role when directly loading optical traps from the MOT. Taking advantage of our reliable blow-out spectroscopy scheme and the tunability of the Ti:Sapph laser source, we will measure the differential light shifts of the $^1S_0 \rightarrow {}^3P_1$ and $^1S_0 \rightarrow {}^1P_1$ transitions in this region of the electromagnetic spectrum. By benchmarking our theoretical expectations with experimental data will allow to further refine the polarizability model, which could be extended to describe arbitrary elliptical polarization and employed to guide future choices of trapping wavelengths displaying the desired state-dependent or magic character.

Several extensions on our fast imaging scheme are possible. First, it would be interesting to investigate cooling protocols in non-magic traps allowing to reach the same cooling rates observed for magic trapping conditions in ^{174}Yb. In case this is not possible, the repeated-detection rate in non-magic traps will be limited by the long cooling time, and schemes for parallelizing recooling of the measured qubits with other quantum operations could be explored. Another interesting prospect is the capability of performing repeated low-loss multi-atom detections, which we have briefly explored in this work. In this regard, we believe that the observed losses are caused by the high initial temperature of atoms in a multiply-filled trap. Protocols for appropriate cooling of multiple atoms within a trap could help perform successive number-resolved detections, which would be relevant for studies of population dynamics, including a study of LACs-dynamics aimed at near-deterministic loading of ^{173}Yb.

A fundamental improvement on our free-space imaging scheme is to add a vertical confinement to allow for longer expansion times. This could be implemented through the tight optical dipole trap presented in this work or through an accordion lattice developed in our group [122, 275], which would provide an even tighter vertical confinement, ensuring that atoms remain in the objective's focal plane. Letting the atoms expand in a harmonic confinement before imaging will also allow to explore matter-wave magnification schemes to access information on both atomic momentum and position [192]. Moreover, high-fidelity detection of multiple freely-propagating atoms will require some form of reconstruction algorithm to pin-point atomic positions in a larger region of the camera sensor, also when the signal of multiple particles is spatially overlapped. We plan to implement this with a convolutional neural network that is currently under development within our group. The network has been trained through supervised learning on simulated images and we plan to test its performance on experimental data in the near future.

Our imaging scheme allows to detect single atoms with high-fidelity, but it gives no information on the nuclear spin of the detected atoms. Extending our atom imaging to a spin-sensitive qubit readout is crucial for both quantum information and simulation schemes. A straightforward implementation of this consists in mapping one nuclear-spin state to the $^3P_0$ state, rendering it dark to the imaging light. Such shelving of nuclear-spin states has been performed in the context of mid-circuit readout in ^{171}Yb arrays [51, 65] and fast imaging of ground-state atoms while preserving the clock-state coherence has been demonstrated for both ytterbium and

strontium [48–50]. On the other hand, clock-state shelving seems challenging for spin-sensitive detection of freely-propagating atoms due to possible difficulties in addressing the clock transition for expanding atoms. We therefore plan to employ two different approaches for spin-sensitive imaging of freely-propagating multi-atom ensembles.

The first approach consists in extending the optical Stern-Gerlach (OSG) [85, 86] technique to single-atom resolved experiments, which would be particularly beneficial for studying mesoscopic systems of ^{173}Yb atoms. In this case, we plan to couple into our broadband AOD both the 532 nm tweezers light and an OSG beam tuned to have a frequency between the $^1\mathrm{S}_0|F = 5/2\rangle \rightarrow {}^3\mathrm{P}_1|F' = 7/2\rangle$ and the $^1\mathrm{S}_0|F = 5/2\rangle \rightarrow {}^3\mathrm{P}_1|F' = 5/2\rangle$ resonances. Through a small displacement in the AOD, we will be able to realize an array of focused OSG beams, in which each beam is slightly displaced with respect to its corresponding trap. By switching off the optical tweezers and quickly turning on the OSG beams, we will induce a spin-dependent kick to the atoms that, after an appropriate expansion, allows to map the spin states into the final atomic positions after an expansion time. This technique would allow the detection of the spin population also in multiply-filled traps.

Both spin and momentum-resolved imaging could instead be achieved by splitting the $^1\mathrm{P}_1$ nuclear-spin manifold through a sufficiently large magnetic fields, similar to what is done with lithium [175], albeit a much larger fields. For ^{171}Yb we envision the following scheme. With a magnetic field of many hundreds Gauss we will split the $^1\mathrm{P}_1$ manifold, approaching the the Paschen-Back regime, where eigenstates are best approximated by product states of the electronic angular momentum and nuclear-spin projections, i.e. by $|m'_J, m'_I\rangle$. However, only levels originating from $|F' = 3/2, m'_F = \pm 3/2\rangle$ are pure product states $|m'_J, m'_I\rangle$ and the other levels are linear combinations of states with different m_J, m_I quantum numbers. By driving a transition to a pure product state, such as $^1\mathrm{P}_1|m'_J = 1, m'_I = +1/2\rangle$, only atoms in one spin state, in this case $^1\mathrm{S}_0|m_F = +1/2\rangle$, will be bright to the imaging light, as light cannot flip the nuclear spin. After the first spin-sensitive image, we will jump with the imaging beam frequency, and possibly also with the magnetic field, to perform a second, spin-insensitive, image. These jumps could be performed with our offset lock and flyback circuit, with timescales of the order of $\sim 100\,\mu$s which are compatible with typical expansion times in a harmonic potential. We expect that the main limitation of this scheme will be the presence of spin-flips during the first image. Considering our example of a bright $|m_F = +1/2\rangle$ state, spin-flips would be induced by unwanted $^1\mathrm{S}_0|m_F = -1/2\rangle \rightarrow {}^1\mathrm{P}_1|m'_J = 1, m'_I = -1/2\rangle$ excitations, caused by the relatively small detuning ($\simeq 250$ MHz) of this transition compared to the desired one. Spin-flips happen because the state that we label as $^1\mathrm{P}_1|m'_J = 1, m'_I = -1/2\rangle$ retains a small $|m'_J = 0, m_I\prime = +1/2\rangle$ component and an atom decaying back from it could thus flip its spin from $|m_F = -1/2\rangle$ to $|m_F = +1/2\rangle$. This would be extremely detrimental to the spin-detection fidelity. We plan to overcome this by working at very high fields, between 500 and 1000 G, which help in reducing mixing and of nuclear-spin states [101, 102]. With a magnetic field $B = 800\,G$ we expect a $\simeq 2\%$ mixing and thus a $\simeq 2\%$ spin-flip probability for every unwanted excitation of the dark state $|m_F = -1/2\rangle$. By reducing the imaging saturation intensity to $s \sim 1$, we could suppress off-resonant excitations without excessively compromising the photon scattering rate. For an illumination time of 8 µs and ~ 15 collected photons from the bright atoms, which are enough for high-fidelity imaging, we estimate a $\simeq 5\%$ spin-flip probability.

In this regard, we are currently working towards the realization of degenerate mesoscopic systems and we are exploring prospects in the preparation of low-entropy states, leveraging the high probability of occupying the lower harmonic oscillator levels. To this end, we are developing schemes for loading as many atoms as possible into a single tweezer and exploring evaporative cooling protocols. In this context, leveraging the recycled power of the crossed ODT will allow us to prepare a denser and colder reservoir before loading into the tweezer. This could be

further improved by implementing clock-cooling schemes in our clock-magic ODT [91, 93], for which we already have tested the required 1389 nm repumping laser. Once we have a degenerate sample, we will concentrate our efforts to implement gravity-assisted spilling in order to prepare deterministic few-fermion systems. Finally, we will be able to combine these preparation and detection schemes with clock-state excitations, employing optical tweezers at magic and tune-out wavelengths to investigate orbital impurity models with single-atom resolution.

Appendices

A Hyperfine transitions line strengths

When addressing a hyperfine $|F\rangle \rightarrow |F'\rangle$ transition in fermionic ytterbium isotopes, it is necessary to consider that both the involed hyperfine states present a set of m_F Zeeman sublevels. Notably, different $|F, m_F\rangle$ and $|F', m'_F\rangle$ states are more or less coupled by light, resulting in different line strengths for different $|F, m_F\rangle \rightarrow |F', m'_F\rangle$ transitions. The optical coupling between two Zeeman sublevels states is quantified by the dipole matrix element

$$\langle n, F, m_F|\mathbf{d}|n', F', m'_F\rangle = \langle n, L|\mathbf{r}|n', L', \rangle A_{|F,m_F\rangle,|F',m'_F\rangle} \tag{4}$$

where the $\langle n, L|\mathbf{r}|n', L', \rangle$ and $A_{|F,m_F\rangle,|F',m'_F\rangle}$ account for the radial and angular part of the dipole matrix element respectively [106]. The angular part can be explicitly written as a function of the states' quantum numbers as:

$$\begin{aligned} A_{|F,m_F\rangle,|F',m'_F\rangle} = (-1)^{1+L'+S+J+J'+I-mF'} \\ \sqrt{(2J+1)(2J'+1)(2F+1)(2F'+1)} \\ \begin{Bmatrix} L' & J' & S \\ J & L & 1 \end{Bmatrix} \begin{Bmatrix} J' & F' & I \\ F & J & 1 \end{Bmatrix} \begin{pmatrix} F & 1 & F' \\ m_F & q & -m'_F \end{pmatrix} \end{aligned} \tag{5}$$

where the term in parentheses and in curly braces are the Wigner 3-j and the Wigner 6-j symbols, respectively. The relative transitions strengths are then defined as $|A_{|F,m_F\rangle,|F',m'_F\rangle}|^2$. We report the line strengths relevant for this work in Fig. A1. As the dipole operator does not couple the electronic spin, the transition strengths do not show any dependence on S' and the line strengths are therefore the same for transitions to the ^{1}P$_1$ and ^{3}P$_1$ excited states.

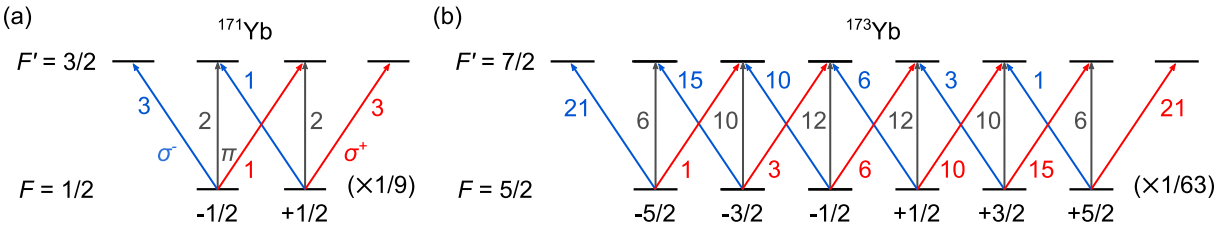

Figure A1| Line strengths for hyperfine transitions in ^{171}Yb and ^{173}Yb. We report only the line strength of $|F, m_F\rangle \rightarrow |F' = F + 1, m'_F\rangle$ transitions as these are the ones relevant for this work. The line strengths are the same for the ^{1}P$_1$ and ^{3}P$_1$ states because they do not depend on the excited state electronic spin. All line strengths are computed as $|A_{|F,m_F\rangle,|F',m'_F\rangle}|^2$ (see Eq. (5)).

B Transition data for polarizability calculations

Here we collect the properties of the optical transitions employed for computing the polarizabilities of the different ytterbium states. The branching ratio between different pathways can be computed as:

$$\beta = \tau\left(n'J'\right)\,\Gamma_{n'J'\to nJ} = \frac{\omega^3_{n'J'\to nJ}}{\tilde{\omega}^3_{n'J'}}\,(2J+1)\left(2L'+1\right)\begin{Bmatrix} L & L' & 1 \\ J' & J & S \end{Bmatrix}^2 \tag{6}$$

Transitions from $(6s^2)^1S_0$

Final state	λ (nm)	Final state energy (cm^{-1})	τ (ns)	β	Γ (MHz)	Source
$(6s6p)^1P_1$	398.911	25068.222	5.464	1	183.02	[276]
$(6s6p)^3P_1$	555.802	17992.01	866.1	1	1.15	[240]
$(7/2,\,5/2)_{J=1}$	346.536	28857.01	14.4	1	69.44	[240]
$(6s7p)^1P_1$	246.524	40563.97	8.9	0.9964	111.96	[240]
$(6s8p)^1P_1$	227.182	44017.60	39.1	0.9887	25.29	[240]

Transitions from $(6s6p)^3P_1$

Final state	λ (nm)	Final state energy (cm^{-1})	τ (ns)	β	Γ (MHz)	Source
$(6s^2)^1S_0$	-555.802	0	866.1	1	1.15	[240]
$(6s5d)^3D_1$	1539.149	24489.10	329.3	0.3519	1.07	[277]
$(6s5d)^3D_2$	1479.303	24751.95	500	0.8786	1.76	[72]
$(6s7s)^3S_1$	680.148	32694.69	15.9	0.3951	24.85	[278]
$(6s6d)^3D_1$	458.364	39808.72	22.7	0.3970	17.49	[278]
$(6s6d)^3D_2$	457.749	39838.04	24.2	0.7932	32.78	[278]
$(6s8s)^3S_1$	423.316	41615.04	34.3	0.3714	10.83	[278]
$(6s7d)^3D_1$	379.948	44311.38	38.4	0.4003	10.42	[278]
$(6s7d)^3D_2$	379.924	44313.05	66.5	0.7860	11.82	[278]
$(6p^2)^3P_0$	409.1	42511.30	3.76	0.6837	181.84	[279]
$(6p^2)^3P_1$	387.4	43835.42	3.13	0.1734	55.40	[279]
$(6p^2)^3P_2$	373.6	44540.60	3.91	0.2449	62.63	[279]
$(6s9s)\ ^3S_1$	368.604	45121.37	35[1]	0.3663	10.47	[279]

Transitions from $(6s6p)^3P_0$

Final state	λ (nm)	Final state energy (cm^{-1})	τ (ns)	β	Γ (MHz)	Source
$(6s5d)^3D_1$	1388.761	24489.10	329.3	0.6388	1.94	[277]
$(6s7s)^3S_1$	649.087	32694.69	15.9	0.1515	9.53	[278]
$(6s6d)^3D_1$	444.044	39808.72	22.7	0.5823	25.65	[278]
$(6s8s)^3S_1$	411.073	41615.04	34.3	0.1352	3.94	[278]
$(6s7d)^3D_1$	370.056	44311.38	38.4	0.5777	15.04	[278]
$(6p^2)^3P_1$	377.117	43835.42	3.13	0.2506	80.13	[279]
$(6s9s)^3S_1$	359.287	45121.37	35[1]	0.1319	3.77	[279]

[1]Missing value for the lifetime in our references:
the value is set to be close to similar states (6s8s) and (6s9s), as reported in Ref. [279].

Table A1| Transitions employed for computing the polarizability of $^3P_1$ and $^3P_0$ states. The reduced matrix element is computed starting from the excited state lifetime τ and transition energy as detailed in Sec. 1.2.1 . β and Γ are computed from the final states' lifetimes τ using Eq. (6). We report the references for energy and lifetime values.

Transitions from $(6s6p)^1P_1$

Final state	λ (nm)	Final state energy (cm^{-1})	τ (ns)	β	$\Gamma = \beta/\tau$ (10^6/s)	Source
$(6s^2)^1P_1$	-398.911	0	5.464	1	183.02	[276]
$(6s7s)^1S_0$	1077.3	34350.65	45.8	0.8283	151.60	[240]
$(6s8s)^1S_0$	592.709	41939.90	37.9	0.6818	14.89	[240]
$(6s10s)^1S_0$	458.191	46893.2	377	0.6285	16.58	[240]
$(6s11s)^1S_0$	439.748	47808.5	15.6	0.6189	1.64	[240]
$(6s12s)^1S_0$	422.739	48723.5	33.6	0.6093	39.96	[240]
$(6s13s)^1S_0$	417.046	49046.4	53.1	0.6059	18.03	[240]
$(6s14s)^1S_0$	412.639	49302.5	115	0.6032	11.36	[240]
$(6s15s)^1S_0$	409.316	49499.2	190.9	0.6012	5.23	[240]
$(6s16s)^1S_0$	406.804	49650.1	243.8	0.5996	3.14	[240]
$(6s17s)^1S_0$	404.864	49767.9	377	0.5984	2.45	[240]
$(6p^2)^1S_0$	429.624	48344.4	25.3	0.6133	1.63	[240]
$(6p^2)^1D_2$	447.372	47421.0	21.8	0.6230	24.62	[240]
$(6s6d)^1D_2$	666.965	40061.51	35.2	0.7055	32.36	[240]
$(6s7d)^1D_2$	518.42	44357.60	49.8	0.6551	18.61	[240]
$(6s8d)^1D_2$	468.661	46405.60	466	0.6336	12.72	[240]
$(6s9d)^1D_2$	439.493	47821.70	16.1	0.6188	1.33	[240]
$(6s10d)^1D_2$	428.536	48403.50	57.4	0.6126	38.05	[240]
$(6s11d)^1D_2$	419.906	48883.10	49.4	0.6076	10.59	[240]
$(6s12d)^1D_2$	414.804	49176.00	177	0.6046	12.24	[240]
$(6s13d)^1D_2$	410.84	49408.6	260.6	0.6021	3.40	[240]
$(6s14d)^1D_2$	407.912	49583.3	363	0.6003	2.30	[240]
$(6s15d)^1D_2$	405.696	49717.2	533	0.5989	1.65	[240]

Table A2| Transitions employed for computing the polarizability of the $^1P_1$ state. The reduced matrix element is computed starting from the excited state lifetime τ and the transition energy as detailed in Sec. 1.2.1. β and Γ are computed from states' lifetimes τ using Eq. (6). We report the references for energy and lifetime values.

References

[1] W. Ketterle, "Nobel lecture: when atoms behave as waves: Bose-Einstein condensation and the atom laser", Rev. Mod. Phys. **74** (2002) (See page 1).

[2] E. A. Cornell and C. E. Wieman, "Nobel lecture: Bose-Einstein condensation in a dilute gas, the first 70 years and some recent experiments", Rev. Mod. Phys. **74** (2002) (See page 1).

[3] M. Greiner, O. Mandel, T. Esslinger, T. W. Hänsch, and I. Bloch, "Quantum phase transition from a superfluid to a Mott insulator in a gas of ultracold atoms", Nature **415** (2002) (See page 1).

[4] M. M. Ludlow Andrew D. and, J. Ye, E. Peik, and P. O. Schmidt, "Optical atomic clocks", Rev. Mod. Phys. **87** (2015) (See pages 1, 2, 6, 11, 12, 20, 21, 32, 69, 112, 153).

[5] I. H. Deutsch, "Harnessing the power of the second quantum revolution", PRX Quantum **1** (2020) (See page 1).

[6] A. J. Daley, I. Bloch, C. Kokail, S. Flannigan, N. Pearson, M. Troyer, and P. Zoller, "Practical quantum advantage in quantum simulation", Nature **607** (2022) (See page 1).

[7] A. M. Kaufman and K.-K. Ni, "Quantum science with optical tweezer arrays of ultracold atoms and molecules", Nat. Phys. **17** (2021) (See pages 1, 25, 103, 138).

[8] P. Scholl et al., "Quantum simulation of 2D antiferromagnets with hundreds of Rydberg atoms", Nature **595** (2021) (See pages 1, 33, 103).

[9] G. Semeghini et al., "Probing topological spin liquids on a programmable quantum simulator", Science **374** (2021) (See pages 1, 33).

[10] J. Koepsell, J. Vijayan, P. Sompet, F. Grusdt, T. A. Hilker, E. Demler, G. Salomon, I. Bloch, and C. Gross, "Imaging magnetic polarons in the doped Fermi–Hubbard model", Nature **572** (2019) (See pages 1, 19, 36, 133, 134).

[11] A. W. Young, W. J. Eckner, N. Schine, A. M. Childs, and A. M. Kaufman, "Tweezer-programmable 2D quantum walks in a Hubbard-regime lattice", Science **377** (2022) (See pages 1, 36).

[12] R. Tao, M. Ammenwerth, F. Gyger, I. Bloch, and J. Zeiher, "High-fidelity detection of large-scale atom arrays in an optical lattice", Phys. Rev. Lett. **133** (2024) (See pages 1, 10, 19, 29, 30, 79, 103, 120, 138).

[13] F. Serwane, G. Zürn, T. Lompe, T. B. Ottenstein, A. N. Wenz, and S. Jochim, "Deterministic preparation of a tunable few-fermion system", Science **332** (2011) (See pages 1, 36, 98, 146, 149).

[14] L. Bayha, M. Holten, R. Klemt, K. Subramanian, J. Bjerlin, S. M. Reimann, G. M. Bruun, P. M. Preiss, and S. Jochim, "Observing the emergence of a quantum phase transition shell by shell", Nature **587** (2020) (See pages 1, 36, 133, 146, 149).

[15] M. Holten, L. Bayha, K. Subramanian, S. Brandstetter, C. Heintze, P. Lunt, P. M. Preiss, and S. Jochim, "Observation of Cooper pairs in a mesoscopic two-dimensional Fermi gas", Nature **606** (2022) (See pages 1, 36, 103, 133, 146).

[16] S. Brandstetter et al., "Emergent interaction-driven elliptic flow of few fermionic atoms", Nat. Phys. **21** (2025) (See pages 1, 36, 133, 146, 154).

[17] A. Browaeys and T. Lahaye, "Many-body physics with individually controlled Rydberg atoms", Nat. Phys. **16** (2020) (See pages 1, 30, 103).

[18] C. Gross and W. S. Bakr, "Quantum gas microscopy for single atom and spin detection", Nat. Phys. **17** (2021) (See pages 1, 79, 103, 122).

[19] J. Berges, S. Brandstetter, J. Brewer, G. Bruun, T. Enss, S. Floerchinger, K. Fujii, M. Galka, G. Giacalone, Q. Guan, et al., "Few is different: deciphering many-body dynamics in mesoscopic quantum gases", arXiv:2509.05049 (2025) (See pages 1, 36, 133, 146).

[20] M. Saffman, T. G. Walker, and K. Mølmer, "Quantum information with Rydberg atoms", Rev. Mod. Phys. **82** (2010) (See page 1).

[21] M. Saffman, "Quantum computing with atomic qubits and Rydberg interactions: progress and challenges", Journal of Physics B: Atomic, Molecular and Optical Physics **49** (2016) (See pages 1, 29).

[22] D. Bluvstein, H. Levine, G. Semeghini, T. T. Wang, S. Ebadi, M. Kalinowski, A. Keesling, N. Maskara, H. Pichler, M. Greiner, et al., "A quantum processor based on coherent transport of entangled atom arrays", Nature **604** (2022) (See pages 1, 29).

[23] D. Bluvstein, S. J. Evered, A. A. Geim, S. H. Li, H. Zhou, T. Manovitz, S. Ebadi, M. Cain, M. Kalinowski, D. Hangleiter, et al., "Logical quantum processor based on reconfigurable atom arrays", Nature **626** (2024) (See pages 1, 29, 31, 103).

[24] D. Bluvstein, A. A. Geim, S. H. Li, S. J. Evered, J Ataides, G. Baranes, A. Gu, T. Manovitz, M. Xu, M. Kalinowski, et al., "Architectural mechanisms of a universal fault-tolerant quantum computer", arXiv:2506.20661 (2025) (See pages 1, 29, 154).

[25] T. Bothwell, D. Kedar, E. Oelker, J. M. Robinson, S. L. Bromley, W. L. Tew, J. Ye, and C. J. Kennedy, "JILA SrI optical lattice clock with uncertainty of 2.0 10^{-18}", Metrologia **56** (2019) (See pages 1, 32).

[26] X.-Y. Liu, P. Liu, J. Li, Y.-C. Zhang, Y.-B. Wang, Z.-P. Jia, X. Zhang, X.-Q. Zhu, D.-Q. Kong, W.-L. Song, et al., "A zero-dead-time strontium lattice clock with a stability at 10^{-19} level", arXiv:2509.15100 (2025) (See pages 1, 32).

[27] I. S. Madjarov, A. Cooper, A. L. Shaw, J. P. Covey, V. Schkolnik, T. H. Yoon, J. R. Williams, and M. Endres, "An atomic-array optical clock with single-atom readout", Phys. Rev. X **9** (2019) (See pages 1, 30, 32, 75, 103).

[28] M. A. Norcia, A. W. Young, W. J. Eckner, E. Oelker, J. Ye, and A. M. Kaufman, "Seconds-scale coherence on an optical clock transition in a tweezer array", Science **366** (2019) (See pages 1, 32, 103).

[29] A. W. Young, W. J. Eckner, W. R. Milner, D. Kedar, M. A. Norcia, E. Oelker, N. Schine, J. Ye, and A. M. Kaufman, "Half-minute-scale atomic coherence and high relative stability in a tweezer clock", Nature **588** (2020) (See pages 1, 32, 103).

[30] A. Cao, W. J. Eckner, T. Lukin Yelin, A. W. Young, S. Jandura, L. Yan, K. Kim, G. Pupillo, J. Ye, N. Darkwah Oppong, et al., "Multi-qubit gates and Schrödinger cat states in an optical clock", Nature **634** (2024) (See pages 1, 2, 32).

[31] R. Finkelstein, R. B.-S. Tsai, X. Sun, P. Scholl, S. Direkci, T. Gefen, J. Choi, A. L. Shaw, and M. Endres, "Universal quantum operations and ancilla-based read-out for tweezer clocks", Nature **634** (2024) (See pages 1, 2, 29, 31, 32, 71, 103, 154).

[32] V. Giovannetti, S. Lloyd, and L. Maccone, "Quantum metrology", Phys. Rev. Lett. **96** (2006) (See pages 1, 32).

[33] L. Pezzè, A. Smerzi, M. K. Oberthaler, R. Schmied, and P. Treutlein, "Quantum metrology with nonclassical states of atomic ensembles", Rev. Mod. Phys. **90** (2018) (See pages 1, 32).

[34] M. S. Safronova, D. Budker, D. DeMille, D. F. J. Kimball, A. Derevianko, and C. W. Clark, "Search for new physics with atoms and molecules", Rev. Mod. Phys. **90** (2018) (See pages 2, 32).

[35] S. Kolkowitz, I. Pikovski, N. Langellier, M. D. Lukin, R. L. Walsworth, and J. Ye, "Gravitational wave detection with optical lattice atomic clocks", Phys. Rev. D **94** (2016) (See pages 2, 32).

[36] W. F. McGrew et al., "Atomic clock performance enabling geodesy below the centimetre level", Nature **564** (2018) (See pages 2, 11, 32).

[37] C. J. Kennedy, E. Oelker, J. M. Robinson, T. Bothwell, D. Kedar, W. R. Milner, G. E. Marti, A. Derevianko, and J. Ye, "Precision metrology meets cosmology: improved constraints on ultralight dark matter from atom-cavity frequency comparisons", Phys. Rev. Lett. **125** (2020) (See pages 2, 32).

[38] T. Bothwell, C. J. Kennedy, A. Aeppli, D. Kedar, J. M. Robinson, E. Oelker, A. Staron, and J. Ye, "Resolving the gravitational redshift across a millimetre-scale atomic sample", Nature **602** (2022) (See pages 2, 32).

[39] X. Zheng, J. Dolde, V. Lochab, B. N. Merriman, H. Li, and S. Kolkowitz, "Differential clock comparisons with a multiplexed optical lattice clock", Nature **602** (2022) (See pages 2, 32).

[40] D. Bourgund, T. Chalopin, P. Bojović, H. Schlömer, S. Wang, T. Franz, S. Hirthe, A. Bohrdt, F. Grusdt, I. Bloch, et al., "Formation of individual stripes in a mixed-dimensional cold-atom Fermi-Hubbard system", Nature **637** (2025) (See page 2).

[41] M. Xu, L. H. Kendrick, A. Kale, Y. Gang, C. Feng, S. Zhang, A. W. Young, M. Lebrat, and M. Greiner, "A neutral-atom Hubbard quantum simulator in the cryogenic regime", Nature (2025) (See page 2).

[42] L. H. Kendrick, A. Kale, Y. Gang, A. D. Deters, M. Lebrat, A. W. Young, and M. Greiner, "Pseudogap in a Fermi-Hubbard quantum simulator", arXiv:2509.18075 (2025) (See page 2).

[43] T. Graham, Y Song, J Scott, C Poole, L Phuttitarn, K Jooya, P Eichler, X Jiang, A Marra, B Grinkemeyer, et al., "Multi-qubit entanglement and algorithms on a neutral-atom quantum computer", Nature **604** (2022) (See pages 2, 29).

[44] A. J. Daley, M. M. Boyd, J. Ye, and P. Zoller, "Quantum computing with alkaline-earth-metal atoms", Phys. Rev. Lett. **101** (2008) (See pages 2, 6, 11, 12, 29).

[45] A. V. Gorshkov, A. M. Rey, A. J. Daley, M. M. Boyd, J. Ye, P. Zoller, and M. D. Lukin, "Alkaline-earth-metal atoms as few-qubit quantum registers", Phys. Rev. Lett. **102** (2009) (See pages 2, 6, 11, 12).

[46] K. Shibata, S. Kato, A. Yamaguchi, S. Uetake, and Y. Takahashi, "A scalable quantum computer with ultranarrow optical transition of ultracold neutral atoms in an optical lattice", Appl. Phys. B **97** (2009) (See pages 2, 11).

[47] A. V. Gorshkov, M. Hermele, V. Gurarie, C. Xu, P. S. Julienne, J. Ye, P. Zoller, E. Demler, M. D. Lukin, and A. M. Rey, "Two-orbital SU(N) magnetism with ultracold alkaline-earth atoms", Nat. Phys. **6** (2010) (See pages 2, 6, 11, 30, 33, 34, 37, 112, 133, 148, 153).

[48] S. Ma, G. Liu, P. Peng, B. Zhang, S. Jandura, J. Claes, A. P. Burgers, G. Pupillo, S. Puri, and J. D. Thompson, "High-fidelity gates and mid-circuit erasure conversion in an atomic qubit", Nature **622** (2023) (See pages 2, 9, 30, 31, 71, 103–105, 110–112, 118, 154, 156).

[49] P. Scholl, A. L. Shaw, R. B.-S. Tsai, R. Finkelstein, J. Choi, and M. Endres, "Erasure conversion in a high-fidelity Rydberg quantum simulator", Nature **622** (2023) (See pages 2, 9, 30, 31, 71, 103–105, 110, 111, 154, 156).

[50] R. Tao, O. Lib, F. Gyger, H. Timme, M. Ammenwerth, I. Bloch, and J. Zeiher, "Universal gates for a metastable qubit in strontium-88", arXiv:2506.10714 (2025) (See pages 2, 9, 29–31, 71, 103, 105, 154, 156).

[51] A. Senoo, A. Baumgärtner, J. W. Lis, G. M. Vaidya, Z. Zeng, G. Giudici, H. Pichler, and A. M. Kaufman, "High-fidelity entanglement and coherent multi-qubit mapping in an atom array", arXiv:2506.13632 (2025) (See pages 2, 9, 30, 31, 71, 103, 105, 154, 155).

[52] S. Saskin, J. T. Wilson, B. Grinkemeyer, and J. D. Thompson, "Narrow-line cooling and imaging of ytterbium atoms in an optical tweezer array", Phys. Rev. Lett. **122** (2019) (See pages 2, 9, 10, 20, 23, 29, 30, 63, 69, 71, 75, 79, 80, 103, 153).

[53] A. Jenkins, J. W. Lis, A. Senoo, W. F. McGrew, and A. M. Kaufman, "Ytterbium nuclear-spin qubits in an optical tweezer array", Phys. Rev. X **12** (2022) (See pages 2, 3, 9, 10, 26, 29, 30, 63, 67, 69, 75, 79, 82, 83, 95, 112, 133, 138–140, 143, 153, 154).

[54] S. Ma, A. P. Burgers, G. Liu, J. Wilson, B. Zhang, and J. D. Thompson, "Universal gate operations on nuclear spin qubits in an optical tweezer array of ^{171}Yb atoms", Phys. Rev. X **12** (2022) (See pages 2, 10, 20, 24, 29, 30, 69, 75, 79, 103, 112, 154).

[55] M. A. Norcia, A. W. Young, and A. M. Kaufman, "Microscopic control and detection of ultracold strontium in optical-tweezer arrays", Phys. Rev. X **8** (2018) (See pages 2, 9, 20, 21, 29, 30, 69, 71, 75, 79, 83, 153).

[56] T. O. Höhn, E. Staub, G. Brochier, N. Darkwah Oppong, and M. Aidelsburger, "State-dependent potentials for the ^{1}S$_0$ and ^{3}P$_0$ clock states of neutral ytterbium atoms", Phys. Rev. A **108** (2023) (See pages 2, 20, 21, 30, 36, 37, 66, 67, 154).

[57] T. O. Höhn, R. A. Villela, E. Zu, L. Bezzo, R. M. Kroeze, and M. Aidelsburger, "Determining the ^{3}P$_0$ excited-state tune-out wavelength of ^{174}Yb in a triple-magic lattice", arXiv:2412.14163 (2024) (See pages 2, 20–23, 37, 71, 154).

[58] A. Amaricci, A. Richaud, M. Capone, N. Darkwah Oppong, and F. Scazza, "Engineering the Kondo impurity problem with alkaline-earth-atom arrays", Phys. Rev. A **112** (2025) (See pages 2, 11, 20, 33, 37, 69, 148, 154).

[59] F. M. Surace, P. Fromholz, N. D. Oppong, M. Dalmonte, and M. Aidelsburger, "Ab initio derivation of lattice-gauge-theory dynamics for cold gases in optical lattices", PRX Quantum **4** (2023) (See pages 2, 20, 33, 154).

[60] G. De Paciani, L. Homeier, J. C. Halimeh, M. Aidelsburger, and F. Grusdt, "Quantum simulation of fermionic non-Abelian lattice gauge theories in (2+1)D with built-in gauge protection", arXiv:2506.14747 (2025) (See pages 2, 20, 154).

[61] G. Pagano, F. Scazza, and M. Foss-Feig, "Fast and scalable quantum information processing with two-electron atoms in optical tweezer arrays", Advanced Quantum Technologies **2** (2019) (See pages 2, 11, 19, 30).

[62] M. A. Cazalilla and A. M. Rey, "Ultracold Fermi gases with emergent SU(N) symmetry", Reports on Progress in Physics **77** (2014) (See pages 2, 6, 33, 153).

[63] X. Zhang, M. Bishof, S. L. Bromley, C. V. Kraus, M. S. Safronova, P. Zoller, A. M. Rey, and J. Ye, "Spectroscopic observation of SU(N)-symmetric interactions in Sr orbital magnetism", Science **345** (2014) (See pages 2, 33).

[64] F. M. Surace, P. Fromholz, F. Scazza, and M. Dalmonte, "Scalable, ab initio protocol for quantum simulating SU(N)×u(1) Lattice Gauge Theories", Quantum **8** (2024) (See pages 2, 33).

[65] J. W. Lis, A. Senoo, W. F. McGrew, F. Rönchen, A. Jenkins, and A. M. Kaufman, "Midcircuit operations using the omg architecture in neutral atom arrays", Phys. Rev. X **13** (2023) (See pages 2, 10, 11, 19, 20, 30–32, 69, 75, 79, 103, 112, 148, 153–155).

[66] T. Grünzweig, A. Hilliard, M. McGovern, and M. F. Andersen, "Near-deterministic preparation of a single atom in an optical microtrap", Nat. Phys. **6** (2010) (See pages 3, 133, 138, 139).

[67] B. J. Lester, N. Luick, A. M. Kaufman, C. M. Reynolds, and C. A. Regal, "Rapid production of uniformly filled arrays of neutral atoms", Phys. Rev. Lett. **115** (2015) (See pages 3, 138).

[68] M. O. Brown, T. Thiele, C. Kiehl, T.-W. Hsu, and C. A. Regal, "Gray-molasses optical-tweezer loading: controlling collisions for scaling atom-array assembly", Phys. Rev. X **9** (2019) (See pages 3, 138, 139).

[69] R. M. Kroeze, S. L. Kristensen, and S. Pucher, "^{171}Yb reference data", arXiv:2509.04416 (2025) (See page 6).

[70] NIST atomic spectra database (See page 7).

[71] C. J. Foot, "Atomic physics", Oxford University Press (2005) (See pages 7, 15, 83).

[72] J. W. Cho, H.-g. Lee, S. Lee, J. Ahn, W.-K. Lee, D.-H. Yu, S. K. Lee, and C. Y. Park, "Optical repumping of triplet-P states enhances magneto-optical trapping of ytterbium atoms", Phys. Rev. A **85** (2012) (See pages 8, 9, 113, 116, 159).

[73] A. V. Taichenachev, V. I. Yudin, C. W. Oates, C. W. Hoyt, Z. W. Barber, and L. Hollberg, "Magnetic field-induced spectroscopy of forbidden optical transitions with application to lattice-based optical atomic clocks", Phys. Rev. Lett. **96** (2006) (See page 8).

[74] Z. W. Barber, C. W. Hoyt, C. W. Oates, L. Hollberg, A. V. Taichenachev, and V. I. Yudin, "Direct excitation of the forbidden clock transition in neutral ^{174}Yb atoms confined to an optical lattice", Phys. Rev. Lett. **96** (2006) (See page 8).

[75] S. Dörscher, A. Thobe, B. Hundt, A. Kochanke, R. Le Targat, P. Windpassinger, C. Becker, and K. Sengstock, "Creation of quantum-degenerate gases of ytterbium in a compact 2D-/3D-magneto-optical trap setup", Review of Scientific Instruments **84** (2013) (See pages 9, 88).

[76] J. P. Covey, I. S. Madjarov, A. Cooper, and M. Endres, "2000-times repeated imaging of strontium atoms in clock-magic tweezer arrays", Phys. Rev. Lett. **122** (2019) (See pages 9, 10, 19, 75, 79, 103, 153).

[77] O Abdel Karim, A Muzi Falconi, R Panza, W Liu, and F Scazza, "Single-atom imaging of ^{173}Yb in optical tweezers loaded by a five-beam magneto-optical trap", Quantum Science and Technology **10** (2025) (See pages 9, 23, 25).

[78] A. Muzi Falconi, R. Panza, S. Sbernardori, R. Forti, R. Klemt, O. Abdel Karim, M. Marinelli, and F. Scazza, "Microsecond-scale high-survival and number-resolved detection of ytterbium atom arrays", arXiv:2507.01011 (2025) (See pages 9, 20, 23).

[79] S. G. Porsev, Y. G. Rakhlina, and M. G. Kozlov, "Electric-dipole amplitudes, lifetimes, and polarizabilities of the low-lying levels of atomic ytterbium", Phys. Rev. A **60** (1999) (See pages 9, 113, 116).

[80] M. M. Boyd, T. Zelevinsky, A. D. Ludlow, S. Blatt, T. Zanon-Willette, S. M. Foreman, and J. Ye, "Nuclear spin effects in optical lattice clocks", Phys. Rev. A **76** (2007) (See pages 10, 12).

[81] A. Cooper, J. P. Covey, I. S. Madjarov, S. G. Porsev, M. S. Safronova, and M. Endres, "Alkaline-Earth atoms in optical tweezers", Phys. Rev. X **8** (2018) (See pages 10, 19, 79, 120).

[82] M. A. Norcia et al., "Midcircuit qubit measurement and rearrangement in a ^{171}Yb atomic array", Phys. Rev. X **13** (2023) (See pages 10, 19, 20, 30, 31, 69, 75, 79, 103, 112, 154).

[83] J. A. Muniz et al., "High-fidelity universal gates in the ^{171}Yb ground-state nuclear-spin qubit", PRX Quantum **6** (2025) (See page 10).

[84] W. Huie, L. Li, N. Chen, X. Hu, Z. Jia, W. K. C. Sun, and J. P. Covey, "Repetitive readout and real-time control of nuclear spin qubits in ^{171}Yb atoms", PRX Quantum **4** (2023) (See pages 10, 30, 31, 75, 79, 103, 154).

[85] S. Taie, Y. Takasu, S. Sugawa, R. Yamazaki, T. Tsujimoto, R. Murakami, and Y. Takahashi, "Realization of a SU(2) x SU(6) system of fermions in a cold atomic gas", Phys. Rev. Lett. **105** (2010) (See pages 11, 16, 66, 149, 156).

[86] S. Stellmer, R. Grimm, and F. Schreck, "Detection and manipulation of nuclear spin states in fermionic strontium", Phys. Rev. A **84** (2011) (See pages 11, 16, 156).

[87] F. Scazza, "Probing SU(N)-symmetric orbital interactions with ytterbium Fermi gases in optical lattices", PhD diss., LMU München (2015) (See pages 11, 33, 34, 101).

[88] S. G. Porsev and A. Derevianko, "Hyperfine quenching of the metastable $^3P_{0,2}$ states in divalent atoms", Phys. Rev. A **69** (2004) (See page 11).

[89] M. Kanász-Nagy, Y. Ashida, T. Shi, C. u. u. u. u. P. m. c. Moca, T. N. Ikeda, S. Fölling, J. I. Cirac, G. Zaránd, and E. A. Demler, "Exploring the anisotropic Kondo model in and out of equilibrium with alkaline-earth atoms", Phys. Rev. B **97** (2018) (See pages 11, 33, 37).

[90] A. Sotnikov, N. Darkwah Oppong, Y. Zambrano, and A. Cichy, "Orbital ordering of ultracold alkaline-earth atoms in optical lattices", Phys. Rev. Res. **2** (2020) (See pages 11, 133).

[91] X. Zhang, K. Beloy, Y. S. Hassan, W. F. McGrew, C.-C. Chen, J. L. Siegel, T. Grogan, and A. D. Ludlow, "Subrecoil clock-transition laser cooling enabling shallow optical lattice clocks", Phys. Rev. Lett. **129** (2022) (See pages 11, 49, 157).

[92] C.-C. Chen, J. L. Siegel, B. D. Hunt, T. Grogan, Y. S. Hassan, K. Beloy, K. Gibble, R. C. Brown, and A. D. Ludlow, "Clock-line-mediated Sisyphus cooling", Phys. Rev. Lett. **133** (2024) (See page 11).

[93] R. M. Kroeze, R. A. Villela, E. Zu, T. O. Höhn, and M. Aidelsburger, "Isotope-agnostic motional ground-state cooling of neutral Yb atoms", arXiv:2506.09031 (2025) (See pages 11, 26, 49, 157).

[94] J. P. Covey, A. Sipahigil, S. Szoke, N. Sinclair, M. Endres, and O. Painter, "Telecom-band quantum optics with ytterbium atoms and silicon nanophotonics", Phys. Rev. Appl. **11** (2019) (See pages 11, 29).

[95] L. Li, X. Hu, Z. Jia, W. Huie, W. K. C. Sun, Aakash, Y. Dong, N. Hiri-O-Tuppa, and J. P. Covey, "Parallelized telecom quantum networking with an ytterbium-171 atom array", Nature Physics (2025) (See pages 11, 29).

[96] A. Asenjo-Garcia, M. Moreno-Cardoner, A. Albrecht, H. J. Kimble, and D. E. Chang, "Exponential improvement in photon storage fidelities using subradiance and "selective radiance" in atomic arrays", Phys. Rev. X **7** (2017) (See pages 11, 97).

[97] G. Ferioli, A. Glicenstein, L. Henriet, I. Ferrier-Barbut, and A. Browaeys, "Storage and release of subradiant excitations in a dense atomic cloud", Phys. Rev. X **11** (2021) (See pages 11, 97, 133).

[98] G. Ferioli, A. Glicenstein, I. Ferrier-Barbut, and A. Browaeys, "A non-equilibrium superradiant phase transition in free space", Nature Physics **19** (2023) (See pages 11, 97, 133).

[99] S. J. Masson, J. P. Covey, S. Will, and A. Asenjo-Garcia, "Dicke superradiance in ordered arrays of multilevel atoms", PRX Quantum **5** (2024) (See page 11).

[100] D. A. Steck, *Quantum and atom optics*, `http://steck.us/teaching`, 2011 (See pages 12, 13, 16, 17).

[101] I. Reichenbach and I. H. Deutsch, "Sideband cooling while preserving coherences in the nuclear spin state in group-II-like atoms", Phys. Rev. Lett. **99** (2007) (See pages 12, 156).

[102] R. M. Sandner, M. Müller, A. J. Daley, and P. Zoller, "Spatial Pauli blocking of spontaneous emission in optical lattices", Phys. Rev. A **84** (2011) (See pages 12, 156).

[103] R. Grimm, M. Weidemüller, and Y. B. Ovchinnikov, "Optical dipole traps for neutral atoms", Advances in atomic, molecular, and optical physics **42** (2000) (See pages 13, 27).

[104] M. J. Martin, "Quantum metrology and many-body physics: pushing the frontier of the optical lattice clock", PhD diss., University of Colorado at Boulder (2013) (See pages 15, 57, 153).

[105] L. Riegger, "Interorbital spin exchange in a state-dependent optical lattice", PhD diss., LMU München (2019) (See pages 15, 16, 33, 153).

[106] H. J. Metcalf and P. Van der Straten, "Laser cooling and trapping", Springer Science & Business Media (1999) (See pages 19, 158).

[107] C. Weitenberg, M. Endres, J. F. Sherson, M. Cheneau, P. Schauß, T. Fukuhara, I. Bloch, and S. Kuhr, "Single-spin addressing in an atomic Mott insulator", Nature **471** (2011) (See pages 19, 36).

[108] M. Martinez-Dorantes, W. Alt, J. Gallego, S. Ghosh, L. Ratschbacher, and D. Meschede, "State-dependent fluorescence of neutral atoms in optical potentials", Phys. Rev. A **97** (2018) (See pages 20, 71).

[109] L. Riegger, N. Darkwah Oppong, M. Höfer, D. R. Fernandes, I. Bloch, and S. Fölling, "Localized magnetic moments with tunable spin exchange in a gas of ultracold fermions", Phys. Rev. Lett. **120** (2018) (See pages 20, 33, 69, 133, 149, 153).

[110] K. Ono, T. Higomoto, Y. Saito, S. Uchino, Y. Nishida, and Y. Takahashi, "Observation of spin-space quantum transport induced by an atomic quantum point contact", Nature communications **12** (2021) (See pages 20, 149, 153).

[111] N. Darkwah Oppong, G. Pasqualetti, O. Bettermann, P. Zechmann, M. Knap, I. Bloch, and S. Fölling, "Probing transport and slow relaxation in the mass-imbalanced Fermi-Hubbard model", Phys. Rev. X **12** (2022) (See pages 20, 31, 33, 69, 133, 153).

[112] B. W. Reichardt et al., "Logical computation demonstrated with a neutral atom quantum processor", arXiv:2411.11822 (2024) (See page 20).

[113] J. Muniz et al., "Repeated ancilla reuse for logical computation on a neutral atom quantum computer", arXiv:2506.09936 (2025) (See page 20).

[114] R. Yamamoto, J. Kobayashi, T. Kuno, K. Kato, and Y. Takahashi, "An ytterbium quantum gas microscope with narrow-line laser cooling", New J. Phys. **18** (2016) (See pages 20, 63, 67, 69, 75, 80, 103, 122).

[115] Z. W. Barber et al., "Optical lattice induced light shifts in an Yb atomic clock", Phys. Rev. Lett. **100** (2008) (See pages 20, 21, 69).

[116] J. A. Sherman, N. D. Lemke, N. Hinkley, M. Pizzocaro, R. W. Fox, A. D. Ludlow, and C. W. Oates, "High-accuracy measurement of atomic polarizability in an optical lattice clock", Phys. Rev. Lett. **108** (2012) (See page 20).

[117] B. J. Bloom, T. L. Nicholson, J. R. Williams, S. L. Campbell, M. Bishof, X. Zhang, W. Zhang, S. Bromley, and J. Ye, "An optical lattice clock with accuracy and stability at the 10^{-18} level", Nature **506** (2014) (See page 20).

[118] T. Nicholson et al., "Systematic evaluation of an atomic clock at 2 x 10^{-18} total uncertainty", Nature communications **6** (2015) (See pages 20, 32).

[119] V. A. Dzuba and A Derevianko, "Dynamic polarizabilities and related properties of clock states of the ytterbium atom", J. Phys. B **43** (2010) (See page 21).

[120] N. Schlosser, G. Reymond, I. Protsenko, and P. Grangier, "Sub-poissonian loading of single atoms in a microscopic dipole trap", Nature **411** (2001) (See pages 25, 29).

[121] I. S. Madjarov, "Entangling, controlling, and detecting individual strontium atoms in optical", PhD diss., California Institute of Technology (2021) (See pages 25, 71, 79, 83).

[122] O. Abdel Karim, "Realization of a new experimental apparatus for the microscopic control of individual ytterbium atoms", PhD thesis (2024) (See pages 25, 38, 43, 47, 51, 64, 65, 67, 76, 155).

[123] A. M. Kaufman, B. J. Lester, and C. A. Regal, "Cooling a single atom in an optical tweezer to its quantum ground state", Phys. Rev. X **2** (2012) (See page 26).

[124] V. Vuletic, C. Chin, A. J. Kerman, and S. Chu, "Degenerate Raman sideband cooling of trapped cesium atoms at very high atomic densities", Phys. Rev. Lett. **81** (1998) (See page 26).

[125] D.-J. Han, S. Wolf, S. Oliver, C. McCormick, M. T. DePue, and D. S. Weiss, "3D Raman sideband cooling of cesium atoms at high density", Phys. Rev. Lett. **85** (2000) (See page 26).

[126] T. A. Savard, K. M. O'Hara, and J. E. Thomas, "Laser-noise-induced heating in far-off resonance optical traps", Phys. Rev. A **56** (1997) (See pages 26, 27).

[127] M. E. Gehm, K. M. O'Hara, T. A. Savard, and J. E. Thomas, "Dynamics of noise-induced heating in atom traps", Phys. Rev. A **58** (1998) (See pages 26, 27).

[128] S. Blatt, A. Mazurenko, M. F. Parsons, C. S. Chiu, F. Huber, and M. Greiner, "Low-noise optical lattices for ultracold ^{6}Li", Phys. Rev. A **92** (2015) (See page 26).

[129] M. Endres, H. Bernien, A. Keesling, H. Levine, E. R. Anschuetz, A. Krajenbrink, C. Senko, V. Vuletic, M. Greiner, and M. D. Lukin, "Atom-by-atom assembly of defect-free one-dimensional cold atom arrays", Science **354** (2016) (See page 27).

[130] T.-W. Hsu, "A high optical access cryogenic optical tweezer array", PhD diss., University of Colorado (2024) (See page 27).

[131] O. Daichi, "Single ytterbium atoms in an optical tweezer array: high-resolution spectroscopy, single-photon Rydberg excitation, and a scheme for nondestructive detection", PhD diss., Kyoto University (2015) (See pages 27, 65).

[132] Z. Zhang, T.-W. Hsu, T. Y. Tan, D. H. Slichter, A. M. Kaufman, M. Marinelli, and C. A. Regal, "High optical access cryogenic system for Rydberg atom arrays with a 3000-second trap lifetime", PRX Quantum **6** (2025) (See pages 27, 74, 79).

[133] C. Tuchendler, A. M. Lance, A. Browaeys, Y. R. P. Sortais, and P. Grangier, "Energy distribution and cooling of a single atom in an optical tweezer", Phys. Rev. A **78** (2008) (See pages 28, 73, 74, 116, 130).

[134] N. Schlosser, G. Reymond, and P. Grangier, "Collisional blockade in microscopic optical dipole traps", Phys. Rev. Lett. **89** (2002) (See pages 29, 95, 133, 134, 138).

[135] D. Bloch, B. Hofer, S. R. Cohen, A. Browaeys, and I. Ferrier-Barbut, "Trapping and imaging single dysprosium atoms in optical tweezer arrays", Phys. Rev. Lett. **131** (2023) (See pages 29, 79).

[136] D. S. Grün, S. J. M. White, A. Ortu, A. Di Carli, H. Edri, M. Lepers, M. J. Mark, and F. Ferlaino, "Optical tweezer arrays of erbium atoms", Phys. Rev. Lett. **133** (2024) (See pages 29, 79, 83, 103, 133–135, 138).

[137] M. Saffman, "Quantum computing with neutral atoms", National Science Review **6** (2019) (See page 29).

[138] F. Gyger, M. Ammenwerth, R. Tao, H. Timme, S. Snigirev, I. Bloch, and J. Zeiher, "Continuous operation of large-scale atom arrays in optical lattices", Phys. Rev. Res. **6** (2024) (See pages 29, 31, 32).

[139] M. A. Norcia et al., "Iterative assembly of ^{171}Yb atom arrays with cavity-enhanced optical lattices", PRX Quantum **5** (2024) (See pages 29, 82, 103, 138).

[140] R. Lin et al., "AI-enabled parallel assembly of thousands of defect-free neutral atom arrays", Phys. Rev. Lett. **135** (2025) (See pages 29, 138).

[141] H. J. Manetsch, G. Nomura, E. Bataille, X. Lv, K. H. Leung, and M. Endres, "A tweezer array with 6100 highly coherent atomic qubits", Nature (2025) (See page 29).

[142] N.-C. Chiu, E. C. Trapp, J. Guo, M. H. Abobeih, L. M. Stewart, S. Hollerith, P. L. Stroganov, M. Kalinowski, A. A. Geim, S. J. Evered, et al., "Continuous operation of a coherent 3,000-qubit system", Nature (2025) (See pages 29, 31, 32, 82, 138).

[143] J. P. Covey, H. Weinfurter, and H. Bernien, "Quantum networks with neutral atom processing nodes", npj Quantum Information **9** (2023) (See page 29).

[144] Y. Wu, S. Kolkowitz, S. Puri, and J. D. Thompson, "Erasure conversion for fault-tolerant quantum computing in alkaline earth Rydberg atom arrays", Nature communications **13** (2022) (See pages 30, 31, 111, 154).

[145] B. Zhang, G. Liu, G. Bornet, S. P. Horvath, P. Peng, S. Ma, S. Huang, S. Puri, and J. D. Thompson, "Leveraging erasure errors in logical qubits with metastable ^{171}Yb atoms", arXiv:2506.13724 (2025) (See pages 30, 31, 154).

[146] Z. Z. Yan, B. M. Spar, M. L. Prichard, S. Chi, H.-T. Wei, E. Ibarra-García-Padilla, K. R. A. Hazzard, and W. S. Bakr, "Two-dimensional programmable tweezer arrays of fermions", Phys. Rev. Lett. **129** (2022) (See pages 30, 133, 134).

[147] J. T. Wilson, S. Saskin, Y. Meng, S. Ma, R. Dilip, A. P. Burgers, and J. D. Thompson, "Trapping alkaline earth Rydberg atoms optical tweezer arrays", Phys. Rev. Lett. **128** (2022) (See page 30).

[148] S. Buob, J. Höschele, V. Makhalov, A. Rubio-Abadal, and L. Tarruell, "A strontium quantum-gas microscope", PRX Quantum **5** (2024) (See pages 30, 36, 122).

[149] Y. Li, Y. Bao, M. Peper, C. Li, and J. D. Thompson, "Fast, continuous and coherent atom replacement in a neutral atom qubit array", arXiv:2506.15633 (2025) (See pages 31, 32, 82).

[150] K. Singh, C. E. Bradley, S. Anand, V. Ramesh, R. White, and H. Bernien, "Mid-circuit correction of correlated phase errors using an array of spectator qubits", Science **380** (2023) (See page 31).

[151] H. J. Briegel, D. E. Browne, W. Dür, R. Raussendorf, and M. Van den Nest, "Measurement-based quantum computation", Nature Physics **5** (2009) (See page 31).

[152] L. Pezzè and A. Smerzi, "Heisenberg-limited noisy atomic clock using a hybrid coherent and squeezed state protocol", Phys. Rev. Lett. **125** (2020) (See page 31).

[153] E. Deist, Y.-H. Lu, J. Ho, M. K. Pasha, J. Zeiher, Z. Yan, and D. M. Stamper-Kurn, "Mid-circuit cavity measurement in a neutral atom array", Phys. Rev. Lett. **129** (2022) (See page 31).

[154] T. M. Graham, L. Phuttitarn, R. Chinnarasu, Y. Song, C. Poole, K. Jooya, J. Scott, A. Scott, P. Eichler, and M. Saffman, "Midcircuit measurements on a single-species neutral alkali atom quantum processor", Phys. Rev. X **13** (2023) (See page 31).

[155] N. Dimarcq, M. Gertsvolf, G. Mileti, S. Bize, C. Oates, E. Peik, D. Calonico, T. Ido, P. Tavella, F. Meynadier, et al., "Roadmap towards the redefinition of the second", Metrologia **61** (2024) (See page 32).

[156] M. C. Marshall et al., "High-stability single-ion clock with 5.5 10 $^{-19}$ systematic uncertainty", Phys. Rev. Lett. **135** (2025) (See page 32).

[157] W. J. Eckner, N. Darkwah Oppong, A. Cao, A. W. Young, W. R. Milner, J. M. Robinson, J. Ye, and A. M. Kaufman, "Realizing spin squeezing with Rydberg interactions in an optical clock", Nature **621** (2023) (See page 32).

[158] N. Schine, A. W. Young, W. J. Eckner, M. J. Martin, and A. M. Kaufman, "Long-lived Bell states in an array of optical clock qubits", Nature Physics **18** (2022) (See page 32).

[159] A. L. Shaw, R. Finkelstein, R. B.-S. Tsai, P. Scholl, T. H. Yoon, J. Choi, and M. Endres, "Multi-ensemble metrology by programming local rotations with atom movements", Nat. Phys. **20** (2024) (See pages 32, 103).

[160] S. Ebadi et al., "Quantum phases of matter on a 256-atom programmable quantum simulator", Nature **595** (2021) (See pages 33, 103).

[161] F. Scazza, C. Hofrichter, M. Höfer, P. De Groot, I. Bloch, and S. Fölling, "Observation of two-orbital spin-exchange interactions with ultracold SU(N)-symmetric fermions", Nature Physics **10** (2014) (See pages 33–35, 101, 148, 149).

[162] G. Cappellini et al., "Direct observation of coherent interorbital spin-exchange dynamics", Phys. Rev. Lett. **113** (2014) (See pages 33, 34).

[163] G. Pagano, M. Mancini, G. Cappellini, P. Lombardi, F. Schäfer, H. Hu, X.-J. Liu, J. Catani, C. Sias, M. Inguscio, et al., "A one-dimensional liquid of fermions with tunable spin", Nature Physics **10** (2014) (See pages 33, 149).

[164] C. Hofrichter, L. Riegger, F. Scazza, M. Höfer, D. R. Fernandes, I. Bloch, and S. Fölling, "Direct probing of the mott crossover in the SU(N) Fermi-Hubbard model", Phys. Rev. X **6** (2016) (See pages 33, 133).

[165] D. Tusi, L. Franchi, L. F. Livi, K. Baumann, D Benedicto Orenes, L. Del Re, R. E. Barfknecht, T.-W. Zhou, M. Inguscio, G. Cappellini, et al., "Flavour-selective localization in interacting lattice fermions", Nat. Phys. **18** (2022) (See pages 33, 133, 149).

[166] S. Taie, E. Ibarra-García-Padilla, N. Nishizawa, Y. Takasu, Y. Kuno, H.-T. Wei, R. T. Scalettar, K. R. Hazzard, and Y. Takahashi, "Observation of antiferromagnetic correlations in an ultracold SU(N) Hubbard model", Nature Physics **18** (2022) (See page 33).

[167] C. Chin, R. Grimm, P. Julienne, and E. Tiesinga, "Feshbach resonances in ultracold gases", Rev. Mod. Phys. **82** (2010) (See pages 33, 35).

[168] O. Bettermann, "Interorbital interactions in ytterbium-171", PhD diss. LMU München (2023) (See page 33).

[169] K. Ono, J. Kobayashi, Y. Amano, K. Sato, and Y. Takahashi, "Antiferromagnetic interorbital spin-exchange interaction of ^{171}Yb", Phys. Rev. A **99** (2019) (See pages 34, 35, 37).

[170] T. O. Höhn, "State-dependent potentials and clock ground-state cooling in an ytterbium quantumsimulator", PhD diss., LMU München (2024) (See pages 35, 47, 83, 88, 153, 154).

[171] M. Kitagawa, K. Enomoto, K. Kasa, Y. Takahashi, R. Ciuryło, P. Naidon, and P. S. Julienne, "Two-color photoassociation spectroscopy of ytterbium atoms and the precise determinations of s-wave scattering lengths", Phys. Rev. A **77** (2008) (See pages 35, 99, 149).

[172] L Franchi, L. Livi, G Cappellini, G Binella, M Inguscio, J Catani, and L Fallani, "State-dependent interactions in ultracold ^{174}Yb probed by optical clock spectroscopy", New Journal of Physics **19** (2017) (See page 35).

[173] M. Höfer, L. Riegger, F. Scazza, C. Hofrichter, D. R. Fernandes, M. M. Parish, J. Levinsen, I. Bloch, and S. Fölling, "Observation of an orbital interaction-induced feshbach resonance in ^{173}Yb", Phys. Rev. Lett. **115** (2015) (See pages 35, 45).

[174] O. Bettermann, N. Darkwah Oppong, G. Pasqualetti, L. Riegger, I. Bloch, and S. Fölling, "Clock-line photoassociation of strongly bound dimers in a magic-wavelength lattice", Phys. Rev. A **108** (2023) (See pages 35, 45, 98, 150).

[175] A. Bergschneider, V. M. Klinkhamer, J. H. Becher, R. Klemt, G. Zürn, P. M. Preiss, and S. Jochim, "Spin-resolved single-atom imaging of li 6 in free space", Phys. Rev. A **97** (2018) (See pages 36, 37, 62, 103–105, 127, 133, 147, 149, 153, 156).

[176] P. Lunt, P. Hill, J. Reiter, P. M. Preiss, M. Gałka, and S. Jochim, "Realization of a Laughlin state of two rapidly rotating fermions", Phys. Rev. Lett. **133** (2024) (See pages 36, 146).

[177] A. N. Wenz, G. Zürn, S. Murmann, I. Brouzos, T. Lompe, and S. Jochim, "From few to many: observing the formation of a Fermi sea one atom at a time", Science **342** (2013) (See page 36).

[178] L. Sonderhouse, C. Sanner, R. B. Hutson, A. Goban, T. Bilitewski, L. Yan, W. R. Milner, A. M. Rey, and J. Ye, "Thermodynamics of a deeply degenerate SU(N)-symmetric Fermi gas", Nature Physics **16** (2020) (See pages 36, 98–101, 149, 154).

[179] M. Dixmerias, J. Verstraten, C. Daix, B. Peaudecerf, T. de Jongh, and T. Yefsah, "Fluctuation thermometry of an atom-resolved quantum gas: beyond the fluctuation-dissipation theorem", arXiv:2502.05132 (2025) (See pages 36, 131, 154).

[180] M. Cetina et al., "Ultrafast many-body interferometry of impurities coupled to a fermi sea", Science **354** (2016) (See page 36).

[181] N. Darkwah Oppong, L. Riegger, O. Bettermann, M. Höfer, J. Levinsen, M. M. Parish, I. Bloch, and S. Fölling, "Observation of coherent multiorbital polarons in a two-dimensional fermi gas", Phys. Rev. Lett. **122** (2019) (See page 36).

[182] F. Scazza, M. Zaccanti, P. Massignan, M. M. Parish, and J. Levinsen, "Repulsive Fermi and Bose polarons in quantum gases", Atoms **10** (2022) (See page 36).

[183] J. Kondo, "Resistance minimum in dilute magnetic alloys", Progress of theoretical physics **32** (1964) (See page 36).

[184] A. C. Hewson, *The Kondo problem to heavy fermions* (Cambridge university press, 1997) (See page 37).

[185] D. Goldhaber-Gordon, H. Shtrikman, D. Mahalu, D. Abusch-Magder, U Meirav, and M. Kastner, "Kondo effect in a single-electron transistor", Nature **391** (1998) (See page 37).

[186] M. Pustilnik and L. Glazman, "Kondo effect in quantum dots", Journal of Physics: Condensed Matter **16** (2004) (See page 37).

[187] P. Coleman, C Pépin, Q. Si, and R. Ramazashvili, "How do Fermi liquids get heavy and die?", Journal of Physics: Condensed Matter **13** (2001) (See page 37).

[188] Q. Si and F. Steglich, "Heavy fermions and quantum phase transitions", Science **329** (2010) (See page 37).

[189] M. Foss-Feig, M. Hermele, and A. M. Rey, "Probing the Kondo lattice model with alkaline-earth-metal atoms", Phys. Rev. A **81** (2010) (See page 37).

[190] M. Foss-Feig, M. Hermele, V. Gurarie, and A. M. Rey, "Heavy fermions in an optical lattice", Phys. Rev. A **82** (2010) (See page 37).

[191] S. Goto and I. Danshita, "Quasiexact Kondo dynamics of fermionic alkaline-earth-like atoms at finite temperatures", Phys. Rev. Lett. **123** (2019) (See page 37).

[192] S. Brandstetter, C. Heintze, P. Hill, P. M. Preiss, M. Gałka, and S. Jochim, "Magnifying the wave function of interacting fermionic atoms", Phys. Rev. Lett. **135** (2025) (See pages 37, 122, 127, 155).

[193] M. Knap, A. Shashi, Y. Nishida, A. Imambekov, D. A. Abanin, and E. Demler, "Time-dependent impurity in ultracold fermions: orthogonality catastrophe and beyond", Phys. Rev. X **2** (2012) (See page 37).

[194] P. Nordlander, M. Pustilnik, Y. Meir, N. S. Wingreen, and D. C. Langreth, "How long does it take for the Kondo effect to develop?", Phys. Rev. Lett. **83** (1999) (See page 37).

[195] W. Lunden, L. Du, M. Cantara, P. Barral, A. O. Jamison, and W. Ketterle, "Enhancing the capture velocity of a Dy magneto-optical trap with two-stage slowing", Phys. Rev. A **101** (2020) (See pages 39, 47, 88).

[196] B. Plotkin-Swing, A. Wirth, D. Gochnauer, T. Rahman, K. E. McAlpine, and S. Gupta, "Crossed-beam slowing to enhance narrow-line ytterbium magneto-optic traps", Review of Scientific Instruments **91** (2020) (See pages 39, 47, 88).

[197] A. Trenkwalder, M. Zaccanti, and N. Poli, "A flexible system-on-a-chip control hardware for atomic, molecular, and optical physics experiments", Review of Scientific Instruments **92** (2021) (See page 40).

[198] P. T. Starkey, "A software framework for control and automation of precisely timed experiments", PhD diss. Monash University (2019) (See page 40).

[199] M. Miranda, A. Nakamoto, Y. Okuyama, A. Noguchi, M. Ueda, and M. Kozuma, "All-optical transport and compression of ytterbium atoms into the surface of a solid immersion lens", Phys. Rev. A **86** (2012) (See pages 43, 103).

[200] G. Pagano, M. Mancini, G. Cappellini, L. Livi, C. Sias, J. Catani, M. Inguscio, and L. Fallani, "Strongly interacting gas of two-electron fermions at an orbital Feshbach resonance", Phys. Rev. Lett. **115** (2015) (See page 45).

[201] P. Holzenkamp, "An optical dipole trap with tunable geometry for dysprosium", Bachelor thesis, Heidelber University (2020) (See page 50).

[202] E. D. Black, "An introduction to Pound–Drever–Hall laser frequency stabilization", American Journal of Physics **69** (2001) (See pages 51, 53–55).

[203] S. Sbernardori, "Coherent control of the ytterbium atom optical qubit", Master thesis, Trieste University (2024) (See pages 52, 53).

[204] E. A. Donley, T. P. Heavner, F. Levi, M. Tataw, and S. R. Jefferts, "Double-pass acousto-optic modulator system", Review of Scientific Instruments **76** (2005) (See page 53).

[205] J. N. Tinsley, S. Bandarupally, J.-P. Penttinen, S. Manzoor, S. Ranta, L. Salvi, M. Guina, and N. Poli, "Watt-level blue light for precision spectroscopy, laser cooling and trapping of strontium and cadmium atoms", Opt. Express **29** (2021) (See page 55).

[206] G. D. Domenico, S. Schilt, and P. Thomann, "Simple approach to the relation between laser frequency noise and laser line shape", Appl. Opt. **49** (2010) (See page 55).

[207] E. Pultinevicius, M. Rockenhäuser, F. Kogel, P. Groß, T. Garg, O. E. Prochnow, and T. Langen, "A scalable scanning transfer cavity laser stabilization scheme based on the Red Pitaya STEMlab platform", Review of Scientific Instruments **94** (2023) (See page 57).

[208] A. Holman, Y. Xu, X. Sun, J. Wu, M. Wang, B. Seo, N. Yu, and S. Will, "Trapping of single atoms in metasurface optical tweezer arrays", arXiv:2411.05321 (2024) (See page 79).

[209] W. S. Bakr, J. I. Gillen, A. Peng, S. Fölling, and M. Greiner, "A quantum gas microscope for detecting single atoms in a Hubbard-regime optical lattice", Nature **462** (2009) (See pages 79, 103, 122).

[210] J. F. Sherson, C. Weitenberg, M. Endres, M. Cheneau, I. Bloch, and S. Kuhr, "Single-atom-resolved fluorescence imaging of an atomic Mott insulator", Nature **467** (2010) (See pages 79, 103, 122).

[211] A. Impertro, J. F. Wienand, S. Häfele, H. von Raven, S. Hubele, T. Klostermann, C. R. Cabrera, I. Bloch, and M. Aidelsburger, "An unsupervised deep learning algorithm for single-site reconstruction in quantum gas microscopes", Commun. Phys. **6** (2023) (See pages 79, 122, 147).

[212] C. M. Holland, Y. Lu, and L. W. Cheuk, "Bichromatic imaging of single molecules in an optical tweezer array", Phys. Rev. Lett. **131** (2023) (See page 81).

[213] P. Ilzhöfer, G. Durastante, A. Patscheider, A. Trautmann, M. J. Mark, and F. Ferlaino, "Two-species five-beam magneto-optical trap for erbium and dysprosium", Phys. Rev. A **97** (2018) (See pages 82, 83, 153).

[214] J. Arlt, O. Maragò, S. Webster, S. Hopkins, and C. Foot, "A pyramidal magneto-optical trap as a source of slow atoms", Optics Communications **157** (1998) (See page 83).

[215] A. Camposeo, A. Piombini, F. Cervelli, F. Tantussi, F. Fuso, and E. Arimondo, "A cold cesium atomic beam produced out of a pyramidal funnel", Optics Communications **200** (2001) (See page 83).

[216] C. Nshii, M. Vangeleyn, J. P. Cotter, P. F. Griffin, E. A Hinds, C. N. Ironside, P. See, A. G. Sinclair, E. Riis, and A. S. Arnold, "A surface-patterned chip as a strong source of ultracold atoms for quantum technologies", Nature Nanotechnology **8** (2013) (See page 83).

[217] J. P. McGilligan, P. F. Griffin, R. Elvin, S. J. Ingleby, R. Erling, and A. S. Arnold, "Grating chips for quantum technologies", Scientific Reports **7** (2017) (See page 83).

[218] G. A. Phelps, A. Hébert, A. Krahn, S. Dickerson, F. Öztürk, S. Ebadi, L. Su, and M. Greiner, "Sub-second production of a quantum degenerate gas", arXiv:2007.10807 (2020) (See page 83).

[219] T. Kuwamoto, K. Honda, Y. Takahashi, and T. Yabuzaki, "Magneto-optical trapping of Yb atoms using an intercombination transition", Phys. Rev. A **60** (1999) (See page 88).

[220] J. Lee, J. H. Lee, J. Noh, and J. Mun, "Core-shell magneto-optical trap for alkaline-earth-metal-like atoms", Phys. Rev. A **91** (2015) (See page 88).

[221] B. Seo, P. Chen, Z. Chen, W. Yuan, M. Huang, S. Du, and G.-B. Jo, "Efficient production of a narrow-line erbium magneto-optical trap with two-stage slowing", Phys. Rev. A **102** (2020) (See page 88).

[222] T. Mukaiyama, H. Katori, T. Ido, Y. Li, and M. Kuwata-Gonokami, "Recoil-limited laser cooling of ^{87}Sr atoms near the fermi temperature", Phys. Rev. Lett. **90** (2003) (See page 91).

[223] S. Stellmer, F. Schreck, and T. C. Killian, "Degenerate quantum gases of strontium", in *Annu. rev. cold atoms mol.* (2014) Chap. Chapter 1 (See page 91).

[224] A. Fuhrmanek, Y. R. P. Sortais, P. Grangier, and A. Browaeys, "Measurement of the atom number distribution in an optical tweezer using single-photon counting", Phys. Rev. A **82** (2010) (See pages 95, 134).

[225] P. Sompet, A. V. Carpentier, Y. H. Fung, M. McGovern, and M. F. Andersen, "Dynamics of two atoms undergoing light-assisted collisions in an optical microtrap", Phys. Rev. A **88** (2013) (See pages 95, 133, 134, 138).

[226] S. Stellmer, B. Pasquiou, R. Grimm, and F. Schreck, "Laser cooling to quantum degeneracy", Phys. Rev. Lett. **110** (2013) (See pages 98, 100).

[227] C. Gross and I. Bloch, "Quantum simulations with ultracold atoms in optical lattices", Science **357** (2017) (See pages 103, 122).

[228] A. Mazurenko, C. S. Chiu, G. Ji, M. F. Parsons, M. Kanász-Nagy, R. Schmidt, F. Grusdt, E. Demler, D. Greif, and M. Greiner, "A cold-atom Fermi-Hubbard antiferromagnet", Nature **545** (2017) (See page 103).

[229] R. Yao, S. Chi, M. Wang, R. J. Fletcher, and M. Zwierlein, "Measuring pair correlations in Bose and Fermi gases via atom-resolved microscopy", Phys. Rev. Lett. **134** (2025) (See pages 103, 127, 146, 152, 154).

[230] T. de Jongh, J. Verstraten, M. Dixmerias, C. Daix, B. Peaudecerf, and T. Yefsah, "Quantum gas microscopy of fermions in the continuum", Phys. Rev. Lett. **134** (2025) (See pages 103, 127, 146, 152, 154).

[231] J. Xiang, E. Cruz-Colón, C. C. Chua, W. R. Milner, J. de Hond, J. F. Fricke, and W. Ketterle, "In situ imaging of the thermal de Broglie wavelength in an ultracold Bose gas", Phys. Rev. Lett. **134** (2025) (See pages 103, 127, 152, 154).

[232] R Bücker, A Perrin, S Manz, T Betz, C. Koller, T Plisson, J Rottmann, T Schumm, and J Schmiedmayer, "Single-particle-sensitive imaging of freely propagating ultracold atoms", New Journal of Physics **11** (2009) (See pages 103, 105).

[233] L. Su, A. Douglas, M. Szurek, R. Groth, S. F. Ozturk, A. Krahn, A. H. Hébert, G. A. Phelps, S. Ebadi, S. Dickerson, et al., "Dipolar quantum solids emerging in a hubbard quantum simulator", Nature **622** (2023) (See pages 103, 122, 134, 154).

[234] L. Su, A. Douglas, M. Szurek, A. H. Hébert, A. Krahn, R. Groth, G. A. Phelps, O. Marković, and M. Greiner, "Fast single atom imaging for optical lattice arrays", Nat. Comm. **16** (2025) (See pages 103–105, 107–109, 122, 127, 128, 133, 134, 153).

[235] W. P. Su, J. R. Schrieffer, and A. J. Heeger, "Solitons in Polyacetylene", Phys. Rev. Lett. **42** (1979) (See page 104).

[236] R. G. Littlejohn, *Representations of the angular momentum operators and rotations*, `https://bohr.physics.berkeley.edu/classes/221/1112/notes/repsamos.pdf`, 2019 (See page 108).

[237] R. G. Littlejohn, *Emission and absorption of radiation*, `https://bohr.physics.berkeley.edu/classes/221/1112/notes/radnmatt.pdf`, 2020 (See page 108).

[238] K. Honda, Y. Takahashi, T. Kuwamoto, M. Fujimoto, K. Toyoda, K. Ishikawa, and T. Yabuzaki, "Magneto-optical trapping of Yb atoms and a limit on the branching ratio of the $^1P_1$ state", Phys. Rev. A **59** (1999) (See page 113).

[239] T. Loftus, J. R. Bochinski, R. Shivitz, and T. W. Mossberg, "Power-dependent loss from an ytterbium magneto-optic trap", Phys. Rev. A **61** (2000) (See pages 113, 116).

[240] K. Blagoev and V. Komarovskii, "Lifetimes of levels of neutral and singly ionized lanthanide atoms", Atomic Data and Nuclear Data Tables **56** (1994) (See pages 118, 159, 160).

[241] J. Rui, D. Wei, A. Rubio-Abadal, S. Hollerith, J. Zeiher, D. M. Stamper-Kurn, C. Gross, and I. Bloch, "A subradiant optical mirror formed by a single structured atomic layer", Nature **583** (2020) (See page 122).

[242] L. Asteria, H. P. Zahn, M. N. Kosch, K. Sengstock, and C. Weitenberg, "Quantum gas magnifier for sub-lattice-resolved imaging of 3D quantum systems", Nature **599** (2021) (See pages 122, 127).

[243] A. Omran, M. Boll, T. A. Hilker, K. Kleinlein, G. Salomon, I. Bloch, and C. Gross, "Microscopic observation of Pauli blocking in degenerate fermionic lattice gases", Phys. Rev. Lett. **115** (2015) (See page 122).

[244] A La Rooij, C Ulm, E Haller, and S Kuhr, "A comparative study of deconvolution techniques for quantum-gas microscope images", New J. Phys. **25** (2023) (See page 122).

[245] L. R. Picard, M. J. Mark, F. Ferlaino, and R. van Bijnen, "Deep learning-assisted classification of site-resolved quantum gas microscope images", Meas. Sci. Technol. **31** (2019) (See page 122).

[246] A Fuhrmanek, A. M. Lance, C Tuchendler, P Grangier, Y. R. P. Sortais, and A Browaeys, "Imaging a single atom in a time-of-flight experiment", New Journal of Physics **12** (2010) (See pages 127–129).

[247] N. Gemelke, X. Zhang, C.-L. Hung, and C. Chin, "In situ observation of incompressible Mott-insulating domains in ultracold atomic gases", Nature **460** (2009) (See page 129).

[248] Q. Zhou and T.-L. Ho, "Universal thermometry for quantum simulation", Phys. Rev. Lett. **106** (2011) (See page 129).

[249] T. Hartke, B. Oreg, N. Jia, and M. Zwierlein, "Doublon-hole correlations and fluctuation thermometry in a Fermi-Hubbard gas", Phys. Rev. Lett. **125** (2020) (See pages 129, 133, 134).

[250] W. Ketterle and M. W. Zwierlein, "Making, probing and understanding ultracold Fermi gases", La Rivista del Nuovo Cimento **31** (2008) (See page 129).

[251] J. Verstraten, K. Dai, M. Dixmerias, B. Peaudecerf, T. de Jongh, and T. Yefsah, "In situ imaging of a single-atom wave packet in continuous space", Phys. Rev. Lett. **134** (2025) (See pages 131, 154).

[252] M. Brown, S. Muleady, W. Dworschack, R. Lewis-Swan, A. Rey, O Romero-Isart, and C. Regal, "Time-of-flight quantum tomography of an atom in an optical tweezer", Nature Physics **19** (2023) (See page 131).

[253] M. T. DePue, C. McCormick, S. L. Winoto, S. Oliver, and D. S. Weiss, "Unity occupation of sites in a 3D optical lattice", Phys. Rev. Lett. **82** (1999) (See pages 133, 134).

[254] A. Fuhrmanek, R. Bourgain, Y. R. P. Sortais, and A. Browaeys, "Light-assisted collisions between a few cold atoms in a microscopic dipole trap", Phys. Rev. A **85** (2012) (See pages 133, 134, 138, 139).

[255] P. M. Preiss, R. Ma, M. E. Tai, J. Simon, and M. Greiner, "Quantum gas microscopy with spin, atom-number, and multilayer readout", Phys. Rev. A **91** (2015) (See pages 133, 134).

[256] M. Boll, T. A. Hilker, G. Salomon, A. Omran, J. Nespolo, L. Pollet, I. Bloch, and C. Gross, "Spin- and density-resolved microscopy of antiferromagnetic correlations in Fermi-Hubbard chains", Science **353** (2016) (See pages 133, 134).

[257] M. L. Prichard, B. M. Spar, I. Morera, E. Demler, Z. Z. Yan, and W. S. Bakr, "Directly imaging spin polarons in a kinetically frustrated Hubbard system", Nature **629** (2024) (See pages 133, 134).

[258] M. Lebrat, M. Xu, L. H. Kendrick, A. Kale, Y. Gang, P. Seetharaman, I. Morera, E. Khatami, E. Demler, and M. Greiner, "Observation of Nagaoka polarons in a Fermi-Hubbard quantum simulator", Nature **629** (2024) (See pages 133, 134).

[259] M. Holten, L. Bayha, K. Subramanian, C. Heintze, P. M. Preiss, and S. Jochim, "Observation of pauli crystals", Phys. Rev. Lett. **126** (2021) (See pages 133, 146).

[260] A Goban, R. Hutson, G. Marti, S. Campbell, M. Perlin, P. Julienne, J. D'incao, A. Rey, and J Ye, "Emergence of multi-body interactions in a fermionic lattice clock", Nature **563** (2018) (See page 134).

[261] W. R. Milner, L. Yan, R. B. Hutson, C. Sanner, and J. Ye, "High-fidelity imaging of a band insulator in a three-dimensional optical lattice clock", Phys. Rev. A **107** (2023) (See page 134).

[262] D. Barredo, S. de Léséleuc, V. Lienhard, T. Lahaye, and A. Browaeys, "An atom-by-atom assembler of defect-free arbitrary two-dimensional atomic arrays", Science **354** (2016) (See page 138).

[263] M. Weyland, S. S. Szigeti, R. A. B. Hobbs, P. Ruksasakchai, L. Sanchez, and M. F. Andersen, "Pair correlations and photoassociation dynamics of two atoms in an optical tweezer", Phys. Rev. Lett. **126** (2021) (See page 138).

[264] S. K. Pampel, M. Marinelli, M. O. Brown, J. P. D'Incao, and C. A. Regal, "Quantifying light-assisted collisions in optical tweezers across the hyperfine spectrum", Phys. Rev. Lett. **134** (2025) (See pages 138, 139, 141, 143, 154).

[265] D. S. Grün, L. Bellinato Giacomelli, A. Tashchilina, R. Donofrio, F. Borchers, T. Bland, M. J. Mark, and F. Ferlaino, "Light-assisted collisions in tweezer-trapped lanthanides", arXiv:2506.05123 (2025) (See page 138).

[266] A. V. Carpentier, Y. H. Fung, P. Sompet, A. J. Hilliard, T. G. Walker, and M. F. Andersen, "Preparation of a single atom in an optical microtrap", Laser Physics Letters **10** (2013) (See page 139).

[267] Y. Fung and M. Andersen, "Efficient collisional blockade loading of a single atom into a tight microtrap", New Journal of Physics **17** (2015) (See page 139).

[268] D. R. Fernandes, F. Sievers, N. Kretzschmar, S. Wu, C. Salomon, and F. Chevy, "Sub-doppler laser cooling of fermionic ^{40}K atoms in three-dimensional gray optical molasses", Europhysics Letters **100** (2012) (See page 140).

[269] A. T. Grier, I. Ferrier-Barbut, B. S. Rem, M. Delehaye, L. Khaykovich, F. Chevy, and C. Salomon, "Lambda-enhanced sub-Doppler cooling of lithium atoms in D1 gray molasses", Phys. Rev. A **87** (2013) (See page 140).

[270] P. A. Murthy, D. Kedar, T. Lompe, M. Neidig, M. G. Ries, A. N. Wenz, G. Zürn, and S. Jochim, "Matter-wave Fourier optics with a strongly interacting two-dimensional fermi gas", Phys. Rev. A **90** (2014) (See page 147).

[271] S. Omanakuttan, A. Mitra, M. J. Martin, and I. H. Deutsch, "Quantum optimal control of ten-level nuclear spin qudits in ^{87}Sr", Phys. Rev. A **104** (2021) (See page 153).

[272] D. González-Cuadra, T. V. Zache, J. Carrasco, B. Kraus, and P. Zoller, "Hardware efficient quantum simulation of non-abelian gauge theories with qudits on rydberg platforms", Phys. Rev. Lett. **129** (2022) (See page 153).

[273] H. Ahmed, A. Litvinov, P. Guesdon, E. Maréchal, J. Huckans, B. Pasquiou, B. Laburthe-Tolra, and M. Robert-de Saint-Vincent, "Coherent control over the high-dimensional space of the nuclear spin of alkaline-earth atoms", PRX Quantum **6** (2025) (See page 153).

[274] L. Su, R. Sahay, M. Szurek, A. Douglas, O. Markovic, C. B. Dag, R. Verresen, and M. Greiner, "Topological phases, criticality, and mixed state order in a Hubbard quantum simulator", arXiv:2505.17009 (2025) (See page 154).

[275] S. Vigneri, "Realizzazione di un reticolo ottico "accordion" per l'intrappolamento di atomi di itterbio in due dimensioni", Master thesis, Trieste University (2022) (See page 155).

[276] Y. Takasu, K. Komori, K. Honda, M. Kumakura, T. Yabuzaki, and Y. Takahashi, "Photoassociation spectroscopy of laser-cooled ytterbium atoms", Phys. Rev. Lett. **93** (2004) (See pages 159, 160).

[277] K. Beloy, J. A. Sherman, N. D. Lemke, N. Hinkley, C. W. Oates, and A. D. Ludlow, "Determination of the $5d6s\,^3D_1$ state lifetime and blackbody-radiation clock shift in Yb", Phys. Rev. A **86** (2012) (See page 159).

[278] M Baumann, M Braun, A Gaiser, and H Liening, "Radiative lifetimes and g_J factors of low-lying even-parity levels in the Yb I spectrum", Journal of Physics B: Atomic and Molecular Physics **18** (1985) (See page 159).

[279] B. Karaçoban and L Özdemır, "Energies, Landé factors, and lifetimes for some excited levels of neutral ytterbium (Z= 70)", Acta Physica Polonica A **119** (2011) (See page 159).

Acknowledgments

Questi anni di dottorato sono stati un viaggio intenso, pieno di momenti felici, momenti meno felici, grandi e soddisfazioni e anche qualche delusione. In tanti momenti avrei voluto ringraziare qualcuno per un risultato condiviso o per un supporto in un momento difficile. Non sempre l'ho fatto e spero, in piccola parte, di riassumere qua i miei ringraziamenti alle persone che mi sono state vicine in questo percorso.
Grazie Francesco per tutto quello che mi hai insegnato in questi anni, per la fiducia e stima che mi hai dimostrato. costruire il lab è stata una vera sfida ma sono davvero soddisfatto dei nostri risultati. Grazie soprattutto per avermi insegnato come stare in laboratorio e cosa significhi fare scienza, per essere stato una guida e un modello in questi anni. Costruire il lab è stata una vera sfida ma sono davvero soddisfatto dei nostri risultati, grazie perchè senza di te questo non sarebbe stato possibile.
Grazie Omar, la tua presenza in questi anni è stata fondamentale. Quando ci siamo conosciuti il lab non aveva neanche i controsoffitti, negli anni siamo cresciuti insieme a lui. Congratulazioni per il tuo dottorato e tutti i risultati ottenuti, è stata dura ma ce l'abbiamo fatta! Ho in mente infiniti momenti passati assieme, dalla caccia alla prima fluorescenza con gli oscilloscopi coperti dalle magliette agli allenamenti a Barcola (essere senza maglietta è chiaramente un tema comune). Grazie per essere stato un amico, un complice e un compagno per tutti questi anni, nei momenti felici e anche in quelli più difficili.
Grazie Riccardo per tutto il tempo e il lavoro condiviso. Grazie per il prezioso aiuto che hai sempre offerto e per la pazienza con cui mi hai(ci siamo) sopportato(i) quando eravamo in disaccordo, e quando dovevi ascoltare le mie lamentele o preoccupazioni. Il tuo approccio così diverso dal mio ha portato a confronti stimolanti e mi ha aiutato a mettermi in discussione e guardare le cose da un punto di vista diverso. Tieni duro che sei al rettilineo finale!
Grazie Sara per la pazienza con cui hai sopportato i miei stress, per essere sempre disponibile al dialogo anche quando non la vediamo allo stesso modo e per il prezioso lavoro in lab. Grazie anche a Nino, assieme avete portato un pò di gioventù e leggerezza nel gruppo. Il futuro del lab è nelle vostre mani, non vedo l'ora di vedere i vostri risultati!
Grazie Matteo per il grande contributo scientifico e umano che hai portato al gruppo. Avere anche il tuo punto di vista, spesso da un angolo leggermente diverso dal nostro, è una grandissima ricchezza per il lab. Grazie anche a Christian e Federica, non abbiamo lavorato molto assieme ma è sempre stato un piacere condividere momenti con voi. In bocca al lupo per il vostro lab! Spero di tornare presto a Trieste per vederlo costruito e operativo.
Thank you Philipp for the time spent together, it has been great and too short. Your enthusiasm and passion are really inspiring and I greatly enjoyed doing physics with you. Thank you also for your counsel about future and life choice, I am sure we will see each other soon. Thank you Wenliang for the help and technical knowledge you provided in the lab. Especially thank you for being an extremely nice and fun person, your wisdom and unique sayings will not be forgotten. I hope you are having a great time with your wife and daughter in Shanxi.
Vorrei poi ringraziare anche tutte le persone che sono passate per il lab in questi anni e quelle che ci hanno aiutato in tutti gli aspetti tecnici del nostro lavoro. In particolare vorrei ringraziare Riccardino: grazie per il tuo importante contributo allo sviluppo del laboratorio. Ammiro molto la tua conoscenza in campi che a me sono totalmente oscuri e la tua pazienza e chiarezza nello spiegare.

Grazie Martina per l'amicizia e il supporto che è stato molto importante per me soprattutto durante i primi anni. Grazie Cami per tutto il tempo passato assieme, i momenti divertenti e per esserci stata insieme a Omar quando ne avevo più bisogno. E' stato un piacere e una fortuna conoscerti, tu e Omar vi siete scelti bene.
Un grazie speciale alla città di Trieste, un posto che ho imparato ad amare, considerare casa e che so che mi mancherà. Grazie agli amici triestini conosciuti in questi anni che ci hanno fatto sentire parte di questa città: Andrea, Sophie, Alice e Mike. Grazie a Ralph per tutti i giri in barca. Grazie al SISSA team per tutte le partite e belle serate assieme, soprattutto a Zeno per essere da anni il perno della nostra, altrimenti traballante, difesa.
Grazie a tutta la mia famiglia per avermi sempre incoraggiato. Grazie Giulia e Pietro, vorrei poter passare più tempo con voi. Grazie ai miei genitori, siete il mio riferimento per quello che vorrei ottenere dalla vita.
E, infine, grazie a te Ca. Sei la persona con cui voglio condividere tutto, i piccoli successi, i dubbi, i fallimenti. Grazie per tutti i sacrifici che hai fatto, per aver scelto di rendere Trieste anche casa tua, per vedere qualche pregio tra tutti i miei difetti. Grazie di essere te stessa. Non vedo l'ora di scoprire cosa ci aspetta nei prossimi anni. Conoscerti è stata la sorpresa più bella e inaspettata di questi anni di dottorato.

Trieste, 19/12/2025